Part Load Flow in Radial Centrifugal Pumps

THÈSE N^{O} 4422 (2009)

PRÉSENTÉE LE 3 JUILLET 2009

À LA FACULTÉ SCIENCES ET TECHNIQUES DE L'INGÉNIEUR
LABORATOIRE DE MACHINES HYDRAULIQUES
PROGRAMME DOCTORAL EN MÉCANIQUE

ÉCOLE POLYTECHNIQUE FÉDÉRALE DE LAUSANNE

POUR L'OBTENTION DU GRADE DE DOCTEUR ÈS SCIENCES

PAR

Olivier BRAUN

acceptée sur proposition du jury:

Prof. J.-F. Molinari, président du jury
Prof. F. Avellan, directeur de thèse
Prof. M. Deville, rapporteur
Dr Ph. Dupont, rapporteur
Prof. Y. Tsujimoto, rapporteur

ÉCOLE POLYTECHNIQUE
FÉDÉRALE DE LAUSANNE

Suisse
2009

wo chiemte mer hi
wenn alle seite
wo chiemte mer hi
und niemer giengte
für einisch z'luege
wohi dass me chiem
we me ging

Kurt Marti

où est-ce qu'on en arriverait
si tout le monde demandait
où on en arriverait
et que personne n'allait
pour regarder
où l'on arriverait
si on y allait

Kurt Marti

Remerciements

Le présent travail a été rendu possible uniquement par l'engagement et l'implication, de près ou de loin, d'un grand nombre de personnes auxquelles je tiens à adresser les plus sincères remerciements.

En premier, je tiens à remercier mon directeur de thèse, le Professeur François Avellan pour m'avoir accordé sa confiance et m'avoir donc permis d'effectuer ce travail de recherche. Conçu d'abord comme une étude purement numérique, il a su le rediriger au bon moment vers une étude complémentaire expérimentale, nécessaire pour aboutir à un ensemble complet. Il a à tout moment su assurer la gestion des projets et des installations du Laboratoire de Machines Hydrauliques (LMH) et m'a ainsi permis d'effectuer mes recherches dans les meilleures conditions.

Que les membres du jury, les Professeurs Yoshinobu Tsujimoto, Michel Deville et François Molinari ainsi que le Dr. Philippe Dupont, soient remerciés pour leur intérêt, leurs critiques enrichissantes et l'attention qu'ils ont portés à la relecture minutieuse de ce travail.

Ce travail n'aurait pas été possible sans le soutien financier des fonds de recherche de la CTI et SwissElectric ainsi que les contributions des partenaires industriels, Sulzer Pompes, Alstom, Voith Siemens et Andritz Hydro. Je les remercie vivement pour cela, ainsi que pour l'intérêt que leurs représentants ont apporté à mes recherches du début à la fin en y contribuant par leurs questions et leurs suggestions à l'occasion de nombreuses rencontres. Je tiens à remercier spécialement les Drs. Philippe Dupont et Johann Guelich pour leur implication dans la définition du cadre du projet de recherche qui a fondé la première phase de ma thèse.

Je tiens aussi à adresser mes remerciements aux chefs de groupe de l'équipe de simulation numérique au LMH, Jean-Louis Kueny et Pierre Maruzewski, pour avoir garanti une bonne ambiance de travail et m'avoir donné les conseils nécessaires en cas de besoin, ainsi qu'à Mohamed Farhat et l'équipe des expérimentateurs qui m'ont fait bénéficier d'équipements et de procédures de mesures établies.

Ce travail comportant des travaux numériques et expérimentaux s'appuie autant sur le soutien du system manager Philippe Cerrutti qui garantit le fonctionnement de nos moyens informatiques ainsi que de toute l'équipe des plateformes sous la direction de Henri-Pascal Mombelli ainsi que de l'équipe des mécaniciens du laboratoire sous direction de Louis Bezençon qui ont toujours répondu à tous les besoins dans les meilleurs délais et ont contribué ainsi au bon déroulement des campagnes de mesures. Que les collaborateurs du bureau d'études soient remerciés pour les fichiers CAO et les dessins techniques qu'ils ont fourni. Merci à tout le laboratoire pour l'excellent travail d'équipe et la bonne ambiance, confirmée mémorablement dans la sortie du laboratoire en été 2008 qui restera un excellent souvenir.

Ma transition douce du LMH vers le Laboratoire d'Ingénierie Numérique (LIN) en fin de thèse m'a fait découvrir d'autres perspectives. Je remercie le Professeur Michel Deville ainsi que Mark Sawley pour m'avoir laissé la liberté de gérer ce passage au mieux pour aboutir à un travail de thèse complet et de mettre parallèlement en oeuvre le savoir-faire acquis dans le domaine des turbomachines dans le contexte du voilier oiseau qu'est l'Hydroptère.

Les nombreuses discussions fructueuses entre doctorants, post-docs et stagiaires de toutes générations, que ce soit autour d'un café ou accroupis derrière un ordinateur, ont beaucoup apporté à ce travail par l'échange généreux de savoir-faire. Youcef, Lluis, Christophe, Alexandre, Ali, Cécile, Philippe, Nicolas, Stefan, Eric, Bernd, Sébastien, Vlad, Marco, Amir, Steven, soyez vivement remerciés, autant pour cela que pour toutes les activités communes au delà du laboratoire, que ce soit les compétitions internationales de fondue, les barbecues au bord du lac ou les fameux jeudis de l'angoisse par la suite!

Ainsi que le travail avec les collaborateurs et stagiaires, l'encadrement de nombreux étudiants de l'EPFL ou d'ailleurs au fil de leurs projets de semestre et de master m'a toujours donné beaucoup de satisfaction. Nombreux sont ceux qui ont su apporter de bonnes idées et des éléments de solution reliés de près ou de loin aux problématiques dont traite ce travail, et je tiens aussi à les remercier pour ces apports.

Le travail intense de recherche n'est pas possible sans les moments de détente en soirée et en weekend. Y ont partagé mes loisirs avant tout les membres du Rushteam Ecublens, autant en vélo que à pied, sous le soleil et sous la pluie, à l'air et dans ce merveilleux Lac Léman. Quand l'heure était moins à la recherche de la performance sportive et que j'étais plus disponible en fin qu'en début de soirée, c'est surtout les amatrices et amateurs de danses de salon brésiliennes de l'association Gafieira de Danse qui m'ont apporté la distraction ainsi que le soutien moral nécessaire dans la course de longue distance qu'a été la rédaction de cette thèse.

Malgré la distance qui me séparait de mes racines durant ces cinq années, modeste à l'échelle mondiale, mais assez conséquente pour empêcher de se voir très régulièrement, à savoir mes amis en Allemagne et surtout ma famille proche derrière moi m'a été d'un grand soutien. Ma soeur Isabelle et mon père Friedrich m'ont ainsi soutenu jusqu'à la fin de l'aventure. Je dédie ce document à ma mère Françoise qui nous a soudainement quitté avant l'aboutissement de ces travaux de recherche.

Résumé

Une pompe centrifuge doit contribuer à la stabilité de foctionnement de l'installation qu'elle alimente, quel que soit le point de fonctionnement. Des modifications subtiles des surfaces mouillées de pompes centrifuges radiales peuvent influencer considérablement la tendance à l'instabilité. Les mécanismes d'action de ces modifications ne sont pas complètement maîtrisés, ce qui mène à des approches empiriques coûteuses dans la solution de ces instabilités de fonctionnement.

L'écoulement dans une pompe centrifuge est fonction du temps par son principe de fonctionnement basé sur l'interaction entre la roue en rotation et les aubes du diffuseur stationnaire (interaction rotor-stator, RSI). Les écoulements à gradients de pression adverses sont potentiellement sujets au décollement de la couche limite, susceptible de mener à des écoulements asymétriques. Les nonuniformités circonférentielles qui en résultent peuvent être fixes ou tournantes dans l'espace et stationnaires ou intermittentes dans le temps. Le décollement tournant, observé dans les turbomachines thermiques et hydrauliques à débit partiel, est caractérisé par la présence de cellules de décollement dont l'ensemble tourne à une fraction de la vitesse de rotation de la roue. La complexité de l'écoulement dans les pompes centrifuges à charge partielle constitue un défi majeur pour les méthodes de simulation numérique d'écoulements.

La présente étude approche l'écoulement dans les pompes centrifuges à charge partielle par des méthodes expérimentales ainsi que des simulations numériques dernières basées sur une discrétisation par volumes finis des équations Navier-Stokes moyennées (RANS). Différents phénomènes sont mis en évidence dans trois cas étudiés. La capacité des méthodes numériques à reproduire l'écoulement de facon qualitative ainsi que leur précision quantitative sont evaluées.

L'étude numérique de l'écoulement dans une pompe-turbine de haute vitesse spécifique est établie sous les hypothèses d'un écoulement stationnaire et d'une périodicité entre les canaux. Les résultats mettent en évidence un changement de topologie de l'écoulement lié à une augmentation des pertes visqueuses qui se répercute sur la caractéristique énergie-débit de la pompe, augmentant ainsi le risque d'instabilité de fonctionnement. Au dessous d'un seuil de débit critique, un écoulement sain avec des poches de décollement localisées sur les aubes de diffuseur au centre du canal donne place à un écoulement asymétrique caractérisé par une dissipation visqueuse accrue dans une large structure comparable à un vortex.

En plus des décollements dans certains canaux du diffuseur, une étude numérique sur une pompe à double ouïe met en évidence une interaction possible entre un décollement unilatéral dans le diffuseur et un déséquilibre des débits à travers les deux côtés de la roue. L'augmentation des pertes visqueuses liée à l'apparition de ce déséquilibre correspond bien

à un segment de pente positive sur la caractéristique énergie-débit, cependant le débit auquel elle apparait diffère sensiblement de celui mesuré.

Différents modes de décollement tournant sont identifiés par des mesures de pression instationnaires dans une pompe-turbine de faible vitesse spécifique. Selon le point de fonctionnement, ces modes présentent entre 3 et 5 cellules de décollement, l'ensemble tourne à des vitesses de rotation entre 0.016 et 0.028 fois celle de la roue. Pour des conditions avec un mode à 4 cellules bien établi, des mesures de vitesse par la méthode Laser-Doppler sont effectuées. L'évolution du champ de vitesse en fonction du passage des zones de décollement est reconstruit à l'aide d'une phase définie à partir d'un signal de pression mesuré simultanément. Des simulations numériques instationnaires reproduisent le mode de décollement tournant à 4 cellules et des champs de vitesse semblables à ceux mesurés, cependant pour des conditions de débit nettement différentes de celles de l'expérience.

Compte tenu des défauts quantitatifs des résultats des simulations numériques effectuées, une nouvelle approche de modélisation est proposée. La partie majeure du domaine de simulation tridimensionelle est remplacée par un modèle monodimensionnel, ce qui permet une économie considérable en ressources de calcul, permettant ainsi d'améliorer la modélisation dans le restant du domaine à coût de calcul constant. L'approche est validée par comparaison aux calculs comprenant le domaine tridimensionnel complet sur le cas présentant le décollement tournant ainsi que dans le cas du déséquilibre des débits dans la pompe double ouïe. La cohérence des résultats obtenus est satisfaisante, ainsi l'approche est applicable à de nombreuses applications dans le domaine des turbomachines. Elle peut par exemple fournir des conditions aux limites physiquement cohérentes pour les simulations du phénomène de la torche dans les diffuseur de turbines hydrauliques et cela à un coût de calcul raisonnable. La méthode établie ouvre une voie pour des études paramétriques variant délibérément les quantités de l'écoulement moyen et de la turbulence sur les sections de connection des domaines de calcul mono- et tridimensionnels.

Mots-clés:

Pompe-turbine, simulation numérique, moyenne de Reynolds, décollement tournant, Interaction rotor-stator, instabilité, vélocimétrie laser-Doppler, moyenne de phase

Zusammenfassung

Eine wesentliche Anforderung an Kreiselpumpen ist, dass sie zu einem stabilen Betrieb der umgebenden Anlage beitragen. Geringfügige Veränderungen an den strömungsführenden Flächen radialer Kreiselpumpen können die Betriebsstabilität der Anlagen erheblich beeinflussen. Die Wirkungsweise derartiger Veränderungen ist nicht vollständig erforscht, so dass derzeit bei notwendigen Verbesserungen der Betriebsstabilität aufwändige empirische Vorgehensweisen die Regel sind.

Die Strömung in Kreiselpumpen ist zeitabhängig aufgrund des Wirkprinzips und der daraus folgenden Wechselwirkung des rotierenden Laufrads mit der stillstehenden Diffusorbeschaufelung (Rotor-Stator-Interaktion, RSI). Des Weiteren tendieren die auftretenden Strömungen entgegen dem Druckgradienten zu Grenzschichtablösung und Rückströmungen. Letztere führen unter Umständen zu Strömungsbildern, die der Symmetrie und Periodizität der Pumpe nicht entsprechen. Ungleichförmigkeiten in Umfangsrichtung können ebenso ortsfest wie rotierend und gleichermassen stetig wie intermittent auftreten. Als Rotating Stall wird das Auftreten mehrerer Ablösegebiete am Umfang bezeichnet, die mit einem Bruchteil der Laufraddrehzahl umlaufen. Die hieraus resultierende komplexe Teillastströmung in radialen Kreiselpumpen stellt eine Herausforderung für numerische Strömungssimulationsverfahren dar.

Die vorliegende Arbeit untersucht die Teillastströmung in Kreiselpumpen mit experimentellen Methoden und numerischen Simulationen unter Anwendung der finite-Volumen Diskretisierung der reynoldsgemittelten Navier-Stokes (RANS) Gleichungen. Verschiedene Aspekte werden anhand von drei Testfällen beleuchtet und die Fähigkeit numerischer Methoden, die auftretende Strömung qualitativ und quantitativ richtig wiederzugeben, wird beurteilt.

Bei numerischen Untersuchungen an einer Pumpturbine hoher spezifischer Drehzahl werden zeitunabhängige Strömung sowie Periodizität unter den Schaufelkanälen vorausgesetzt. Die Ergebnisse zeigen einen Zusammenhang zwischen einer Veränderung des Strömungsbildes und erhöhten viskosen Verlusten auf. Diese schlagen sich auf die Kennlinie der Pumpturbine in einer Art und Weise nieder, die die Betriebsstabilität nachteilig beeinflusst. Beim Unterschreiten eines bestimmten Förderstroms geht die darüber bestehende geradlinige Durchströmung mit mittig im Kanal liegenden Ablösungen an den Leitschaufeln in eine asymmetrische Strömung über. Diese wirbelartige Strömung generiert erhebliche Strömungsverluste.

Neben der Strömungsablösung in einzelnen Diffusorkanälen zeigen numerische Simulationen der zeitabhängigen Strömung in einer doppelflutigen Kreiselpumpe eine mögliche Wechselwirkung einer einseitigen Strömungsablösung im Diffusor mit einem Ungleichgewicht der Förderströme der beiden Laufradseiten. Die Zunahme der Strömungsverluste

mit dem Auftreten dieses Ungleichgewichts entspricht einem Abschnitt positiver Steigung auf der gemessenen Kennlinie, jedoch entspricht der zugehörige Förderstrom nicht dem experimentell ermittelten.

Unterschiedliche Modi des Rotating Stall werden durch transiente Druckmessungen in einer Pumpturbine niedriger spezifischer Drehzahl identifiziert. Abhängig vom Förderstrom treten 3 bis 5 Zonen abgelöster Strömung im Diffusor auf, die mit Winkelgeschwindigkeiten vom 0.016− bis zum 0.028−fachen der Laufraddrehzahl umlaufen. Unter Bedingungen, in denen Rotating Stall mit 4 Zellen am deutlichsten auftritt, werden Strömungsgeschwindigkeiten mit den Laser-Doppler-Verfahren gemessen. Die zeitliche Abhängigkeit des Geschwindigkeitsfeldes vom Passieren der Ablösungszonen wird durch Phasenmittelung anhand einer aus Druckmessungen ermittelten Phase rekonstruiert. Numerische Simulation der zeitabhängigen Strömung ist in der Lage, Rotating Stall sowie die Geschwindigkeitsfelder qualitativ zufriedenstellend wiederzugeben, die Abweichung des dazugehörigen Förderstroms vom experimentell bestimmten ist jedoch erheblich.

In Anbetracht der quantitativen Defizite der ausgeführten numerischen Simulation wird ein neuartiger Modellansatz entwickelt: Das Ersetzen der aufwändigen 3-dimensionalen Abbildung eines Grossteils der Laufradkanäle durch ein 1-dimensionales Modell bringt eine erhebliche Einsparung an Rechenaufwand mit sich. Dies ermöglicht eine verbesserte Abbildung des verbleibenden 3-dimensionalen Rechengebiets bei gleichbleibendem Aufwand. Das Verfahren wird anhand der Fälle des Rotating Stall und des Ungleichgewichts der Laufradseitenmassenströme durch Vergleich mit den Ergebnissen aus der vollständigen 3-dimensionalen Abbildung validiert. Die zufriedenstellende Übereinstimmung qualifiziert die Vorgehensweise für zahlreiche Anwendungen im Turbomaschinenbereich, etwa können so verbesserte, zeitabhängige Eintrittsrandbedingungen für die Simulation von Wirbelzöpfen in Diffusoren von Wasserturbinen mit vertretbarem Rechenaufand generiert werden. Parameterstudien, in denen die Grössen der gemittelten Strömung sowie der Turbulenz an den modellierten Randbedingungen bewusst variiert werden, können im Rahmen dieses Verfahrens umgesetzt werden.

Schlüsselwörter:

Pumpturbine, numerische Simulation, Reynoldsgemittelte Navier-Stokes Gleichungen, Rotating Stall, Rotor-Stator-Interaktion, Instabilität, Strömungsablösung, Laser-Doppler-Velozimetrie, Phasenmittelung

Abstract

Centrifugal pumps are required to sustain a stable operation of the system they support under all operating conditions. Minor modifications of the surfaces defining the pump's water passage can influence the tendency to unstable system operation significantly. The action of such modifications on the flow are yet not fully understood, leading to costly trial and error approaches in the solution of instability problems.

The part-load flow in centrifugal pumps is inherently time-dependent due to the interaction of the rotating impeller with the stationary diffuser (Rotor-Stator Interaction, RSI). Furthermore, adverse pressure gradients in the pump diffuser may cause flow separation, potentially inducing symmetry-breaking non-uniformities, either spatially stationary or rotating and either steady or intermittent. Rotating stall, characterized by the presence of distinct cells of flow separation on the circumference, rotating at a fraction of the impeller revolution rate, has been observed in thermal and hydraulic turbomachines. Due to its complexity, the part-load flow in radial centrifugal pumps is a major challenge for numerical flow simulation methods.

The present study investigates the part-load flow in radial centrifugal pumps and pump-turbines by experimental and numerical methods, the latter using a finite volume discretization of the Reynolds-averaged Navier-Stokes (RANS) equation. Physical phenomena of part load flow are evidenced based on three case studies, and the ability of numerical simulation methods to reproduce part-load flow in radial centrifugal pumps qualitatively and quantitatively is assessed.

A numerical study of the flow in a high specific speed radial pump-turbine using steady approaches and the hypothesis of angular periodicity between neighboring blade channels evidences the relation of sudden flow topology changes with an increase of viscous losses, impacting on the energy-discharge characteristic, and thus increasing the risk of unstable operation. When the flow rate drops below a critical threshold, the straight through-flow with flow separation zones attached to the guide vanes changes to an asymmetrical flow. Energy is drawn off the mean flow and dissipated in a large vortex-like structure.

Besides flow separation in some diffuser channels, time-dependent numerical simulations of the flow in a double suction pump evidence a flow rate imbalance between both impeller sides interacting with asymmetric flow separation in the diffuser. Viscous losses increase substantially as this imbalance occurs, the resulting segment of positive slope in the energy-discharge characteristic is found for a flow rate sensibly different from measurements.

Different modes of rotating stall are identified by transient pressure measurements in a low-specific-speed pump-turbine, showing 3 to 5 zones of separated flow, rotating at 0.016

to 0.028 times impeller rotation rate, depending on discharge. For operating conditions where stall with 4 cells is most pronounced, velocity is measured by Laser-Doppler methods at locations of interest. The velocity field is reconstructed with respect to the passage of stall cells by definition of a stall phase obtained from simultaneous transient pressure measurements. Time-dependent numerical simulation predicting rotating stall with 4 cells shows velocity fields that are in reasonable agreement with the measured velocity fields, but occurring at a sensibly higher flow rate than found from experiments.

In consideration of the quantitative shortcomings of the numerical simulation, a novel modelling approach is proposed: Replacing the costly 3-dimensional simulation of the major part of the impeller channels by a 1-dimensional model allows a significant economy in computational resources, allowing an improved modeling for the remainder of the domain at constant computational cost. The model is validated with the challenging cases of rotating stall and impeller side flow rate imbalance. The satisfying coherence of the results with the simulation including the entire impeller channels qualifies this approach for numerous turbomachinery applications. It could also provide improved, time-dependent boundary conditions for draft tube vortex rope simulations at reasonable computational cost. Parameter studies modifying deliberately some quantities of mean flow and turbulence at the modeled boundary surfaces can be implemented in the framework of the method.

Keywords:

Pump-turbine, numerical simulation, Reynolds-averaged Navier Stokes equation, rotating stall, rotor-stator-interaction, instability, flow separation, laser-Doppler velocimetry, phase averaging

Contents

Notations

Latin

b	Channel width	[m]
f_n	Rotational frequency	[s^{-1}]
$\mathbf{f}$	Body force	[m s^{-2}]
g	Gravitational acceleration: $g \simeq 9.81$ m/s^2	[m s^{-2}]
$\mathbf{g}$	Gravitational acceleration vector, cartesian coordinates [0 0 -g]	[m s^{-2}]
k	Turbulent kinetic energy	[m^2 s^{-2}]
k_s	Circumferential stall wave number	[–]
$\mathbf{n}$	Normal vector	[–]
p	Static pressure	[Pa]
p^*	Numerical simulation pressure $p^* = p - \rho g_i X_i$	[Pa]
s	Curvilinear coordinate	[m]
t	Time	[s]
x, y, z	Cartesian coordinates	[m]
y^+	Dimensionless sublayer-scaled distance: $y^+ = \frac{\rho C_\tau y}{\mu}$	[–]
z	Number of blades, number of channels	[–]
A	Surface	[m^2]
$\mathbf{C}$	Absolute velocity	[m s^{-1}]
C	Bulk velocity	[m s^{-1}]
C_m	Meridional velocity component	[m s^{-1}]
C_n	Velocity component normal to section	[m s^{-1}]
C_u	Circumferential absolute velocity	[m s^{-1}]
C_t	Velocity component tangential to wall	[m s^{-1}]
C_τ	Friction velocity: $C_\tau = \frac{\tau_w}{\rho}$	[m s^{-1}]
$\mathbb{D}$	Rate of deformation tensor	[s^{-1}]
E	Pump specific hydraulic energy: $E = gH_I - gH_{\bar{I}}$	[J kg^{-1}]
H	Net hydraulic head	[m]
H^{rel}	Relative net hydraulic head in rotating frame	[m]
$\mathbb{K}$	Centering operator matrix $\mathbb{K} = \mathbb{I} - 1/z_b \mathbb{J}$	[–]

K	Loss coefficient	[–]
L	Length, length coordinate	[m]
L_S	System hydraulic inductance	[m^{-1}]
L_b	Impeller channel hydraulic inductance	[m^{-1}]
N	Rotational speed: N=60f$_n$	[min^{-1}]
P_h	Hydraulic Power	[W]
Q	Flow rate	[m^3 s^{-1}]
Q_L	Leakage flow rate	[m^3 s^{-1}]
R	Radius	[m]
R_b	Impeller channel hydraulic Resistance	[m^{-4}]
T	Torque	[N m]
$\mathbb{T}$	Stress tensor	[s^{-1}]
U	Peripheral velocity: $U = \omega R$	[m s^{-1}]
V	Volume	[m^3]
$\mathbf{W}$	Relative velocity	[m s^{-1}]
$\mathbf{X}$	Location vector	[m]

Greek

α	Absolute flow angle	[–]
β	Relative flow angle	[–]
β_r	Impeller channel resistance parameter	[s^{-1}]
β_L	Impeller channel impedance parameter	[m^{-1}]
β_q^*	Impeller channel flow rate parameter	[s^{-1}]
β_p^*	Impeller channel pressure impedance parameter	[s^{-1}]
γ	Body force, ref. to gravitational acceleration	[–]
ε	Turbulent dissipation rate	[m^2 s^{-3}]
	Arbitrary small value	[–]
η	Efficiency	[–]
θ	Angular coordinate	[-]
μ	Dynamic (molecular) viscosity	[kg m^{-1} s^{-1}]
μ_t	Turbulent (eddy) viscosity	[kg m^{-1} s^{-1}]
φ	Rotating Mode Phase	[–]
φ_s	Stall Phase	[–]
ρ	Density	[kg m^{-3}]
τ	Shear stress	[Pa]
ω	Rotational velocity (Impeller)	[rad s^{-1}]

ω_s	Stall rotational velocity	[rad s^{-1}]
ω	Specific dissipation rate (Turbulence)	[s^{-1}]
Δ	Peak-to-peak amplitude of phase average	[–]
Δ	Variation per time step (1D-Modelling)	[–]

Subscripts

0	Reference for non-dimensional numbers
b	Impeller (blade, domain, channel)
c	Chord
m	Mechanic (power, torque)
n	Nominal conditions
n	Normal to section
o	Guide vane (blade, domain, channel)
r	Viscous loss (energy, coefficients)
r	Rotating frame (angular coordinates)
ref	Reference value
∞	Free-stream value
s	Stationary frame (angular coordinates)
s	Stall
S	System
t	Transferred by impeller (torque, power), through impeller (flow rate)
v	Stay Vane or diffuser (blade, domain, channel)
xx	Auto-spectral power density
xy	Cross-spectral power density

Superscripts

$\bar{}$	Average quantity in Reynolds averaging
$'$	Fluctuating quantity in Reynolds averaging
$\bar{}$	Time average of measured quantity, signal mean
$\tilde{}$	Fluctuation of measured quantity, centered signal
$\hat{}$	Phase average
$'$	Quantity per channel referenced to the average of all channels
$*$	Referenced to the best efficiency point (pump)
0	Last time step value
00	Previous time step value

Dimensionless Numbers

c_f	Skin friction coefficient	$c_f = \frac{\tau}{\frac{1}{2}\rho U_{1e}^2}$
c_p	Pressure coefficient	$c_p = \frac{p - p_{ref}}{\frac{1}{2}\rho U_{1e}^2}$
C_p	Discrete Fourier transform of the pressure coefficient c_p	
Re	Reynolds number	$Re = \frac{\rho C_0 L_0}{\mu}$
ν	Specific speed coefficient	$\nu = \frac{\varphi^{1/2}}{\psi^{3/4}}$
φ	Flow rate coefficient (Pump-turbine)	$\varphi = \frac{Q}{\pi \omega R^3}$
φ	Flow rate coefficient (Centrifugal pump)	$\varphi = \frac{C_{m,1}}{U_1} = \frac{Q}{2\pi b_1 R_1 \omega R_1}$
ψ	Specific energy coefficient	$\psi = \frac{2E}{\omega^2 R^2}$

Abbreviations

EPFL	Ecole Polytechnique Fédérale de Lausanne
LMH	Laboratoire de Machines Hydrauliques
BEP	Best Efficiency Point
BPF	Blade Passing Frequency
CV	Control Volume
CFD	Computational Fluid Dynamics
DES	Detached Eddy Simulation
GV	Guide Vane
LDV	Laser Doppler Velocimetry
LE	Leading Edge
LES	Large Eddy Simulation
RANS	Reynolds Averaged Navier-Stokes
RSI	Rotor Stator Interaction
SST	Shear Stress Transport

Section Nomenclature see figure 4, p.7.

Introduction

Part Load Flow in Radial Centrifugal Pumps

Introduction to Centrifugal Pumps

Centrifugal pumps are machines converting driving mechanical power into hydraulic power of a liquid flow. Their working principle is the transfer of angular momentum from the rotating impeller to the continuous flow through the pump. The flow path remains at all times open towards the high and low energy flanges of the pump, the momentum transfer in the impeller relies exclusively on hydrodynamic effects. This classifies centrifugal pumps amongst turbomachines and distinguishes them from positive displacement pumps, relying on hydrostatic working principles. Turbocompressors are the counterparts of centrifugal pumps acting on compressible fluid flows. Turbines are turbomachines extracting power out of a fluid flow to convert it into mechanical power. The density difference of liquid versus gaseous fluids leads to very different designs, by consequence centrifugal pumps are differentiated from fans and blowers, though those are turbomachines working in regimes where the gases can be considered incompressible. The combination of a centrifugal pump with a thermal turbine as a drive instead of the widespread electrical drives is termed turbopump.

	fluid type		pumping machine	generating machine
hydraulic turbomachines	incompressible	liquid	**centrifugal pump**	hydraulic turbine
			reversible pump-turbine	
		gas	fan, blower	wind turbine
thermal turbomachines	compressible	gas	turbo-compressor	gas turbine steam turbine

Table 1: Classification of turbomachines

Centrifugal pumps are key components of numerous technical processes. Industrial pumps are deployed for example in applications in power generation, process industries and transport of fluid flows through pipelines. Simpler designs are omnipresent, e.g. sewage water pumps in domestic appliances, oil circulation pumps in engines or circulation pumps in heating installations. Prevalent working fluids are water and liquid hydrocarbons, but centrifugal pumps can be used to displace or pressurize almost any fluid, including mixtures containing gases or solids up to a certain mixture fraction. A wide spectrum of different layouts of impellers and casings exists. Multistage layouts, as in figure 1a are characterized by several impellers of identical diameter and similar design,

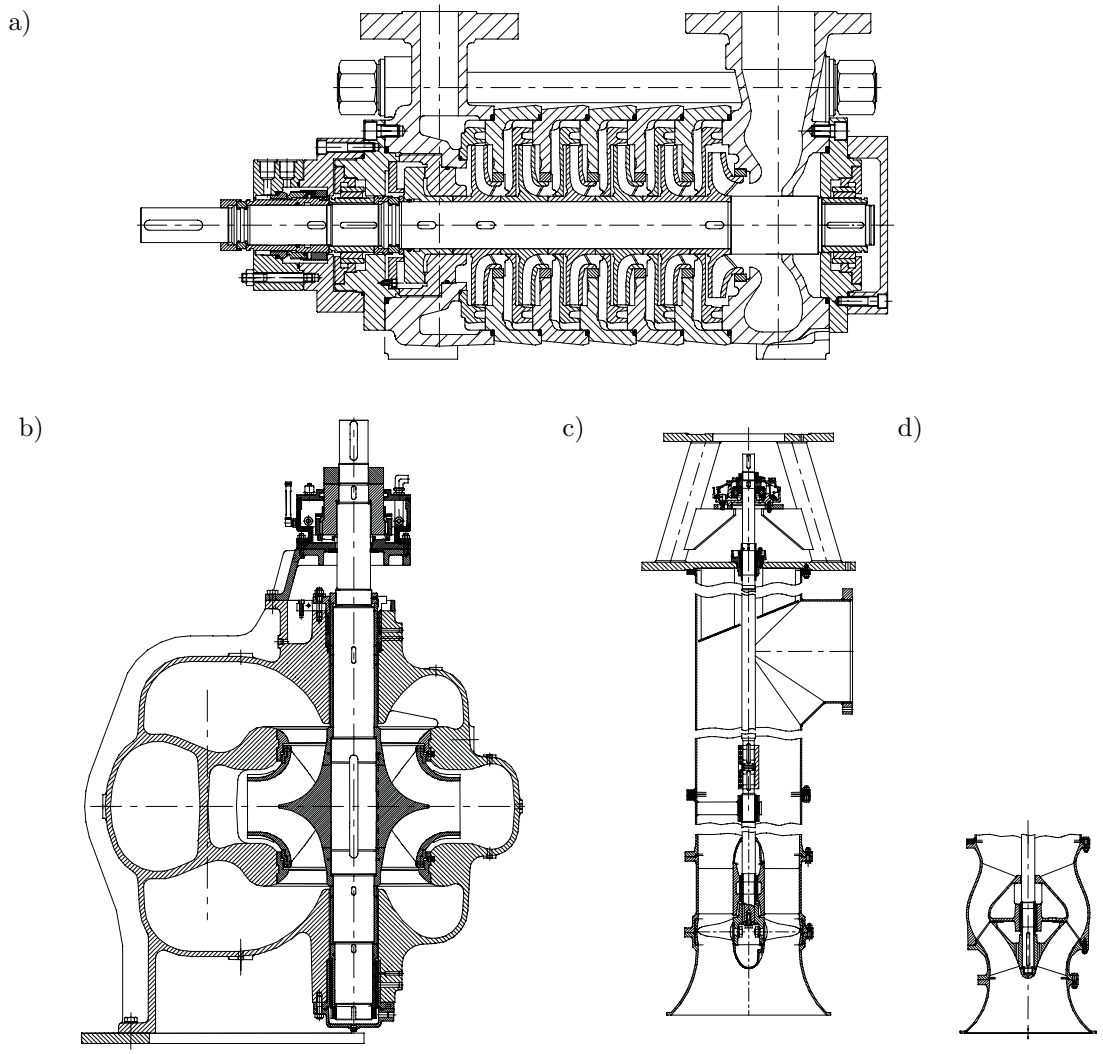

Figure 1: Centrifugal Pumps. a) Multistage segmental pump, b) Double entry vertical pump, c) Axial pump for wet-pit installation d) Semi-axial variant of c). a-d) Courtesy of Sulzer Pumps, Winterthur, [54]

the flow is guided from one impeller outlet to the next impeller inlet (eye) by stationary components termed return channels. The first and last stage can have a modified design to meet specific requirements. In the double entry or double suction layout represented in figure 1b, the two sides of the symmetrical impeller deliver the flow into a common spiral casing. In these first two examples the flow enters the impellers axially and leaves them radially on a considerably higher radius, they are therefore called radial pumps. Axial pumps, figure 1c, are designed for applications requiring high flow rates with relatively low energy input. The intermediate type of impeller, figure 1d, is termed mixed-type, semi-axial or diagonal impeller. The example shows how modified hydraulic parts can be used on identical mechanical setups. Particularly large centrifugal pumps are deployed in hydropower installations, either as reversible pump-turbines, see figure 2, or as separate units termed storage pumps.

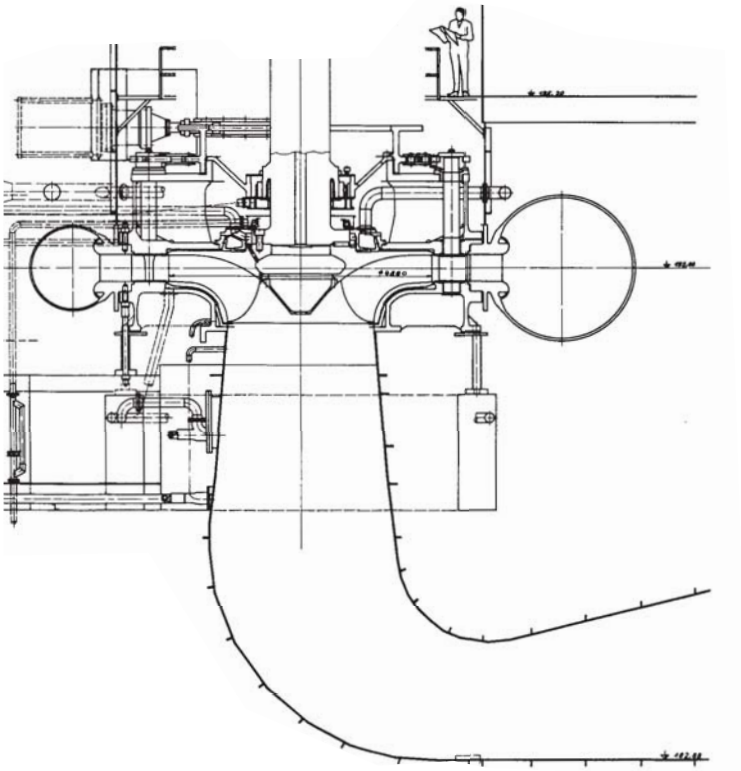

Figure 2: Reversible pump-turbine, Palmiet, South Africa, 198MW [59]

Figure 3 represents a pump in an open system with two large reservoirs defining the quantities determining the operation point of the pump and the system. Neglecting hydroacoustic phenomena caused by the compressibility of the fluid and system component deformation, the flow rate Q is constant along all the sections in the system. On an arbitrary section A_k it is obtained with the velocity vector $\mathbf{C}$ and section normal vector $\mathbf{n}$, defining the section's bulk velocity C_k:

$$Q = C_k A_k = \int_{A_k} \mathbf{C} \cdot \mathbf{n} \, dA \tag{1}$$

The mean specific hydraulic energy of a fluid in any section k is defined with pressure p, gravitational acceleration g and height coordinate Z as

$$gH_k = \frac{1}{Q} \int_{A_k} \left(\frac{p}{\rho} + gZ + \frac{C^2}{2} \right) \mathbf{C} \cdot \mathbf{n} \, dA \tag{2}$$

And we obtain the hydraulic power P_h supplied by the pump to the working fluid:

$$P_h = \rho Q (gH_I - gH_{\bar{I}}) \tag{3}$$

The specific Energy E and head H of the pump are defined as

$$E = gH = gH_I - gH_{\bar{I}} \tag{4}$$

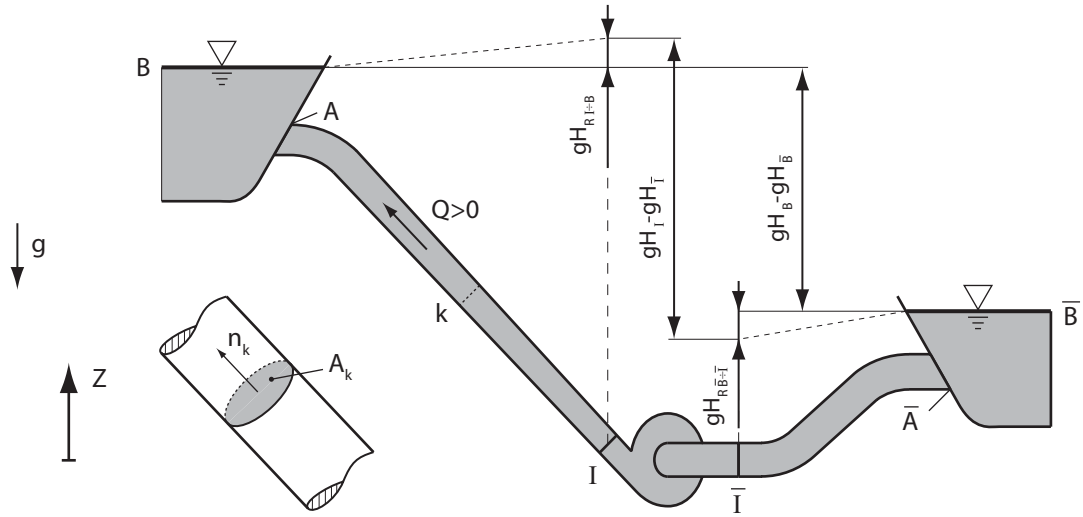

Figure 3: Centrifugal pump in a two-reservoir system

The orientation of the normal vector $\mathbf{n}$ on the sections determines the sign convention for flow rate and power. As only pumping operation is considered in this thesis, it is chosen to define positive flow rate and power in this direction according to the normal vector $\mathbf{n_k}$ represented in figure 3. When implied in conditional statements, the low energy sections denoted by an overbar, ($\bar{I}$, $\bar{A}$, $\bar{B}$) are treated as negative.

Energy-Discharge Characteristics of Centrifugal Pumps

First manuscripts mentioning the use of the centrifugal effect to transport water are credited to Leonardo da Vinci, the first working implementation of a centrifugal pump documented was built in 1689 in the laboratories of University of Marburg by Denis Papin [127]. Despite this working proof of concept, the market distribution of the technology was delayed till the second half of the 19th century with the emergence of engines, bearings and gears reliably sustaining the necessary high revolution rates. The largest step ahead in turbomachinery science is credited to L. Euler (1707-1783) who first formulated the conservation of angular momentum in the impeller to yield the Euler Turbomachine equation.

The working principle of a centrifugal pump and the nomenclature of passage sections and wetted surfaces used in the remainder of this document are represented in figure 4. Angular momentum is conserved in the impeller control volume limited by blade(b), hub (i) and shroud (e) material surfaces and the passage sections $\bar{1}$ and 1. Considering an inviscid fluid, the angular momentum transfer from the wetted surface to the fluid throughflow is expressed by:

$$P_t = \omega T_t = \int_{A_1 \cup A_{\bar{1}}} (\rho \mathbf{C} \cdot \mathbf{U})\, \mathbf{C} \cdot \mathbf{n} dA \tag{5}$$

Averaged velocity triangles at sections $\bar{1}$, and 1 and constant relative flow angle β_1 are considered. Inflow is assumed to have no circumferential component, $\mathbf{C_{\bar{1}}} \cdot \mathbf{U_{\bar{1}}} = 0$. The meridional velocity C_{1m} is determined by the fluid flow $Q_t = Q + Q_L = Q/\eta_Q$ through

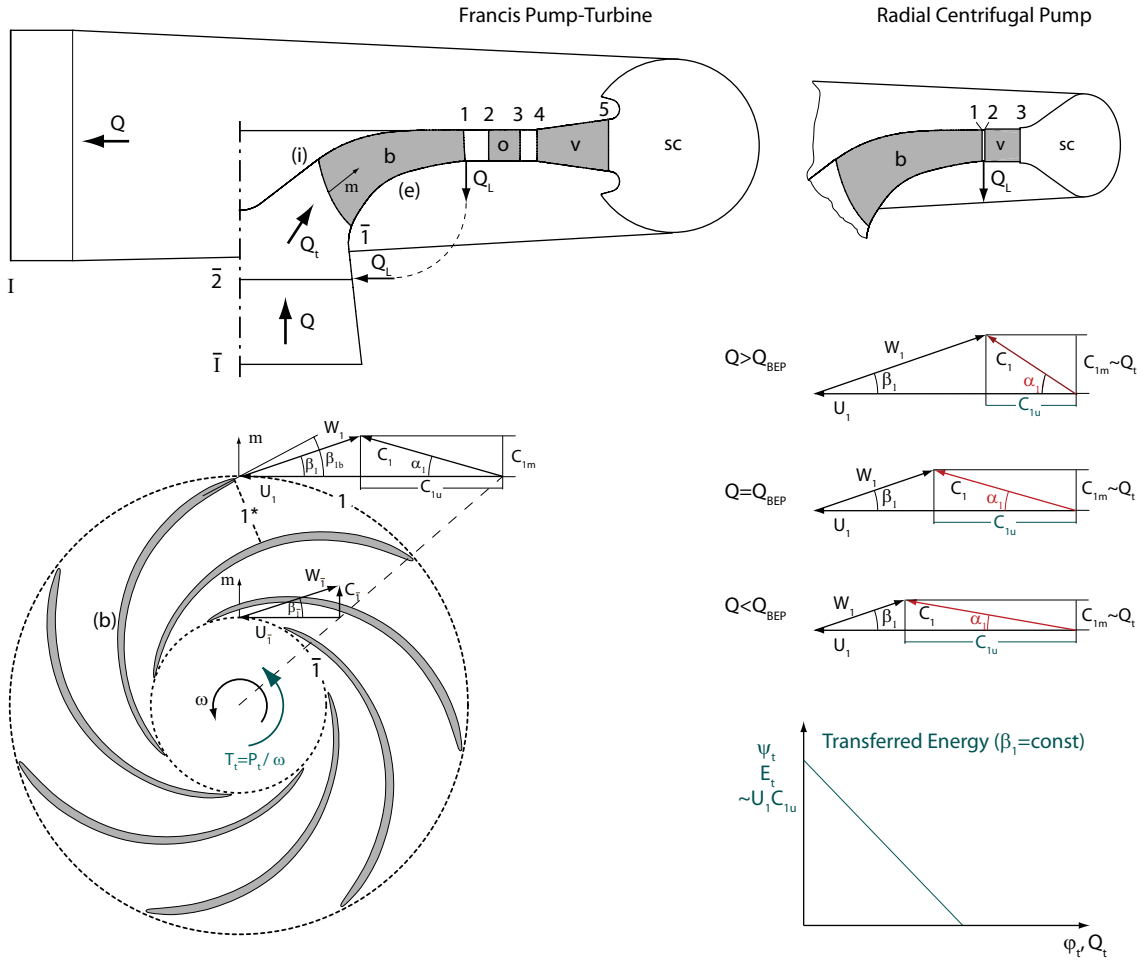

Figure 4: Working principle of a centrifugal pump impeller, velocity triangles and section nomenclature for a pump-turbine and a radial centrifugal pump with diffuser

the impeller, increased by the leakage flow Q_L through the labyrinths. The linear Euler energy-discharge characteristic equation for the transferred specific energy E_t is obtained as qualitatively represented in figure 4

$$E_t = U_1 C_{1u} = U_1 \left(U_1 - \frac{1}{\tan \beta_1} \frac{Q_t}{A_1} \right) \tag{6}$$

The specific hydraulic energy gH_1 at the impeller outlet is available in form of pressure $\frac{p_1}{\rho}$ and kinetic specific energy $\frac{C_1^2}{2}$. A considerable amount of the latter is usually converted into pressure energy to obtain economically reasonable velocity levels at the high pressure section I of the pump and in the following pipes. The major part of this deceleration takes place in the components termed diffuser (components o and v, sections 2 to 5 for a pump-turbine, component v, sections 2 to 3 for a centrifugal pump with a diffuser with a single blade cascade).

Dimensional analysis considering this working principle of a centrifugal pump of outer impeller diameter $2R_{1e}$ rotating at velocity ω yields the basic dependencies for flow rate, $Q \sim \omega R_{1e}^3$, head, $gH \sim \omega^2 R_{1e}^2$ and power, $P \sim \rho \omega^3 R_{1e}^5$. The operating point of a pump is

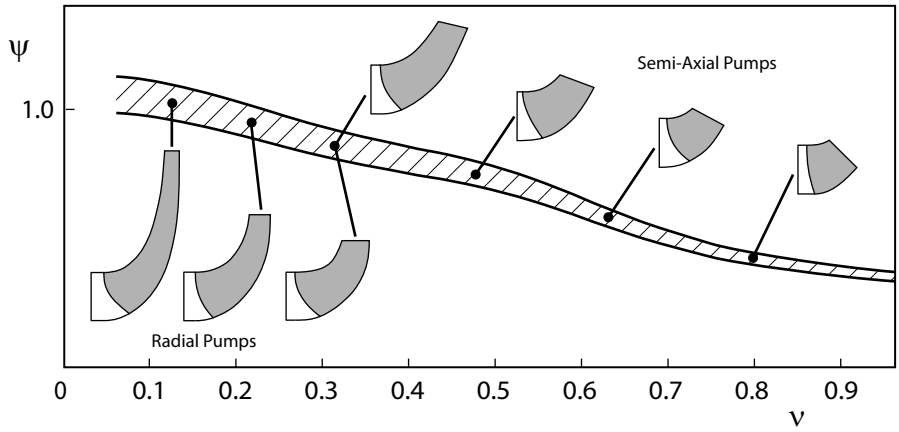

Figure 5: Meridional shapes and attainable energy coefficient ψ with maximum efficiency following [54], depending on the specific speed coefficient ν

expressed in dimensionless form by the flow coefficient φ

$$\varphi = \frac{Q}{\pi \omega R_{1e}^3} \tag{7}$$

and the energy coefficient ψ

$$\psi = \frac{E}{0.5\, U_{1e}^2} = \frac{E}{0.5\, \omega^2 R_{1e}^2} \tag{8}$$

Accordingly, flow velocities in centrifugal pumps are expressed by their ratio over the rotation velocity at impeller outlet U_{1e} and pressure p is expressed as non-dimensional pressure coefficient c_p:

$$c_p = \frac{p - p_{ref}}{0.5\, \rho U_{1e}^2} \tag{9}$$

with the reference pressure p_{ref} usually taken at section $\bar{I}$. The specific speed coefficient, the dimensionless key parameter for centrifugal pump design is determined from the nominal conditions denoted by index n.

$$\nu = \frac{\varphi_n^{1/2}}{\psi_n^{3/4}} = \omega\, \frac{(Q_n/\pi)^{1/2}}{(2E_n)^{3/4}} \tag{10}$$

The specific speed primarily determines the appropriate impeller type for given nominal conditions. Radial impellers are suitable for low specific speeds, axial impellers for high specific speeds, the mixed type or diagonal impellers are successfully applied in the intermediate range. Figure 5 shows the application ranges and attainable energy coefficients for single stage centrifugal pumps.

The dimensionless form of Euler's linear impeller characteristic is obtained:

$$\psi_t = 2\left(1 - \frac{1}{\tan\beta_2}\frac{\pi R_1^2}{A_1}\varphi_t\right) \tag{11}$$

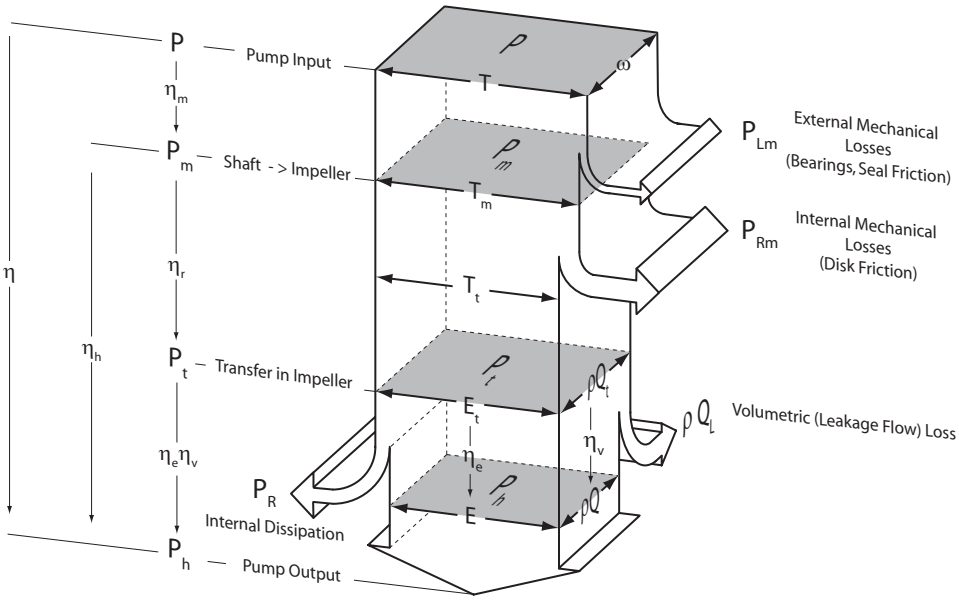

Figure 6: Definition of losses and internal efficiencies [1]

The main objective of centrifugal pump design is to convert a maximum of the power input P at the shaft of the pump to useful hydraulic power P_h. Several types of losses are distinguished and efficiencies are defined in figure 6 according to the annex proposals of the IEC 60193 standard [1] with minor nomenclature changes. Detailed classifications of losses according to their physical causes and rules to estimate the resulting efficiency of the pump are proposed in the literature [140; 54]. The operating point with the maximum pump efficiency η is termed best efficiency point(BEP). The linear Euler characteristics together with well founded quantitative estimates for the different types of losses generally provide sufficient estimates for the real pump characteristic close to the BEP. While mechanical and disk friction losses can be well predicted over a large range of operating conditions, the viscous dissipation losses depend on the complex three dimensional flow and cannot be predicted reliably from algebraic rules and statistics . The deviation of the real flow from the flow path intended by design for the BEP tends to have serious consequences in part load operation. Two mechanisms are obvious from the velocity triangles in figure 4 and are further detailed in figure 7.

- The change in absolute flow angle α_1 with decreasing flow rate results in a bad alignment of the oncoming flow on the diffuser vanes if the latter were designed free of or with little incidence at BEP. Incidence is defined as the deviation of the blade (metal) angle α_{1b} from flow angle α_1 at the diffuser blade leading edge 1.

- With a given section area of the guide vane or diffuser channels, the bulk velocity in the sections 2^* and 3^* decreases proportionally with the flow rate. At the same time, the impeller outlet velocity in the absolute frame C_1 increases towards part load.

Decelerated flows and flows with high incidence angles tend to become unstable and separate from the surfaces supposed to guide the flow. This gives place to flow patterns

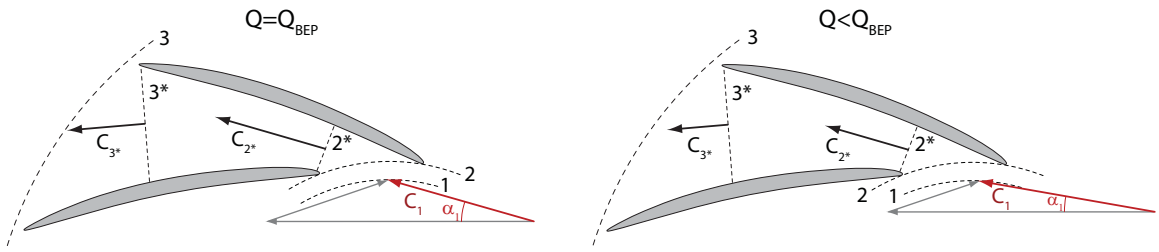

Figure 7: Velocity triangles: Flow misalignment and intense deceleration at part load

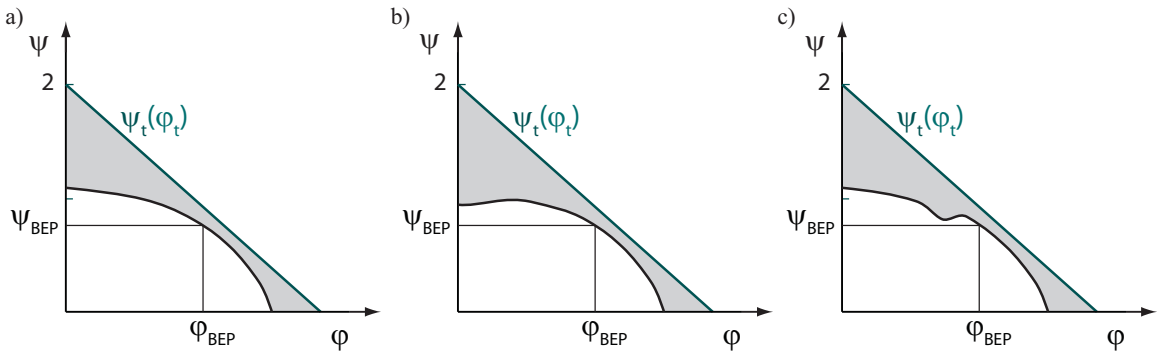

Figure 8: Schematic Characteristics of pumps. a)Monotonically decreasing, b)Positive slope at shutoff, c)Saddle type characteristic

characterized by recirculating flow zones, dissipating considerably more energy than a smooth through-flow. Flow separation occurs in axisymmetric conical diffusers at opening angles above $6^{\circ} - 10^{\circ}$ [131]. Simple turbomachinery design rules specify limits for the deceleration ratio C_{3*}/C_{2*} in a blade row. Whatever limit is imposed, in a diffuser designed to yield good efficiencies at BEP and keeping the pump size in economically reasonable limits, the flow separates at some point in part load. Besides such phenomena concerning the diffuser, the three-dimensional flow in the impeller can substantially deviate from the idealized flow path in part load, affecting the transfer of angular momentum from the impeller to the flow. Nonuniform impeller outlet flow further amplifies the tendency towards diffuser flow separation.

The aforementioned phenomena result in the real energy-discharge characteristic of the pump, schematically represented in figure 8. Typically, the difference of the real characteristic from the Euler characteristic $\psi_t(\varphi_t)$ is smallest around BEP. The real characteristic depending on the evolution of the losses represented by the gray area is characterized by its slope. A distinction is made between characteristics with a monotonically negative slope, 8a, characteristics with a positive slope close to shut-off, 8b, and so-called saddle-type characteristics, 8c, where positive slope of the characteristic occurs close to BEP. The latter type is typical for axial and semi-axial, high specific speed centrifugal pumps, and largely understood and accepted as unavoidable for those. However, some radial pump and pump-turbine designs result in such a saddle type characteristic while

other designs of same specific speed or even the same designs after minor modifications feature a monotonically decreasing energy-discharge characteristic [54; 55].

Pumping System Dynamic Behavior

Let us now consider how a positive slope in the energy-discharge characteristic compromises the operation of pumping systems, leading to the simplified expression of an "unstable characteristic" or even an "unstable pump". The hydraulic energy balance applied to the control volume V_S containing the system's pipe segments from $\bar{B}$ to $\bar{I}$ and from I to B yields the differential equation governing the dynamic operation for such a system:

$$gH_I - gH_{\bar{I}} = gH_B - gH_{\bar{B}} + gH_{r\,\bar{B}\div\bar{I}} + gH_{r\,I\div B} + \frac{1}{Q}\int_{V_S}\frac{\partial}{\partial t}\left(\frac{C^2}{2}\right)dV \tag{12}$$

The behavior of real systems can depend on the flow rate in a fairly complex manner. The storage system represented in figure 3 is sufficient to introduce main aspects of pumping system stability: Due to the large reservoir area we assume $C^2/2 = 0$ at B and $\bar{B}$. The atmospheric pressure difference $p_B - p_{\bar{B}}$ is negligible. The losses are resumed into a single system loss coefficient K_S and an according reference section area A_S:

$$gH_{r\,\bar{B}\div\bar{I}} + gH_{r\,I\div B} = K_S\frac{Q^2}{2A_S^2} \tag{13}$$

Neglecting hydro-acoustic phenomena and considering the bulk velocity $C = Q/A$, the inertia term is simplified introducing the system's hydraulic inductance L_S:

$$\frac{1}{Q}\int_{V_S}\frac{\partial}{\partial t}\left(\frac{C^2}{2}\right)dV = \int_L \frac{1}{C\,A}C\frac{\partial C}{\partial t}AdL = \int_L \frac{1}{A(s)}dL\,\frac{\partial Q}{\partial t} = L_S\frac{dQ}{dt} \tag{14}$$

The energy contribution of the pump is assumed to be a function of flow rate Q, impeller rotational velocity ω and other unknowns y:

$$gH_I - gH_{\bar{I}} = E\left(Q,\omega,y\right) \tag{15}$$

Introducing $\Delta Z = Z_B - Z_{\bar{B}}$ the simplified equation governing the system's behavior is obtained:

$$g\Delta Z + K_S\frac{Q^2}{2A_S^2} + L_h\frac{dQ}{dt} = E\left(Q,\omega,y\right) \tag{16}$$

The static equilibrium $E\left(Q,\omega,y\right) = g\Delta Z + K_S Q^2/(2A_S^2)$ defines a steady operating point of a pumping system at the intersection of the parabola describing the system with the energy-discharge characteristic of the pump. Main influence factors on the operating point are schematically represented in figure 9. A variation of the loss coefficient typically occurs when the flow rate of a process is regulated by a valve, a variation of static head is typical for marine applications (dock pump) as for pump-turbines when the reservoir level variation is relevant. Advances in technology and economy-of-scale effects due to higher production numbers have made variable speed drives an economically attractive

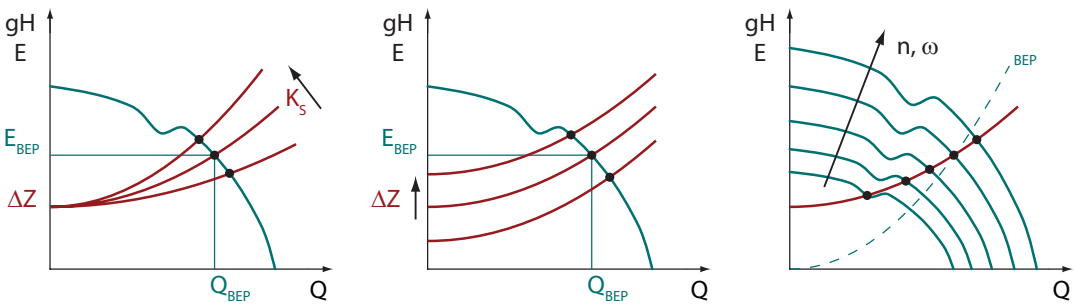

Figure 9: Operating point of a pumping system. a)Loss coefficient variation, b)Static system head variation, c)Pump revolution rate variation

option to optimize pump operation, even for large pump-turbine units [63; 128; 110]. Since the power consumption of a centrifugal pump scales with the third power of the rotation rate, decreasing this rate is an interesting alternative to throttling the flow rate by a valve. Large variable-speed pump-turbine units have recently been installed and are being planned. They offer a high flexibility to use the available hydraulic resources optimally to satisfy the irregular demand of present-day electricity networks, both in pumping and generating mode.

The stability of a pumping system with respect to flow rate fluctuations is analyzed by introducing a perturbation δQ, δE

$$g\Delta Z + L_h\left[\frac{dQ}{dt} + \frac{d\delta Q}{dt}\right] + K_S\frac{[Q+\delta Q]^2}{2A_S^2} = E\left(Q,\omega,y\right) + \delta E \tag{17}$$

and substituting the balance condition (16) yields:

$$L_h\frac{d\delta Q}{dt} + \frac{K_S}{2A_S^2}\left[2\frac{\delta Q}{Q} + \left(\frac{\delta Q}{Q}\right)^2\right] = \delta E \tag{18}$$

Leading to the first order:

$$L_h\delta\dot{Q} + K_S\frac{Q}{A_S^2}\delta Q + = \delta E \tag{19}$$

Assuming that the pump specific energy can be perturbed by both discharge and other parameters, we write

$$\delta E = \frac{\partial E}{\partial Q}\delta Q + \delta E'(t) \tag{20}$$

This leads to

$$L_h\delta\dot{Q} + \left[K_S\frac{Q}{A_S^2} - \frac{\partial E}{\partial Q}\right]\delta Q = \delta E'(t) \tag{21}$$

The stability condition derived from the homogenous part of the latter implies:

$$K_S\frac{Q}{A_S^2} - \frac{\partial E}{\partial Q} > 0 \Rightarrow \frac{\partial E}{\partial Q} < K_S\frac{Q}{A_S^2} \tag{22}$$

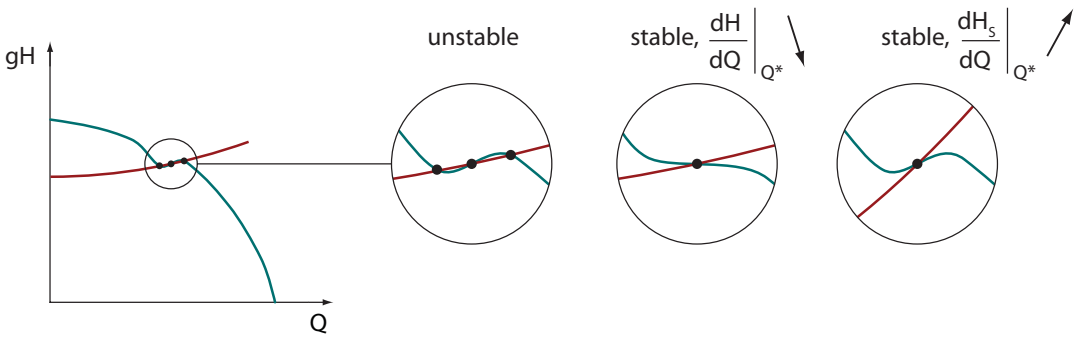

Figure 10: Unstable pump system and stabilizing modifications of the pump and system characteristics

On figure 9 this condition is identified by the slope of the pump and system characteristic at the intersection point:

$$\frac{\partial E}{\partial Q} < \frac{\partial}{\partial Q}\left(K_S \frac{Q^2}{2A_S^2}\right) \tag{23}$$

More detailed considerations including also compressibility effects (capacitive character) are given in [105; 49].

Figure 10 shows the typical case of unstable system operation due to a saddle type pump characteristic. To cure the problem, the positive slope in the characteristic must be avoided, as changing the system characteristics is rarely an option. For more complex systems, a regular negative slope of the pump characteristic contributes to the operation stability. As figure 9c illustrates, use of variable speed drives allows to shift the entire characteristics following the similitude relations. The zone of potential instability can be avoided by an increase in revolution rate when an increased static system head is required. On the other hand, lowering the revolution rate to save energy instead of using a throttling valve may lead to unstable operation.

The subject of this thesis is the numerical and experimental investigation of the internal flow in radial centrifugal pumps exhibiting positive slope on their energy-discharge characteristic at part load close to BEP ($Q > 0.75Q_{BEP}$).

Time-Dependency of Centrifugal Pump Flow

Flow in turbomachines is inherently time-dependent due to the relative motion of the impeller with its number of blades z_b in the stationary diffuser featuring z_v blades, $z_v =$ 1or2 for a volute pump without diffuser blades. The flow in the annular region close to sections 1 and 2 is governed by this so-called Rotor-Stator-Interaction (RSI).

The flow fields are governed by circumferentially periodic contributions from the rotating and the stationary frame [16] flow fields. In a pump this is commonly attributed to an interaction of the nonuniform velocity field exiting the impeller with the nonuniform pressure field generated by the diffuser blades, as represented in figure 11. With the angular coordinates in stationary frame θ_s and rotating frame θ_r, taking the pressure p as a quantity of interest, we consider that the periodic contributions $p_s(\theta_s, t)$ from stationary

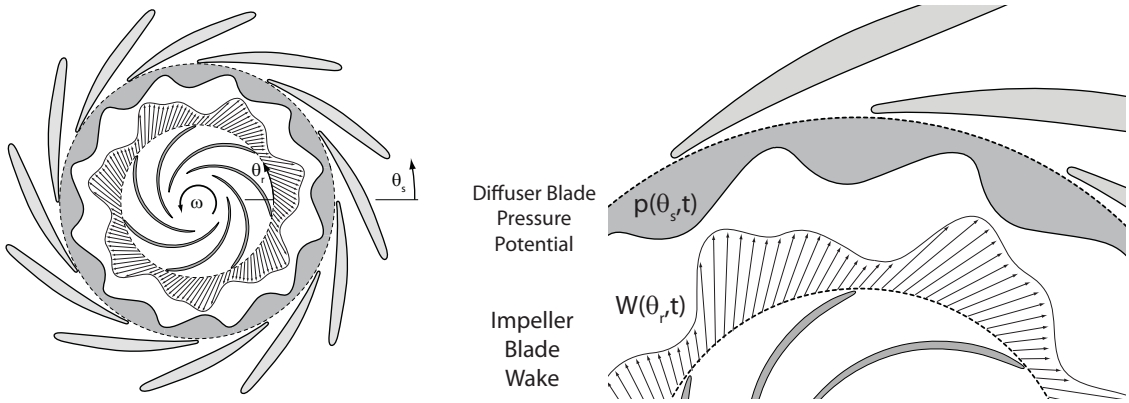

Figure 11: Rotor-Stator Interaction

frame and $p_r(\theta_r, t)$ from rotating frame can be expressed by Fourier series:

$$p_s(\theta_s, t) = \sum_n A_n^s \cos(n z_v \theta_s + \phi_n^s) \tag{24}$$

$$p_r(\theta_r, t) = \sum_m A_m^r \cos(m z_b \theta_r + \phi_m^r) \tag{25}$$

With the relation $\theta_r = \theta_s - \omega t$, p_r becomes:

$$p_r(\theta_s, t) = \sum_m A_m^r \cos(m z_b \theta_s - m z_b \omega t + \phi_m^r) \tag{26}$$

Together with the assumption that $p = p(p_s, p_r)$, this leads to the following relationship defining the phase-shifted periodicity in the stationary frame

$$p\left(\theta_s + 2\pi \frac{k_v}{z_v}, t + \frac{2\pi}{\omega}\left(\frac{k_v}{z_v} + \frac{k_b}{z_b}\right)\right) = p(\theta_s, t) \qquad \forall k_b \in \{0, ..., z_b\},\ k_v \in \{0, ..., z_v\} \tag{27}$$

and in the rotating frame

$$p\left(\theta_r + 2\pi \frac{k_b}{z_b}, t + \frac{2\pi}{\omega}\left(-\frac{k_b}{z_b} + \frac{k_v}{z_v}\right)\right) = p(\theta_r, t) \qquad \forall k_b \in \{0, ..., z_b\},\ k_v \in \{0, ..., z_v\} \tag{28}$$

Inserting $k_v = 0$ into equation (27) respectively $k_b = 0$ into equation (28) yields the time periodicity of period $2\pi/(\omega z_b)$, respectively $2\pi/(\omega z_v)$, for a fixed location in the considered frame of reference.

The presence of a volute or a nonuniform inlet flow field due to bends upstream of the impeller can induce further terms in the pressure distribution in the RSI region.

An essential feature of flow separation that has been observed in axisymmetric configurations such as a centrifugal pump diffusers is the appearance of cells of separated flow concerning only some of the diffuser channels. If the location of the stall cells remains fixed with time, the phenomenon is termed alternate stall, characterized by the number of stall cells k_s on the circumference. In numerous studies, the stall cell patterns were found to rotate with a stall precession rate ω_s, that is sensibly different from the impeller

revolution rate. The phenomenon is then termed rotating stall. Alternate and rotating stall are manifest in the circumferential pressure distribution by the presence of circumferential waves of low wave number k_s and their harmonics, rotating at the stall precession rate ω_s. The rotating low wave number modes $k_s = 0$ to $k_s = 4$ are represented in figure 12.

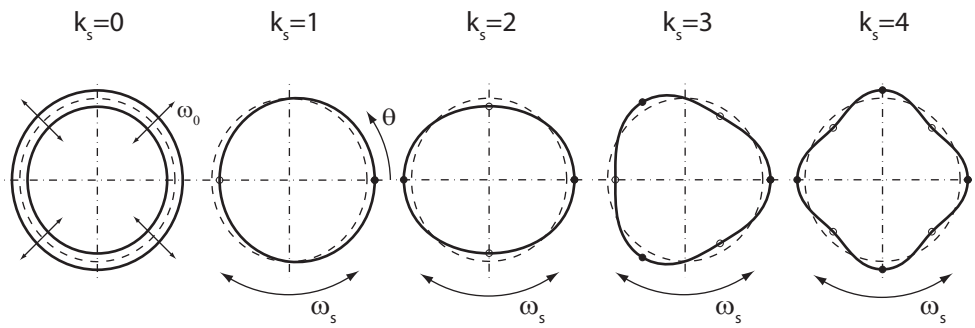

Figure 12: Synchronous and rotating wave modes of wave numbers $k_s = 0$ to $k_s = 4$

Any signal can be represented with the definition of an analytic signal defining instantaneous amplitude and phase as functions of space and time:

$$p(\theta, t) = a(\theta_s, t)cos(\varphi(\theta_s, t)) \tag{29}$$

As well as any single periodic Fourier component of equation (26), a pure rotating stall mode can be expressed with a constant amplitude a_0 and the phase given by:

$$\varphi_s(\theta, t) = k_s\omega_s t + k_s\theta_s + \varphi_{s,0} \tag{30}$$

With this representation of rotating modes by the phase φ, function of space and time, wave number k_s and rotation velocity ω_s are obtained by the following relations:

$$\frac{\partial\varphi}{\partial t} = k_s\omega_s \qquad \text{and} \qquad \frac{\partial\varphi}{\partial\theta_s} = k_s \tag{31}$$

For RSI expressed by equation (26) the wave number is given by the number of blades z_b and its multiples for the higher harmonics. The blade passage phase φ_b is defined by

$$\varphi_b(\theta_s, t) = z_b\omega t + z_b\theta_s + \varphi_{b,0} \tag{32}$$

Experimental and Numerical Flow Investigations

Fluid flow is governed by physical laws expressed by partial differential equations in space and time that can be solved analytically only for the very simplest cases. Nevertheless, generations of researchers have achieved a remarkable level of understanding of fluid flow phenomena based on observation, thorough analysis and subtle formulation of simplified models adapted to the considered application domain. Experimental techniques have evolved along the decades driving and following the ongoing advances in technological

domains involved in instrumentation for investigations of fluid flows. This allows more and more detailed observations and the efficient handling and representation of large datasets thanks to digital data processing and storage.

Since the appearance of the first machines resembling modern computers in the 1940's, the computing power to cost ratio has regularly increased. Starting with machines able to execute a few hundreds floating point operations per second, the barrier of 10^{15} floating point operations per second ($flops$) was broken in 2008 by the two largest supercomputers, while average desktop personal computers achieve $50 \cdot 10^9 flops$. Along with this went the development of numerical methods making use of computers to solve mathematical problems that have no analytical solution. Numerical simulations contribute as well to the solution of applied fluid dynamics problems in engineering as to the understanding of basic flow physics in research. They are commonly termed Computational Fluid Dynamics(CFD).

The considered centrifugal pump flows are continuous flows through a domain of interest that is bounded by solid walls and passage sections clearly identified as inlet and outlet. Mesh-based Eulerian approaches are the most straightforward and most used method to set up the model and discretize the resulting equations of such internal fluid flow. The continuous flow field is represented by the values of variables, namely pressure p and velocity $\mathbf{C}$, at discrete locations that remain fixed with the domains boundaries. The ensemble of locations (nodes) and rules defining their relative position (connectivity) form the simulation mesh. In a fixed frame of reference, the conservation of momentum in the control volume V is expressed for incompressible fluids considered in this study:

$$\frac{d}{dt}\int_V \rho \mathbf{C}\, dV = \rho \left(\frac{\partial}{\partial t} \int_V \mathbf{C}\, dV + \int_{\partial V} \mathbf{C}\, \mathbf{C}.\mathbf{n}\, dA \right) \tag{33}$$

The second term, currently called advective or convective term, expresses the flux of momentum through the control volume boundary surfaces ∂V. Its accurate expression as a function of the nodal variables is the major challenge for the Eulerian discretization methods for incompressible flows. Other (meshless, Lagrangian) approaches are evolving and find widespread use in particular areas of interest, especially to simulate sprays, jets and other multiphase flow [4]. Panel methods based on conservation of vorticity have successfully been applied to turbomachinery flow [139; 147], they require only the wetted surfaces to be discretized by a mesh. The principal mesh based Eulerian methods to assemble a linear equation system containing the nodal variable values as unknowns are finite differences, finite element and finite volume methods [43]. When considering time-dependent problems, the state of the flow field is solved sequentially in discrete time steps, evolving from some initial condition. This determines the main factors defining the computing resources necessary to solve a problem: Size of the domain and spatial resolution of the mesh, length of the considered time interval and temporal resolution needed to capture the phenomena of interest.

As almost all fields of fluid dynamics research, the knowledge on turbomachinery flow is actually driven by complementary contributions of experimental, analytical and numerical studies.

Studies on Flow Phenomena involved in Centrifugal Pump Flow

The flow in a centrifugal pump is characterized by features that can hardly be separated from each other in their complex interaction but that constitute active research topics of their own. This research generally focusses the interest on a single flow feature isolated in basic flow configurations, such as:

- **Separation of turbulent boundary layers:** A review on the subject is given by [132]. Experimental investigations of the boundary layer in vicinity of separation have been carried out by [32]. Both publications focus on the separation under steady surrounding flow condition. Detailed experimental surveys of separated flow over hydrofoils at conditions relevant to turbomachinery flow become available with advances of experimental techniques [20]. Such cases constitute a major challenge for the most advanced numerical simulation techniques [129; 157]. Recent research focusses on the separation under time-dependent conditions, found with oscillating airfoils [83; 18; 19] or in the context of active control of flow separation by external forcing [76; 60]. While a clear definition of the phenomenon and the location of steady flow separation was given by Prandtl in 1904, a thorough definition of the (eventually moving) location of flow separation of a time-dependent flow was given by Haller in 2004 [56].

- **Secondary flows in curved ducts:** The equilibrium of forces governing the flow in curved ducts gives place to flow fields of striking complexity. Secondary flow, the deviation from the naive through-flow normal to the cross section, has been studied extensively [15; 21] and provided numerous study cases during the evolution of numerical simulation techniques [112; 67]. Experimental investigations on 90° pipe bends [145] have revealed symmetry-breaking secondary flows. Advanced numerical techniques requiring important computing resources have recently reproduced these results and allow for a better understanding of their origins [124]. Practical applications of such simulation techniques include predictions of vibration and heat transfer in single rocket engine cooling ducts [102]. The role of the impeller rotation sustaining secondary flows in centrifugal pump impeller channels is qualitatively explained by [65; 78; 54], while there is no simple solution to quantify them. Shortcomings of nowadays common numerical simulation techniques and the tremendous computing resources required by advanced numerical techniques to predict secondary flows in curved channels are pointed out by the cited research papers based on the stationary configurations. The inclusion of effects due to reference frame rotation are not a fundamental issue per se in numerical simulation.

- **Symmetry breaking flow topology bifurcations:** Due to the nonlinear nature of the behavior of fluid flow, numerous study cases exist where small changes in parameters lead to drastic changes of flow topology from one pattern to another. Such parameters may concern the geometry of solid walls bounding the flow, or parameters of flow velocity and direction such as the intensity of swirl of a rotating flow. A comprehensive review on this subject in the context of flow around three-dimensional obstacles is given by [143]. The phenomenon of vortex breakdown described by [40] can be reproduced numerically [149]. Going beyond the accurate reproduction of the observed phenomenon by means of simulation, Gallaire et al.

[45] develop a theory of vortex flow stability and spiral vortex breakdown based on the numerical results of [123]. An example of identification of such a flow topology bifurcation in a swirling flow in Francis turbine draft tube is given in [89; 90]. On the macroscopic level of symmetry breaking in systems of symmetric configuration, Ehrich [37] studied the dynamic behavior of a simple branched diffuser undergoing alternating flow separation in its two branches.

- **Self sustained instability, vortex shedding:** Boundary layer separation is often companion to time-dependent periodic shedding of large scale vortices originating in the region of separation. A well known phenomenon is the alternate periodic shedding of vortex pairs behind obstacles in flow, termed von Kármán vortex street. Such self-induced periodic instabilities of flow can appear locally under the most stable outer conditions [14]. Considerable insight has been gained by experimental and numerical studies on simple bluff bodies (circular and square cylinders, spheres) [156; 152]. Investigations on the von Kármán street found with blunt trailing edges of hydrofoils under flow conditions that are relevant for industrial pumps are presented by [11].

Advanced experimental and numerical techniques are applied in the research on turbomachinery flow, as insight into the flow features is at the base of potential improvements of the design of turbomachines in means of performance and reliability. Main areas of interest are:

- **Blade wake interaction:** As an isolated detail of the flow in multi-stage axial machines, the flow on a single blade located in the wake of another one has been extensively studied [85; 134]. Numerical investigations on such configurations have shown that considerable computational resource are required to accurately simulate such flows [79].

- **Pressure fluctuations and time dependent forces at the rotor-stator interface:** The local pressure fluctuations are the root cause for dynamic loading on the blades that can lead to fatigue with consequence of blade cracking. Numerous investigations were conducted to understand the influence of different design parameters on the pressure fluctuations and time-dependent radial forces on the impeller, especially of the relative radial distance between impeller and diffuser blades [10; 98]. Since the development of the necessary simulation tools to handle the relative motion of the impeller [52], numerical simulations have shown to be accurate in predicting pressure fluctuations and amplitudes at the blade passing frequencies and their harmonics [130; 111; 148; 160; 163; 138]. The influence of adding so-called splitter blades was investigated both experimentally and numerically [75].

- **Flow instabilities in axisymmetric configurations:** As for basic cases of symmetry breaking in a branched diffuser [37], the strong nonlinearity related to flow separation can lead to flow patterns where some channels of a turbomachine component exhibit flow separations and others do not, termed alternate or rotating stall. Appearing as a predictor of complete surge that must be avoided in aircraft engines, rotating stall was studied intensively in the thermal turbomachinery domain [92; 91; 66; 68]. The phenomenon was observed on diffusers of radial centrifugal

pumps [61; 69; 125; 113; 77; 99] and in impellers at part load flow rates below 60% of BEP flow rate [74; 115; 114; 70]. Numerical studies using 2-dimensional approaches [126; 86; 48] have reproduced the phenomenon with a satisfactory agreement. Recently, 3-dimensional flow simulations reproducing rotating stall on centrifugal pumps [150] were conducted. A qualitatively similar phenomenon of flow separation and vortex formation breaking the axisymmetry, the formation of backflow vortices at the inlet of an inducer was reproduced by simulations using a high spatial and temporal resolution [159].

Experimental and Numerical Evaluation of Part-Load Performance

Former research on flow separation in turbomachinery flow and more specifically on rotating and alternate stall addresses the prediction of pressure fluctuations, time-dependent forces and global performances of the considered turbomachines. Nevertheless, all but the most recent [150] numerical studies consider laboratory scale pumps with geometries that lend themselves to two-dimensional considerations [126; 125; 148] or apply a reduction of the three dimensional flow to two-dimensional considerations on a stream-surface [48; 86]. Given the limits in computing resources, earlier numerical studies assume periodicity with blade channel pitch and consider a time-averaged flow field, resulting mostly in a deceiving agreement of numerical vs. experimental studies [101; 38]. The present work addresses the capacity of three-dimensional time dependent simulation techniques to predict flow separation under its various forms, focussing on industrially relevant geometries.

Objective of this Study and Document Organization

It was hypothesized that, a positive slope in the energy-discharge characteristic of radial centrifugal pumps occurring close to the best efficiency point is related to a change of flow topology in the diffuser. The diffuser flow topology change induces increased losses while flow and energy transfer in the impeller remain essentially unaffected. The verification of this hypothesis is the primary motivation of the numerical and experimental investigations that are conducted along three case studies of radial centrifugal pumps and pump-turbines showing positive slope on the energy-discharge characteristic relatively close to BEP. The part load flow in radial centrifugal pumps may show complex phenomena such as the self induced periodic instability commonly termed rotating stall. The ability of numerical simulation methods to accurately reproduce such phenomena must be assessed, regardless of their direct causal relation to the positive slope in the characteristics, since their influence on the part-load flow in centrifugal pumps is essential. This leads to the following structure of the document:

- **Part I** is dedicated to the presentation of the numerical and experimental methods and tools used for the investigations presented in the remainder of the document.
- The simplifying assumption of a stationary flow, similar in all impeller and diffuser channels, allows stationary numerical simulation approaches. Assuming spatial periodicity in both the rotating and the stationary frame reduces the simulation domain size significantly, allowing for systematic mesh refinement, thus eliminating doubts on the influence of spatial discretization error on the energy balances. The analysis of such numerical simulations, presented in **Part II**, focusses on the relation of

diffuser flow topology with viscous energy dissipation and its impingement on the energy-discharge characteristic.

Time-dependent numerical simulations on a double-suction pump study case show a similar flow separation in some diffuser channels, leading furthermore to an imbalance of the flow rates through both impeller sides when discharge decreases below 80% of BEP.

- In consideration of the lack of detailed experimental flow surveys of the two numerical case studies presented in Part II, complementary time-dependent experimental and numerical investigations of a pump-turbine scale model with a specific speed coefficient of $\nu = 0.19$ are carried out and described in **Part III**. Rotating stall at part load conditions is evidenced by transient pressure measurements in the rotor-stator interface region. Stall phase correlated Laser-Doppler velocimetry techniques are developed and the time-dependent velocity field at relevant locations in the diffuser is specified as a function of the stall phase. Time-dependent numerical simulations are conducted to validate the ability of present-day numerical simulation techniques to capture rotating stall phenomena qualitatively and quantitatively.

- In consideration of the quantitative disagreement between the results of numerical simulations compared to experiments, a novel boundary condition approach is developed: Parts of the finite volume model of the impeller channels is replaced by a one-dimensional modelling approach. This multi-scale modelling method results in an economy in computational cost and potentially allows to increase the spatial resolution in the remainder of the domain. This is a step towards feasibility of advanced numerical methods requiring a significant increase of spatial resolution for radial centrifugal pump applications. **Part IV** describes this mass flow weighted periodic inlet condition approach and its implementation. The method is validated on the pump-turbine scale model showing rotating stall as well as with the case of imbalanced impeller side flow rate in a double suction pump.

Part I

Numerical and Experimental Tools

Chapter 1

Governing Equations

1.1 Basic Flow Mechanics and Conservation Equations

The Incompressible Navier-Stokes Equation

The motion of fluids is governed by the conservation law of momentum and mass. For the present analysis of flow phenomena and their numerical simulation, the fluid is assumed to be incompressible. Considering the 3-dimensional, time dependent motion of fluid in a Cartesian coordinate system in an inertial frame leads to the differential form of the incompressible Navier-Stokes equations. They form a system of four nonlinear partial differential equations in space and time.

$$\frac{\partial C_i}{\partial t} + C_j \frac{\partial C_i}{\partial x_j} = \frac{1}{\rho}\left(\frac{-\partial p}{\partial x_i} + \frac{\partial \tau_{ij}}{\partial x_j}\right) + f_i \tag{1.1}$$

$$\frac{\partial C_i}{\partial x_i} = 0 \tag{1.2}$$

In applications dealing with the transient behavior of large hydraulic systems or diametrical vibration modes of turbomachines, the compressibility of water and the resulting finite pressure wave propagation speed in the fluid is of fundamental interest. Such hydro-acoustic phenomena are fully described by the compressible Navier-Stokes equations, which are of hyperbolic-parabolic type, leading to different requirements for their numerical solution. The wave propagation speed of pressure waves in water is two orders of magnitude higher than typical flow velocities in hydraulic machines. The simulation of convective and propagative phenomena in a common modeling approach involves different time scales and different requirements in spatial resolution, making the numerical modeling particularly difficult and demanding in computing resources. Hydro-acoustic phenomena are commonly analyzed by separating the convective and propagative parts following the Lighthill analogy. In such kind of analysis, results of incompressible simulations serve to derive input conditions for acoustic simulations [8].

The Momentum equation (1.1) expresses the first principle of mechanics: The substantive derivative of the flow velocity depends on the sum of pressure forces, shear stresses (viscous forces) and body forces such as gravity.

Water is considered as Newtonian fluid, the shear stress is determined by the dynamic viscosity μ and the strain rate tensor D_{ij}:

$$\tau_{ij} = 2\mu D_{ij}, \qquad D_{ij} = \frac{1}{2}\left(\frac{\partial C_i}{\partial x_j} + \frac{\partial C_j}{\partial x_i}\right) \tag{1.3}$$

Leading to the incompressible Navier-Stokes equation for Newtonian fluids:

$$\frac{\partial C_i}{\partial t} + C_j \frac{\partial C_i}{\partial x_j} = \frac{1}{\rho}\left(\frac{-\partial p}{\partial x_i} + \mu \frac{\partial^2 C_i}{\partial x_j \partial x_j}\right) + f_i \tag{1.4}$$

Rotating Frame of Reference

When the flow in rotating turbomachinery components is considered, the most straightforward approach for simulation is to use a reference frame moving together with the solid wall boundary geometry. The flow velocities and momentum are considered with respect to this moving frame of reference, adding the frame acceleration as a contribution into the Navier-Stokes equation, either considering it as a body force on the right side or as an additional acceleration on the left side. Defining the absolute velocity $\mathbf{C}$, relative velocity $\mathbf{W}$ and rotation velocity $\mathbf{U} = \mathbf{X} \times \boldsymbol{\omega}$ with the steady rotation rate $\boldsymbol{\omega}$ and the considered location $\mathbf{X}$:

$$\frac{D\mathbf{C}}{Dt} = \frac{D\mathbf{W}}{Dt} + \boldsymbol{\omega} \times (\boldsymbol{\omega} \times \mathbf{X}) + 2\boldsymbol{\omega} \times \mathbf{W} \tag{1.5}$$

Expressing the terms due to centripetal and Coriolis acceleration as body forces:

$$\mathbf{f}_r = -\boldsymbol{\omega} \times (\boldsymbol{\omega} \times \mathbf{X}) - 2\boldsymbol{\omega} \times \mathbf{W} \tag{1.6}$$

the Navier-Stokes equation in a rotating frame of reference with constant rotation rate ω is obtained:

$$\frac{\partial W_i}{\partial t} + W_j \frac{\partial W_i}{\partial x_j} = \frac{1}{\rho}\left(\frac{-\partial p}{\partial x_i} + \mu \frac{\partial^2 W_i}{\partial x_j \partial x_j}\right) + f_i + f_{r,i} \tag{1.7}$$

Laminar and Turbulent Flow

Introducing a characteristic length scale L_0, a characteristic time t_0 and a characteristic velocity c_0 for a specific application, and normalizing the body forces by the gravitational acceleration, g, equation (1.4) is expressed in nondimensional form:

$$St \frac{\partial C_i^*}{\partial t^*} + C_j^* \frac{\partial C_i^*}{\partial x_j^*} = \frac{-\partial p^*}{\partial x_i^*} + \frac{1}{Re} \frac{\partial^2 C_i^*}{\partial x_j^* \partial x_j^*} + \frac{1}{Fr^2}\gamma_i \tag{1.8}$$

with the Strouhal number $St = \frac{L_0}{C_0 t_0}$, the Reynolds number $Re = \frac{\rho C_0 L_0}{\mu}$, the Froude number $Fr = C_0/\sqrt{gL_0}$ and the dimensionless variables $C_i^* = C_i t_0/L_0$, $x_i^* = x_i/L_0$, $p^* = p/(\rho C_0^2)$, $t^* = t/t_0$ and $\gamma_i = f_i/g$.

Depending on the Reynolds number, defined as the ratio of inertial forces and viscous forces, two different flow regimes are identified. Low Reynolds number flows are governed

by viscous effects. Time-independent solutions can be obtained, even analytically for simple cases, this flow regime is termed laminar flow.

High Reynolds number flows are governed by inertia effects. In this regime, termed turbulent flow, the flow becomes highly unsteady as small initial perturbations grow to coherent turbulent vortices drawing energy off the mean flow to sustain their motion [122; 50; 33]. The flow configuration and its particular definition of characteristic length scales together with the level of perturbations determine the critical Reynolds number. Above the critical Reynolds number the flow does not revert to its laminar state after a perturbation. For internal pipe flows, critical Reynolds numbers ranging from 1760 to 2300 are quoted [36]. However, in absence of perturbations, the laminar state can be maintained even with higher Reynolds numbers. Under the laboratory conditions set up by O.Reynolds in 1883, laminar pipe flow was realized up to Reynolds numbers of 12′000. The internal flow in industrial centrifugal pumps considered in this study is characterized by Reynolds numbers of 10^6 to 10^7, considering $R_{\bar{1}e}$ and U_{1e} as characteristic length and velocity scales.

The turbulent fluid motion contributes to the transport of momentum and other conserved quantities. With rising Reynolds number, the size of the relevant turbulent eddies observed in the flow becomes smaller and the involved time scales shorter [142]. The cost of so-called Direct Numerical Simulation (DNS) resolving all relevant eddy scales in space and time, scales with the third power of the Reynolds number for turbulent flows [43]. With the ongoing performance evolution of supercomputers, DNS simulations are applied to more and more complex problems. First DNS applications for isolated turbomachinery component study cases as a single airfoil and a periodic blade cascade at moderate Reynolds numbers of $5 \cdot 10^5$ have recently been reported [157; 158]. For flow configurations including an entire centrifugal pump and simulation times covering at least several impeller revolutions, DNS is still out of reach for the coming decades. Turbulence models that represent the influence on mean flow exercised by turbulent vortices unresolved in time and space are commonly used and will still be needed in numerical simulation.

Reynolds Averaged Navier Stokes Equations

The Reynolds-averaged approach to time-dependent flow applies an average operator to the equations to separate the stochastic, turbulent fluctuations ϕ' of any scalar ϕ from the deterministic mean values $\bar{\phi}$:

$$\phi(x_i, t) = \bar{\phi}(x_i, t) + \phi'(x_i, t) \tag{1.9}$$

The averaging operator is commonly associated with time-averaging for time-independent mean flows or ensemble averaging for a time-dependent mean flow. It satisfies the Reynolds criteria [100]:

- Linearity

$$\begin{aligned} &\overline{\phi + \psi} = \bar{\phi} + \bar{\psi} \\ &\overline{a\phi} = a\bar{\phi} \qquad\qquad \text{for a=const} \\ &\overline{a} = a \end{aligned} \tag{1.10}$$

- Any derivative in space or time of the average is equal to the average of the derivative

$$\overline{\frac{\partial \phi}{\partial s}} = \frac{\partial \bar{\phi}}{\partial s} \tag{1.11}$$

- The average of a product of any scalar with an average is the product of the averages

$$\overline{\bar{\phi}\psi} = \bar{\phi}\bar{\psi} \tag{1.12}$$

Additional properties follow from these requirements, namely $\overline{\bar{\phi}} = \bar{\phi}$ and $\overline{\phi'} = 0$. The average of a product of two variables ϕ and ψ equals the product of the averages plus a covariance term:

$$\overline{\phi\psi} = \overline{\left(\bar{\phi} + \phi'\right)\left(\bar{\psi} + \psi'\right)} = \overline{\bar{\phi}\bar{\psi}} + \underbrace{\overline{\psi'\bar{\phi}} + \overline{\phi'\bar{\psi}}}_{=0\, eq.1.12} + \overline{\phi'\psi'} = \bar{\phi}\bar{\psi} + \overline{\phi'\psi'} \tag{1.13}$$

Applying this to equation (1.4) the incompressible Reynolds-Averaged Navier-Stokes equation (RANS) is obtained:

$$\frac{\partial \bar{C}_i}{\partial t} + \bar{C}_j \frac{\partial \bar{C}_i}{\partial x_j} = \frac{1}{\rho}\left(\frac{-\partial \bar{p}}{\partial x_i} + \mu \frac{\partial^2 \bar{C}_i}{\partial x_j^2}\right) - \frac{\partial \overline{C_i' C_j'}}{\partial x_j} + f_i \tag{1.14}$$

The terms $\rho\overline{C_i' C_j'}$ called Reynolds stresses are 6 new unknowns in which equation (1.14) differs from equation (1.4). The essence of turbulence modeling based on RANS equations is to close the equation system by defining laws to predict the Reynolds stresses.

1.2 Turbulence Modeling

In the effort of modeling the turbulent stresses in equation (1.14) different approaches have been developed over the last 40 years, they can roughly be divided into the following classes ranging from low to high computational effort:

- Zero-Equation Models: Only algebraic relations are used to determine the viscous stresses based on local quantities and average scale considerations.
- One-equation models have found widespread use in aerodynamic external flow applications [136; 96].
- Two-Equation Models: The viscous stresses are computed with models using two additional transport equations to determine turbulence intensity and length scale. These are the models most widely used during the last decades.
- Reynolds Stress Models, also termed second moment closure models: A separate transport equations is used for each of the six components of the Reynolds Stress Tensor. These models have been found to be superior over two equation models in swirling flows [80; 51]. Their use implies higher requirements in mesh quality to avoid convergence problems, often resulting in higher computational effort or even the impossibility to achieve converged solutions where two-equation models converge.

- Large Eddy Simulation (LES): Using a spatial and temporal resolution that allows to simulate the largest turbulent structures carrying most energy and contributing most to the increased momentum transport is a compromise in computational effort between RANS turbulence modeling and DNS. The modeling approach for the stresses representing the unresolved scales, called subgrid stress model, has to take into account the grid resolution and the numerical discretization method [84]. The requirements of mesh resolution for boundary layer flows at high Reynolds numbers restricts the application of LES to simple, but relevant configurations, e.g. single air- or hydrofoils [93] and ducts [149; 124]. Simulations of a three-stage centrifugal pump using LES presented by [103] were run on one the worlds biggest available supercomputers in 2004. They could by far not satisfy the criteria of spatial and temporal resolution given in the literature [73; 117] for the application of LES methods to internal channel flow.

Hybrid RANS-LES methods using RANS models in the boundary layers and the LES method for the remainder of the simulation domain [107; 137; 24; 30] have recently been developed. They propose a solution to the tremendous increase of required computing resources to resolve the flow near the wall using LES approaches [141]. After thorough validation on relevant study cases they are promising for application in turbomachinery simulation in the close future. The following sections expose the two-equation turbulence model used for the numerical simulations presented in the remainder of the document.

1.2.1 Eddy Viscosity Turbulence Models

The most straightforward way to determine Reynolds stresses in equation (1.14) is to use a formulation equivalent to the viscous stresses of a Newtonian fluid. The prevalent turbulence models for engineering applications are based on the Boussinesq hypothesis, adding a turbulent viscosity μ_t to the fluid Newtonian viscosity μ:

$$-\rho\frac{\partial\overline{C_i'C_j'}}{\partial x_j} = \mu_t\left(\frac{\partial\overline{C_i}}{\partial x_j} + \frac{\partial\overline{C_j}}{\partial x_i}\right) - \frac{2}{3}\rho\delta_{ij}k = 2\mu_t\overline{D_{ij}} - \frac{2}{3}\rho\delta_{ij}k \tag{1.15}$$

The turbulent kinetic energy k introduced as:

$$k = \frac{1}{2}\overline{C_i'C_i'} \tag{1.16}$$

determines the characteristic velocity $q = \sqrt{k}$ of the turbulent fluid motion. Together with a characteristic length scale L it is at the basis of the Prandtl-Kolmogorov analogy establishing a relation based on dimensional analysis:

$$\mu_t = C_\mu\rho q L \tag{1.17}$$

The character of turbulent eddies of being convected with the mean flow suggests the use of scalar transport equations to determine the characteristic velocity and length scale. The first of these is in almost all models the equation of turbulent kinetic energy k as it is a conserved quantity and the exact equation can be derived [154]:

$$\frac{\partial\rho k}{\partial t} + \frac{\partial\rho C_j k}{\partial x_j} = \frac{\partial}{\partial x_j}\left(\mu\frac{\partial k}{\partial x_j}\right) - \frac{\partial}{\partial x_j}\left(\frac{\rho}{2}\overline{C_j'C_i'C_i'} + \overline{p'C_j'}\right) - \rho\overline{C_i'C_j'}\frac{\partial\bar{C}_i}{\partial x_j} - \mu\overline{\frac{\partial C_i'}{\partial x_k}\frac{\partial C_i'}{\partial x_k}} \tag{1.18}$$

The transport of the turbulent kinetic energy by the turbulent fluid motion is modeled by the gradient diffusion hypothesis, defining the turbulent Prandtl number σ_k:

$$-\left(\frac{\rho}{2}\overline{C_j'C_i'C_i'}+\overline{p'C_j'}\right)\approx\frac{\mu_t}{\sigma_k}\frac{\partial k}{\partial x_j} \tag{1.19}$$

The eddy viscosity hypothesis (1.15) is used to determine the rate of production of turbulent kinetic energy:

$$\rho\overline{C_i'C_j'}\frac{\partial\bar{C}_i}{\partial x_j}\approx\mu_t\left(\frac{\partial\bar{C}_i}{\partial x_j}+\frac{\partial\bar{C}_j}{\partial x_i}\right)\frac{\partial\bar{C}_i}{\partial x_j} \tag{1.20}$$

It is in the determination of the last term of the turbulent kinetic energy transport equation, related to the dissipation of turbulent kinetic energy and needed to determine the turbulent length scale, that the following two-equation models differ

k-ε Turbulence Model

The k-ε model, first proposed by Jones and Launder in 1972 [71], introduces the rate of viscous eddy dissipation ε to yield a simple expression for the last term in the k-equation (1.18)

$$\frac{\partial\rho k}{\partial t}+\frac{\partial\rho C_jk}{\partial x_j}=\frac{\partial}{\partial x_j}\left(\mu\frac{\partial k}{\partial x_j}\right)+\frac{\partial}{\partial x_j}\left(\frac{\mu_t}{\sigma_k}\frac{\partial k}{\partial x_j}\right)+\mu_t\left(\frac{\partial\bar{C}_i}{\partial x_j}+\frac{\partial\bar{C}_j}{\partial x_i}\right)\frac{\partial\bar{C}_i}{\partial x_j}-\rho\varepsilon \tag{1.21}$$

For equilibrium flows, where production and dissipation of turbulent kinetic energy are in balance, ε is related to the turbulence length scale by

$$\varepsilon\approx\frac{k^{3/2}}{L} \tag{1.22}$$

and with equation (1.17), the eddy viscosity is specified as:

$$\mu_t=C^{ste}\rho qL=\rho C_\mu\frac{k^2}{\varepsilon} \tag{1.23}$$

The transport equation for the rate of viscous eddy dissipation is given by:

$$\frac{\partial\rho\varepsilon}{\partial t}+\frac{\partial\rho C_j\varepsilon}{\partial x_j}=\frac{\partial}{\partial x_j}\left(\left(\mu+\frac{\mu_t}{\sigma_\varepsilon}\right)\frac{\partial\varepsilon}{\partial x_j}\right)+\frac{\varepsilon}{k}\left(C_{\varepsilon1}\tau_{ij}\frac{\partial C_i}{\partial x_j}-C_{\varepsilon2}\rho\varepsilon\right) \tag{1.24}$$

The constant closure coefficients introduced in the transport equations are derived from basic experiments like boundary layer flows on a flat plate, the most commonly used values are:

$C_\mu=0.09;\quad \sigma_k=1.00;\quad \sigma_\varepsilon=1.30;\quad C_{1\varepsilon}=1.44;\quad C_{2\varepsilon}=1.92.$

k-ω Turbulence Model

Another proposal to determine the length scale, first introduced by Saffman, but popularized by Wilcox [154], is to solve for an inverse time scale, termed turbulent eddy frequency or specific dissipation rate ω

$$\omega = \frac{\sqrt{k}}{C_\mu L_t} \tag{1.25}$$

leading to an expression for turbulent viscosity

$$\mu_t = \rho \frac{k}{\omega} \tag{1.26}$$

The turbulence kinetic energy equation (1.18) undergoes minor changes to express the viscous eddy dissipation as a function of ω

$$\frac{\partial \rho k}{\partial t} + \frac{\partial \rho C_j k}{\partial x_j} = \frac{\partial}{\partial x_j}\left((\mu + \sigma^* \mu_t)\frac{\partial k}{\partial x_j}\right) + \tau_{ij}\frac{\partial C_i}{\partial x_j} - \beta^* \rho k \omega \tag{1.27}$$

Specific Dissipation Rate :

$$\frac{\partial \rho \omega}{\partial t} + \frac{\partial \rho C_j \omega}{\partial x_j} = \frac{\partial}{\partial x_j}\left((\mu + \sigma \mu_t)\frac{\partial \omega}{\partial x_j}\right) + \frac{\omega}{k}\left(\alpha \tau_{ij}\frac{\partial C_i}{\partial x_j} - \beta \rho k \omega\right) \tag{1.28}$$

The commonly used closure coefficients of the standard k-ω Model are:

$\alpha = 5/9; \qquad \beta = 3/40; \qquad \beta^* = 9/100; \quad \sigma = 1/2; \qquad \sigma^* = 1/2.$

The transport variables of the k-ε and k-ω models are related by the following equation:

$$\varepsilon = \beta^* \omega k \tag{1.29}$$

SST Turbulence Model

The k-ε and the k-ω models have for long been the two major turbulence models for industrial application involving complex geometries [104; 81; 135; 17]. Along a large number of practical applications, the $k - \varepsilon$ model augmented by a stagnation region production limiter introduced by Kato and Launder was found to be most reliable in modeling the flow far from the solid walls. The k-ω model has proven to be superior in accuracy and robustness for solving boundary layer flow and does not require artificial damping close to the wall [154]. Near wall modifications of the k-ε-model have been proposed [27; 17]. The blended model termed Shear Stress Transport (SST) model proposed by Menter [94] aims to combine both models strengths while circumventing their weaknesses. Comparative studies are presented by [95; 26]. A comprehensive study comparing results obtained with the k-ε, k-ω and SST models as with nonlinear eddy viscosity and Reynolds stress models on a separating and reattaching diffuser flow was conducted by Apsley [9]. A numerical study on pump flow using a variety of 2-equation turbulence models [53] concludes that the SST-model is the most suitable for simulations over a large range of operating conditions when flow separation is expected.

The SST model defines the blending function F_1 to weight the dissipation terms of the k-ε model in the free shear flow and the k-ω model (by $1 - F_1$) close to solid walls. The formulation is based on the scalar variables k and ω, expressing all the terms of the original k-ε model in terms of ω. This leads to the modified equations for turbulence kinetic energy :

$$\frac{\partial \rho k}{\partial t} + \frac{\partial \rho C_j k}{\partial x_j} = \frac{\partial}{\partial x_j}\left((\mu + \sigma_{k3}\mu_t)\frac{\partial k}{\partial x_j}\right) + \tau_{ij}\frac{\partial C_i}{\partial x_j} - \beta^* \rho k \omega \tag{1.30}$$

And specific dissipation rate :

$$\begin{aligned}\rho\frac{\partial \omega}{\partial t} + \rho C_j \frac{\partial \omega}{\partial x_j} = \frac{\partial}{\partial x_j}\left((\mu + \sigma_{\omega 3}\mu_t)\frac{\partial \omega}{\partial x_j}\right) + \frac{\omega}{k}\left(\alpha_3 \tau_{ij}\frac{\partial C_i}{\partial x_j} - \beta_3 \rho k \omega\right) \\ + 2(1 - F_1)\rho\sigma_{\omega 2}\frac{1}{\omega}\frac{\partial k}{\partial x_j}\frac{\partial \omega}{\partial x_j}\end{aligned} \tag{1.31}$$

Blended closure coefficients are applied: $(\Phi_3 = F_1\Phi_1 + (1 - F_1)\Phi_2)$.

Closure coefficients :

k-ω:	$\alpha_1 = 5/9$;	$\beta_1 = 3/40$;	$\sigma_{k1} = 0.5$;	$\sigma_{\omega 1} = 0.5$;	$\beta^* = C_\mu = 9/100$;
k-ε:	$\alpha_2 = 0.44$;	$\beta_2 = 0.0828$;	$\sigma_{k2} = 1$;	$\sigma_{\omega 2} = 0.856$;	$C_\mu = 0.09$;

This model combines advantages of both underlying models, but does not predict the flow separation on smooth surfaces in adverse pressure gradients correctly. This is found to be due to the over-prediction of the turbulent viscosity in the boundary layer. A better behavior is obtained by limiting the turbulent viscosity in the boundary layer that leads to a behavior similar to Reynolds stress models accounting for the transport of the main turbulent stress:

$$\mu_t = \rho\frac{a_1 k}{\max(a_1\omega, F_2 S)} \tag{1.32}$$

The blending functions F_2 and F_1 depend on the wall distance and flow variables, with values of 1 close to the wall and 0 in the free stream. Details about the blending functions and the numerical implementation to determine the wall distance are given in [94; 3].

1.2.2 Boundary Layer Modelling

The presence of the no-slip condition $\mathbf{C} = \mathbf{0}$ at solid walls leads to a zone of low velocity and strong shear in its vicinity termed Boundary Layer (BL). The accuracy of turbulence modelling approaches in the prediction of velocity profiles in the boundary layer and the resulting wall shear stress is essential to the overall accuracy of the simulation results.

Figure 1.1 represents a typical turbulent boundary layer profile in logarithmic and linear axis scaling using the following definitions of nondimensional values:

- The shear velocity $C_\tau = \sqrt{\tau_w/\rho}$
- Nondimensional velocity $C^+ = \frac{\overline{C_t}}{C_\tau}$
- Nondimensional wall distance $y^+ = \frac{\rho C_\tau y}{\mu}$

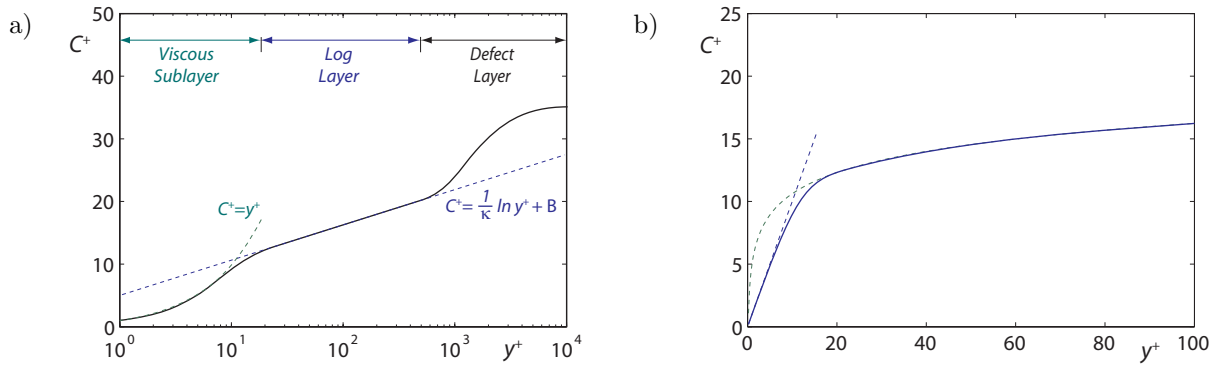

Figure 1.1: Typical turbulent boundary layer profile. a) Logarithmic representation [155], b) Linear representation

Three different zones are identified: The zone close to the wall is termed viscous sublayer, the flow is governed by laminar shear stresses due to their strength and to the inhibition of formation of turbulent structures by the presence of the wall. The zone far from the wall is characterized by a velocity defect due to the influence of the wall shear. Turbulent momentum transfer according to the modeling equations along with its constants takes place in this zone. The intermediate transition zone is characterized by a logarithmic velocity profile:

$$C^+ = \frac{1}{\kappa} \ln y^+ + B \tag{1.33}$$

with the von Karmán constant $\kappa = 0.41$ and an empirical constant $B = 5.0$, the latter usually derived from flat plate boundary layer flow.

The SST model takes advantage of the fact that the k-ω model used in the boundary layer leads to stable numerical solution without arbitrary damping factors required to apply k-ϵ models close to the wall. It allows to resolve the boundary layer consistently using mesh resolutions down to the viscous sublayer. However, in engineering applications in complex three dimensional geometries, including turbomachinery applications, the resolution down to the viscous sublayer is often impractical with reasonable mesh sizes. It could be achieved by coarsening other mesh region or disregarding the profile of the boundary layer: Using a first node very close to the wall and a fast transition to larger mesh spacings does not allow an accurate flow modeling in the boundary layer. In this case, it is preferable to use the wall function approach proposed by Launder and Spalding [82] to determine the relationship of wall shear stress τ_w and wall tangential velocity C_t on the first mesh node based on equation (1.33).

1.3 Energy Conservation and Viscous Losses

The main objective of a centrifugal pump is the transfer of energy from mechanical energy at the shaft into a specific hydraulic energy difference from low pressure ($\bar{I}$) to high pressure (I) sections of the machine. The conservation of energy is an important issue

in numerical simulation of turbomachinery flows. Taking the scalar product of equation (1.1) with the velocity results in the conservation equation for kinetic energy for a control volume V enclosed by boundaries ∂V:

$$\begin{aligned}\frac{\partial}{\partial t}\int_V \frac{C^2}{2}dV = &-\int_{\partial V}\left(\frac{C^2}{2}+\frac{p}{\rho}\right)C_i n_i dA + \frac{1}{\rho}\int_{\partial V}\tau_{ij}C_i n_j dA \\ &-\frac{1}{\rho}\int_V \tau_{ij}\frac{\partial C_i}{\partial x_j}dV - \int_V f_i C_i dV\end{aligned} \tag{1.34}$$

For Newtonian fluids

$$\begin{aligned}\frac{\partial}{\partial t}\int_V \frac{C^2}{2}dV = &-\int_{\partial V}\left(\frac{C^2}{2}+\frac{p}{\rho}\right)C_i n_i dA + \frac{1}{\rho}\int_{\partial V}2\mu D_{ij}C_i n_j dA \\ &-\frac{1}{\rho}\int_V 2\mu D_{ij}D_{ij}dV - \int_V f_i C_i dV\end{aligned} \tag{1.35}$$

The principle of conservation of specific hydraulic energy gH is easily derived from this assuming:

- steady flow, $\frac{\partial}{\partial t}\int_V \frac{C^2}{2}dV = 0$
- Inviscid flow, $\mu = 0$
- the gravity field as only body force, $\mathbf{f} = \nabla(-gz)$
- the inlet section k and outlet section l as only passage sections
- zero velocity (stationary solid walls Σ) at the rest of the domain boundary

$$\int_{A_k \cup A_l}\left(\frac{C^2}{2}+\frac{p}{\rho}+gz\right)C_i n_i dA = 0 \tag{1.36}$$

Defining the specific hydraulic energy gH on any section k as

$$gH_k = \frac{1}{Q}\int_{A_k}\left(\frac{C^2}{2}+\frac{p}{\rho}+gz\right)C_i n_i dA \tag{1.37}$$

the losses $gH_{r\,k\div l}$ due to the viscous dissipation term $\int_V 2\mu D_{ij}D_{ij}dV$ between section A_k and section A_l in a time-independent flow are obtained from equation (1.35)

$$gH_{r\bar{1}\div 1} = gH_k - gH_l + \frac{1}{\rho Q}\int_{\partial V}2\mu D_{ij}C_i n_j dA \tag{1.38}$$

Energy Conservation in Rotating Domains

Considering the equation of motion in a rotating frame, (1.7), the Coriolis term does not contribute to the energy equation as the resulting body force is perpendicular to the velocity vector C_i. The centrifugal term can be written under potential form:

$$\boldsymbol{\omega}\times(\boldsymbol{\omega}\times\mathbf{X}) = \nabla\frac{\omega^2 R^2}{2} = \nabla\frac{U^2}{2} \tag{1.39}$$

to transfer it into a surface integral using Green's law:

$$\frac{\partial}{\partial t}\int_V \frac{W^2}{2}dV = -\int_{\partial V}\left(\frac{W^2-U^2}{2}+\frac{p}{\rho}\right)W_i n_i dA + \frac{1}{\rho}\int_{\partial V}\tau_{ij}W_i n_j dA \\ -\frac{1}{\rho}\int_V \tau_{ij}\frac{\partial W_i}{\partial x_j}dV - \int_V f_i W_i dV \tag{1.40}$$

The conserved quantity corresponding to the specific hydraulic energy gH in a rotating frame of reference is termed relative hydraulic specific energy gH^{rel} or specific rothalpy.

$$gH_k^{rel} = \frac{1}{Q}\int_{A_k}\left(\frac{W^2-U^2}{2}+\frac{p}{\rho}+gz\right)W_i n_i dA \tag{1.41}$$

Energy Conservation and Eddy-Viscosity Turbulence Models

In the context of the Reynolds averaged turbulence modeling, the kinetic energy of the mean flow can be determined by the velocity field of the flow simulation. The kinetic energy of the fluctuating part of the velocity, turbulent kinetic energy k, is available as a separate modeled transport variable. According to the models equation, turbulent kinetic energy is not recovered into energy of the mean flow and is considered as lost from an engineering stand point. Following the turbulent energy dissipation cascade it will finally be dissipated into thermal energy. The production term in the k transport equations (1.21) expresses the energy transfer from the main flow loss due to the turbulent viscosity consistently with equation (1.15). Consistently, the turbulent viscosity behaves as the fluid viscosity and leads to a supplementary viscous loss. This leads to the mean flow kinetic energy conservation equation in the context of eddy viscosity turbulence models:

$$\frac{\partial}{\partial t}\int_V \frac{C^2}{2}dV = -\int_{\partial V}\left(\frac{C^2}{2}+\frac{p}{\rho}\right)C_i n_i dA + \frac{1}{\rho}\int_{\partial V}\tau_{ij}C_i n_j dA \\ -\frac{1}{\rho}\int_V 2(\mu+\mu_t)D_{ij}D_{ij}dV - \int_V f_i C_i dV \tag{1.42}$$

With the Reynolds averaged approach of separation of mean and fluctuating part of the flow fields and the Boussinesq hypothesis 1.15, the power of viscous momentum flux through the boundaries $\int_{\partial V}\tau_{ij}C_i n_j dA$ becomes accessible to considerations based on the mean velocity and its gradients. It is zero under any of the following conditions:

- Zero flow velocity at solid wall boundary $\Sigma : C_i = 0$
- Plane passage section A: $\frac{\partial n_i}{\partial x_j} = 0$,
  Mean flow normal to A: $C_i = n_i C$, and
  Zero gradient in the flow direction: $n_i \frac{\partial C}{\partial x_i} = 0$

$$\tau_{ij}C_i n_j = 2\mu\left(n_i\frac{\partial C}{\partial x_j}+n_j\frac{\partial C}{\partial x_i}\right)n_i C n_j = \mu C\left(n_i n_i \underbrace{\frac{\partial C}{\partial x_j}n_j}_{=0} + n_j n_j \underbrace{\frac{\partial C}{\partial x_i}n_i}_{=0}\right) = 0$$

Flow conditions in passage sections considered in practice typically come so close to the last condition that the resulting terms are negligible and can safely be ignored in loss analysis. For centrifugal pump study cases presented in this work, the terms evaluated on the circular sections that are normal to the main flow are found to be smaller than 0.5% of the overall losses. On the cylindrical section in the rotor-stator interface region, the power of viscous momentum flux through the interface is found to take values of up to 0.1% of the power transferred from the impeller to the fluid. Though small compared to the considered balances, the latter should not be neglected when power balances of the different components are established.

Internal Energy Loss Coefficients

Numerical simulation allows the evaluation of the flow field and of energy integrals at all internal sections of the machine. In order to determine the considered control volume, the energy coefficients ψ, and the energy loss coefficients ψ_r are indexed by the limiting passage sections. For practical reasons, notwithstanding the precise definition of sections in IEC 60193, sections 1 and 2 and other such pairs are evaluated on the same location representing the simulation grid boundaries, using the rotating frame variables for section 1 and stationary frame variables for section 2. The losses in the rotating impeller domain V_b follow from the principle of conservation of rothalpy:

$$\psi_{r,\bar{1}\div 1} = \frac{2}{U_{1e}^2}\left(gH_{\bar{1}} - gH_1 - \frac{1}{\rho Q}\int_{A_{\bar{1}}\cup A_1} \tau_{ij} W_i n_j dA - \frac{1}{Q}\frac{\partial}{\partial t}\int_{V_b} \frac{W^2}{2} dV\right) \tag{1.43}$$

Considering the impeller domain in the stationary frame results in extra terms on the rotating surface Σ_b, equivalent to the torque transferred from the impeller to the fluid:

$$\begin{aligned}\psi_{r,\bar{1}\div 1} = \frac{2}{U_{1e}^2}\Bigg(&gH_{\bar{1}} - gH_1 - \frac{1}{\rho Q}\int_{A_{\bar{1}}\cup A_1} \tau_{ij} C_i n_j dA \\ &- \frac{1}{\rho Q}\underbrace{\int_{\Sigma_b} (\tau_{ij} - p\delta_{ij}) U_i n_j dA}_{P_t = \omega T_t} - \frac{1}{Q}\frac{\partial}{\partial t}\int_{V_b} \frac{C^2}{2} dV\Bigg)\end{aligned} \tag{1.44}$$

Yielding the general expression for a control volume $V_{k\div l}$ between sections k and l:

$$\psi_{r,k\div l} = \epsilon_t \psi_t + \frac{2}{U_{1e}^2}\left(gH_{\bar{1}} - gH_1 - \frac{1}{\rho Q}\int_{A_k\cup A_l} \tau_{ij} C_i n_j dA - \frac{1}{Q}\frac{\partial}{\partial t}\int_{V_{k\div l}} \frac{C^2}{2} dV\right) \tag{1.45}$$

$$\text{with} \quad \epsilon_t = \begin{cases} 1 & \text{if the control volume contains the impeller, } k < 0 \quad \textit{and} \quad l > 0 \\ 0 & \text{otherwise} \end{cases}$$

Evaluation of Energy and Loss Coefficients in Time-Dependent Flows

In time dependent flow simulation, the time derivative of kinetic energy in the system can take relevant values and shows to be extremely variable when evaluated by difference of two consecutive simulation time steps, leading to a high variance of the computed coefficients. The evaluation of energy coefficients and loss coefficients based on time integrals over longer time intervals (typically one revolution) yields less variable results.

Depending on the definition of the simulation domain, the sections $\bar{I}$ and I may not be available. The energy coefficient from sections k and l for a time interval $[t_1; t_2]$ is determined as follows:

$$\psi_{k\div l} = \frac{2}{U_{1e}^2(t_2 - t_1)} \int_{t_1}^{t_2} \left(gH_l - gH_k - \frac{1}{\rho Q} \int_{A_k \cup A_l} \tau_{ij} C_i n_j \, dA \right) dt + \frac{2}{U_{1e}^2 Q(t_2 - t_1)} \left| \int_{V_{k\div l}} \frac{C^2}{2} dV \right|_{t_1}^{t_2} \tag{1.46}$$

and the loss coefficient for any two sections k and l is found as:

$$\psi_{r,k\div l} = \frac{\epsilon_t}{\frac{1}{2} U_{1e}^2 Q(t_2 - t_1)} \int_{t_1}^{t_2} \omega T_t(t) dt - \psi_{k\div l} \tag{1.47}$$

In numerical simulation providing results at equidistant time steps, an approximation of the time integrals is obtained by the arithmetic average of time steps values. With increasing length of the simulation time interval, the last terms becomes smaller since there is no physical reason for relevant accumulation of kinetic energy in the simulation domain for intervals covering an integer number of time periods following equation (27).

$$\psi_{k\div l} = \frac{2}{U_{1e}^2} \left(\overline{gH_l} - \overline{gH_k} - \frac{1}{\rho Q} \overline{\int_{A_k \cup A_l} \tau_{ij} C_i n_j \, dA} \right) + \frac{2}{U_{1e}^2 Q(t_2 - t_1)} \left| \int_{V_{k\div l}} \frac{C^2}{2} dV \right|_{t_1}^{t_2} \tag{1.48}$$

Chapter 2

Numerical Simulation

2.1 Finite Element Based Finite Volume Discretization

The above model equations are discretized and solved to predict the complex flow in turbomachines. Amongst the discretization methods for fluid dynamics applications, the finite volume (FV) method is the most used for complex engineering problems. The majority of industrial and open source codes designed for application in complex geometries use this discretization technique. It is an Eulerian, volume mesh-based technique: The volume of investigation is represented by a mesh made of volume elements defined by their vertex nodes. The mesh nodes remain stationary resp. rotate with the solid walls limiting the domain. Vectors of velocity components and pressure at each mesh node constitute the discrete representation of the continuous flow field. The simulation domain is divided into a large number of control volumes (CV) derived from the mesh volume elements and the conservation laws for mass and momentum are established for each CV V bounded by Surfaces ∂V.

$$\int_{\partial V} C_i n_i dA = 0 \tag{2.1}$$

$$\frac{\partial}{\partial t}\int_V C_i dV + \int_{\partial V} C_i C_j n_j dA = \frac{1}{\rho}\int_{\partial V} T_{ij} n_j dA + \int_V f_i dV \tag{2.2}$$

$$T_{ij} = \mu\left(\frac{\partial C_i}{\partial x_j} + \frac{\partial C_j}{\partial x_i}\right) - \delta_{ij} p \tag{2.3}$$

The gravity body force g_i is not explicitly modeled. This is equivalent to the use of a modified pressure $p^* = p - \rho g_i x_i$ such that $-\frac{\partial p^*}{\partial X_i} = -\frac{\partial p}{\partial x_i} + g_i$, compare equation (1.1). In the context of numerical simulation analysis, p and c_p are tacitly used to designate this modified pressure in the remainder of this document. For the evaluation of specific hydraulic energy, this modified pressure regroups the pressure and the gravity term.

Mass and momentum are conserved over the entire simulation domain by principle if the fluxes in and out of adjacent control volumes are defined to be equal, which is the case in almost every straightforward approach. The fluxes are expressed as linear combinations of the unknown flow variables at the mesh nodes to obtain a discrete linear equation system. The node-centered, collocated scheme using finite element shape functions is

briefly presented as implemented in the commercial finite volume solver CFX-5 used for the study cases.

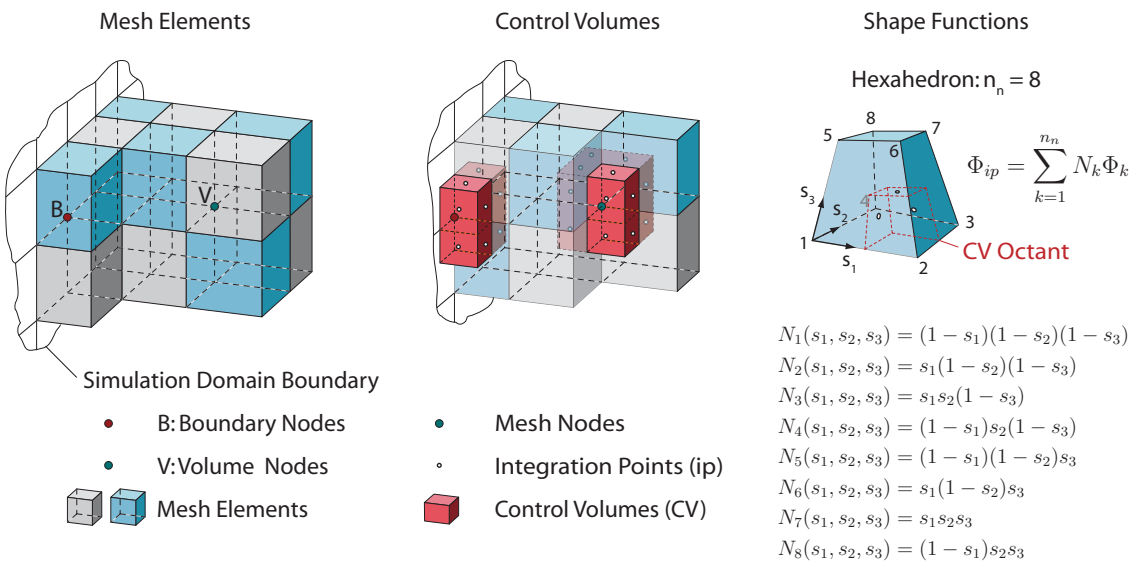

Figure 2.1: Finite element based finite volume discretization: Mesh elements, control volumes and shape functions

The control volumes are built around the mesh nodes according to figure 2.1. In case of block structured hexahedral meshes, the control volumes are composed of eight octants, forming the intersection of the CV with the eight mesh volume elements adjacent to a node. At the boundaries of the domain the node is representative for a control volume half the size of the usual ones. In the finite element based finite volume approach, linear shape functions based on the initial mesh element are used to express values at the integration points. The gradients with respect to the cartesian coordinates are determined via the Jacobian that is invertible for regular element shapes:

$$\frac{\partial \Phi}{\partial x_i} = \sum_{k=1}^{n_n} \frac{\partial N_k}{\partial x_i} \Phi_k \qquad \text{with} \qquad \frac{\partial N_k}{\partial s_j} = \frac{\partial x_i}{\partial s_j} \frac{\partial N_k}{\partial x_i} \tag{2.4}$$

Various methods are applied in engineering practice and fluid dynamics research to express the advection fluxes $\int_{\partial V} \Phi C_j n_j dA$ as a function of nodal variable values since the essential tradeoff between robustness and accuracy lies herein. The schemes available in the used solver are based on the value Φ_{up} at the upwind node together with a gradient based anti-diffusive correction term:

$$\Phi_{ip} = \Phi_{up} + \beta \frac{\partial \Phi}{\partial x_i} \quad \left[(x_i)_{ip} - (x_i)_{up} \right] \tag{2.5}$$

Different options to define the blending factor β and the according methods of gradient evaluation are summarized in table 2.1.

The adaptive scheme termed High Resolution scheme determines the blend factor locally in order to obtain the best accuracy while guaranteeing boundedness of the solution [3]. Along the investigated study cases, this scheme has proven to provide a second order discretization in the major parts of the domain, even in almost all of the zones of high gradients. The blend factor was found to be locally decreased at locations with high skew changes in the block-structured meshes. Single validations against simulations using a fixed blend factor of $\beta = 0.75$ show little differences in the results.

Option	β		Gradient evaluation
Upwind scheme, first order	fixed	0	Surrounding nodes average
Second order		1	
Central difference scheme		1	Element shape functions
High Resolution - bounded	Upwind node	adaptive	

Table 2.1: Advection schemes in CFX-5 [3]

The time-dependent term on the left hand side of equation (2.2) is expressed using a first order implicit Euler formulation with the mid-point integration rule involving the current and previous time level value Φ resp. Φ^0:

$$\rho \frac{\partial}{\partial t} \int \Phi dV = \rho V \frac{\Phi - \Phi^0}{\Delta t} \tag{2.6}$$

or a second order backward Euler scheme involving an additional previous time level Φ^{00}

$$\rho \frac{\partial}{\partial t} \int \Phi dV = \rho V \frac{3\Phi - 2\Phi^0 + \Phi^{00}}{2\Delta t} \tag{2.7}$$

The first order scheme is used for time independent simulations, the time step then takes the role of a convergence acceleration parameter. The time dependent simulations presented in this work have all been carried out using the second order backward Euler scheme. The nonlinear terms and the eddy viscosity provided by the turbulence model are treated by an explicit procedure, using the values obtained from the previous iteration. Several so termed coefficient loop iterations for a physical time step are evaluated to improve the accuracy of these nonlinear terms for time-dependent simulations.

2.2 Boundary Conditions and Interfaces

In the finite volume method, the equation system assembly is based on the fluxes determined from solution field and gradients on the integration points located on the control volume faces. At the boundaries of the domain, a sufficient number of conditions to obtain a determined equation system is needed. Due to the upwind biased nature of the advection schemes, the following procedure to prescribe boundary conditions is the most straightforward and numerically stable.

Inlet Boundary Condition

A constant bulk velocity normal to the boundary surface is imposed at the inlet boundary condition faces. The flow rate is thereby fixed at a constant value. Values for the turbulence model variables k and ω are determined using a typical assumption for technical flows: The turbulence intensity is estimated to be 5% and the ratio of turbulent viscosity to fluid dynamic viscosity μ_t/μ to be 10. The inlet turbulence conditions, especially the dissipation rate of the k-ε-model, were shown by [89] to have a large influence on results in the simulation of a single draft tube of a Francis turbine. Sensitivity studies on the study cases investigated in this thesis did not show a relevant dependency of the results on the turbulence model variables at the inlet. The balance of production and dissipation of turbulent kinetic energy is mainly governed by the shear rate of the flow in the impeller and in the rotor-stator interface region.

Outlet Boundary Condition

The advective fluxes and scalars are determined from the upwind nodes with a zero-gradient hypothesis. It is essential for this that the flow is effectively directed outwards of the domain. The additional equation needed to fix the pressure level in the domain, is currently obtained by imposing a zero value for the area-weighted average of pressure on the outlet boundary surface.

Wall Boundary Conditions

No-slip conditions $\mathbf{C} = \mathbf{0}$ are imposed at all solid walls sharing the revolution rate of the considered control volume. In turbomachinery simulations, surfaces of revolution (esp. hub or casing surfaces) revolving at a different rotation rate than the frame of reference are encountered:

- Rotating solid walls in a stationary frame of reference: $\mathbf{C} = \mathbf{U} = \boldsymbol{\omega} \times \mathbf{X}$
- Stationary walls in a rotating frame of reference: $\mathbf{W} = -\boldsymbol{\omega} \times \mathbf{X}$.

No particular difficulties arise from the implementation of those non-zero velocity boundary conditions.

In the discretization procedure implemented in the CFX-5 solver the mesh boundary nodes are virtually moved to the center of the control volume adjacent to the wall, see figure 2.1. The shear stress on the wall face is determined as a function of the nodes so termed "conservative" velocity values, as opposed to the physically correct "hybrid" boundary value at the wall used for post-processing purposes. The implementation of the SST-model used in the presented study cases automatically switches between the use of logarithmic wall functions, equation (1.33), and the full resolution down to the laminar viscous sublayer to determine the relation of wall shear and wall node's conservative velocity. A threshold value of $y^+ = 11$ of the dimensionless wall distance of the virtual wall node location determines which shear-velocity relation is used. In all time-dependent simulation study cases, the mesh resolution is such that the logarithmic wall function is used for almost all relevant solid walls.

Interfaces for Non-Matching Meshes

Numerical flow simulation requires volume meshes of relatively high quality. Solution accuracy and robustness of the algorithms is severely impaired by highly skewed elements or excessively high aspect ratios, except when the refinement direction is aligned with the main direction of the gradients. In case of complex geometries, an improvement of the overall mesh quality can often be achieved when different parts of geometry can be meshed separately using different meshing approaches and adapted software tools. Block structured meshes made of hexahedral elements are generally considered the most effective discretization inside boundary layers. Unstructured meshes of tetrahedral elements allow representing even the most distorted volume regions with volume elements of regular quality and without biasing the simulation results by the anisotropic character of structured meshes. The most common approach to accommodating the non-matching meshes in the finite-volume method are non-overlapping interface surfaces. The CFX-5 solver implements them in a fully conservative implicit manner via the formulation of additional control surface equations linking the fluxes in and out of the control volumes as represented in figure 2.2. The discretization schemes for the half-control-volumes are adapted to use the nodal variables from the volumes and the control surface variables, details are given in [3].

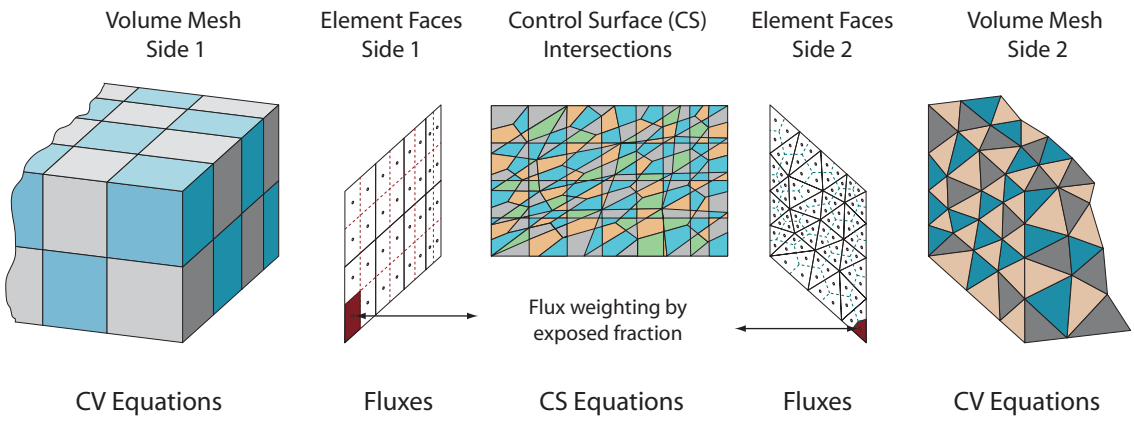

Figure 2.2: Interfaces for non matching non-overlapping meshes based on control surfaces

For the simulation of centrifugal pump flow, the impeller has to be considered in the rotating frame of reference while inlet casing, diffuser and volute are stationary. So-called rotor-stator interfaces, non-matching interfaces defined on surfaces of revolution separating the components are used to deal with the transfer of fluxes between the stationary and the rotating domain. They allow at the same time the use of non-matching meshes between the components.

Frame Change Interfaces for Time-independent Simulations

The mixing plane approach is based on the hypothesis that a time-average flow solution can be obtained by solving for a time-independent solution and averaging the fluxes in circumferential direction on the interface surface. It can be used for simulation of

flow through turbomachinery components featuring different, typically incommensurable, numbers of blades in the impeller and in the diffuser or even to solve a single impeller channel flow together with a volute featuring 360° pitch. It is best applicable to centrifugal pumps with a relatively large radial gap between the impeller blade outer radius R_1 and the diffuser blade or volute tongue inner radius R_2. This is typically the case in pump-turbines. The mixing plane approach has proved to yield useful information about the impeller flow for simple volute pumps without diffuser blades with moderate computing resources. The use of such simulations has become the standard procedure in centrifugal pump impeller design to determine the deviation of the relative flow angle at impeller outlet β_1 from the blade ("metal") angle β_{1b}. Numerically, the circumferential averaging is done by intersecting the control volume faces of both meshes with control surfaces that form circumferential bands. A scaling factor for the fluxes is introduced in the control surface equations to account for the ratio of the angular pitches of the interface sides. Even though this interface type is fully implicit and conservative, it tends to be numerically unstable when intensive back flow occurs. The results obtained in such configurations by a time-independent approach are questionable anyway.

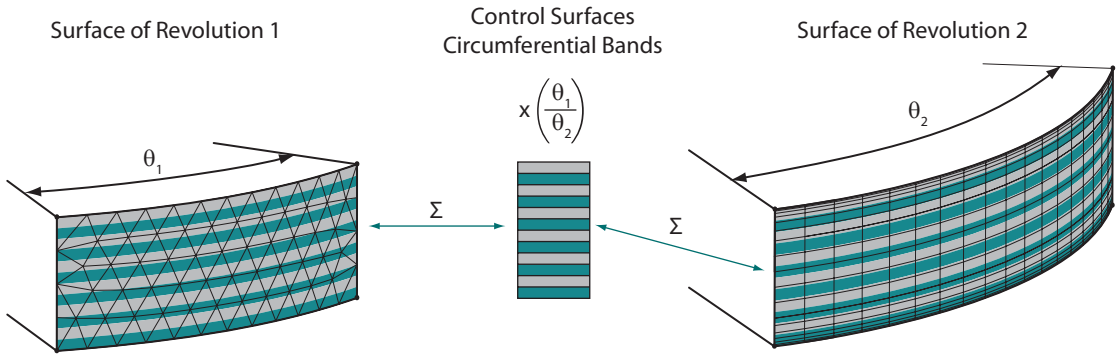

Figure 2.3: Principle of the mixing plane interface

Another steady approach is to intersect the meshes as is, matching the pitches by an angular stretching and matching orphan elements on both sides by periodic matching. This approach termed "frozen rotor" is numerically robust but the results depend heavily on the arbitrary angular position of both components. It is used in the case studies presented herein to get initial values for the time-dependent simulations but these intermediate results are not subject to further analysis.

Frame Change Interfaces for Time-dependent Simulations

While the mixing plane and frozen rotor approaches have proven to provide some understanding of flow features and some useful quantitative information concerning impeller flow and overall performance prediction for pump design, especially around BEP, they cannot be expected to yield relevant information for part-load operating points. The transient rotor-stator interface technique consists in re-intersecting the meshes of the stationary and rotating frame for every angular position of the impeller. Advances in

implementations, studies on requirements on temporal and spatial resolution and considerations on numerical diffusion of blade wake profiles over such interfaces were achieved in the framework of the HPNURSA project [52]. Lardeau and Leschziner [79] investigated a blade wake interaction study case consisting of an axial turbomachine single periodic blade passage in 2006. They concluded that even with RANS approaches, a high temporal and spatial resolution is required to obtain a mesh- and time step independent solution. They propose to use variable inflow conditions, formulated as functions of space and time instead of sliding interface approaches when the potential interaction effect is negligible. This choice is justified for such an axial arrangement of blade cascades with a relatively large axial gap between the blade rows, but infeasible for radial centrifugal pumps, where the time-dependent interaction of rotating and stationary velocity and pressure fields has relevant effects in the upstream and downstream direction of the interface.

2.3 Error Sources in Numerical Simulation

Ferziger and Peric [43] propose the following hierarchy of error sources in numerical simulations:

- Modeling Errors
- Discretization errors
- Iteration and Truncations errors
- Programming and User Errors

Modeling Errors

The modeling errors include all differences between physical reality and the governing equations used, including the assumptions made on steadiness or unsteadiness of the phenomena. In structural mechanics, using Hooke's isotropic linear Law for a material with more complex behavior, namely anisotropic or nonlinear, introduces a substantial modeling error. In fluid mechanics for high Reynolds numbers, the use of turbulence modeling potentially leads to the most serious modeling errors. Another important source of modeling errors is the definition of boundary conditions. In the finite volume method using upwind biased schemes for the advection terms, all fluxes entering into the domain are determined by the inlet boundary condition values. Another error source is the assumption of perfectly incompressible fluid and of rigid solid boundaries. It is known that the propagation of pressure waves has a finite velocity of about $1200\,m/s$ in an infinite domain of water. The hydro-acoustic wave propagation due to the deformation of pipes and turbomachinery components are successfully modeled by compressible methods introducing modified wave propagation velocities [105]. A numerical method based on the incompressible Navier-Stokes equations is not expected to reproduce any of these phenomena correctly.

Discretization Errors

The discretization error is defined as the difference between the exact solution of the governing equations (including all modeling) and the exact solution of the discrete approximation. The finite volume method approximates the time, surface and volume integrals of the control volumes in terms of the nodal variables at given time steps. When applied in complex geometries, the computational effort scales (in best case linearly) with the number of volume elements and nodes that are modeled. Refining the mesh spacing in a uniform and isotropic way by a factor of two, which is required for a reasonable comparison, multiplies the number of nodes by 8. A practical problem to assess the quality of a given spatial discretization is that the exact solution of the governing equations is not known and that further mesh refinement is often beyond the scope of available computing resources. Preliminary studies isolating flow features of interest out of a complex configuration can help to establish rules for discretization of particular regions. Adaptive meshing aims to construct error estimators and automatically generate meshes that reduce the discretization error. While the procedures become practical for steady flow cases [72], a continuous re-meshing for time-dependent application in complex geometries is still out of scope. Care is to be taken when comparing simulation to experimental results, as they do not represent the solution of the governing equations when turbulence models are used, so a comparison with experimental results can suffer from canceling of modeling versus discretization errors. Detailed discretization error study using highly refined meshes is feasible for steady flow approximations of turbomachinery flow and will be presented in chapter 5.

Iteration and Truncation Errors

In engineering practice, truncation error and iteration errors for truly steady problems can be quantified and avoided rather easily when compared to the two former error classes. Nowadays most common processors are such that the frequent add-multiply instruction of scientific software take the same number of processor cycles in double and single precision. The main issue with the use of double precision representation for complex engineering applications is the doubling of the memory requirements for all real numbers (which represent most of the memory requirement of flow solvers) and doubling the file size of any intermediate result that will consequently be stored as double precision. Single precision representation has been shown to be sufficient for all study cases presented here and is used to reduce the memory and disk space requirements that are one of the main factors limiting the problem size. Iteration errors are defined by [43] as the difference of the exact solution of the discretized equation system and the solution thereof obtained by iteratively linearizing and solving this system. The criterion to determine when to stop the iteration loop is usually determined on the residuals of the solved quantities (mass, momentum and turbulence model variables), that indicates how much these quantities change from one iteration to another. In current CFD Codes, the residuals are normalized with respect to the overall range of the quantity of interest. Despite this normalization, the limits suggested by the code developers and some published best practice guidelines have to be considered only as a guideline for a reasonable level to start the investigations with. In steady flow application, it is relatively easy to store and analyze results at different residual levels, see chapter 5. In time dependent flow applications, the iteration criterion

is applied at every simulation time step, two flow simulations of a representative period have to be conducted to compare results of different iteration criterions. It is difficult to assess the severity of differences in instantaneous flow fields if the global flow properties are sufficiently similar. Furthermore, the choice of the time step (time discretization) interacts with the reasonable level of iteration error reduction. It is advised in [3] that for a given computational effort, a better precision can be achieved by reducing the time step size than by increasing the number of iterations for each time step. In the context of the time-dependent simulation presented in chapter 8 a study of timestep refinement will be presented using a fixed residual convergence criterion.

Energy Conservation and Discretization Errors

Ferziger and Peric [43] state that while the conservation of momentum and mass is easily fulfilled by finite volume methods, the conservation of kinetic energy depends on the interpolation method. Felten and Lund [42] showed that the choice of discretization schemes in finite volume methods affects the conservation of kinetic energy and have proposed energy-conserving first order centered schemes as best choice for channel flows. For reasons of superior numerical stability, upwind schemes with gradient based advection correction are used in the CFX-5 solver. This means equation (1.42) is not inherently conserved, a numerical diffusion loss term, $P_{r,num}$, is introduced in the discretized balance of kinetic energy:

$$\frac{\partial}{\partial t}\int_V \rho\frac{C^2}{2}dV = -\int_{\partial V}(\rho\frac{C^2}{2}+p)C_i n_i dA + \int_{\partial V}\tau_{ij}C_i n_j dA - \int_V 2(\mu+\mu_t)D_{ij}D_{ij}dV - P_{r,num} \tag{2.8}$$

In a numerical simulation covering the time interval $[t_1;\, t_2]$ within the domain V, the numerical diffusion loss is obtained by the difference of energy dissipation evaluated by inlet-outlet balances and the volume integral of viscous dissipation

$$\begin{aligned} P_{r,num} = \quad & \frac{1}{(t_2-t_1)}\left(\int_{t_1}^{t_2}\left(-\int_{\partial V}(\rho\frac{C^2}{2}+p)C_i n_i dA + \int_{\partial V}\tau_{ij}C_i n_j dA\right)dt \right. \\ & \left. -\int_{t_1}^{t_2}\int_V 2(\mu+\mu_t)D_{ij}D_{ij}dV\,dt - \left|\int_V \rho\frac{C^2}{2}dV\right|_{t_1}^{t_2}\right) \end{aligned} \tag{2.9}$$

The numerical diffusion loss is a measure of the accuracy of the discretization scheme, classified as a second order error estimator by [120]. It is shown with the steady pump-turbine study case that the numerical diffusion losses can be reduced with the upwind based schemes by using highly refined meshes. Such meshes can readily not be applied to time-dependent simulations, casting into doubt the time-dependent energy balances obtained from the latter, as will be detailed in the analysis of the double suction pump results.

Programming and User Errors

Programming and user errors can seriously affect the results of numerical simulations. The most evident cases, where a code crashes or yields completely unphysical results are the rather harmless occurrences of such errors, since they are easily identified. The most annoying errors just result in subtle inconsistencies in the flow field and energy balances, that are difficultly descried in complex applications such as time-dependent simulations of turbomachinery flow. Validation on simple study cases with well documented results from experiment and former numerical studies are mandatory after every major code modification. Industrial and open-source code development is typically organized in major release cycles. This includes exhaustive testing of pre-release (beta-) versions on a multitude of documented study cases.

Advanced graphical user interfaces, including post-processing tools with convenient quantitative reporting features, may per se not add much to the scientific capabilities of a simulation software. But they allow to check the consistency of a numerical setup and its results with reasonable expenditure of time, even for complex applications.

2.4 Computing Resources and Parallel Scalability

The simulations described in this document were executed on numerous computing infrastructure available at LMH and at the EPFL central computing facilities. The time dependent simulations described in chapters 8 and 6 were mostly executed in parallel using 16 partitions. The major part of the numerical simulations were run on the LMH compute cluster nodes hosting two Intel Xeon dual core processors each, and equipped with equipped with $1.5GB$ of memory per processor core. The maximum realizable mesh node number with this infrastructure is about $5.0 \cdot 10^6$ when using block-structured hexahedral meshes. The average resulting wall clock time is 31 hours per impeller revolution, resulting in total wall clock times of a month for the simulation of 20 impeller revolutions.

Tentative simulations modeling the domain using a $13 \cdot 10^6$ node mesh, which allows to refine the $4.5 \cdot 10^6$ nodes pump-turbine scale model mesh (chapter 8) by a factor of 1.4 in every spatial direction proved to be difficult to run efficiently. Using 32 respectively 64 partitions (executed on bi-processor AMD-Opteron compute nodes on the EPFL central computing facilities cluster "Mizar"), the wall clock times to simulate an impeller revolution using the same time step and convergence requirements are 2.8 respectively 3.3 times longer than with the $4.5 \cdot 10^6$ node mesh on 16 processors on the same hardware infrastructure. The large mesh simulation was impossible to execute on 16 processors due to the memory limitations of $2GB$ per processor.

The gain in wall clock time using 64 partitions instead of 32 on the large mesh, reducing the computation time by a factor of $2.8/3.3 = 0.85$ while increasing the used resources (compute nodes and parallel licenses) by a factor of 1.7 was judged to be inappropriate. Improvements in the parallel scalability of large cases involving transient rotor stator interfaces are necessary to allow an efficient use of refined meshes. Cluster compute nodes equipped with more memory per processor could overcome this limitation to some extent. Simulations requiring such resources as requested by the $13 \cdot 10^6$ nodes mesh can at the moment not be used when aiming at the discovery of numerical simulation outcomes over a large range of operating conditions.

Chapter 3

Instrumentation for Investigation of Centrifugal Pump Flow

3.1 EPFL Experimental Validation Facilities

The hydraulic turbomachines validation facilities at LMH-EPFL, figure 3.1 are designed and maintained to measure pump and turbine performance according to the IEC standards [1] within an accuracy of 0.2% using the following instrumentation:

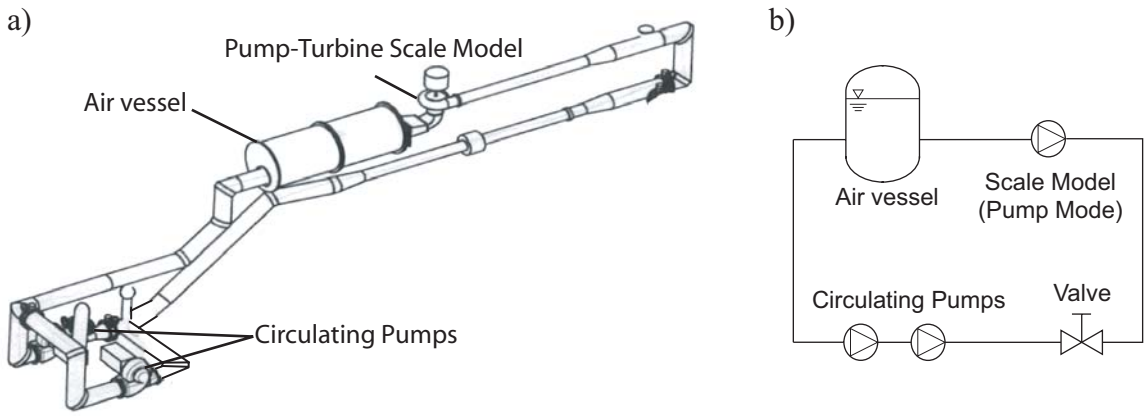

Figure 3.1: Experimental validation facility in closed loop serial pump configuration, a) 3D-View, b) Principal components

- Shaft torque measurement
- Electro-magnetic flow meters
- Differential pressure sensors connected at the high-pressure (I) and low pressure $\bar{I}$ reference sections of the machine

For measurements in pump mode with low specific speed pump-turbine scale models, the valves in the closed loop circuit do not allow sufficient control of the operating conditions,

especially at part load. Therefore, the circulating pumps are operating in serial mode at negative flow rates (following their positive flow rate definition convention) with a positive flow rate of the investigated pump-turbine model. Variation of the circulating pump revolution rate allows a stable operation of the test facility.

3.2 Transient Pressure Measurements

3.2.1 Piezoresistive Pressure Sensors

Piezoresistive pressure sensors are used for the dynamic pressure measurements. They make use of the effect of a thin layer of semiconducting material changing its resistance under the effect of pressure. The sensitive unit features 4 such semiconductor gauges placed on a deformable membrane-like unit in such a way that they are pairwise stretched or compressed under the effect of pressure. They are connected to form a Wheatstone bridge and completed by additional resistances and measures to minimize the temperature sensitivity. The $3mm$ diameter units are arranged in thread-mount inserts for the measurement locations in the stationary parts. The sensors placed in the relatively thin impeller blades and walls are glued in place in the impeller segments, figures 3.2 and 3.3 by their manufacturer, UNISENSOR AG. This guarantees homogeneous embedding into a layer of silicone protecting the sensor and transmitting the pressure. The embedding of the cables in the grooves with epoxy resin and the following surface finishing is accomplished in EPFL workshops.

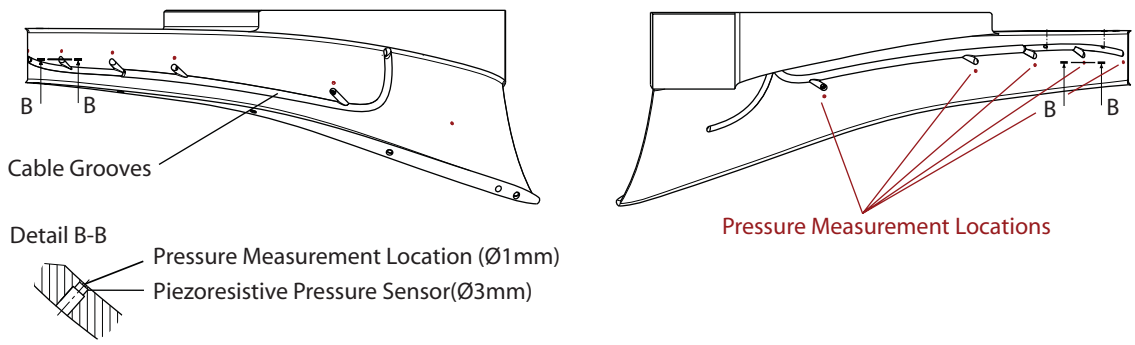

Figure 3.2: Embedded pressure sensors in pump-turbine impeller blade

Pressure Sensor Calibration

The static calibration of the sensors is achieved using the same conditioning electronics than for the measurements. Though the variance due to these components is expected to be lower than the difference of sensor constants, the effects of the conditioning electronics are thus included in the calibration constants. Typical calibration curves showing the linear slope and the error of measured versus linearized values is shown in figure 3.4. The calibration of the sensors mounted in inserts is achieved in a specific vessel compared to a high precision reference sensor. The sensors in the rotating part are calibrated in the mounted machine at rest versus a reference pressure sensor.

Figure 3.3: Assembly of the instrumented impeller

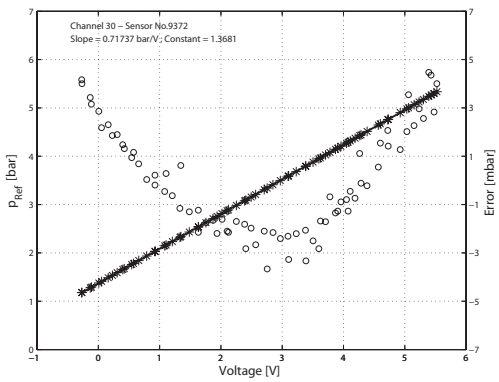

Figure 3.4: Identification of pressure sensor calibration constants by linear regression fit

3.2.2 Digital Data Acquisition Systems

A 40-channel rotating acquisition system described in details in [41; 116] is used for the acquisition of pressure signals from the sensors located in the impeller. The signal conditioning electronics and memory are located on the rotating shaft, the results are transferred in batch mode after acquisition via a slip ring connection using the ARCNet protocol. For measurements in stationary components, a modular 48-channel acquisition system based on the VXI (VME Extensions for Instrumentation) standard bus technology is used. The main characteristics of the acquisition systems are summarized in table 3.1. Both systems are equipped with appropriate pre-amplifiers and anti-aliasing filters. Data acquisition control and storage is achieved by a software system based on standard data acquisition toolboxes (NI-Labview 8.3) running on Personal Computers.

3.3 Two-Dimensional Laser Doppler Velocimetry

3.3.1 Measurements Principle and Equipment

Laser-Doppler Velocimetry (LDV) is a non-intrusive optical flow velocity measurement technique. The measurement principle, figure 3.5, is based on the analysis of the light reflection of a particle crossing the measurement volume formed by the intersection of

-	Rotating system	Stationary system
Maximum number of channels	40	48
A/D converter resolution	2^{12}	2^{16}
Sampling frequency f_s	$20\,kHz$	$40\,Hz - 51.2\,kHz$
Maximum number of samples N_s	2^{16}	2^{20}

Table 3.1: Pressure measurement data acquisition system parameters

two coherent laser beams. Due to the coherence of the laser light waves, an interference fringe pattern is formed in the measurement volume. The spacing of the fringe pattern is determined by the wavelength and the beam intersection angle γ.

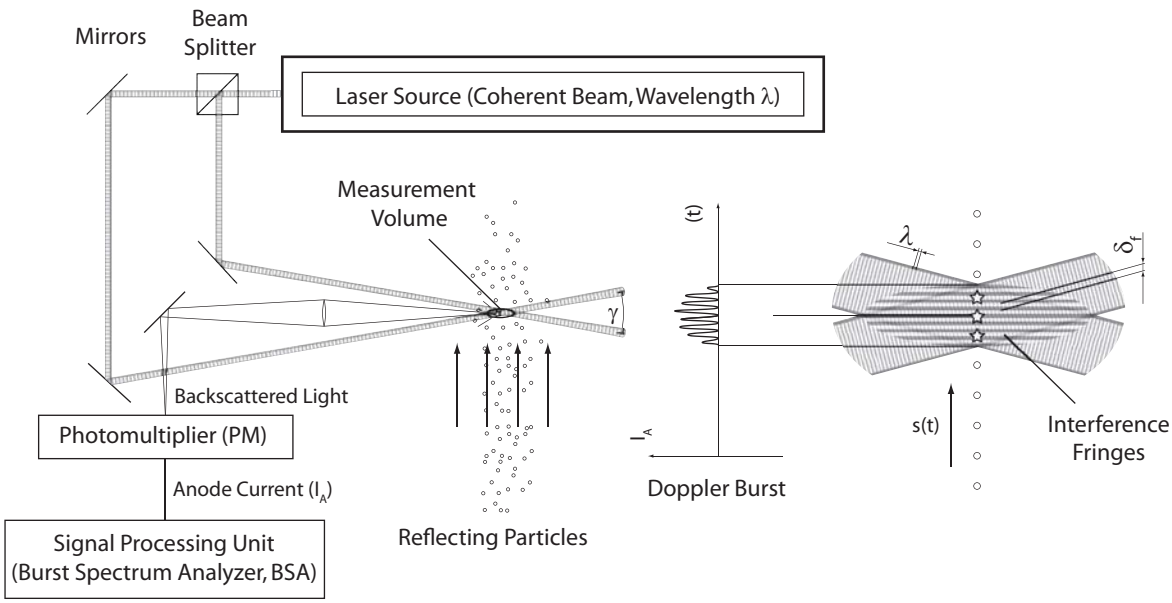

Figure 3.5: Principle of Laser Doppler Velocimetry (LDV)

$$\delta_f = \frac{\lambda}{2sin(\gamma/2)} \tag{3.1}$$

Particles crossing the measurement volume create a typical reflection, called Doppler burst. Receiving optics focused on the measurement volume, together with highly sensitive photomultipliers and dedicated signal processing devices, so-called Burst Spectrum Analyzer (BSA), provide the characteristic frequency of the Doppler burst. This frequency is proportional to the velocity component of the particle in the direction normal to the fringe pattern:

$$f_P = \frac{C}{\delta_f} = \frac{2Csin(\gamma/2)}{\lambda} \tag{3.2}$$

The LDV technique was first proposed in 1964 and came into use in the 1970's. Ongoing development of the required optical components and signal analyzing devices enables the fluid dynamics research community to use this measurement technique in more and more complex applications. Measurements in laboratory scale models of turbomachines manufactured entirely in transparent materials were reported during the late 1980's [57; 97], techniques to realize a measurement volume rotating with the impeller to achieve continuous measurements in the rotating frame are reported by [5]. A comprehensive overview of laser Doppler and the related phase Doppler measurement techniques is given in [7].

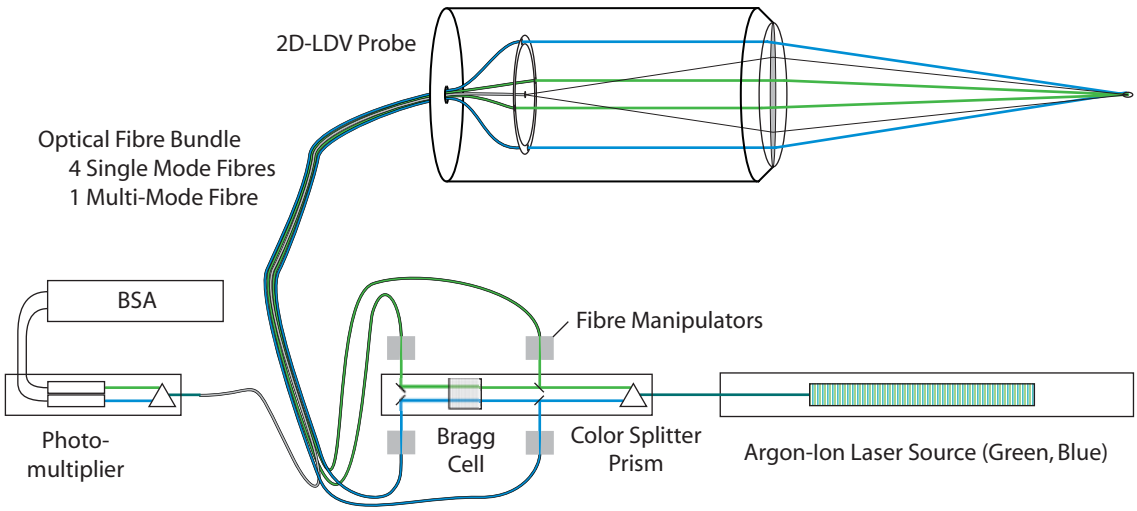

Figure 3.6: 2D-LDV Probe with optical fibre transmission for laser and signal

First LDV systems were made of individual optical components needing a careful alignment of the laser and backscattered light paths through lenses, mirrors and prisms. LDV measurements of cavitating flow around a hydrofoil at Reynolds numbers similar to industrial centrifugal pumps is described in detail in [34]. Traversing the entire optics to cover a grid of measurement points in a given experimental setup is a challenging task. Nowadays, off-the-shelf systems using optical fibers to transmit the laser beams to and the backscattered light from compact optical units termed LDV-probes allow an easier traversing of this unit even in comparatively narrow spaces while allowing a high optical quality. Such a unit, see figure 3.6, includes the 4 laser beams and the receiving optics to measure the two perpendicular velocity components perpendicular to the probes axis. Ion-Argon laser sources together with a color beam splitter are commonly used to supply coherent laser beams on two distinct wavelengths. In the basic LDV system configuration, positive and negative flow velocities cannot be distinguished and the signal processing must cover a wide frequency range to measure high and low velocities accurately. For this reason, it is convenient to shift the frequency of one of the beams of each color by a Bragg cell. This frequency shift of one beam leads to a shift of the burst signal frequency. A zero-velocity particle reflects a signal at the Bragg cells frequency. The Bragg cell frequency is chosen large enough that the entire expected velocity range can be measured without ambiguity.

In the study case presented in chapter 7 a borosilicate glass window provides optical access to a zone in the diffuser of a pump turbine, covering a flow passage constituted by two guide vanes as well as the circumference of one guide vane. Residual stresses from production or machining of perspex windows can result in variable refraction indices deflecting the beams differently. The choice of borosilicate glass guarantees that the laser beam intersect at the focus point of the receiving optics. In the backscattered arrangement using a two-component LDV probe, it is essential to minimize the reflections of the beams on other surfaces, as this affects the signal to noise ratio of the usable backscattered signal. To this effect, galvanic black chrome coating is applied on the diffuser side wall opposite to the window as well as on the surrounding guide vanes.

The Parameters of the LDV measurement system are enumerated in table 3.2.

Laser type	Ion-Argon
Laser wave length (green/blue)	$488\,nm$ / $514.5\,nm$
Laser Power (Max/Used)	$10\,W$ / $3.5\,W$
Beam-Receiver Arrangement	Backscattered
Optical system	2D-Laser probe
Laser Transmission	4 Single mode fibers ($10\,m$)
Signal Transmission	Multi-mode fiber ($10\,m$)
Probe diameter	$60\,mm$
Beam diameter	$2.2\,mm$
Focal length	$250\,mm$
Fringe spacing	$3.3\,\mu m$
Measurement volume minor axis / major axis	$0.075\,mm$ / $1.250\,mm$
Bragg cell frequency /shift velocity	$40\,MHz$ / $130\,m/s$
Particle type	Hollow glass spheres
Particle density	$1.1\,kg/m^3$
Average particle size	$10\,\mu m$
Optical Access	Borosilicate Glass Window
Surface treatment	Galvanic Black Chrome Plating
Traverse resolution (Linear / angular)	$0.01\,mm$ / 0.01°
Positioning precision (X,Y / Z / W)	$0.2\,mm$ / $0.5\,mm$ / 0.2°

Table 3.2: Properties of the LDV System

3.3.2 Traversing System Alignment and Position Referencing

A 4-axis automatic traversing system represented in figure 3.7 is used to traverse the LDV-probe over the hundreds of measurement locations constituting the grids for experimental investigation.

The following steps guarantee positioning precision within the tolerances specified in table 3.2.

- Coplanarity of the traverse $X'Y'$-plane with the model xy-plane, the deflection measured with a caliper on the maximum course of the X' and Y' axis is less than

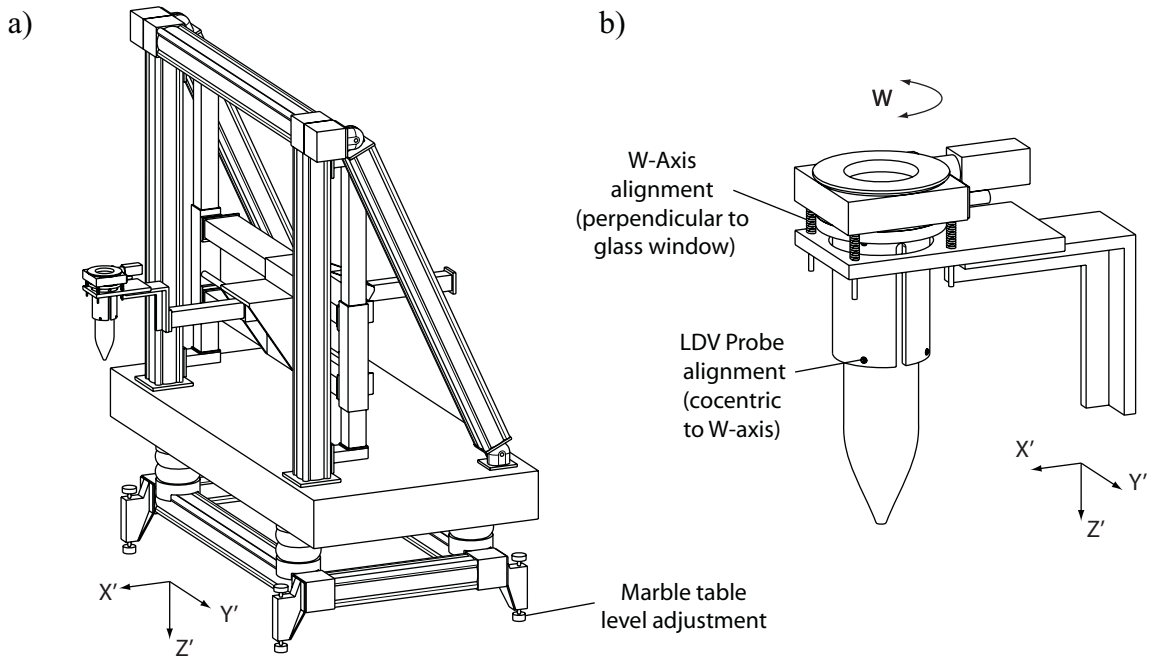

Figure 3.7: 4 axis traversing system. a) Overview of the translation axes, b) Detail of the rotation axis and LDV-probe alignment

0.05 mm. Adjustments are made by mechanical alignment of the positioning system marble base plate.

- Concentricity of the probe inside the rotation axis is checked by the passage of all 4 beams by a 50 μm pinhole undergoing an entire rotation of the W axis. Adjustments is made by mechanical alignment of the LDV Probe in the probe holder.

- Perpendicularity of the LDV Probe (and W-rotation) axis with the model xy-Plane is checked by an autocollimation-like method on the thick glass window. The light spots created by the reflection of a beam pair on the upper window-water interface have to be symmetrical with the light reflection spots seen where the beams pass the lower window-air interface first, see figure 3.8c.

- As references in the xy-planes, the position of 3 targets inserted at positions defined by NC-machined pressure sensor holes specified with 0.1 mm tolerance is identified. The targets have a black front surface, a 0.5 mm hole with a thin reflecting chamfer. The photomultiplier anode current is measured while traversing along both the x and the y axes over the reflecting circle. The center of the measured profile is taken to be the reference position, see figure 3.8a and 3.8b. This procedure proves to be repeatable within 0.05 mm. A translation-rotation transform in the xy-plane is determined from the three points by a least squares fit algorithm. The individual residuals of the three positions are below 0.1 mm.

- A reference position for the w-axis is determined by adjusting the axis at a known position ($\theta = 15^{\circ}$) using the inner cylindrical surface of the window cutout. The

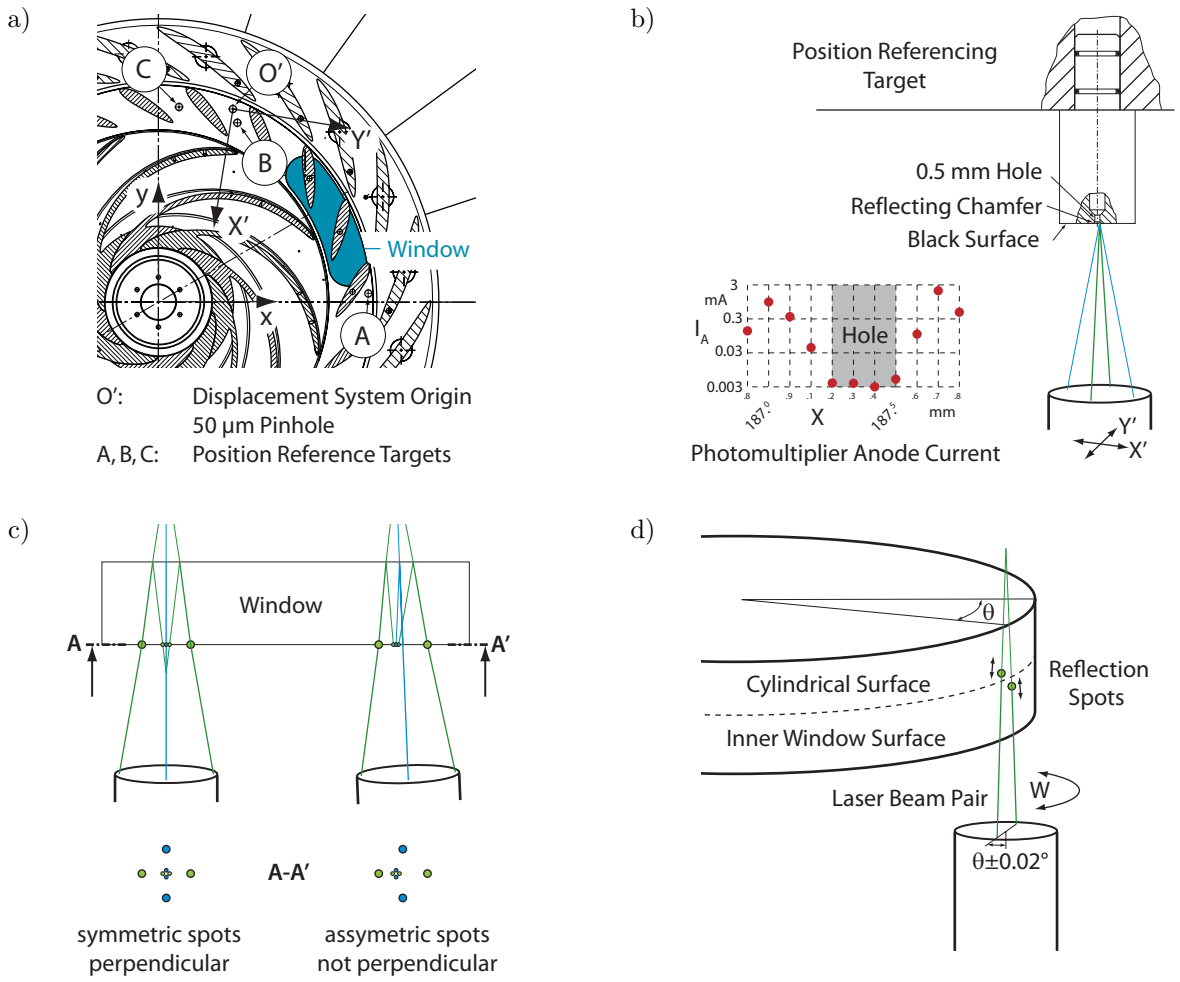

Figure 3.8: Probe alignment and referencing a) Target positions and coordinate systems, b) Target referencing procedure, c) Perpendicular alignment by autocollimation, d) Rotation axis reference

height alignment of a laser beam pair's reflection spots on this surface is highly sensitive to the w-axis position, see 3.8d. The reflection spots become misaligned within very few angular steps of 0.01° from the position where they appear at same height.

- The z-position is determined by visual detection of the intersection of the measurement volume center with the glass-water interface and with the opposite wall. As a second criterion, the transition of first detection of rare burst-like signals to higher acquisition rates is taken into account. Using both criteria, the size in z-direction of the beam intersection zone can be well reproduced to be about $1\,mm$, corresponding to the measurement volume size. So the given precision indication of $0.5\,mm$ is rather conservative. The scaling of Z' probe displacement in air and z measurement volume displacement is found to be reasonably close to the ratio of refraction indices.

As a comprehensive validation of position referencing, geometry representation and guide vane angle control, a path line around the 4th guide vane with $0.2\,mm$ normal distance is generated with the same software tools than the measurement grids and the numerical simulation meshes. The rotation axis w position is prescribed such that the green beam plane is always parallel to the blade surface. On the entire path, the laser beams just streak the guide vane surface. For a path line programmed exactly on the guide vane contour, the laser beams are intercepted by the lower edge of the guide vane for some segments of the circumference. This confirms the positioning error estimate on the x and y coordinates. All the alignment procedures involving the laser beams are carried out using a minimal laser power. Laser beam spots and traces on surfaces are barely visible.

From former measurement campaigns realized with the described equipment, it is known that the achievable data rate of the two LDV components differs by a factor of 10, reaching maximum data rates of about $30 z_b f_n$ on the green wavelength and $3 z_b f_n$ on the blue component. These data rates decrease due to reflections on the opposite wall and on the window-water interface when measuring close to the diffuser side walls. Under these circumstances, it was chosen to orient the 2D Laser probe in a way that one principal component of interest is directly measured by the high data rate component, taking the second component as an additional, though less precise information.

3.4 Simultaneous Pressure-Velocity Measurements

For the correlation of the point-wise velocity measurements by LDV with phenomena like rotating stall, that can well be identified by pressure measurements, the experiments are set up in a way to achieve the simultaneous measurement of pressure in the stationary frame and velocity by LDV. An overview of the equipment and the links of its component is represented in figure 3.9.

A TTL-signal available from the Burst Spectrum Analyzer when a new point measurement is started triggers the pressure data acquisition. As the pressure acquisition system works with zero trigger delay, synchronicity of the acquired data is achieved. As an additional check, the impeller revolution key phasor signal is recorded both in the pressure acquisition system and by the Burst Spectrum Analyzer. The correlation of both signal recordings is checked when merging the independent files from the LDV acquisition system and the pressure measurements into a common file in hdf-5 format for further analysis. This check confirms that the offset between both systems is within ± 1 sample interval of the pressure acquisition system and is corrected by shifting the LDV burst arrival times in the common files.

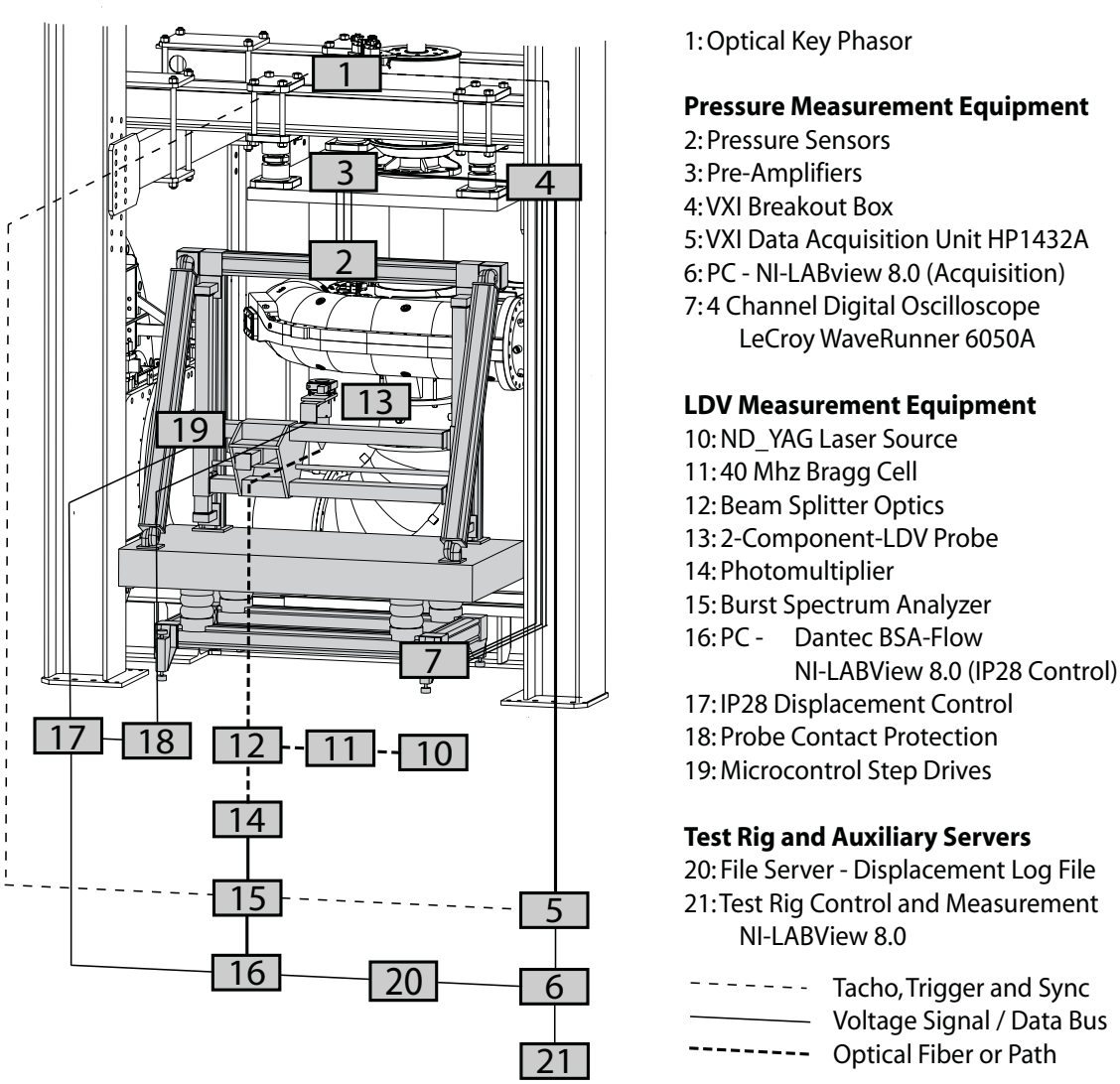

Figure 3.9: Instrumentation overview for simultaneous LDV and pressure measurements

Chapter 4

Analysis Techniques for Turbomachinery Flow

4.1 Centering, Phase Averaging and Resampling

Centering of Pressure Signals

In numerous aspects of analysis provided in this study, the absolute level of pressure is not of interest. Representing fluctuations is more convenient in time domain and artefacts are avoided that can appear in common spectral estimation techniques due to the application of window function on signals with a relevant mean value. The pressure fluctuation denoted $\tilde{p}$ is obtained by substracting the time average $\bar{p}$ from a set of data of N pressure samples:

$$\tilde{p}[n] = p[n] - \bar{p}\,, \qquad \bar{p} = \frac{1}{N}\sum_{n=0}^{N-1} p[n] \tag{4.1}$$

Phase Averaging of Pressure Signals

Pressure fluctuations at blade passing frequencies and their higher harmonics due to RSI are one of the root sources of mechanical excitation of turbomachinery components. They can excite vibrational eigenmodes of components, rotor-dynamic phenomena or hydro-acoustic waves leading under some circumstances to resonance in the machine or the circuit and to unacceptable stresses, noise, damage or unstable operation of systems. While the frequencies and excitation patterns occurring with different combinations of blade numbers in the rotating and stationary frames are well understood [23], only measurements and time-dependent flow simulations can provide the amplitudes and phases of all harmonics of these fluctuations. In addition to the frequencies related to the number of blades of the components, other sources, such as asymmetry due to the volute or elbow bends may cause relevant pressure fluctuations. Presence of splitter vanes or the stagger of the opposite impeller sides on double suction pumps influence the excitation patterns.

In the stationary frame, the expected frequencies are the impeller blade passing frequency $z_b f_n$ and its harmonics while measurements taken in the rotating frame exhibit the diffuser blade passing frequency $z_o f_n$ and its harmonics. To isolate these periodic,

deterministic components, phase averaging techniques are used, usually taking an impeller revolution as a base period. Phase averaging of regularly sampled pressure data is implemented by resampling the signal to a given number of samples per revolution and averaging over the values from all recorded revolutions. For a signal p, resampled to have M samples per revolution and with NM available samples the phase averaged signal is obtained by:

$$\widehat{p}[m] = \frac{1}{N}\sum_{n=0}^{N-1} p[nM+m] \tag{4.2}$$

The phase average is an ideal comb filter that eliminates all frequencies except the averaging base frequency and its harmonics [22]. Developing the discrete Fourier transform (DFT) of the original signal for the frequencies $kN, 0 \leq k < M$ yields:

$$\begin{aligned} P[kN] &= \sum_{n=0}^{N-1}\sum_{m=0}^{M-1} p[nM+m]e^{2\pi i\frac{(kN)(nM+m)}{MN}} = \sum_{n=0}^{N-1}\sum_{m=0}^{M-1} p[nM+m]\underbrace{e^{2\pi i\frac{knM}{M}}}_{1}e^{2\pi i\frac{km}{M}} \\ &= \sum_{m=0}^{M-1}(\sum_{n=0}^{N-1} p[nM+m])e^{2\pi i\frac{km}{M}} \\ &= \sum_{m=0}^{M-1}\widehat{p}[m]e^{2\pi i\frac{km}{M}} = \widehat{P}[k] \end{aligned} \tag{4.3}$$

The fact that all other Fourier coefficients vanish is proven by the identity of the discrete Fourier transforms, considering that $\hat{P}$ has only M coefficients, as the phase averaged signal has M samples.

Resampling of Pressure Signals

During different stages of analysis, resampled pressure signals at different resolutions per impeller revolution are needed. To this effect, the efficient implementation of a standard resampling algorithm [119] available in the MATLAB signal processing toolbox is adapted. The original algorithm implements upsampling of the signal by a factor p followed by downsampling by factor q and applies appropriate digital filters.

As it has been shown by the validation of impeller revolution synchronization signal arrival times recorded by the LDV burst analyzer and the recorded signal from the regularly sampled pressure acquisition system, the synchronization signal arrival time can be determined with sub-sample precision by computing the intersection with the TTL threshold level of $2V$ based on linear interpolation of the recorded signal voltage.

Figure 4.1 illustrates how the signal of an impeller revolution interval $[t_1; t_2]$ at a target sampling rate of M samples per revolution is determined from the original signal, specifying a time tolerance ε_t for the first and the last sample. The first step of the algorithm consists in determining appropriate resampling parameters p and q, the smallest integer upsampling factor p where $t_1 - t_t[1] <= \varepsilon_t$ and $t_2 - t_t[M] <= \varepsilon_t$ is selected. The major constraint is that the resulting number of samples in the upsampled signal must be divisible by M. A tolerance $\varepsilon_t = 10^{-3}/f_n$ is generally used. This corresponds to 1/5 of the original signal sample spacing for the simultaneous pressure-LDV measurements. Upsampling ratios lower than 50 have proved to be sufficient to achieve this tolerance.

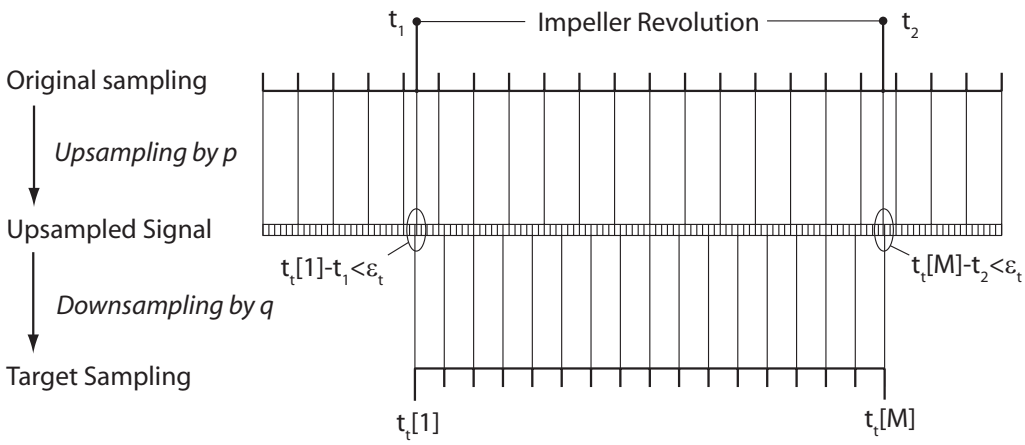

Figure 4.1: Resampling of pressure signals by commensurable integer ratio p/q

Phase Averaging and Resampling of LDV Signals

The stochastic sampling of LDV measurement data in the context of a time-dependent, turbulent flow complicates the signal processing. Numerous proposals have been made in the past decades to refine the accurate determination of mean values (first order moments), higher order moments and spectra for statistically steady flows [6; 35; 108; 13; 25]. As long as concerned with the phase average of a periodically time-dependent flow, it is assumed that the samples are statistically independent. The phase averaging procedure is applied directly by sorting the velocity burst signals into the corresponding phase bin based on their arrival times. To this effect, a fast standard linear interpolation algorithm is used, that proved to be most efficient in the framework of the interpreted MATLAB environment though it computes the phase angle with a later unused decimal sub-bin precision from the synchronization signal arrival times $t_s[k]$, and the LDV burst arrival times $t_{LDV}[j]$:

$$\theta[j] = 2\pi \left(k + \frac{t_{LDV}[j] - t_s[k]}{t_s[k+1] - t_s[k]} \right) \qquad with \quad t_s[k] < t_{LDV}[j] \leq t_s[k+1] \tag{4.4}$$

The integer phase bin number $m_\theta[j]$ is obtained as the next larger integer than the real fraction of elapsed time obtained by:

$$m_\theta[j] = modulo\left(floor\left(M\frac{\theta[j]}{2\pi} \right), M \right) + 1 \tag{4.5}$$

Assuming equality between the different impeller blade passages, the phase space is restricted to a fraction of the impeller revolution. With the number N_c of sub-cycles (typically, $N_c = z_b$ for measurements in the stationary frame) the phase bin number is obtained by:

$$m_\theta[j] = modulo\left(floor\left(M\frac{\theta[j]}{2N_c\pi} \right), \frac{M}{N_c} \right) + 1 \tag{4.6}$$

Defining the sparse boolean δ_θ weight function matrix as follows

$$\delta_\theta[k,j] = \delta_{km_\theta[j]} = \begin{cases} 1 & \text{if } k = m_\theta[j] \\ 0 & \text{otherwise} \end{cases} = \delta_k(\theta) \tag{4.7}$$

The phase averaged velocity values are obtained by a standard sparse matrix product:

$$C[k] = \frac{\sum_{j=1}^{N} \delta_\theta[k,j]C[j]}{\sum_{j=1}^{N} \delta_\theta[k,j]} \tag{4.8}$$

In a review of spectral estimation techniques [13] for LDV Data, a method termed fuzzy slotting technique is presented. It aims to reduce the variance in the slotting technique characterized by definition of sharply edged time slots for correlation analysis. Instead of assigning each measured velocity value to one bin, its influence is distributed on the two neighboring bins according to linear weight functions. A value recorded precisely at the center phase of a bin will enter into this bin only with a weight of 1 while a measurement taken at the edge between two phase bins will enter into both with a weight of 0.5. Considering phase bin intervals centered around the values $\alpha[k] = 2\pi(k-0.5)/M$ the weight factors are obtained:

$$b[j,k] = b_k(\theta) = max\left(1 - \frac{|\theta[j] - \alpha[k]|}{2\pi/M}, 0\right) \tag{4.9}$$

And the fuzzy weighting phase average is computed by:

$$C[k] = \frac{\sum_{j=1}^{N} b[j,k]C[j]}{\sum_{j=1}^{N} b[j,k]} \tag{4.10}$$

Figure 4.2 represents the weighting functions $b_k(\theta)$ used for the fuzzy averaging and the analogous δ functions of the standard phase averaging procedure. No relevant difference

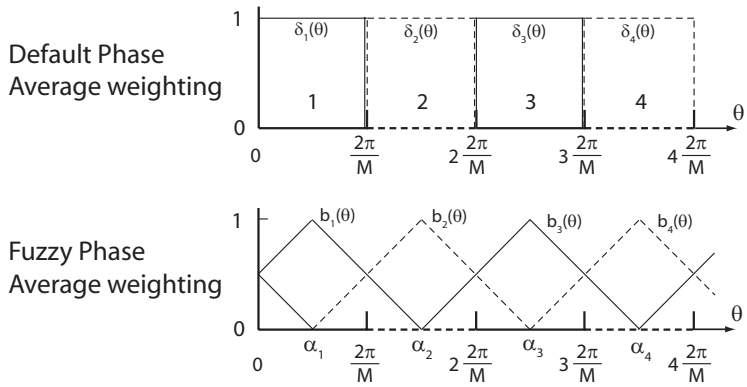

Figure 4.2: Weight functions of standard and fuzzy phase averaging techniques

between the standard and the fuzzy slotted phase averaging procedure is noticed on points of the acquisition grids with a sufficient number of samples per bin. This is the case of data acquired in the central part on the channel fulfilling the practical criteria dressed up by [153]. On points with low data rate, the acquisition is stopped after reaching a fixed maximum time (1 minute per point). When less than 30 samples per bin are available, there are relevant differences in the results, but without a significant gain of plausibility for the slotting technique. The first lines of data points originally planned along the

diffuser side walls show a majority of such data points and were discarded after first tentative measurements. In the intermediate range, (30 to 60 samples per bin), the fuzzy slotting yields results that seem more plausible. The low-pass filtered LDV signals used to determine a time-dependent mean flow for turbulence intensity estimation are obtained by a zero-order hold resampling to a frequency 10 times higher than the average sampling frequency followed by a standard downsampling method with antialiasing filters. This method is confirmed as a valid procedure when the downsampled frequency is an order of magnitude lower than the average sampling frequency [39]; the more evolved methods proposed in the paper were not considered.

4.2 Identification of Rotating Modes by 2-Dimensional DFT

Identification of Rotating Stall Modes from Regularly Spaced Sensors

Using regularly spaced pressure sensors in the stationary frame of a turbomachine, the projection of uniformly sampled measurements in time on the 2-Dimensional Fourier basis is an efficient way to identify rotating modes such as Rotor-Stator-Interaction and rotating stall effects. The 2-dimensional Discrete Fourier Transform (DFT) in time (N uniform samples on time interval T) and space (M uniformly distributed sensors on circumference) of the dynamic pressure signals is given by:

$$P[k,l] = \frac{1}{MN}\sum_{n=0}^{N-1}\sum_{m=0}^{M-1} p[m,n]e^{-2\pi i\frac{mk}{M}}e^{-2\pi i\frac{nl}{N}} \tag{4.11}$$

Its backward transform expresses that all possible signals can be represented by a sum of rotating waves of given frequency $\frac{l}{T}$ and circumferential wave number k:

$$p[m,n] = p\left(\frac{m}{M}2\pi, \frac{n}{N}T\right) = \sum_{l=0}^{N-1}\sum_{k=0}^{M-1} P[k,l]e^{2\pi i\frac{mk}{M}}e^{2\pi i\frac{nl}{N}} \tag{4.12}$$

These equations are the discrete counterparts of equations (24) and (26), generalized in the sense that the range of frequencies and wave numbers is determined by the sampling properties in space and time.

The 2D DFT can be considered and computed decomposing it into two steps, the first one being the usual time-frequency DFT of each pressure sensor. Suppose a given frequency $\frac{l}{T}$ of interest, where all pressure sensors exhibit relevant amplitudes, the one-dimensional DFT of pressure sensor m is given by:

$$P_m[l] = \frac{1}{N}\sum_{n=0}^{N-1} p_m[n]e^{-2\pi i\frac{nl}{N}} \tag{4.13}$$

The second step decomposes a frequency component $\frac{l}{T}$ in M modes, $k = 0$ representing the non-rotating synchronous part, $k \neq 0$ the rotating mode of wave number k:

$$P[k,l] = \frac{1}{M}\sum_{m=0}^{M-1} P_m[l]e^{-2\pi i\frac{mk}{M}} \tag{4.14}$$

The two-dimensional DFT can also be expressed in matrix form introducing the orthonormal weight matrices $\mathbf{W_M}$ and $\mathbf{W_N}$ [1].

$$P[k,l] = \sum_{n=0}^{N-1} w_N[n,l] \sum_{m=0}^{M-1} w_M[k,m]p[m,n] \tag{4.15}$$

equivalent to the short notation:

$$\mathbf{P} = \mathbf{W_M p W_N} \tag{4.16}$$

where the orthogonal, symmetric Fourier coefficient matrices are defined as:

$$w_M[k,m] = \frac{1}{M} e^{\frac{-2\pi imk}{M}}, \qquad w_N[n,l] = \frac{1}{N} e^{\frac{-2\pi inl}{N}} \tag{4.17}$$

The associative property of the matrix multiplication in (4.16) reflects the fact that it makes no difference if the 2D DFT is computed column- or row-wise first.

For the analysis of finite data sets containing unknown frequencies that might have a somewhat stochastic or intermittent character, it is common practice to determine the power spectral densities by averaging power spectral density values of several overlapping time windows [151]. These techniques, initially motivated by the finite memory and processing capacities of digital processors, have advantages in producing spectra with less variance than a single DFT of the entire signal. As an alternative, averaging in the frequency domain after a DFT of the full signal length is feasible at a similar cost if memory size is not an issue [12]. The same technique is applied to the 2-Dimensional DFT in the time dimension for the analysis of rotating stall in the case study presented in chapter 7, using 12 overlapping windows. In this case, the phase information carried by the complex character of the discrete Fourier transform is lost and averaging is done on the modulus of the individual window's DFT.

Identification of Rotating Stall Modes from Irregularly Spaced Sensors

Though the rotating stall modes presented in chapter 7 have finally been identified using all z_o pressure sensor positions in the guide vane channels, a signal processing technique to identify them from fewer, z_p, irregularly spaced sensors is briefly presented here. This procedure allowed to identify the rotating stall, based on only 5 sensors available from a former measurement campaign. The Boolean function γ is defined by the presence of a sensor on a location m of M:

$$\gamma[m] = \begin{cases} 1 & \text{if sensor m is present} \\ 0 & \text{if sensor m is missing} \end{cases} \tag{4.18}$$

The incomplete data set $p_P[m,n]$ is defined as:

$$p_P[m,n] = \gamma[m]p[m,n] \tag{4.19}$$

Considering only the spatial (circumferential) dimension, the problem is termed periodic non-uniform sampling, a signal processing technique based on reconstruction of the missing signals by appropriate filters applied on the available signals is presented in [62]. The

[1] Simple boldface symbols are used for matrices in the remainder of this chapter 4.2

following approach to the missing data problem consists in applying the usual transforms, replacing the missing data by zero values, keeping account of this modification during the analysis in transformed space:

The result $\mathbf{P_P}$ obtained from a 2D DFT with the missing pressure sensors is equivalent to the one obtained from the original data but where the missing pressure sensor columns of the weight matrix $\mathbf{W_M}$ are zero, leading to the rank-deficient modified weight matrix $\mathbf{W_P}$.

$$w_P[k,m] = \gamma[m] w_M[k,m] \tag{4.20}$$

The 2D DFT of a data set with missing pressure sensors is equal to the one obtained from complete data applying the modified weight matrix $\mathbf{W_P}$.

$$\mathbf{P_P} = \mathbf{W_M p_P W_N} = \mathbf{W_P p W_N} \tag{4.21}$$

Together with 4.16 this leads to

$$\mathbf{P_P} = \mathbf{W_P W'_M} * \mathbf{W_M p W_N} = (\mathbf{W_P W'_M})\mathbf{P} = \mathbf{T_P P} \tag{4.22}$$

The matrix $\mathbf{T_P}$ defines a transformation from the 2D DFT of a complete data set to the 2D-DFT obtained from a reduced data set. This matrix depends on the number of sensors and their repartition. Expanding $(\mathbf{W_P W'_M})$ yields

$$\begin{aligned} T_P[k,m] &= \sum_{l=1}^{M} w_P[k,l] w_M[l,m]' = \sum_{l=1}^{M} \gamma[l] e^{-2\pi i \frac{kl}{M}} e^{2\pi i \frac{lm}{M}} \\ &= \sum_{l=1}^{M} \gamma[l] e^{-2\pi i \frac{l}{M}(k-m)} \\ &= \sum_{l=1}^{M} \gamma[l] = z_p \qquad \text{for} \quad k = m \end{aligned} \tag{4.23}$$

Regardless of the pressure sensor repartition, the diagonal terms of $\mathbf{T_P}$ are all equal to the number of pressure sensors while all other terms depend on the repartition of pressure sensors and $k - m$, the difference of original and influenced wave numbers, leading to a circulant and hermitian matrix $\mathbf{T_P}$. Equation (4.23) reflects the wave number domain properties of the particular window function γ with the main lobe on the diagonal and side lobes depending on the pressure sensor distribution. This is an untypical case of spectral leakage, an effect usually considered for common windowing functions applied on finite data sets before computing the DFT. The window function applied on the circumferential dimension due to missing sensors is an irregular comb.

Figure 4.3 shows the wave number domain representation of different pressure sensor distributions. A regular distribution of 5 sensors among the 20 positions leads to typical aliasing properties where a wave mode k cannot be distinguished from a wave mode $k \pm 5$.

Depending on the sensor number and repartition, different techniques are applied to get an improved estimation of $\mathbf{P}$ from $\mathbf{P_P}$. The rank of the matrix $\mathbf{T_P}$ is equal to the number of pressure sensors, so the matrix is not invertible, the equation system 4.22 has no unique solution.

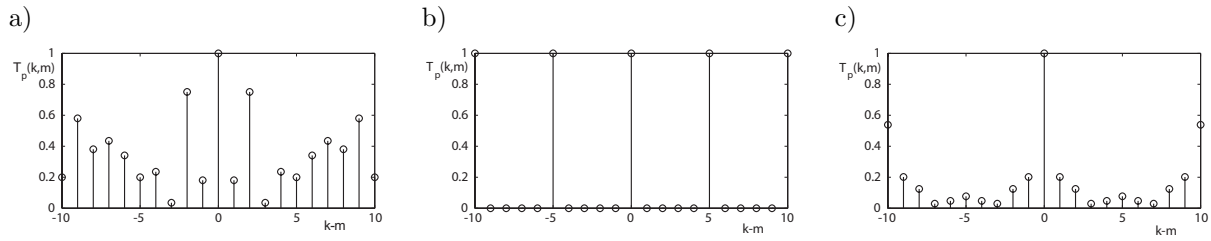

Figure 4.3: Filter coefficients of pressure sensor distributions a) First measurement campaign(1,3,10,12,20), b) Regular Distribution(1,5,9,13,17), c) Distribution during LDV measurements, 13 sensors

For cases with relatively high numbers of pressure sensors z_p, it is possible to solve the equation system searching only for the first z_p coefficients and assuming the other modes to be zero. For fewer pressure sensors (less than half of the regular number) considering only a $(2z_p - 1)$-band-diagonal part of the matrix $\mathbf{W_P W_M^T}$ allows to invert it and to correct the most disturbing artefacts for the neighboring low wave number modes. But the solution obtained is not a solution to the original equation system. Better results with very few pressure sensors are obtained by a technique searching for a single dominant wave mode representing the major part of the signal and going on with the residual to identify the next wave mode. For each column l of the 2D DFT of the incomplete data set the complex amplitudes q_k to minimize the L^2-norm of the residual R_k for each candidate wave mode k is determined by a standard least squares procedure:

$$R_k = \min_{q_k \epsilon \mathbf{C}} \left(\sum_{m=1}^{M} |(q_k T_P[m,k] - P_P[m,l]|^2 \right) \tag{4.24}$$

The minimum among the M determined residuals is identified, the corresponding terms $q_k T_P[m,k]$ subtracted from P_P and the procedure repeated.

Figure 4.4a shows the 2D DFT obtained from 20 sensors at $\varphi = 0.026$, 4.4e and 4.4f show the DFT obtained using 13 pressure sensors, that are sufficient to identify the predominant rotating mode $k = 4$, with no gain of information by considering the filter property. 4.4d and 4.4e show that the correction using an inversed filter matrix restricted to a 9-band diagonal identifies the peaks at $k = 2$ and $k = 6$ as sidebands of $k = 4$ created by the irregular pressure sensor distribution.

It is emphasized that the sketched procedure helps to identify dominant modes under the assumption that there are such, searching for a specific solution of an underdetermined equation system. More evolved signal processing techniques, especially parametric methods, applied successfully in image analysis and other fields are promising to improve the identification of rotating modes on unevenly distributed sensors. For future measurements, considerations of the filter properties of the chosen pressure sensor repartition in space should guide the choice of pressure sensors when only few channels can be instrumented. Distributions of sensors leading to side lobes that are difficult to distinguish (e.g. those at $k - m = \pm 2$ in figure 4.3a) should be avoided.

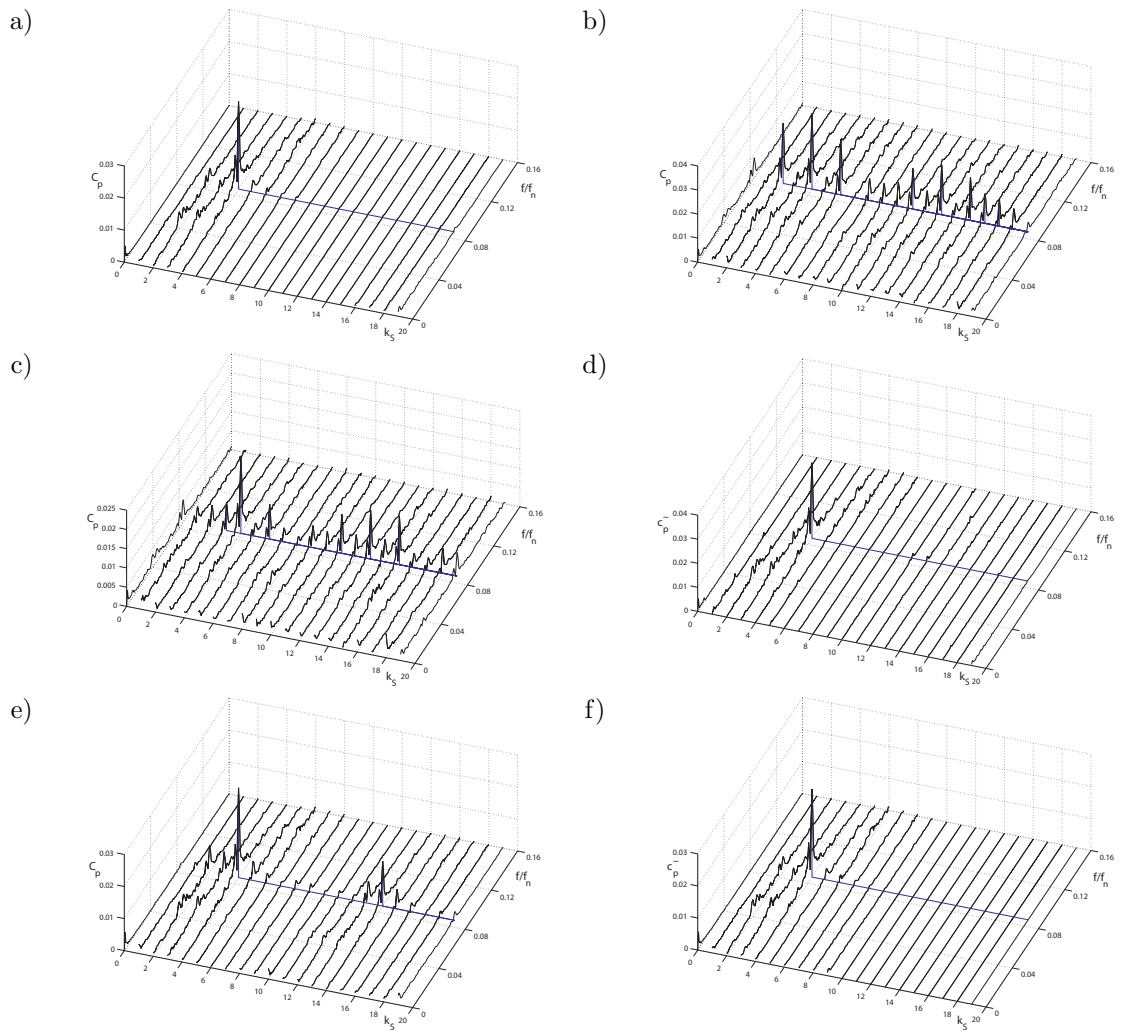

Figure 4.4: 2D DFT using irregularly spaced pressure sensors a) DFT using 20 sensors, b) DFT using 5 sensors (1,3,10,12,20), c) 5 sensor DFT corrected using band-diagonal of filter window, d) 5 sensor DFT corrected using adaptive least squares fitting, e) DFT using 13 sensors, f) 13-sensor DFT corrected assuming only 10 modes

4.3 Stall Phase Based on Pressure Measurements

In order to reconstruct the velocity field measured point-wise by LDV, a technique to determine the phase of the rotating mode as expressed in equation (29) to (31) from the measured pressure signals is needed. Particle image velocimetry (PIV) with acquisitions triggered by pressure measurements have successfully been used for analysis of flow and combustion instabilities [46]. A common technique to determine the phase of self-induced periodic flow phenomena is to identify intersections of a reference signal with fixed threshold levels, typically termed zero-crossing detection though levels differing from zero might be used. Detection of maxima and minima is also reported by experimentalists [146]. Clarke [29] gives a comparison of the zero crossing technique with techniques based on the Hilbert transform in the context of frequency detection algorithms and concludes techniques based on the Hilbert transform of a low-pass filtered signal are generally more robust for noisy and irregular signals. Bourdet [18] uses the phase of the analytic signal as to define an instantaneous Strouhal number in analysis of numerical simulation of Bénard-von Kármán instability. The pressure fluctuations measured with rotating stall in the study case presented in chapter 7 are not perfectly regular. RSI and noise are visible in the pressure signals. The stall phase φ_s used for the analysis of the LDV measurements is determined by definition of an analytic signal from a low pass filtered (butterworth filter of cutoff frequency f_n) pressure fluctuation signal $\tilde{p}_{lp}(t)$ at a fixed location, close to the LDV measurement zone:

$$\mathcal{P}(t) = \tilde{p}_{lp}(t) + i\mathcal{H}(\tilde{p}_{lp}(t)) \tag{4.25}$$

with the Hilbert transform $\mathcal{H}$ shifting the phase of the signal by $\pi/2$ for all frequencies. With the analytic amplitude $a(t) = |\mathcal{P}(t)|$ and the analytic phase $\varphi_s(t) = arg(\mathcal{P}(t))$ the low pass filtered fluctuation signal is reconstructed

$$\tilde{p}_{lp}(t) = a(t)cos(\varphi_s(t)) \tag{4.26}$$

Figure 4.5a shows an example of the analytic phase and amplitude determined by the low pass filtered signal of a pressure sensor in presence of rotating stall obtained by measurements with the study case in chapter 7. The phase is monotonic except for phase jumps from π to $-\pi$ and instants when the original pressure signal is different from its regular shape, as found at 75%-80% of the represented time interval. The sawtooth character of the low frequency pressure fluctuations leads to the nonlinear slope of the phase, which is steeper on the short, increasing slope of the pressure fluctuation signal and less steep on the longer, decreasing slope.

Instants showing a decreasing analytic phase are characterized by small instantaneous amplitudes. In the complex phase plot, figure 4.5b, the moments of ambiguous phase due to irregular occurrence of stall cells are recognizable by small, eccentric circles, while regular stall cycles are characterized by centered complex pointer trajectories with higher radii. The following phase averaging technique corresponds to the phase averaging with respect to the impeller revolution. The phase average of the pressure signal itself, represented in 4.5c shows that the saw-tooth character and peak-to-peak amplitude of the original signal is well reproduced. The main advantage of this processing technique is its robustness in all kinds of exceptional situations and no need to fix arbitrary threshold levels.

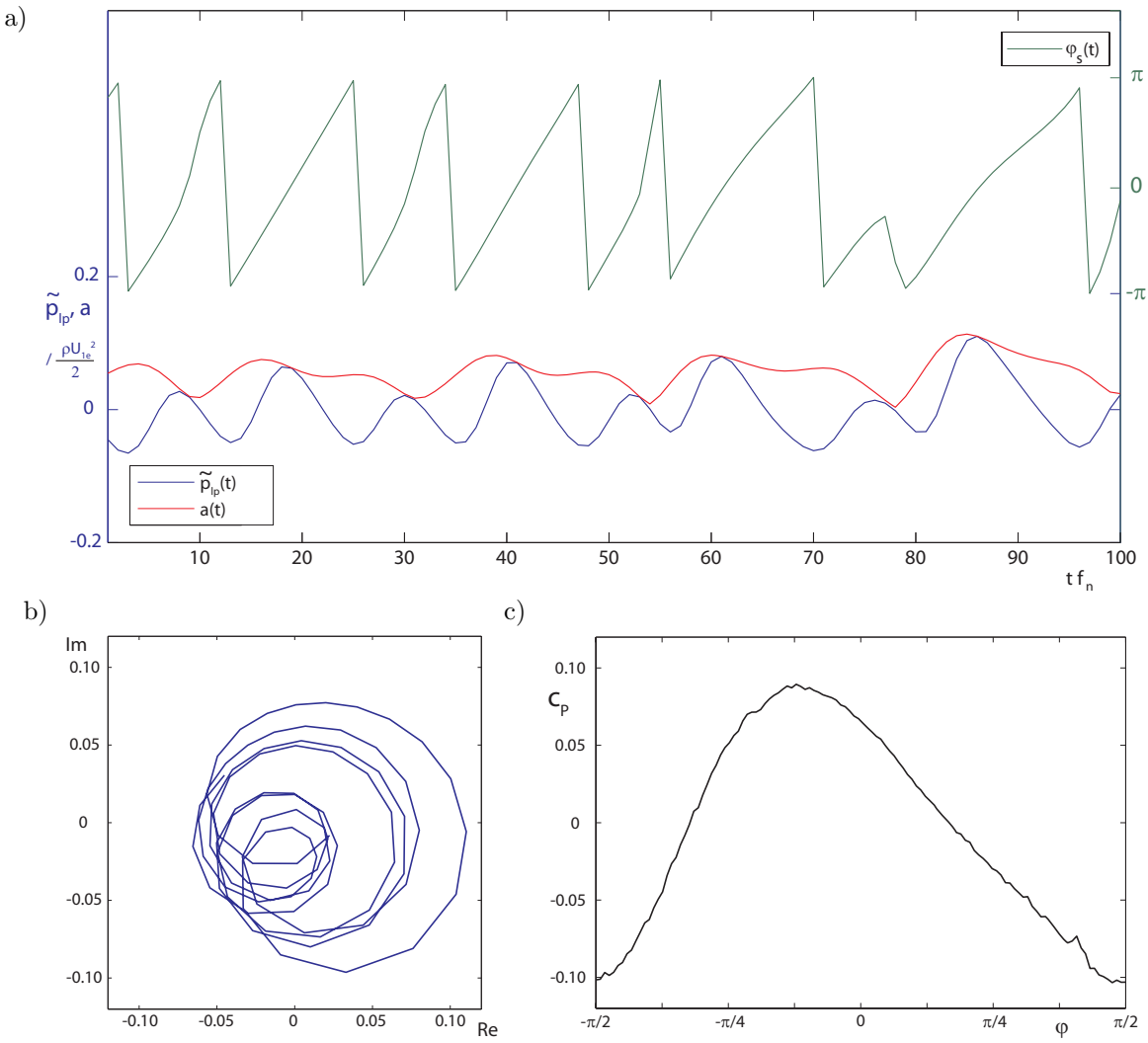

Figure 4.5: Example of analytic decomposition of pressure signal recorded over 100 impeller revolutions, a) $p_{lp}(t)$, analytic amplitude $a(t)$ and phase $\varphi_s(t)$, b) Phase plot, c) Phase averaged pressure signal

Part II

Diffuser Flow Topology Numerical Investigations

Chapter 5

Pump Turbine Scale Model Stationary Numerical Simulations

The QNET-CFD network aims at providing European industries with a knowledge base of challenging CFD applications and best practice guidelines. Study case TA6-04 is a scale model of a pump-turbine with the characteristics given in table 5.1.

ν	Specific speed	0.42
z_b	Number of impeller blades	5
z_o	Number of guide vanes	22
D_{1e}	Outer impeller diameter	$403\,mm$
$D_{\bar{1}e}$	Impeller inlet diameter	$378\,mm$
α_{GV}	Guide vane opening angle	18°
$R_{2e} - R_{1e}$	Radial impeller-diffuser gap	$30\,mm$
$(R_{2e} - R_{1e})/R_{1e}$	Relative impeller-diffuser gap	15%

Table 5.1: Parameter summary of the QNET-CFD-TA6-04 pump-turbine scale model

Experimental and tentative numerical investigations on the scale model have been achieved in the frame of the HPNURSA (High Performance Numerical Unsteady Rotor Stator Analysis) project, whose principal aim was to develop and improve the numerical tools for such simulations, focussing on the development of transient rotor-stator interface algorithms. However, this study case is well suited to stationary simulation approaches, since the use of the circumferential mixing plane hypothesis is possible due to the large radial gap between impeller outlet and diffuser inlet.

5.1 Numerical Setup

The simulation domain represented in figure 5.1 consists of one channel of each component. The meshing approach covers an entire channel between two blades, leading to relatively small periodic interface regions. Three sets of block structured hexahedral meshes with properties summarized in table 5.2 are generated. The following mesh refinement study considers the global pump-turbine performances (energy-discharge characteristic) and local velocity profiles on the guide vane.

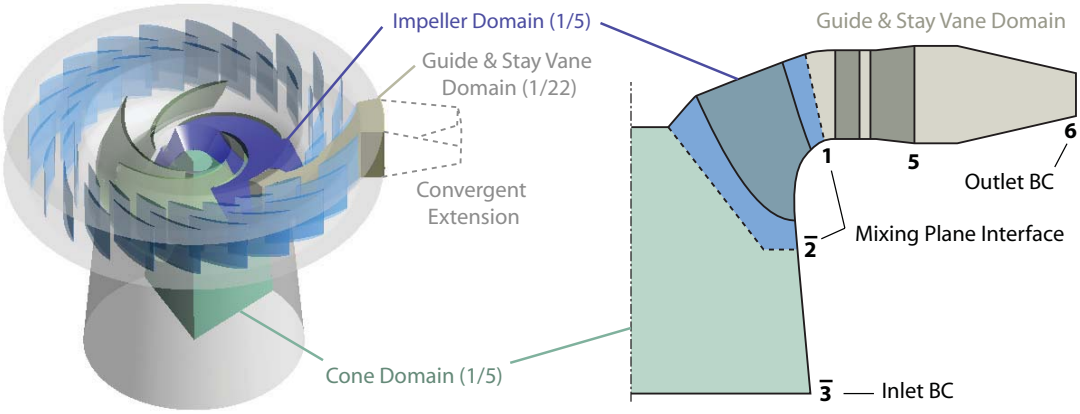

Figure 5.1: Simulation domain of the QNET-CFD-TA6-04 pump-turbine

Level	Component	Nodes	Total	y^+
	Cone	30′000		100
Coarse	Impeller	160′000	245′000	50-80
	Guide & Stay Vane	55′000		40-60
	Cone	105′000		30
Medium	Impeller	455′000	740′000	20-40
	Guide & Stay Vane	180′000		8-12
	Cone	300′000		-
Fine	Impeller	1′570′000	9′120′000	5
	Guide & Stay Vane	7′250′000		2

Table 5.2: Main mesh dimensions, node numbers and achieved boundary layer resolution

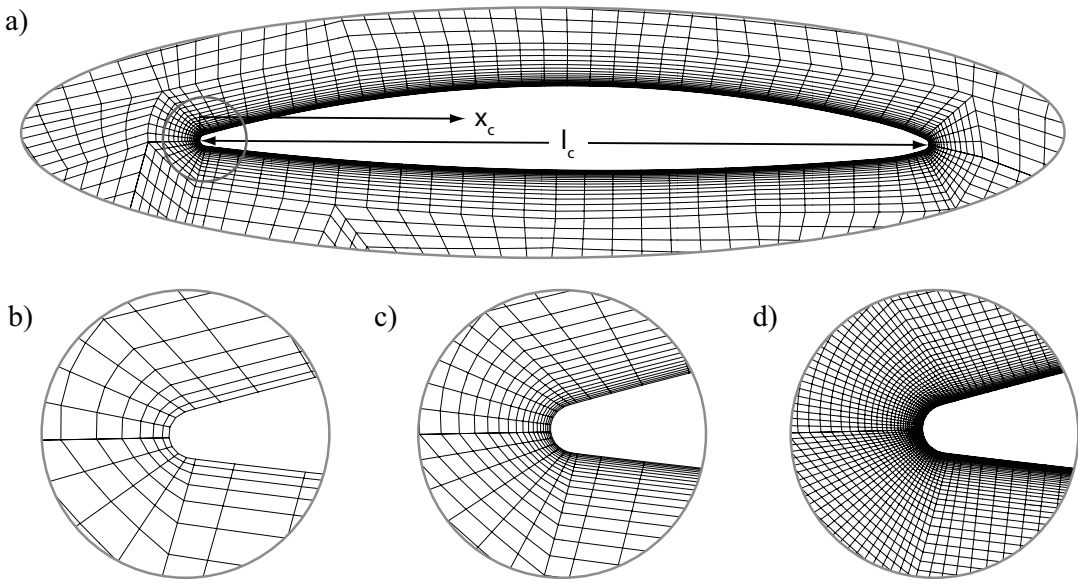

Figure 5.2: Close-up views of the meshes around guide vane. a) Medium mesh, b) Coarse mesh, c) Medium mesh, d) Fine mesh

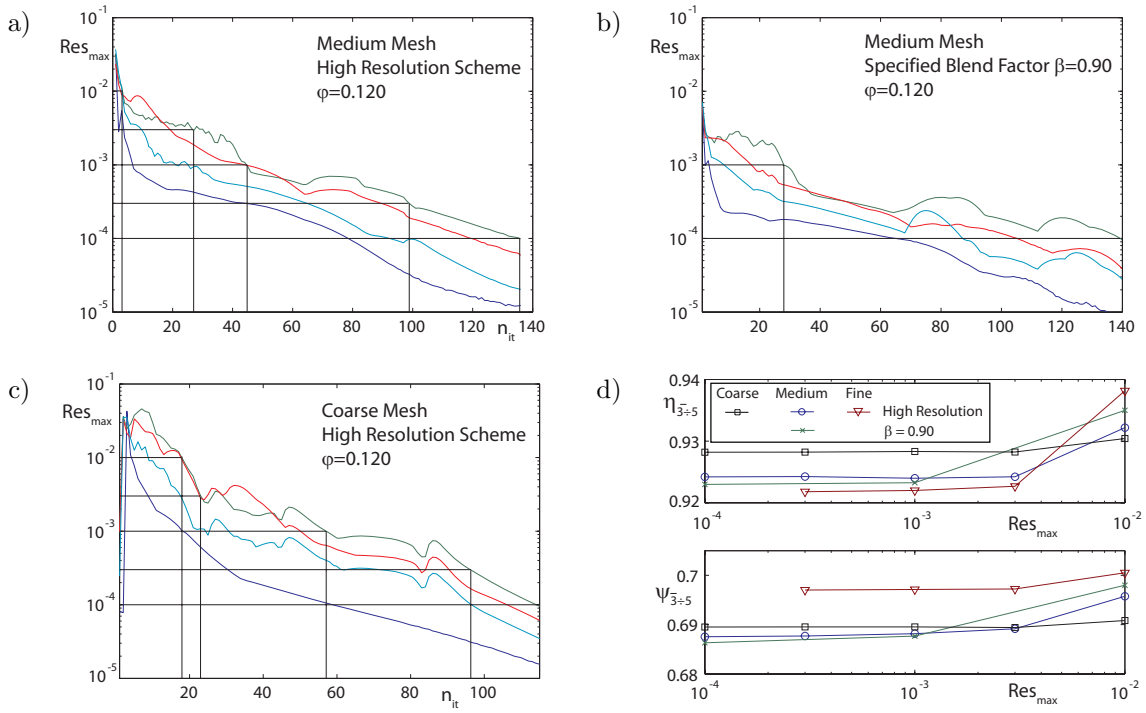

Figure 5.3: Iteration error and discretization scheme study. a) Residuals for high resolution scheme, medium mesh, b) Residuals for specified blend factor,medium mesh c) Residuals for high resolution scheme, coarse mesh, d) Summary of global performance numbers: Energy coefficient and efficiency

5.2 Iteration and Spatial Discretization Error Study

Iteration and Discretization Error Study Based on Global Performance

The iteration error is studied by comparison of global performance numbers evaluated with the results at different convergence levels. The residual evolution along the iteration count of the solver is represented in figure 5.3a to 5.3c for different meshes and discretization schemes. Figure 5.3d summarizes the global performance numbers of the pump turbine with different discretization schemes and at different residual levels. It is confirmed that a maximum residual criterion of 10^{-3} is sufficient for global performance evaluation in time-independent simulations, as the quantity of interest does not change significantly when the solution further converges to yield smaller residuals. The similarity of results between the high resolution scheme and a specified blend factor of 0.9 is confirmed.

Discretization Error Study Based on Viscous Losses

Figure 5.4 shows the decomposition of losses found at $\varphi = 0.110$, depending on the mesh refinement level. The prediction of transferred energy in the impeller is monotonically increasing as the mesh is refined. The losses found by integration between the passage sections $\bar{3}$ and 5 according to equation (1.45) are differentiated according to equation (2.8) into $\psi_{r,\tau}$, the part found consistently by volume integration of the viscous dissipation, and

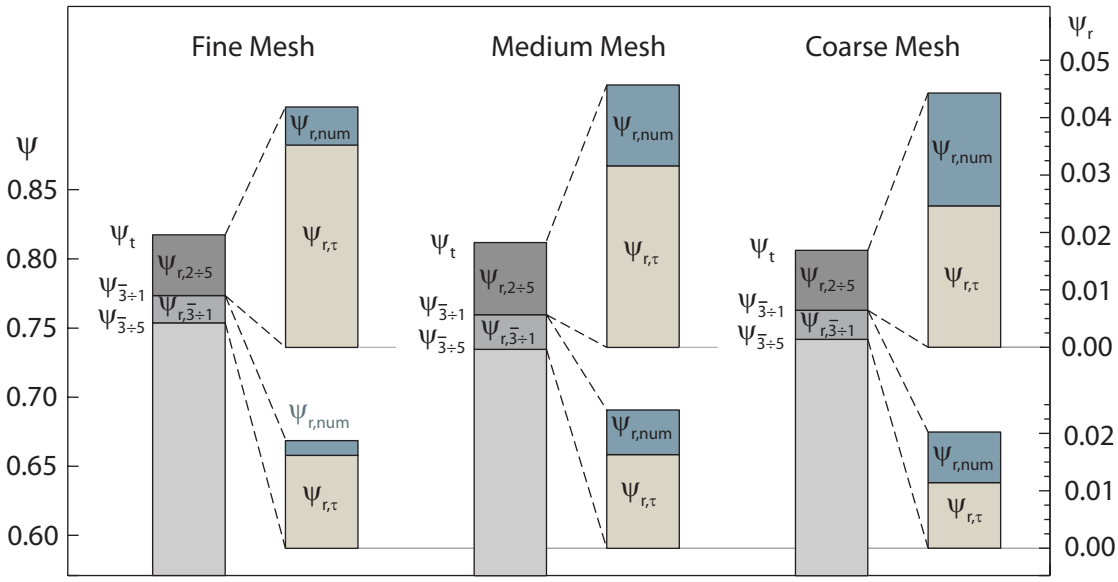

Figure 5.4: Losses obtained with different mesh refinement levels at $\varphi = 0.110$.

the remainder, $\psi_{r,num}$,:

$$\psi_{r,\tau} = \frac{2}{\rho Q U_{1e}^2} \int_V 2(\mu + \mu_t) D_{ij} D_{ij} dV \quad , \quad \psi_{r,num} = \psi_r - \psi_{r,\tau} \tag{5.1}$$

The viscous dissipation losses $\psi_{r,\tau}$ are increasing monotonically, clearly for the impeller domain and less clearly for the diffuser domain, especially from the medium to fine mesh. The evaluation of losses by passage section energy fluxes gives a picture less clear: The predicted losses increase when refining the mesh from coarse to medium while they decrease from medium to fine. Together with the increasing transferred energy from coarse to fine mesh, this results in the non-monotonic behavior of the complete simulation domain energy coefficient $\psi_{\bar{3}\div 5}$. The second order error estimators $\psi_{r,num}$ decrease as the mesh is refined, as expected for this expression quantifying to which degree the spatial discretization conserves kinetic energy.

Discretization Errors Study Based on Local Velocity Profiles

The effects of mesh refinement on the guide vane boundary layer are represented in figure 5.5 by velocity profiles along the guide vane at mid-height of the channel .

The estimated wall distance for the transition of the viscous sub-layer to the logarithmic profile at $y^+ = 11$, based on the finest grid simulation is represented in the profiles. The coarse and the medium mesh refinement levels differ dramatically in the way they predict the evolution of velocity profiles on the first half chord. The prediction of the medium mesh is very close to the fine one, since both have the first integration point inside the viscous sub-layer. Furthermore the medium mesh has a sufficient number of control volumes in the remainder of the boundary layer to reproduce the entire velocity profile similar to the fine mesh. The coarse mesh results differ clearly since the logarithmic wall function, equation (1.33), is used to determine the wall shear. This error occurring under mesh coarsening, typically classified as a discretization error, however, is rather

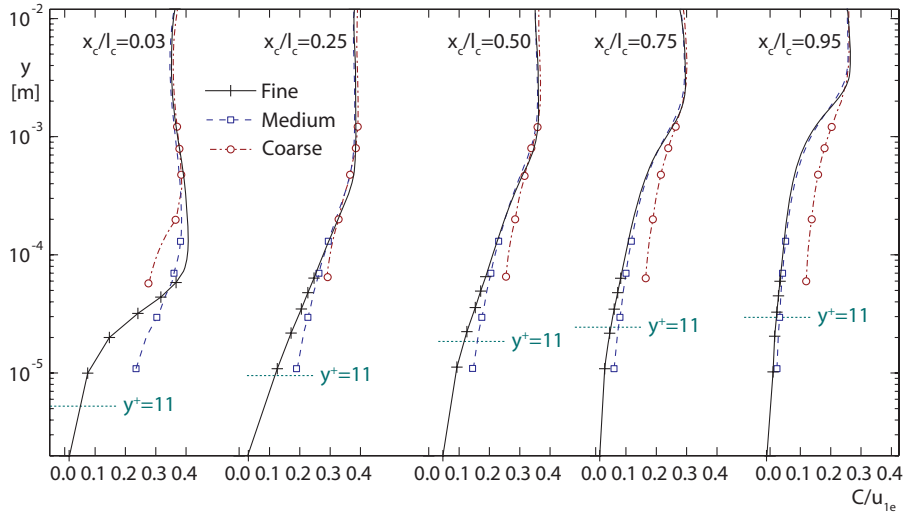

Figure 5.5: Velocity profiles on the guide vane at mid span for different mesh refinements.

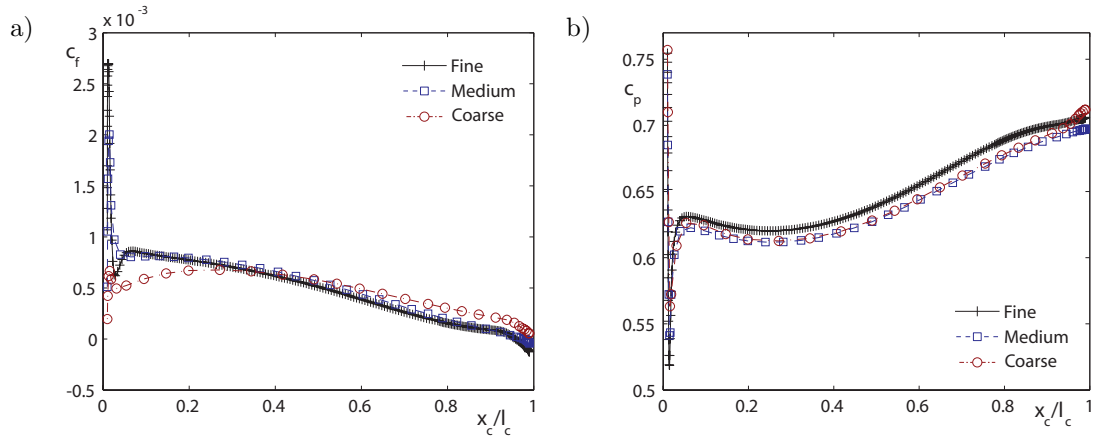

Figure 5.6: Wall shear and pressure along the guide vane for different mesh refinements

a modeling error, since the modeling depends on the discretization. Furthermore, the mesh discretization for the remainder of the boundary layer is so coarse that the velocity profiles cannot be reproduced with satisfying precision. This is most striking close to the leading edge, where the local increase of velocity due to the displacement of the blade is not as pronounced as for the finer meshes. The resulting wall shear predicted with the different mesh refinement levels is in agreement with the velocity profiles, see figure 5.6a. A pronounced peak in wall shear at the leading edge is consistently reproduced by the fine and medium mesh, while the numerical diffusion and averaging over large control volumes smears out this peak entirely for the coarse mesh. The wall shear predicted using fine and medium meshes on the first quarter of the chord is higher than with the coarse mesh. The resulting skin friction depends on the refined resolution of the boundary layer characterized by the opposed effects of acceleration due to displacement and deceleration due to skin friction. The pressure distribution along the chord is more influenced by the surrounding flow field than by the boundary layer resolution. So the results of the fine

mesh are clearly different from the medium and coarse mesh that yield similar results, since the mesh refinement of the medium versus the coarse mesh is largely concentrated in the boundary layer region. The area-averaged pressure at section 3 is used as reference pressure p_{ref}, so the overall difference in pressure level is consistent with the higher energy coefficient predicted using the fine mesh. The slightly higher pressure recovery that can be observed along the chord with the fine mesh goes along with the lower viscous losses prediction, figure 5.4.

5.3 Simulation Results

Energy-Discharge Characteristic

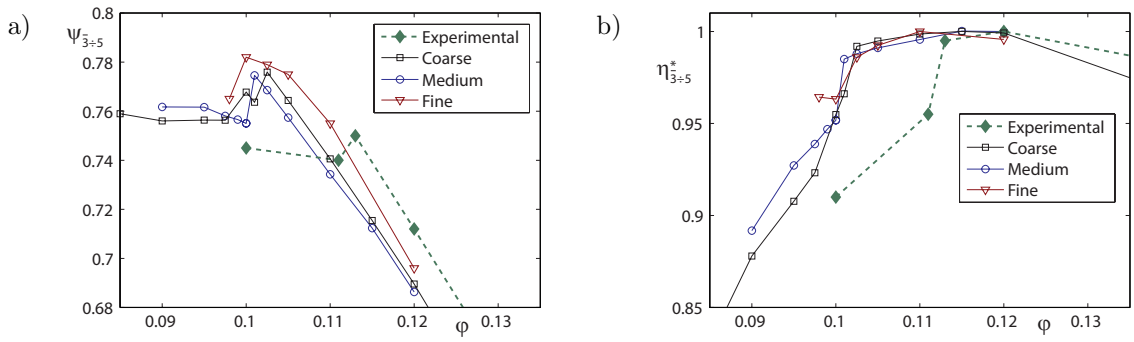

Figure 5.7: Performance evaluated by time-independent numerical simulation for different mesh refinement levels. a) Energy-discharge characteristic, b) Relative efficiency

Figure 5.7 summarizes the performance numbers obtained by time-independent numerical simulation compared to the experimental characteristic curves. The convergence under mesh refinement is not monotonic towards the experimental results: While the finest mesh is the closest to the values from experimental investigations, the use of the medium mesh yields results that differ more from experimental than the coarse one. This kind of non-monotonic convergence behavior is unexpected and makes the use of common error estimating techniques such as the Richardson extrapolation [120] meaningless. The saddle type of the energy-discharge characteristic is predicted by simulations at all refinement levels with a drop of energy coefficient that corresponds fairly well to the experimental findings. The decrease of the energy coefficient as flow rates decrease is connected to a loss of efficiency, indicating that the loss is induced by viscous losses and not by reduced energy transfer in the impeller.

Though, the critical flow rate where positive slope of the energy-discharge characteristic is predicted by simulation is considerably lower than found in experiment. The present numerical simulation method is helpful indicating some flow features connected with positive slope in the characteristic, the quantitative accuracy of prediction is unsatisfactory and the method can thus not be qualified as a reliable tool to ascertain the range of stable operation of such pump-turbines.

Diffuser Flow Patterns

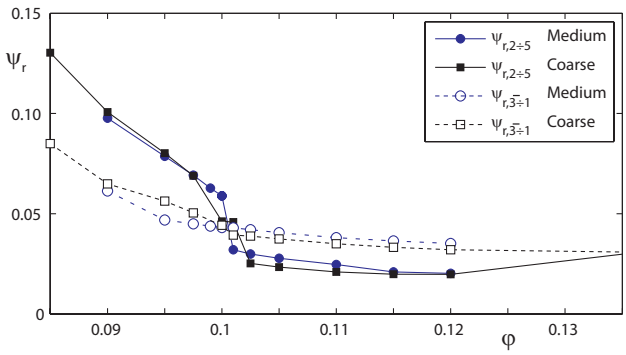

Figure 5.8: Losses in the impeller domain, $\psi_{r,\bar{3}\div 1}$, and in the diffuser domain, $\psi_{r,2\div 5}$, depending on flow rate

The positive slope on the energy-discharge characteristic is connected to an increase of the diffuser viscous loss coefficient $\psi_{r,2\div 5}$ when decreasing flow rate from $\varphi = 0.101$ to $\varphi = 0.100$, while there is no noticeable evolution of impeller losses in this range of flow rates, see figure 5.8. The drastic increase of losses in the stay and guide vane domain is connected with a change of flow topology visualized in figure 5.9 by surface streamlines on the guide and stay vane surfaces. At $\varphi = 0.101$, flow separation is apparent at mid-height of the channel. The zones of stagnant flow do not interfere with the through-flow intensively, and thus do not impact on the energy balances of the flow. They appear at $\varphi = 0.110$ and grow continuously as flow rates decrease. The sudden change from this symmetric flow topology to an asymmetric, swirling flow at $\varphi = 0.100$ is the root cause for the increased viscous losses, since energy is drawn off the mean flow and dissipated.

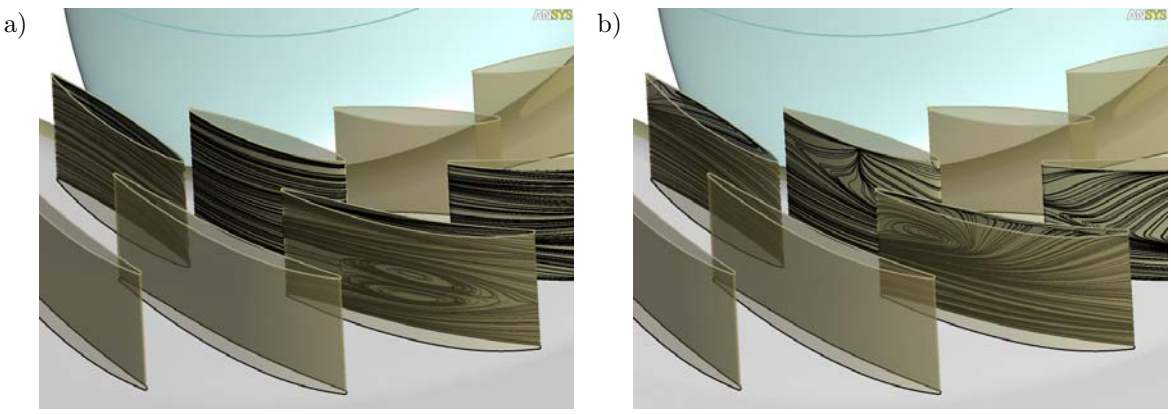

Figure 5.9: Surface streamlines evidencing flow patterns connected with increased losses in the guide vane and stay vane domain. a)Sound through flow, $\varphi = 0.101$, b) Recirculation zone at the interior side wall $\varphi = 0.100$

Chapter 6

Double Suction Pump Time Dependent Simulations

The medium specific speed double suction pump presented in this chapter is an early design stage of an industrial pump. The geometry was provided by Sulzer Ltd., Winterthur, Switzerland, and is interesting in that it exposed a strong saddle type characteristic which was cured by geometrical modifications on the impeller and the diffuser in the final design. The flow in the configuration before that modification is simulated and analyzed to understand the possible reasons for the instability in the characteristic.

ν	Specific speed (entire pump)	0.33 [1]
z_b	Number of impeller blades	2×7 (staggered)
z_o	Number of guide vanes	12
$(R_{2e} - R_{1e})/R_{1e}$	Relative impeller-diffuser gap	9.5%

Table 6.1: Parameter summary of the double suction pump

6.1 Numerical Setup

Computing Domain and Space Discretization

The computing domain is discretized using block-structured hexahedral meshes containing a few prismatic elements in so-called swept blocks to avoid low element face angles or collapsed element edges (figure 6.1a). The moderate mesh size is chosen with respect to the number of operating points to investigate.

[1] Differing from equation (10), $\nu = \frac{\varphi_n^{0.5}}{\psi_n^{0.75}}$ is used in conjunction with a definition of the discharge coefficient defined as the ratio of bulk (meridional, radial) velocity component C_m to circumferential velocity U on the cylindrical section 1: $\varphi = \frac{C_{m,1}}{U_1} = \frac{Q}{2\pi b_1 R_1 \omega R_1}$ with b_1, the channel width at section 1.

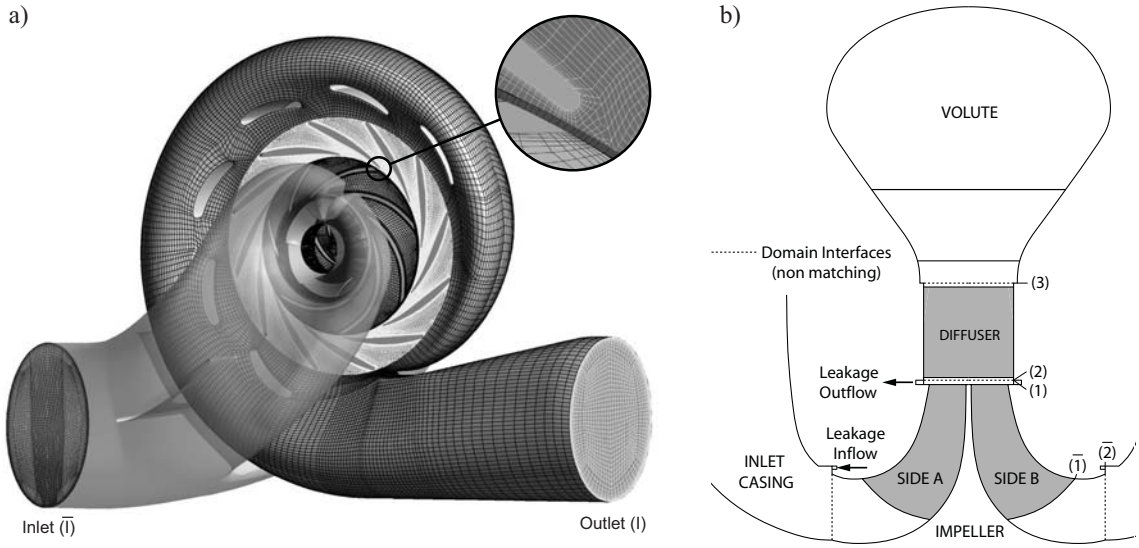

Figure 6.1: Double suction pump computing domain. a) Mesh, b) Mid plane cross-section

Domain	Per Passage	Total
Inlet Casing (ic)		505′000
Impeller (a, b)	61′000	790′000
Diffuser (v)	79′500	824′000
Volute (sc)		417′000
Total		2’536’000

Table 6.2: Mesh sizes per computing domain for the double suction pump

Boundary Conditions

The location of boundary conditions and interfaces in the computing domain mesh are represented in figure 6.1. The study case differs from the former investigated cases by the fact that the leakage flows are represented by additional boundary conditions, the overview of boundary conditions is given in table 6.3.

Type	Location	Option
Inlet	ic ($\bar{I}$)	Constant Flow Rate Q
Outlet	sc (I)	Zero Average Static Pressure
Leakage Out	(a, b)	Flow Rate (0.8%Q per side)
Leakage In	(ic)	Flow Rate, $C_u = 0.5U$
Walls	-	No Slip - Log Wall Functions ($y^+ = 100$)

Table 6.3: Double suction pump boundary condition summary

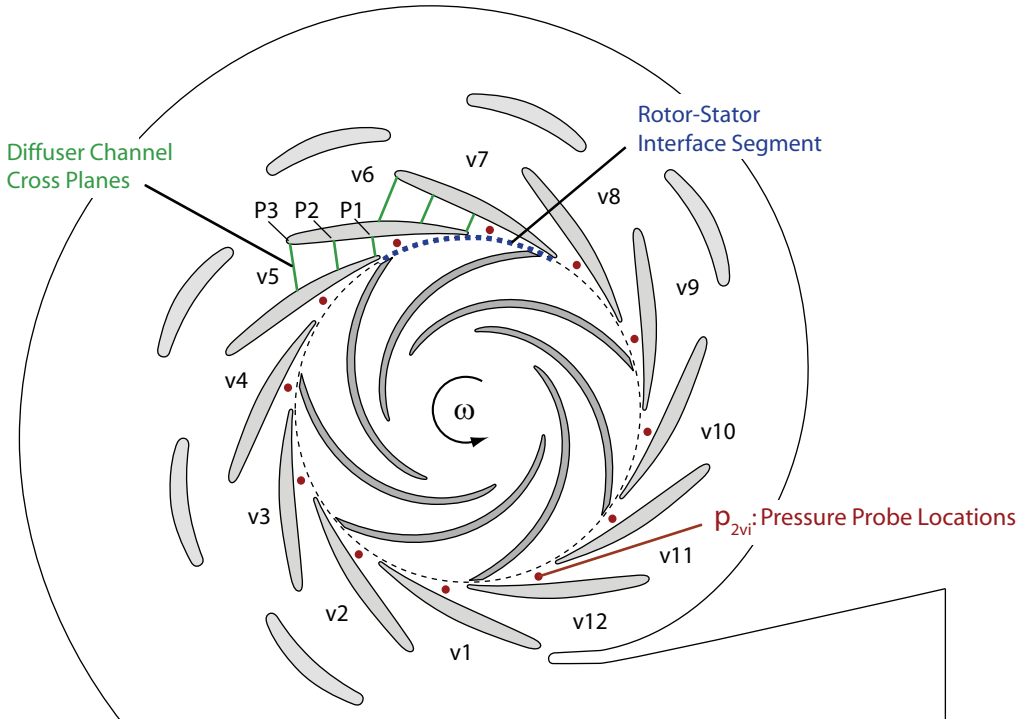

Figure 6.2: Top View of the computing domain

Time Discretization, Convergence and Iteration Error Evaluation

For operating points below 90% of BEP flow rate, low frequency fluctuations of global and local values are observed. Besides the energy coefficient ψ the relative flow rates $Q^*_{v,k}$ of the diffuser channels $v1$ to $v12$ (Fig. 6.2) are used for a convergence and iteration error study:

$$Q^*_{v,k} = \frac{z_v Q_{v,k}}{Q_{BEP}} \tag{6.1}$$

At 80% flow rate, results on one revolution are obtained using different numbers of time steps n_{ts} and different convergence criteria leading to n_{cli} internal coefficient loop iterations. Table 6.4 shows the obtained averaged energy coefficient on the last blade passage and the cumulated RMS-Error of the $Q^*_{v,k}(t)$ compared to the finest one ($n_{ts} = 840$). 420 time steps per revolution and a convergence criterion of 1.10^{-4} for RMS Residuals are chosen as a compromise of cost and accuracy.

$$\Sigma\Delta Q^*_{RMS} = \frac{1}{n_{ts} z_v} \sqrt{\sum_{k=1}^{k=z_v} \sum_{j=1}^{j=n_{ts}} (Q^*_{v,k}(t_j) - Q^*_{v,k840}(t_j))^2} \tag{6.2}$$

n_{ts}	RMS Res.	n_{cli}	ψ^*	$\Sigma\Delta Q^*_{RMS}$
840	$5 \cdot 10^{-6}$	7	1.095	-
420	$1 \cdot 10^{-5}$	7	1.095	0.029
420	$\mathbf{1.10^{-4}}$	**5**	**1.094**	**0.030**
420	$5 \cdot 10^{-4}$	4	1.091	0.038
210	$1 \cdot 10^{-4}$	5	1.085	0.103

Table 6.4: Time steps and convergence criteria

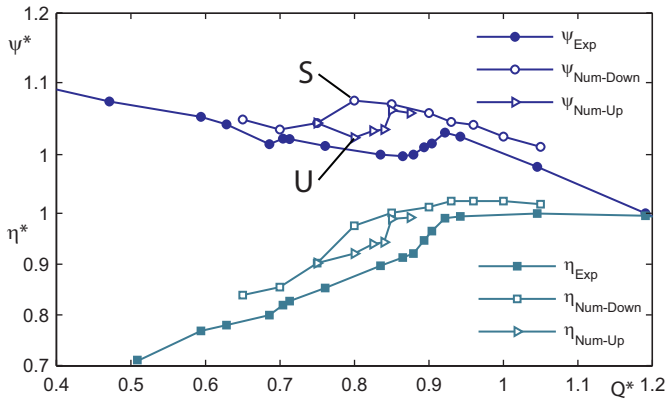

Figure 6.3: Dimensionless double suction pump characteristic

6.2 Simulation Results

The characteristic curve obtained with decreasing flow rate shows a sudden drop of energy coefficient at a flow rate of 75%. The magnitude of the drop in energy coefficient is about 4%. This corresponds well to the performance discontinuity measured on the preliminary design before it was cured. When leading the time-dependent simulations towards higher flow rates again, it reaches the performance numbers obtained downwards at 85% flow rate. A similar hysteresis in numerical simulation results has formerly been described concerning flow separation in the impeller [74], though at considerably lower flow rates.

In the following, the flow fields obtained at 80% flow rate on the downwards branch (S) of the curve will be presented and compared to the simulation results on the upwards branch (U). At operating point S, the diffuser channel flow rates evaluated on 2 impeller revolutions, see figure 6.4, show a quasi-stationary pattern of diffuser channels operating close to BEP flow rate alternating with channels (one of three) that are stalled at about 50% of flow rate. The pattern is not perfectly regular as the alternate stall described by Sano et al.([126], [125]). This is probably due to the presence of a spiral casing with the tongue and additional stay vanes that create a nonuniform pressure field at the diffuser outlet. With one of two channels stalled, the upwards branch, conditions show a pattern more regular, but not stationary. Figure 6.5 represents the diffuser channel flow rate fluctuations, obtained at 70% BEP flow rate, where a clear change in the angular position of the stalled channels is found during the simulation interval. The flow rate distribution

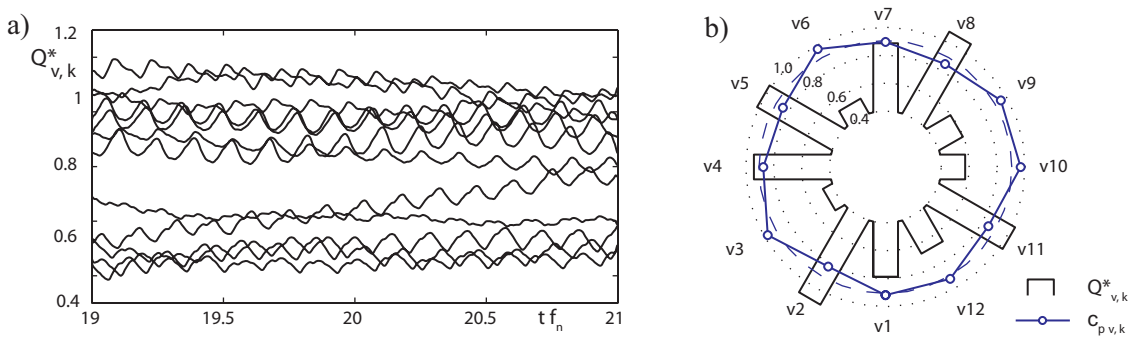

Figure 6.4: Diffuser flow rate distribution and pressure probes at 80% BEP flow rate

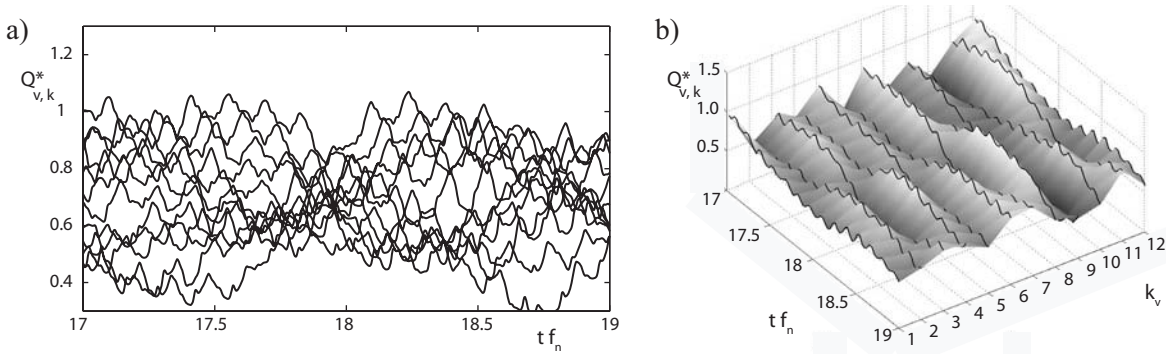

Figure 6.5: Diffuser channel flow rates at 70% BEP flow rate. a) Time evolution of flow rates b) 3D representation of circumferential distribution

is correlated inversely with the average pressure level at the sections. Transient pressure measurements in the diffuser as presented for the pump-turbine investigated in chapter 7 would be suitable to validate this simulation result qualitatively by following the evolution of the circumferential repartition of such rotating or alternate stall.

The time averaged velocity fields in the neighboring diffuser channels v5 and v6 are represented in figure 6.6, for operating conditions U, the time average is taken over the last simulated impeller revolution where the channel flow rates are distributed similarly to case S, see figure 6.5. Under both conditions, channel $v5$ shows an asymmetric flow separation on diffuser side wall A. The asymmetry seems more pronounced for the upwards branch case U, furthermore even the high flow rate channel $v6$ shows the same asymmetry of normal velocity, whereas the flow is symmetrical here for point S. The time-averaged radial and circumferential velocities on the rotor-stator interface surface section represented in figure 6.7 and the averaged spanwise profiles, figure 6.8, confirm that the reverse flow extends back to the impeller in case U only.

By consequence, for the highly asymmetric conditions, the integrated flow rates over the impeller sides are in disequilibrium, potentially leading to axial thrust that the double suction configuration is meant to avoid. Figure 6.9 shows that the disequilibrium leads to a relative difference of about 10% in flow rate between the two impeller sides. This imbalance of impeller side flow rates exhibits the same hysteresis than the energy-discharge characteristic. The disequilibrium appears at $Q^* < 0.80$ at decreasing flow rates while

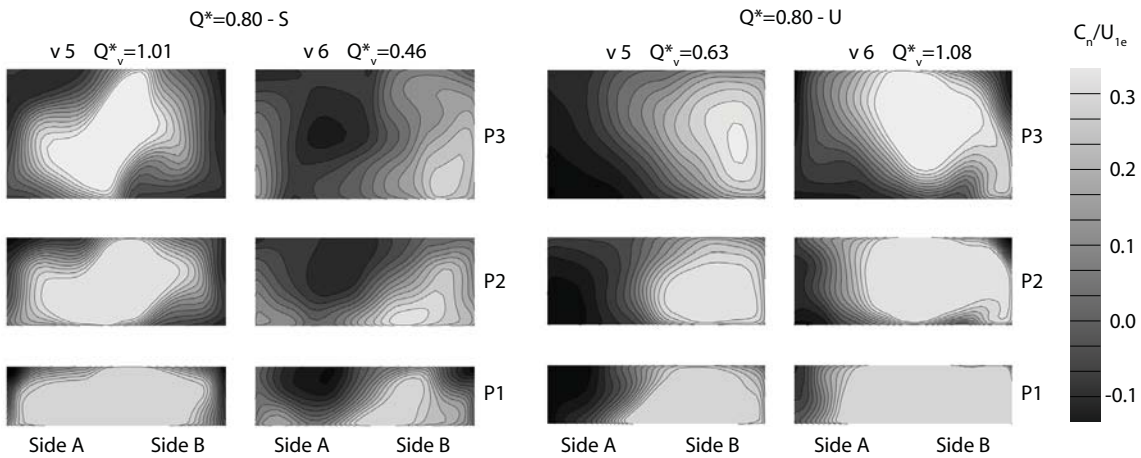

Figure 6.6: Normal velocity on diffuser channel cross planes

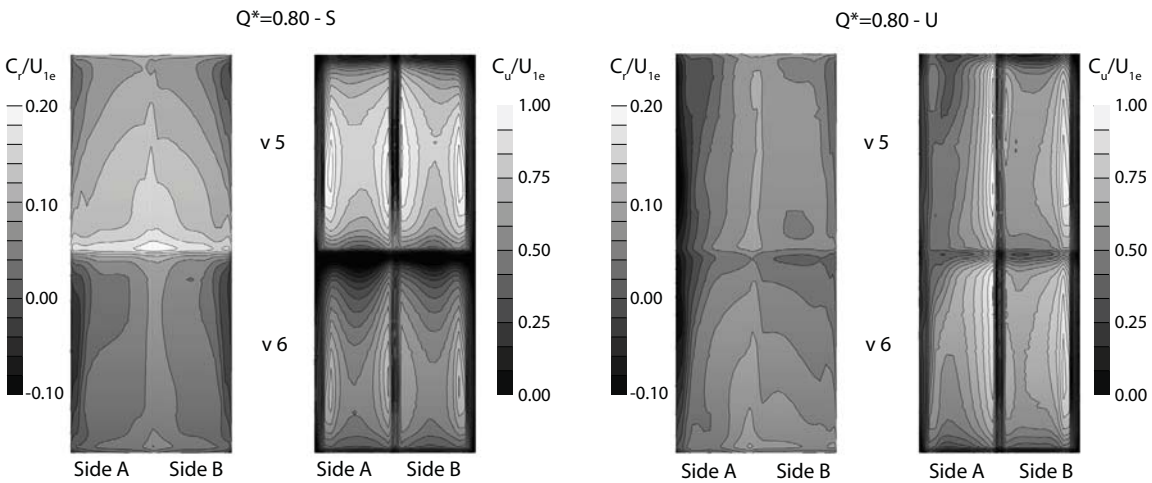

Figure 6.7: Time averaged velocities on rotor-stator interface segment

the flow rate has to be increased to $Q^* > 0.83$ to evolve back to equal flow rates of both impeller sides.

The diffuser channel flow resulting from the asymmetric velocity profiles at the diffuser inlet shows a vortical structure depicted by streamlines based on time-averaged velocity fields of one impeller revolution (Fig. 6.10).

An analysis of energy losses in the pump in two flow configurations reveals that the main difference are additional losses in the diffuser domain v evaluated by the energy balance integrated over one impeller revolution. The loss coefficients obtained from a balance over the sections 2, 3 and I are summarized in table 6.5. The analysis of the volumetric viscous loss term does not reproduce the entire losses which indicates a lack of conservation of kinetic energy as can be expected from the study presented in chapter 5. However, the difference in diffuser losses between both flow configurations is well represented by the differences of the evaluated volumetric loss term.

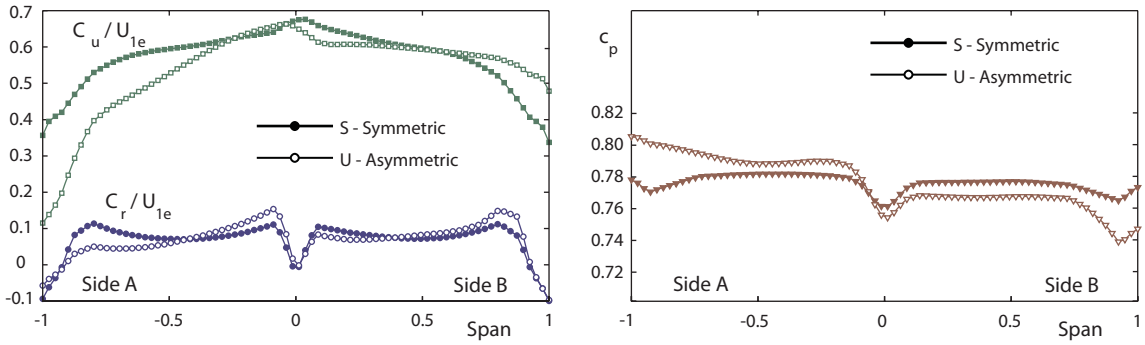

Figure 6.8: Impeller outlet velocity (left graph) and pressure (right graph) profiles, time average over one impeller revolution

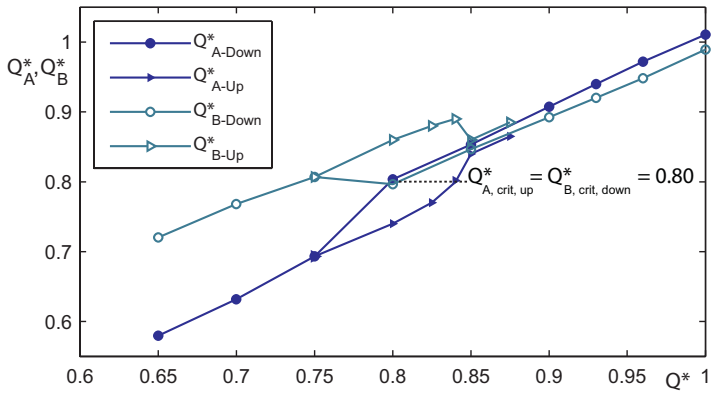

Figure 6.9: Hysteresis on the flow rate balance between the two impeller sides

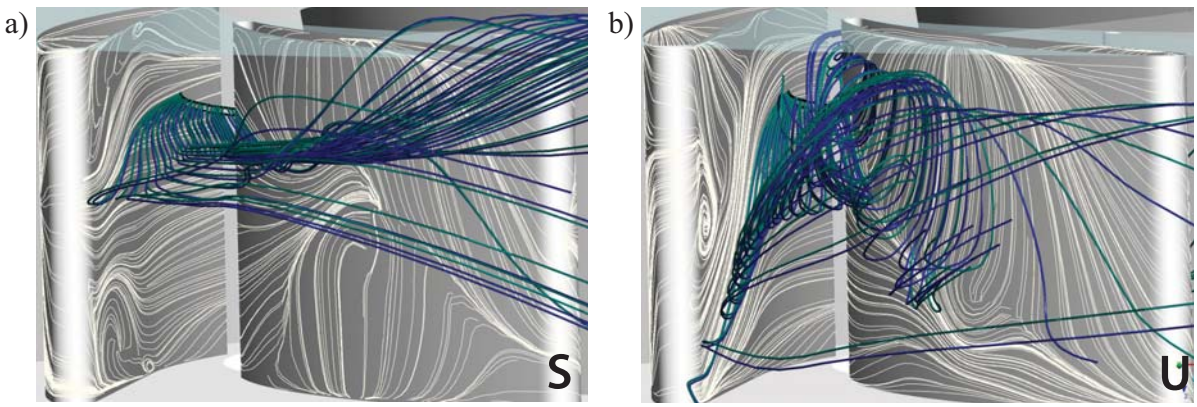

Figure 6.10: Streamline visualization in the diffuser channel $v7$ at 80% BEP flow rate - seen from the volute. a) Downwards branch, symmetric diffuser throughflow, b) Upwards branch, asymmetric, separated diffuser flow with increased energy dissipation

Value	S-Symmetric	U - Asymmetric	Difference U-S
ψ^*	1.094	1.037	0.056
ψ_t	1.260	1.267	0.007
ψ_2^*	1.216	1.212	0.004
$\psi_{r2\div3}^*$	0.104	0.140	0.036
$\psi_{rv2\div3}^*$	0.046	0.077	0.031
$\psi_{r3\div I}^*$	0.019	0.044	0.025

Table 6.5: Summary of energy losses at 80% BEP flow rate

Summary of the Numerical Simulations

The time-dependent flow simulations of an industrial double suction pump show two major governing phenomena: At operating points below 90% of BEP, patterns of alternate stall occur. Below 80% of b.e.p. flow rate, a one-sided flow separation in the diffuser occurs that influences the impeller exit flow profiles and leads to a strongly vortical flow in the diffuser channels where large amounts of energy are dissipated. Furthermore the stall patterns drastically change distribution and are not stationary any more. These two phenomena justify the use of a model including the entire circumference and both impeller sides as the only feasible simulation approach. A symmetrical setup could not reproduce the asymmetrical flow separation properly. A model including only an angular segment of a few flow passages using a periodicity condition imposes an angular periodicity at the chosen pitch which does not correspond to the solution of the model made of all flow passages of the pump, or only by lucky coincidence if it does so for certain operating conditions.

The hypothesis of impeller side flow imbalance is corroborated by field studies on a large number of double suction pumps experiencing vibration problems at part load by Hodkiewicz[64]. Strong axial components of vibration were detected and shown to lead to accelerated wear of the bearings. Axial displacements of the shaft have been measured at part load, showing an intermittent behavior more than a repeatable offset in one direction. This corroborates the existence of asymmetries in part load flow, but indicates that they are rather alternating between both sides of the machine in the investigated pumps, than staying well established on one side as predicted by the numerical simulation on this particular pump.

The losses in the diffuser appearing with the asymmetrical flow are so large that they affect the characteristic to the point of developing a positive slope. This finding is in good agreement with the characteristic measured, though quantitatively, there is an important disagreement in prediction of the critical flow rate where the losses suddenly increase.

Part III

Rotating Stall in a Francis Pump-Turbine Scale Model

Chapter 7

Experimental Investigations of Rotating Stall

The collaborative research project "Hydrodyna" conducted by the Laboratory for Hydraulic Machines at EPFL with the collaboration and support of major pump-turbine manufacturers aims at a better understanding of the transient behavior of pump-turbines.

a)

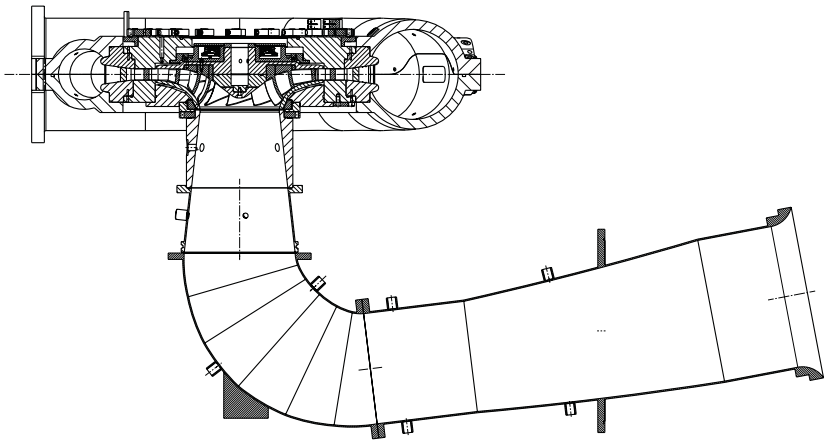

b)

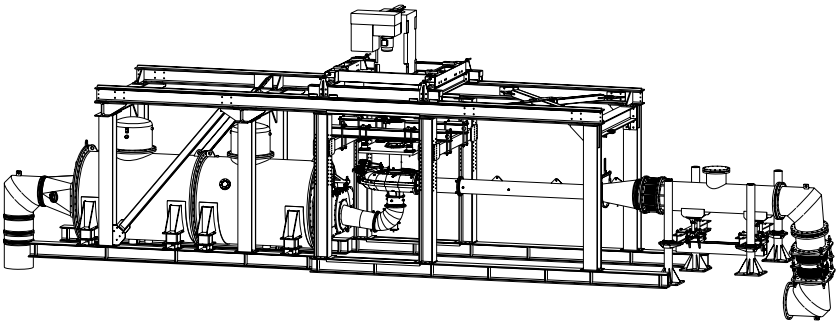

Figure 7.1: Hydrodyna pump-turbine reduced scale model. a) Mid plane cross-section, b) EPFL experimental validation facilities

7.1 Experimental Setup

A reduced scale model of a low specific speed Francis pump-turbine, represented in figure 7.1a, with the characteristics enumerated in table 7.1 is investigated in the EPFL experimental validation facilities, figure 7.1b. Measurements collected during two measurement campaigns are presented in this thesis, the available instrumentation and measurement condition matrix are given in table 7.2.

ν	Specific speed	0.19
z_b	Number of impeller blades	9
z_o	Number of guide vanes	20
D_{1e}	Outer impeller diameter	$523.5\,mm$
$D_{\bar{1}e}$	Impeller inlet diameter	$250\,mm$
α_{GV}	Guide vane opening angle	20°
$R_{2e} - R_{1e}$	Radial impeller-diffuser gap	$25\,mm$
$(R_{2e} - R_{1e})/R_{1e}$	Relative impeller-diffuser gap	9.5%

Table 7.1: Parameter summary of the pump-turbine scale model, pump mode

2006	Turbine LDV measurements, **Discovery pump operation measurements**	
	Pressure, stationary and rotating	
	$\varphi = 0.020..0.028; 0.043$ $N = 900\,rpm$	
	8 sensors in GV channel 20, (i) and (e) 8 sensors in GV channel 1, (i) and (e) 3×4 sensors in GV channel 3, 10, 11, (i) 10 closely spaced sensors on section 2 GV channels 10 and 11 2 sensors in the spiral casing, section I 30 sensors in the impeller	
2008	Off design turbine discovery, **Pump pressure and LDV measurements**	
	Pressure, stationary	LDV
	$\varphi = 0.015..0.036$	$\varphi = 0.026$; $\varphi = 0.031$; $\varphi = 0.034$
	$N = 600\,rpm, 900\,rpm$	$N = 750\,rpm; N = 900\,rpm; N = 900\,rpm$
	20 sensors on section 2, (i)	
	4 sensors in GV channel 3, (i)	1 grids at GV throat GV 3 - GV 4
	4 sensors in GV channel 4, (i)	3 grids around GV 3
	5 sensors in spiral casing	1 grid at impeller outlet $R = 0.277\,m$
	1 sensor in cone	

Table 7.2: Overview of experimental campaigns, pump mode measurement summary

Figure 7.2 shows the numbering of GV channels and the pressure sensor locations that will be subject to closer discussion in the following sections. The time average of the sensor closest to section $\bar{I}$ is used as reference pressure: $c_p = (p - \overline{p_{125}})/(0.5\rho U_{1e}^2)$.

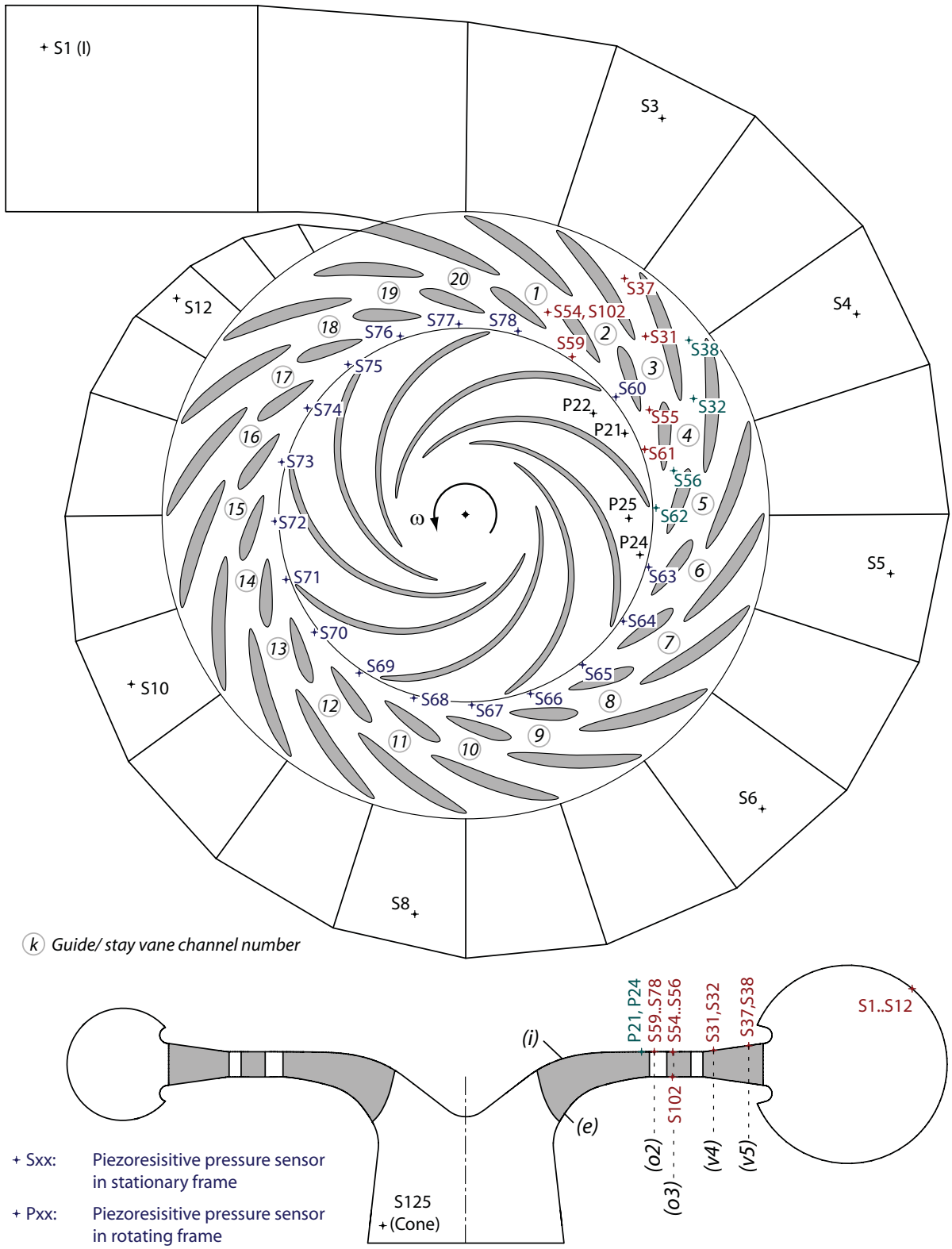

Figure 7.2: Location of the pressure sensors in the pump turbine water passage in rotating and stationary frame

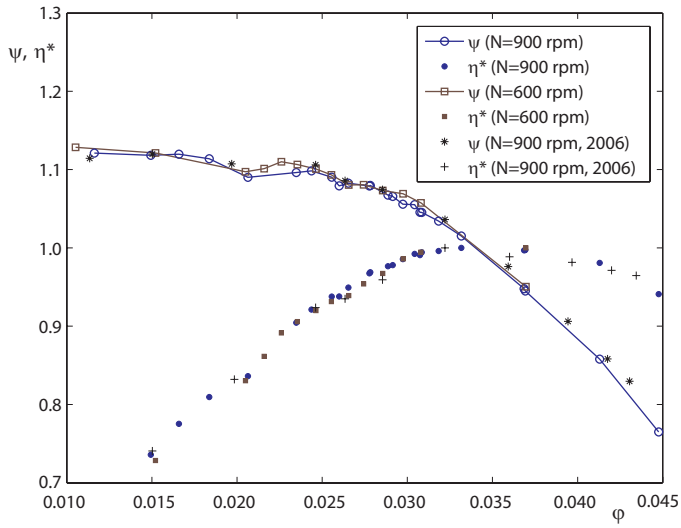

Figure 7.3: Specific energy and scaled efficiency versus discharge of the Hydrodyna pump-turbine. Instrumented impeller (2006) and plain impeller (2008), $N = 600\,rpm$ and $N = 900\,rpm$

7.2 Global Performance and Rotating Stall Patterns

The global performances measured in 2006 with the instrumented impeller compare well to the performances measured in 2008 with the plain impeller manufactured to avoid damage of the onboard instrumentation in turbine mode off-design points. The energy-discharge and efficiency-discharge characteristic are represented in figure 7.3.

The EPFL experimental validation facilities are designed to measure flow coefficient, energy coefficient and efficiency with an accuracy 0.2%. The performance evaluation is based on an average of measurements acquired during $20\,s$. A higher variance of the energy coefficient measured is notified at flow rates below $\varphi = 0.029$. This indicates that the operating conditions of the facility loop are less stable than at higher flow rates. The measured energy-discharge characteristic curve shows locally horizontal or even positive slope, which confirms the hypothesis that the considered pump-turbine is prone to unstable operation when used together with a low-slope system characteristic.

Pressure Fluctuations: Phase Averages and Power Spectra

The phase averaged pressure and the corresponding Fourier series coefficients for sensors close to the rotor-stator interface are represented in figure 7.4 for high discharge and part load operation. Both show the expected dominating blade passage frequencies, $z_b f_n$ and its harmonics in the stationary frame, $z_o f_n$ and its harmonics in the rotating frame. In the rotating frame, the non-uniformity due to the rotational asymmetry of the spiral casing is clearly recognized, more pronounced at part load than at high discharge. It leads to the low frequency coefficients in the Fourier series. In the stationary frame measurement, the only relevant component below the first blade passing frequency is the impeller revolution frequency, showing similar, however low, amplitudes at high discharge and at part load. The plausible reason of this is the eccentricity of the impeller rotation

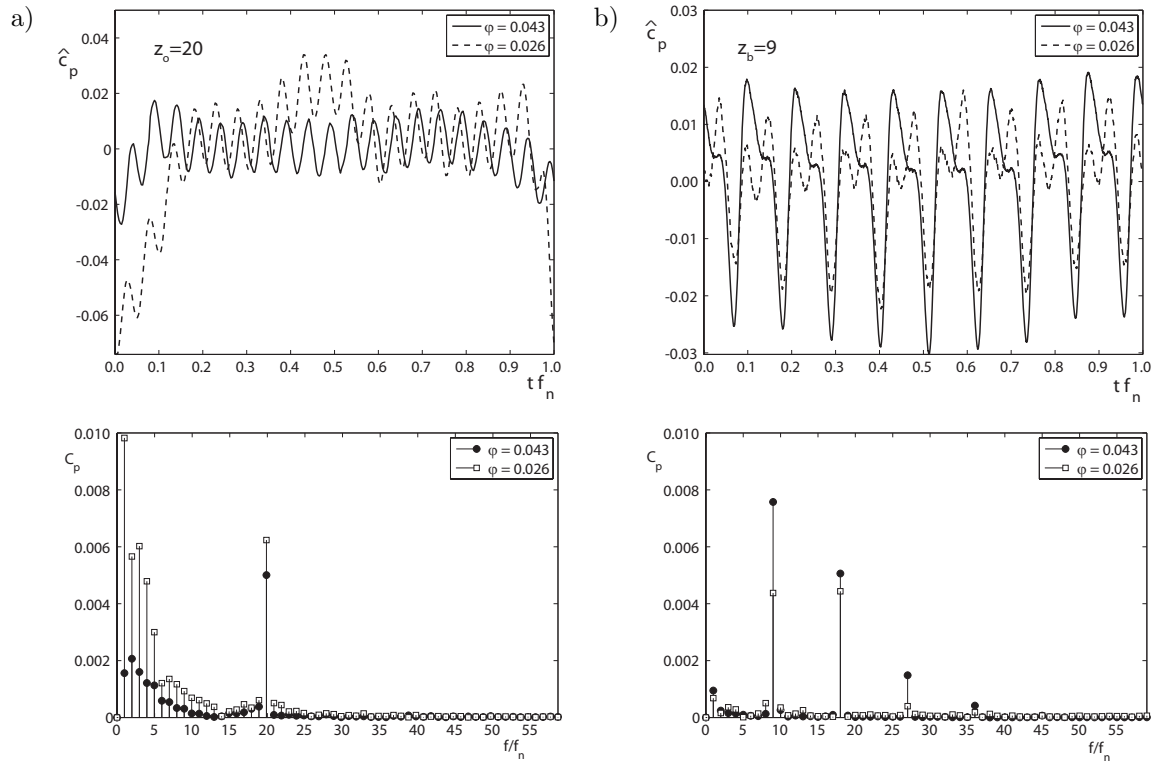

Figure 7.4: Pressure fluctuations. Top: Phase average, Bottom: Discrete Fourier Transform. a) P21, rotating frame, b) S61, stationary frame

axis in the casing due to the radial load on the rotating train. Power spectra estimates are computed using Welchs periodogram method from the resampled pressure signals of stationary frame sensor $S61$ and represented in figure 7.5 for four different flow rate coefficients from $\varphi = 0.036$ down to $\varphi = 0.026$. The strong increase of the broad-band low-frequency fluctuations as the flow rate decreases from $\varphi = 0.030$ to $\varphi = 0.028$ coincides with a discontinuity of slope on the measured energy-discharge characteristic.

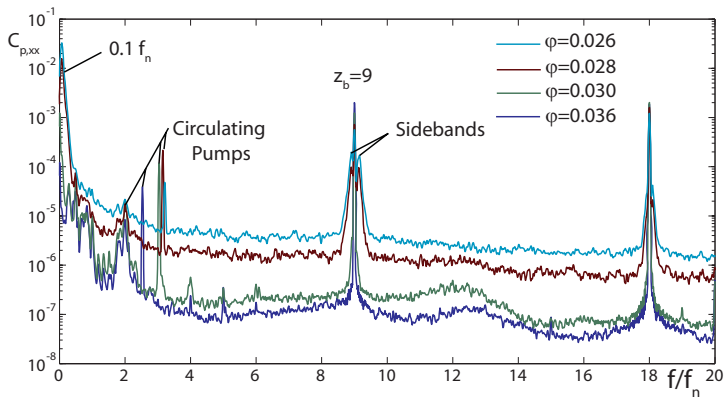

Figure 7.5: Pressure power spectra at point $S61$ in stationary frame, $N = 900\,rpm$

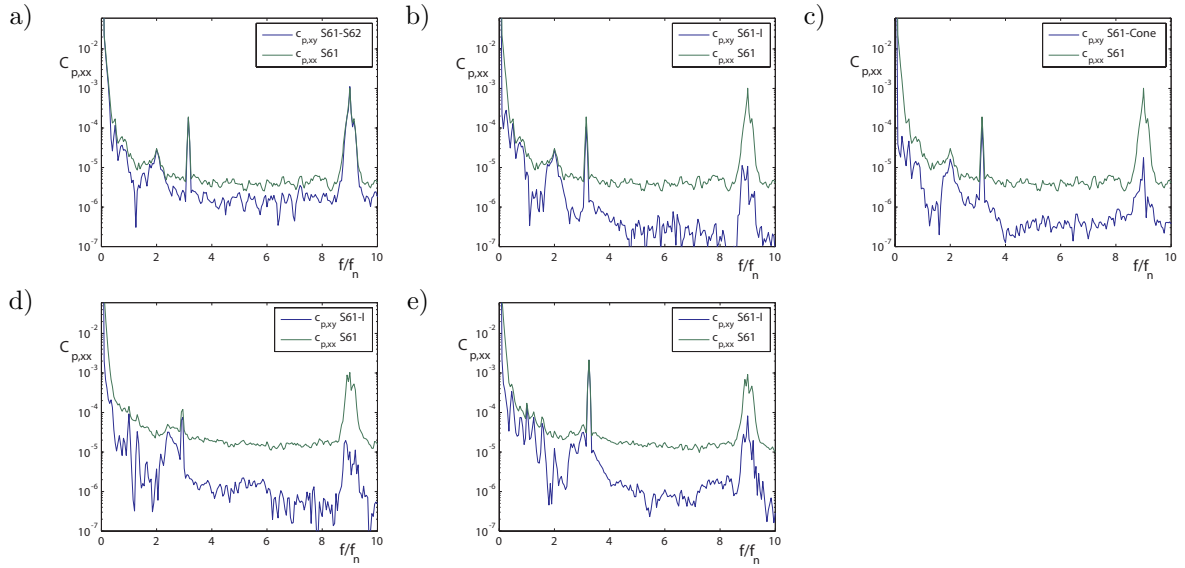

Figure 7.6: Pressure auto-spectral density of $S61$ and cross spectral power density with other sensors at part load conditions, $\varphi = 0.026$. Top: $N = 900\,rpm$ a) Neighboring channel $S62$, b) High pressure flange S1, c) Cone $S125$, d) High pressure flange $S1$ at $N = 750\,rpm$, e) High pressure flange $S1$ at $N = 600\,rpm$

Several peaks are identified in the frequency range below $z_b f_n$ in figure 7.5 . Figure 7.6 compares the auto-spectral power density of pressure sensor $S61$ to the cross spectral densities of $S61$ with other sensors for different revolution rates of the pump-turbine. This allows to ascertain the origins of some power density peaks in the low frequency range:

- A clear peak of increasing frequency with decreasing flow rate ($2.5 f_n$ at $\varphi = 0.036$ to $3.2 f_n$ at $\varphi = 0.026$). This peak is caused by the facility circulating pumps, that are operating at negative flow rates compared to their normal operation driving a turbine mounted in the facility. The frequency of the peak corresponds to the revolution rate of the single volute circulating pumps and their number of blades . Equal spectral power density values are observed at all pressure sensors in the pump-turbine.

- A peak at $2 f_n$ appears at at $N = 900\,rpm$. It appears clearly at high flow rates and is present though nearly hidden in the broad band fluctuations at lower flow rates. The cross spectral densities in figure 7.6 confirm this peak to appear in a correlated manner on all sensors. This peak is shifted to $2.4 f_n$ at $N = 750\,rpm$ and to $3 f_n$ at $N = 600\,rpm$. So, to the peak appears at a fixed frequency of $30\,Hz$ at which the test facility has a low damping due to its hydro-acoustic properties, according to former studies on this pump-turbine scale model [106; 105]. A closer analysis of the phase of this cross spectral density peak at $2 f_n$ represented in figure 7.6b confirms a phase delay of $\theta_{61,1} = 12^\circ$ between the sensors $S61$ and $S1$. The estimate of the velocity of pressure wave propagation obtained with the approximate path length of $l_{61,1} = 1.0m$ is consistent with the former studies:

$$a_{61,1} = \frac{l_{61,1}}{t_{61,1}} = \frac{2\pi * 2 f_n * l_{61,1}}{\theta_{61,1}} = 942\,m/s \tag{7.1}$$

- A low frequency peak around $0.1 f_n$ appears in figure 7.5 for $\varphi = 0.026$ and $\varphi = 0.028$ together with corresponding sidebands on the blade passing frequencies. This is due to rotating stall and will be subject to closer analysis.

- The remainder of pressure fluctuations below $z_b f_n$ are not as closely correlated between the different sensors, especially in the fluctuations in the range above $3f_n$, they are obviously local to the rotor-stator interface and to every single diffuser channel.

Rotating Frame Pressure Fluctuations

The low frequency pressure fluctuations observed in the stationary frame are manifest in the rotating system by pressure fluctuations identified around $4f_n$, as seen in figure 7.7 representing spectral power density at high discharge versus part load in the rotating frame. While at high discharge, $\varphi = 0.043$, all present harmonics of BPF occur at the

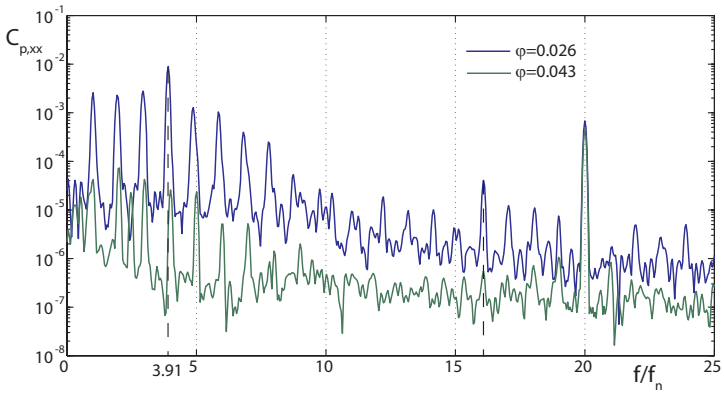

Figure 7.7: Pressure power spectra at point P21 at high discharge and part load

exact multiples of f_n, at part load, $\varphi = 0.026$, there is a frequency shift towards lower frequencies for the low harmonics. The highest power peak's frequency is determined by parabolic interpolation at $3.91 f_n$.

The nature of these fluctuations on sensor $P21$ shows up when considered in the time domain over the entire acquisition interval, see figure 7.8. The blade passing frequency $z_o f_n$ is recognizable but nearly hidden by a regular waveform of about 4 periods during one impeller revolution. On the time axis, a period of $t\, f_n = 1$ corresponds to an impeller revolution, so the rotating sensor is supplying information on the entire circumference during a revolution and passing at the same angular position every with a period of $t\, f_n$. Figure 7.8b represents the signal over the maximum acquisition time of 45 revolutions, filtered with a Butterworth filter of cutoff frequency $10 f_n$. The pressure signal of each revolution is shown on the horizontal axis with the subsequent revolutions shifted in depth, allowing to recognize the angular motion of the cirucumferential pressure pattern of circumferential wave number $k_s = 4$. It shows that the stall pattern slowly rotates in the same sense as the impeller. This representation of time signals form the rotating system validated the low frequency pressure fluctuations to be obviously related to rotating stall. The revolution rate ω_s is estimated by the slope of a line connecting the pressure maxima,

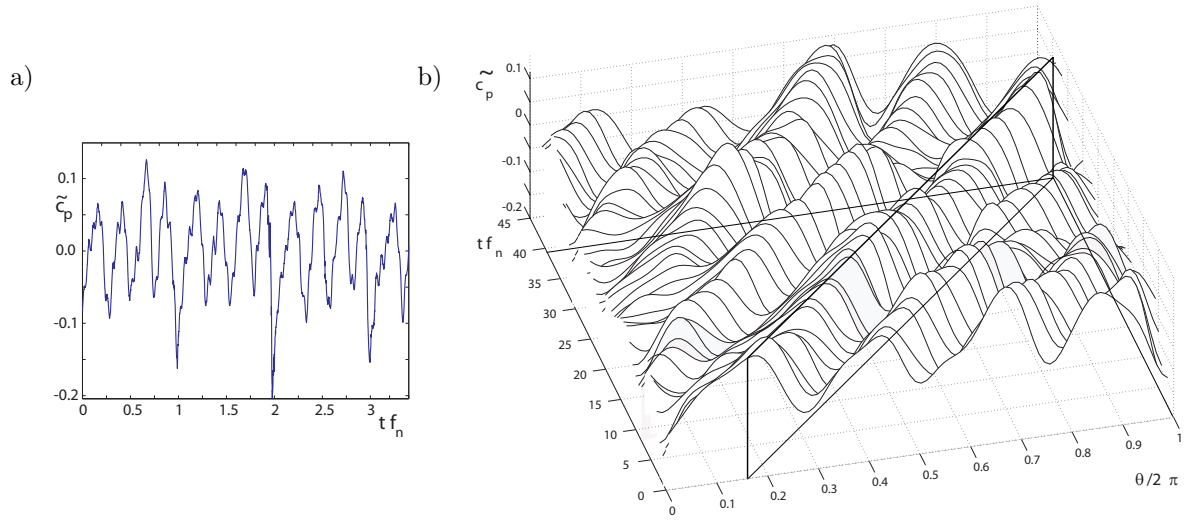

Figure 7.8: Low frequency pressure fluctuation at part load in rotating frame - P21 a) 3.4 revolutions, b) 45 revolutions, low pass filtered and represented revolution per revolution

obtaining:

$$\omega_s \approx \frac{0.84\ \textit{stall revolutions}}{39.00\ \textit{impeller revolutions}}\ \omega = 0.0215\,\omega \tag{7.2}$$

This value corresponds well to the range of values in former rotating stall investigations reported by [133; 148; 126; 125; 77; 99]. Slightly different slopes can be obtained using different datasets. Longer acquisition intervals than the available 45 impeller revolutions were used in the second measurement campaign in order to obtain an accurate measure of the stall rotation rate by 2D DFT of pressure measurement in the stationary frame.

Stationary Frame Pressure Fluctuations

Measurements of the sensors $S59$ to $S78$ close to the rotor-stator interface are represented in figure 7.9 over a time interval corresponding to 200 impeller revolutions for part load operating conditions $\varphi = 0.026$, where the most stable circumferential mode of wave number $k_s = 4$ is identified. The pressure fluctuations due to the passage of the stall cells have a sawtooth-like waveform with a remarkable correlation of waveform from channel to channel. On the other hand, their period and amplitude is not perfectly regular at all times and locations around the circumference. Based on the longer timeseries of the 20 pressure sensor data, the rotating modes are identified by 2D DFT for a large number of operating conditions. Figure 7.10 represents the identified rotating stall modes with their number of cells k_s and their revolution rate ω_s together with the energy-discharge characteristic curve of the pump-turbine model. The 2D DFT results with the rotating stall modes emerging most clearly are represented in figure 7.11. For operating conditions in between the given flow rate values, an intermittent behavior is observed.

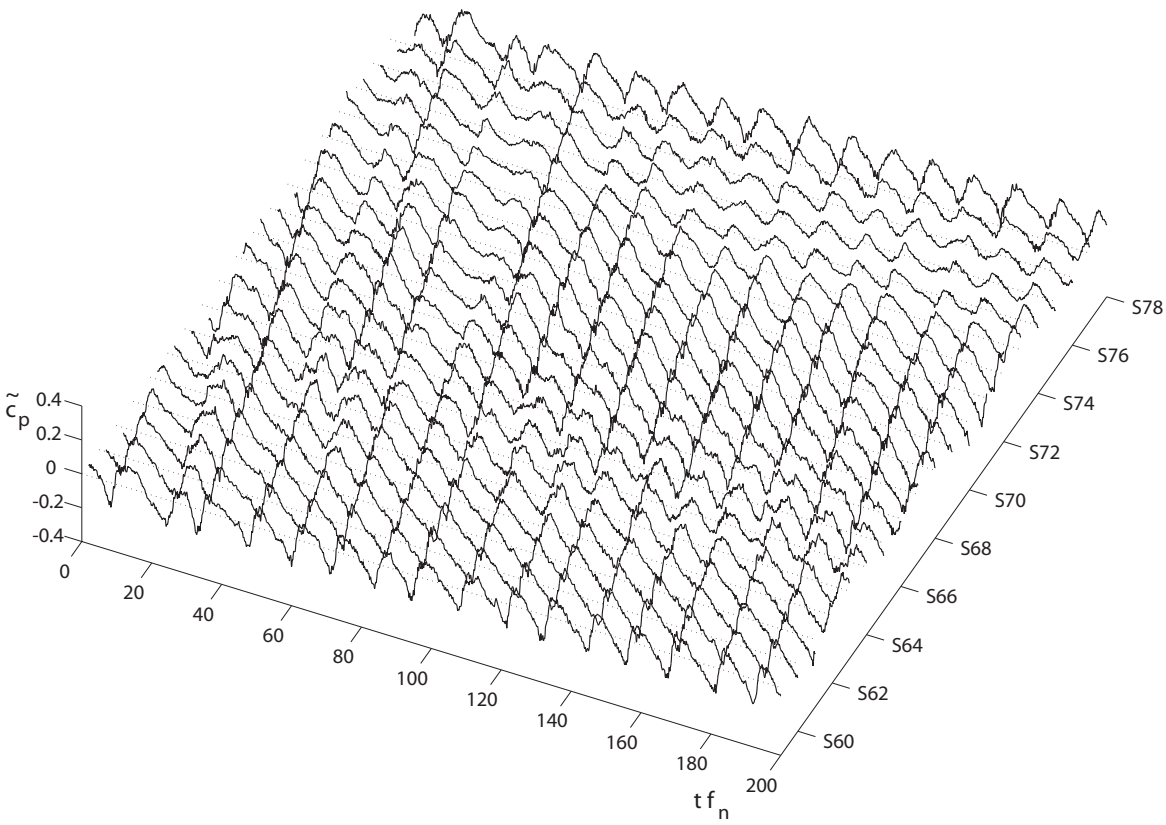

Figure 7.9: Low pass filtered pressure of 20 sensors $S59$ to $S78$ at the rotor-stator interface, section $o2$, over a time interval of 200 impeller revolutions

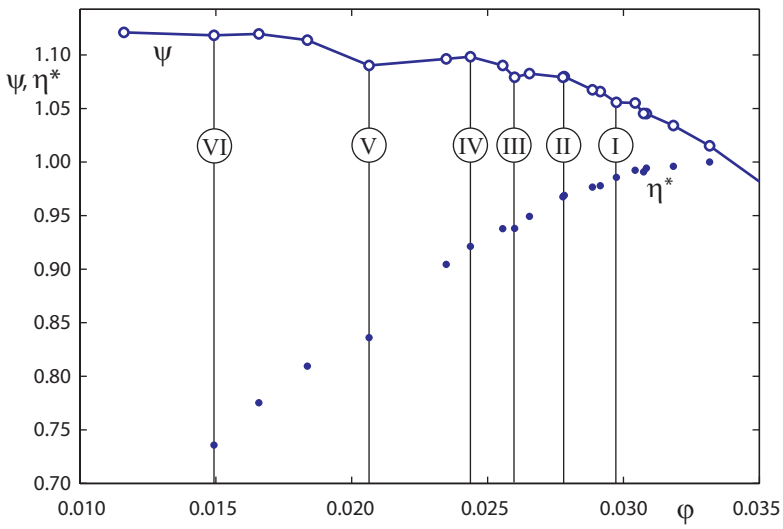

	φ	k_s	ω_s
I	0.030	incipient stall	
II	0.028	3	0.016 ω
III	0.026	4	0.021 ω
IV	0.024	5	0.024 ω
V	0.021	5	0.014 ω
VI	0.015	4	0.028 ω

Figure 7.10: Rotating stall modes and energy coefficient depending on the discharge coefficient

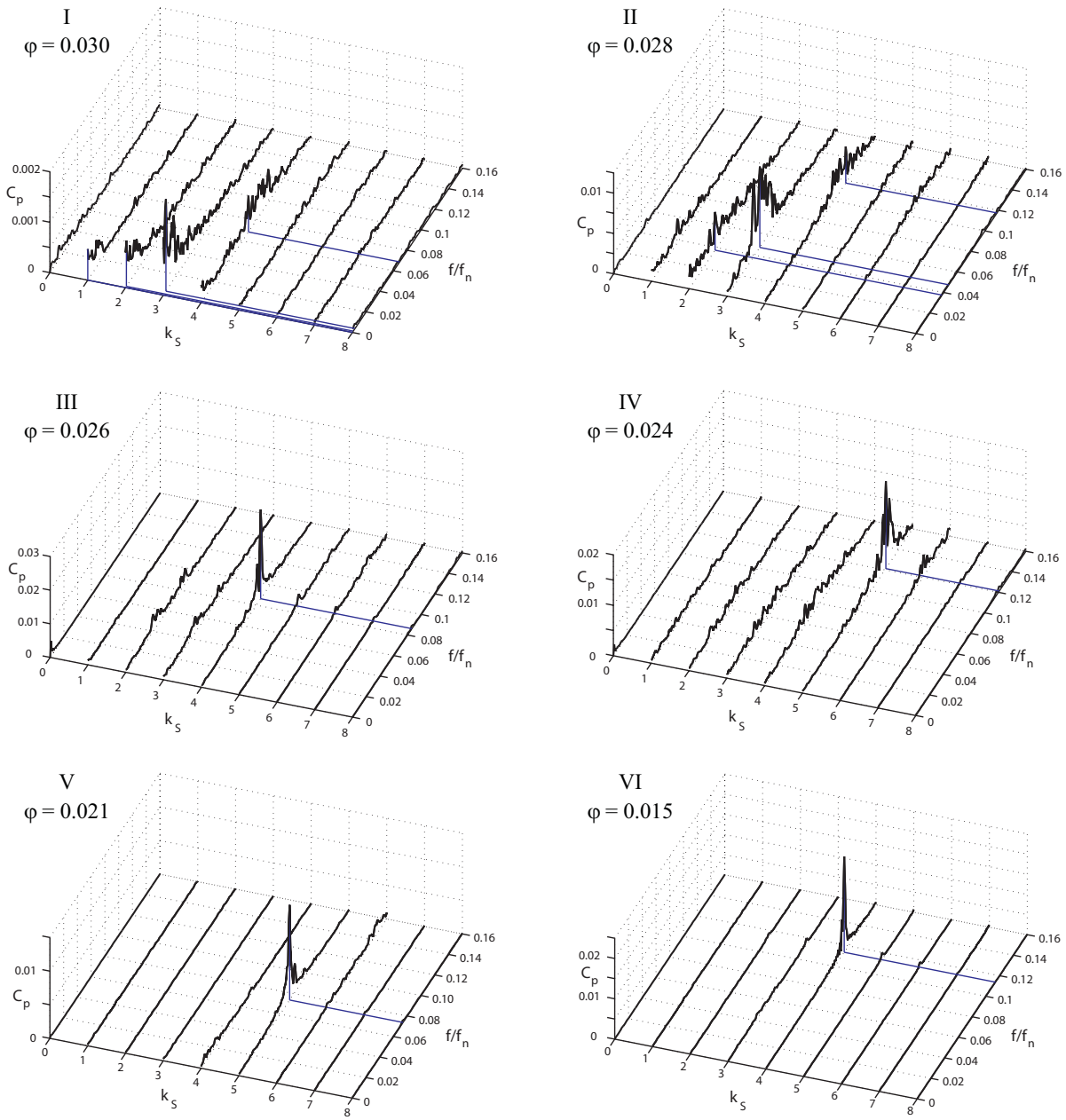

Figure 7.11: Identification of rotating stall modes by 2D DFT

7.3 Local Flow Investigation in the Diffuser

7.3.1 Analysis of Local Pressure Fluctuations

Considerations of the pressure fluctuations of the sensore $S59$ to $S78$ on section $o2$ have provided an overview on the propagation of the stall patterns. Some more sensors placed in two neighboring diffuser channels confirm how the stall cells propagate from one channel to the next.

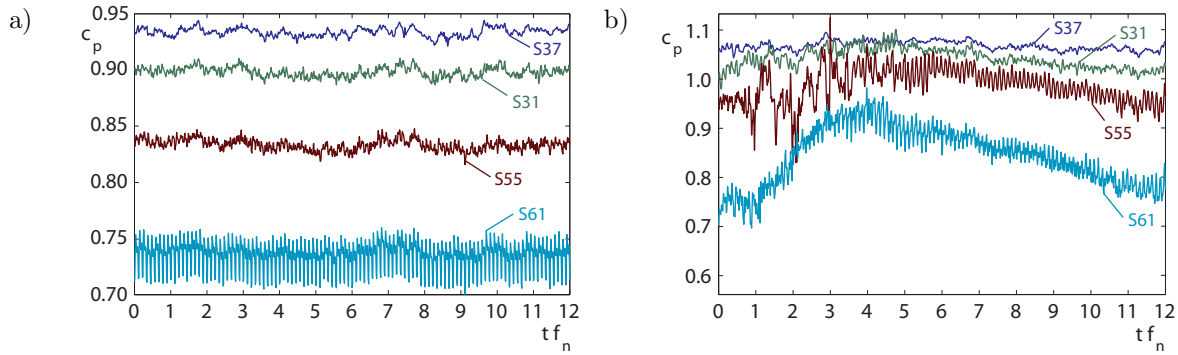

Figure 7.12: Local pressure fluctuation analysis along one diffuser channel. a)at full charge, $\varphi = 0.036$, b)with rotating stall, $\varphi = 0.026$

The detailed view of arbitrary time sequence of pressure measurements along a diffuser channel at full charge ($\varphi = 0.036$) and with rotating stall($\varphi = 0.026$), figure 7.12, shows that the pressure fluctuations encountered at the rotor stator interface can be considered as a lack of pressure recovery due to stalled flow in the diffuser channel. Consequently, the high pressure of the volute zone propagates towards the impeller where the stall cells show up as high pressure. While the flow in the zone between guide vanes and stay vanes seems very regular in the full charge point, with the pressure fluctuations from the rotor-stator interaction nearly decayed, high pressure fluctuations can be observed at the pressure sensor $S55$ during the period of increasing pressure along the channel. During the phase of high pressure, the pressure recovery in the stay vanes is very small, indicating separated or stagnation flow in the channel. The pressure time evolution at sensor $S61$, closest to the impeller, shows more regular repetitions from stall cell to stall cell than at sensor $S55$ close to the guide vane channel throat.

Figure 7.13 represents the pressure fluctuations at sensor locations in two neighboring guide vane passages. The phase of increasing pressure is first detectable by pronounced fluctuation with extreme minima at the points $S62$ and $S61$, located on section $o2$, close to the leading edge of the guide vanes. The plausible explanation is that vortices form at the leading edge and their cores are advected by the separated flow over the pressure sensor. The pressure level in the guide vane passage increases during about 3 impeller revolutions. At the end of this increasing phase, the pressure at section $o3$ in the same channel shows strong fluctuations, they have frequencies and amplitudes similar to the one observed in section $o2$ at the beginning of the phase of increasing pressure. The global level of pressure in section $o3$ follows the increase of pressure only to a small extent. This lack of pressure recovery indicates that the flow is not decelerated as expected. The

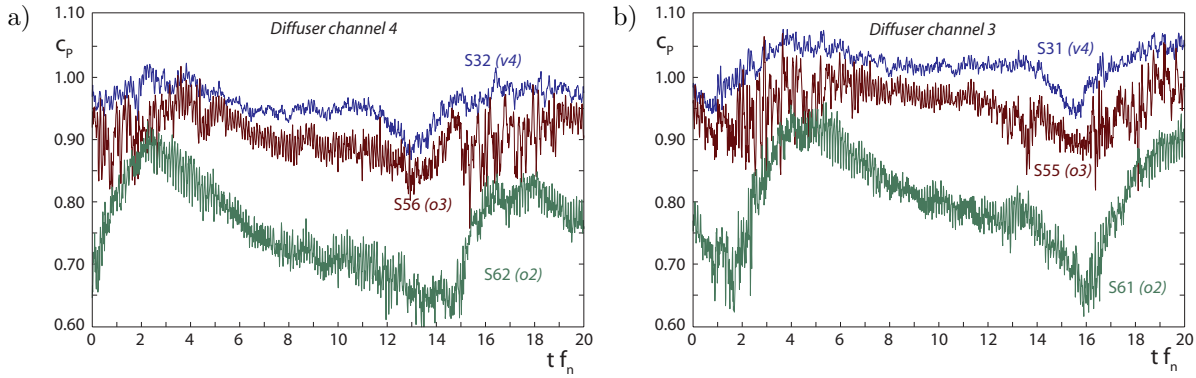

Figure 7.13: Pressure evolution in guide and stay vane channel. a) Channel 4 ($S61$, $S55$, $S31$), b) Channel 3 ($S62$, $S56$, $S32$)

pressure difference of the points in section $o2$ and $o3$ normalizes only after another few impeller revolutions.

As soon as a certain pressure level is reached, the same sequence occurs at the neighboring channel. It takes 2 - 2.3 impeller revolutions for the perturbation pattern to complete the passage from one diffuser channel to another, leading to 40-46 impeller revolutions to complete one revolution of the stall pattern.

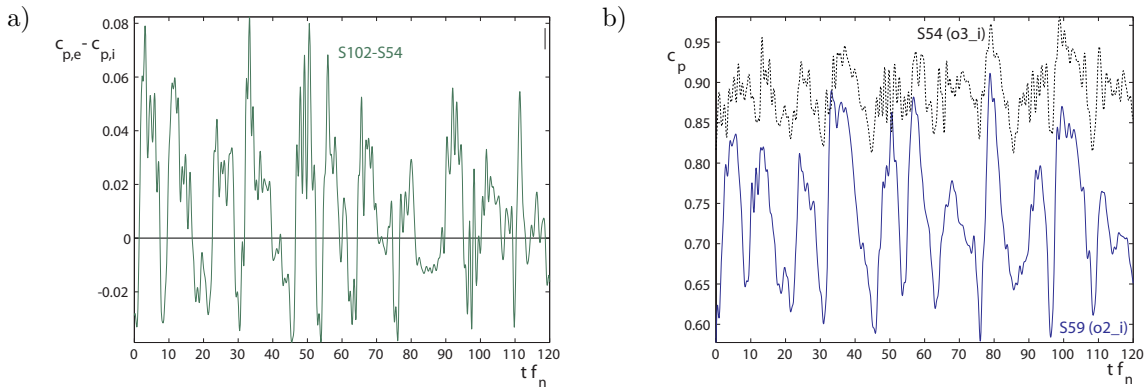

Figure 7.14: Low-pass filtered pressure fluctuations in guide vane channel 1. a) Difference (i)-(e) in section 3 b) Pressure coefficient at section 2 and 3,(i)

Figure 7.14a shows the pressure difference between hub and shroud side, sensors $S54$ and $S102$ with rotating stall, $\varphi = 0.026$ in the first guide vane channel, compared to the overall fluctuations at section 2 and 3, sensors $S59$ and $S54$, in the same channel (b). It appears that the pressure difference between hub and shroud at section 3 is correlated with the stall phase. The peak-to-peak amplitude of the pressure difference represents 10% of the static pressure at the impeller outlet. This indicates that the flow patterns occurring at stall are nonuniform in span-wise direction.

7.3.2 Laser Doppler Velocity Measurements

Figure 7.15 represents the location of the LDV measurement grids and the nomenclature of chosen example points discussed in the remainder of the section:

- A grid in the **guide vane throat section $\mathbf{A_2^*}$**: The LDV probe is oriented in a way that the high acquisition rate (green) LDV component renders C_n the velocity component normal to the section whereas the low data rate (blue) component captures the secondary flow component C_s. The grid is generated on a slightly curved surface to avoid reflection of the laser beams by the pressure sensor $S55$.

- A grid at **0.5 mm normal distance around guide vane** 4 is used to determine the tangential velocity component along the guide vane with the green beam pair. No second component can be measured as close to the wall, since the blue beams intersect with the guide vane.

- Grids on a **cylindrical surface close to the impeller outlet** ($R = 277\,mm$) to determine the impeller outlet profiles. In all investigated operating conditions, C_u is measured using the green component and C_r using the blue component, some validation measurements with a probe orientation shifted by 90° have been accomplished at part load, $\varphi = 0.031$.

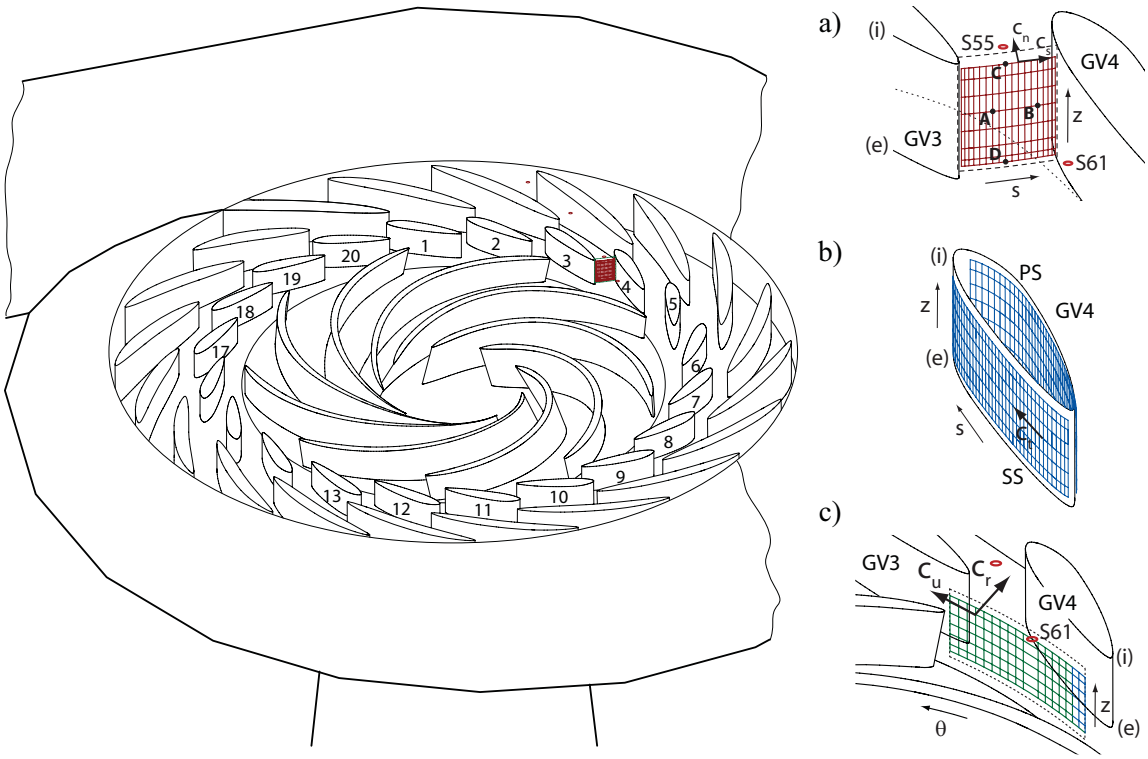

Figure 7.15: Location of the LDV measurement grids and sample points A, B, C, D; orientation of velocity components. a) Guide vane throat grid, b) Grid around guide vane 4, c) Grid at impeller outlet

Phase Averages of Single Point LDV Measurements

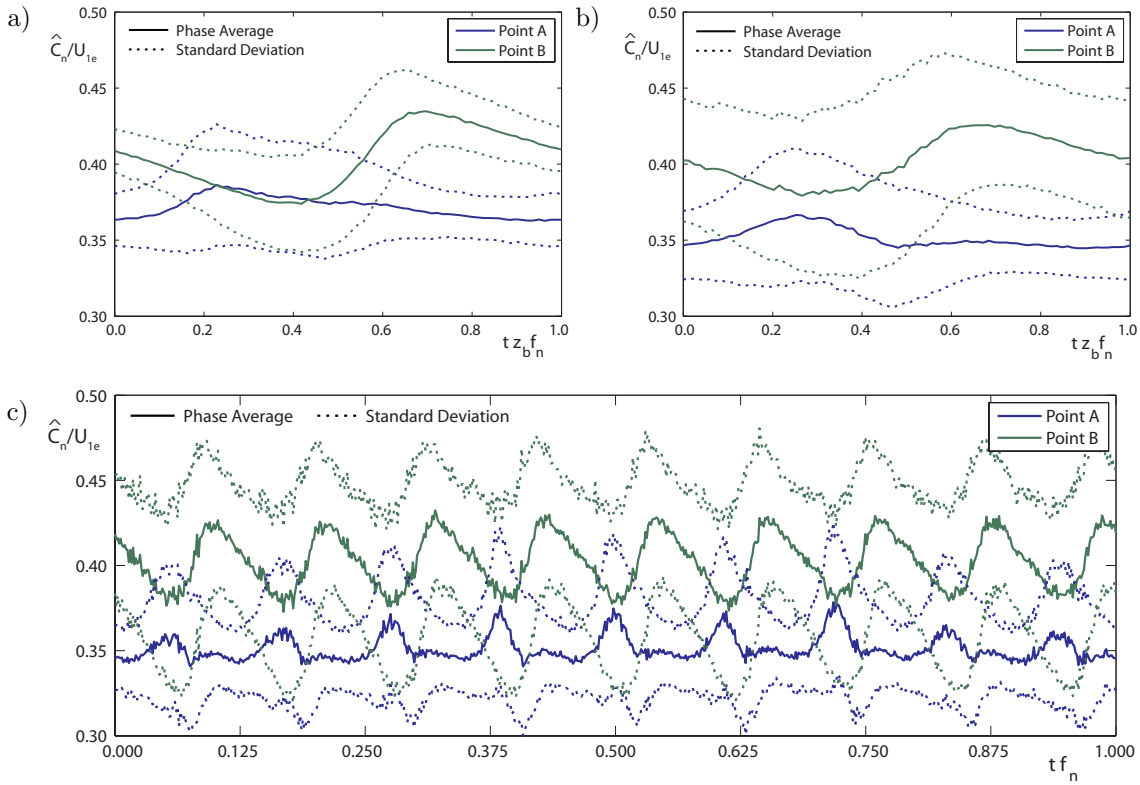

Figure 7.16: Impeller revolution and blade passage phase averages of LDV measurements in the guide vane throat section, points A and B. a) Blade passage phase average for BEP $\varphi = 0.034$, b) Blade passage phase average for part load $\varphi = 0.031$, c) Impeller revolution phase average for part load $\varphi = 0.031$

Figure 7.16 represents the phase averaged normal velocity and its standard deviations based on blade passage and on impeller revolution for points A and B, showing that there are only small differences detectable between the passages of the different blades, comparing well with the phase averaged pressure fluctuations in the guide vane throat section, figure 7.4b. This evidences that the rotor-stator interaction governed by the blade passage is the main source of time-dependency for flow rate coefficients greater than $\varphi = 0.030$. The deterministic fluctuation amplitudes are in the order of 10% of the mean velocity and not in phase on different points of the guide vane throat section. This is expected from the influence of the nonuniform velocity profile from the impeller impacting on different points of the throat at different times.

Figure 7.17 represents the velocity for two selected points C, close to hub (i), and D, close to shroud (e), in operating conditions with rotating stall. The phase average with respect to blade passage is compared to the phase average with respect to the stall phase, identified from the pressure signal at sensor $S61$. Under these conditions, the influence of the blade passage is not detectable by the phase averages as the flow is governed by the stall phenomenon. This shows in an increased standard deviation value for point C located close to the interior diffuser side wall. The phase average with respect to the

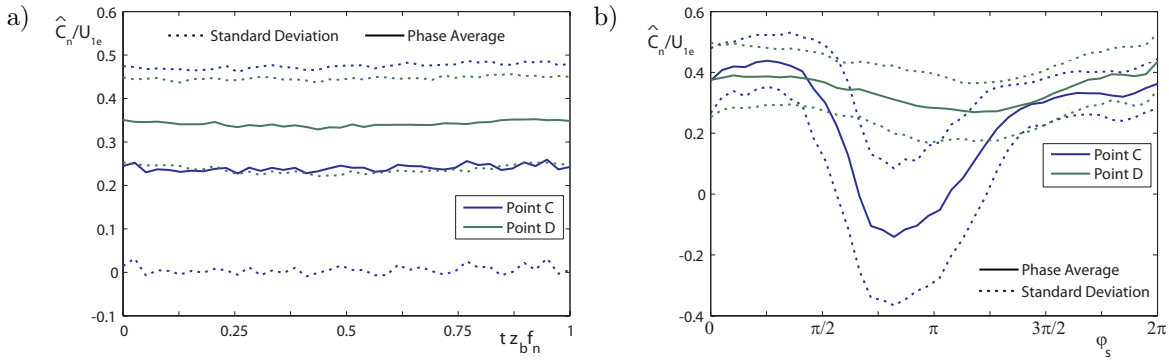

Figure 7.17: Phase averaged velocity and standard deviation at points C and D with rotating stall at $\varphi = 0.026$. a) Blade passage phase average, b) Stall phase average

analytic phase of the pressure signal at sensor $S61$ confirms that the normal velocity on both points depends more on the pressure related to rotating stall than on the impeller blade passage. At point C, the normal velocity stall phase average reaches negative values, indicating zones of flow separation and recirculating flow. The comparison of the single point velocity phase averages at flow rates above stall inception, figure 7.16 and at conditions showing rotating stall, figure 7.17 show clearly that the influence of the rotor stator interaction on the guide vane throat velocity vanishes under stall conditions.

Velocity Profiles in the Guide Vane Throat Section

Figure 7.18a represents the time averaged normal velocity C_n on the guide vane throat at BEP. A region of low average normal velocity is identified on the shroud side wall (e) close to the guide vane suction side (SS). The reflections of the glass-water interface made it impossible to obtain sufficient flow observation closer to the wall, so it is not clear if there is flow recirculation due to a small separation zone at this place or not. Figure 7.18a shows the peak-to-peak amplitudes of the phase averages velocity fluctuations on the guide vane throat section. The maximum fluctuation of $0.08\,u_{1e}$ corresponds to 25% of the average normal velocity. The phase averaged fluctuations are the highest in zones with high average normal velocity. Figure 7.16c shows exemplary time plots of the phase averaged normal velocity at two arbitrary points A and B located in the center plane of the diffuser, A being characterized by a low, B by a high fluctuation level. The standard deviation intervals are represented as dotted lines. Figures 7.18c and d represent the same for a part-load operating point, $\varphi = 0.031$. The mean values do not show the pronounced minimum at the exterior side wall but a trend to lower velocities close to the interior side. The location and the magnitude of phase averaged fluctuations is globally similar to BEP, but the lower normal velocity close to guide vane 4 is more pronounced.

The normal velocity profiles obtained by phase averaging using the analytic phase derived from the pressure at sensor $S61$, see chapter 4.3, are represented in figure 7.19 along the different phase angles. A zone of negative normal velocity indicates the presence of reversed flow at the interior diffuser side wall. At the same time the normal velocity in the rest of the considered section decreases too. This indicates a lower flow rate through this diffuser channel, casting into doubt any steady simulation approach using a

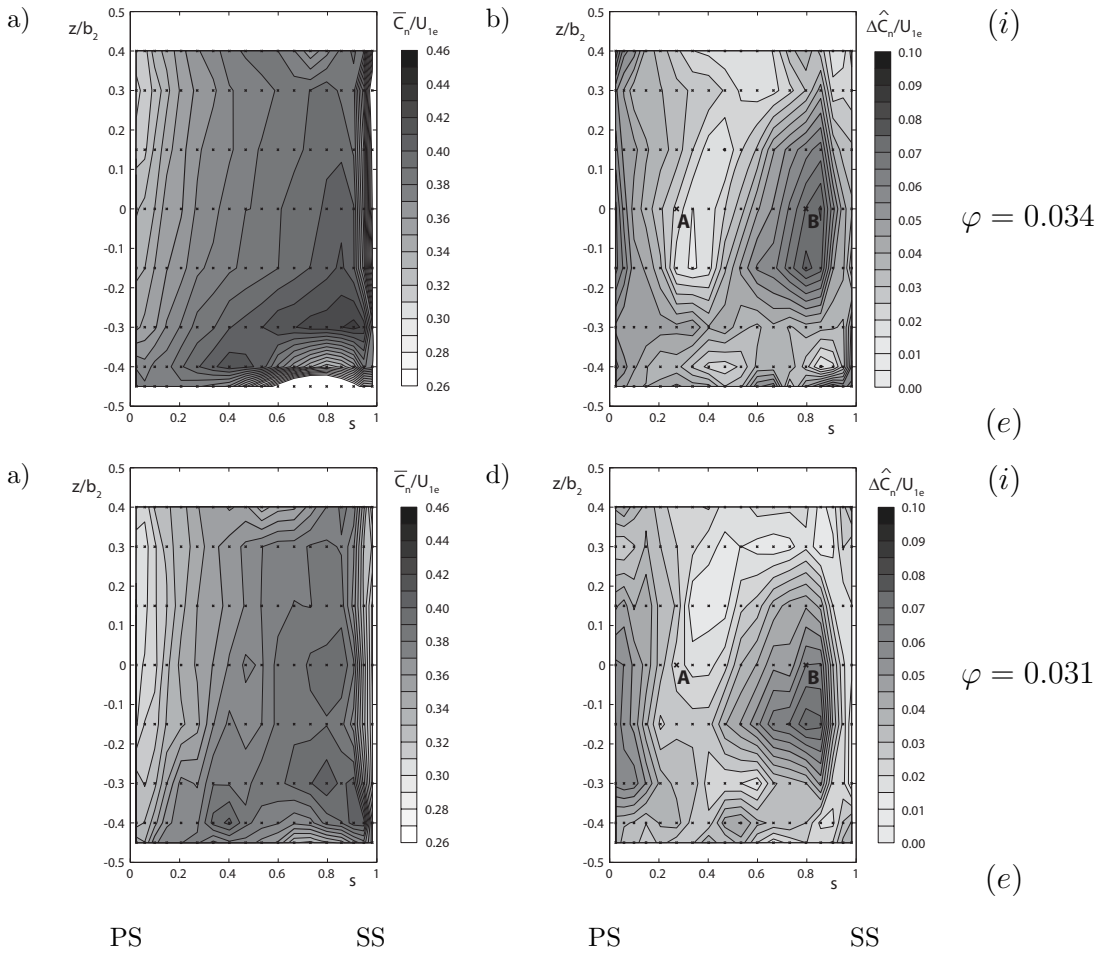

Figure 7.18: Blade-passage-phase averaged velocity component C_n meassured by LDV in the guide vane throat section. Top: BEP, $\varphi = 0.034$. a) Mean normal velocity, b) Peak-to-peak value of phase average, Bottom: Part load $\varphi = 0.031$, c) Mean normal velocity, d) Peak-to-peak value of phase average

single diffuser channel for such operating conditions. The flow obviously deviates towards other channels. The intense flow reversal takes place between $3\pi/4$ and $5\pi/4$. The circumferential wave number of the rotating stall equals $k_s = 4$ at this operating point, implying that one "wave" extends over $z_o/k_s = 5$ channels. The intense reverse flow lasting for a quarter of the phase means that at any one time only one of five diffuser channels shows intense reverse flow.

Integration of Flow Rate at the Guide Vane Throat Area

Evidently, the velocity fluctuations on different locations of the guide vane throat area are not in phase, see figure 7.16. A direct estimation of instantaneous flow rate or fluctuation level from single measurement points as can be done for pipe flows [44] is not practicable under these conditions. A phase averaged bulk flow rate obtained from the integration of all phase averaged velocity values is represented in figure 7.20, showing an estimate for the phase averaged flow rate fluctuation of about 1%, which is considerably lower than

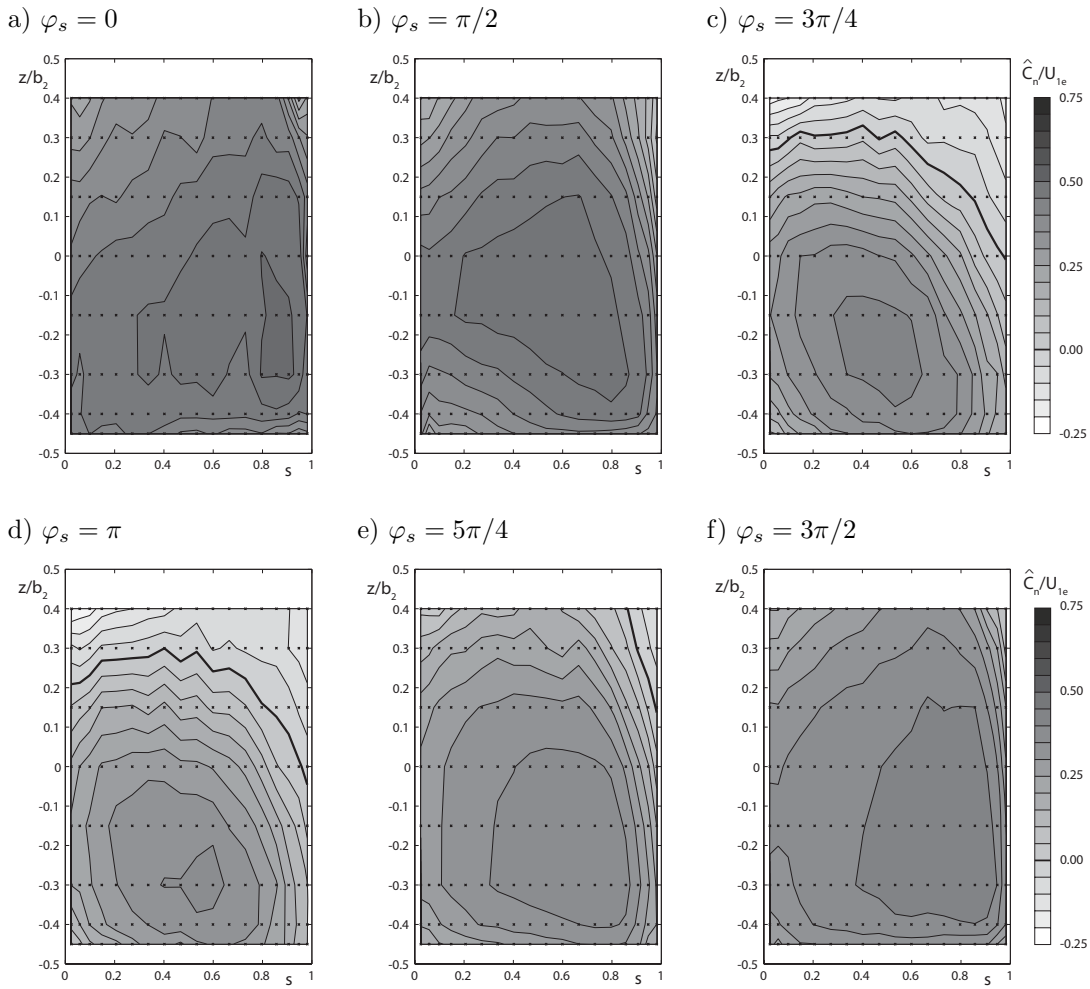

Figure 7.19: Stall phase averages of normal velocity in the guide vane throat section measured by LDV at $\varphi = 0.026$. a-f) Velocity contour plots along different phase angles from 0 to $3\pi/2$

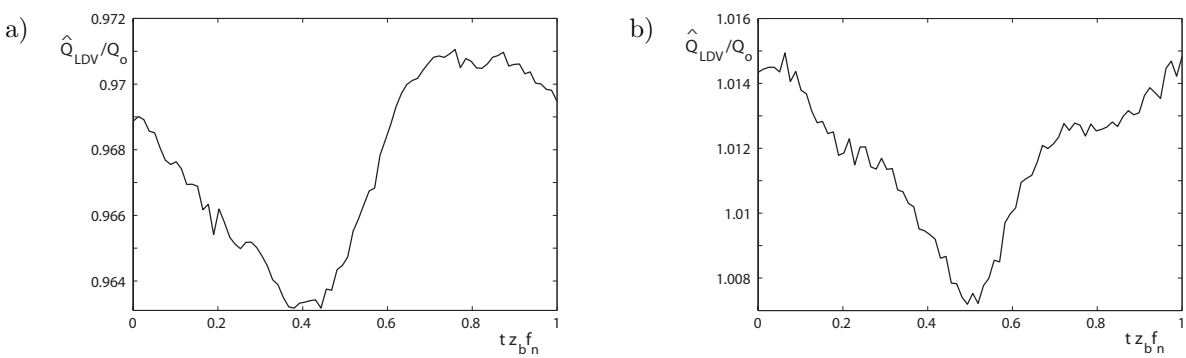

Figure 7.20: Integrated phase averaged channel flow rate. a)$\varphi = 0.034$, b)$\varphi = 0.031$

the local velocity fluctuations. Velocity values have been extrapolated to the walls using the nearest measurement to the wall available to compute the flow rate through the entire section.

As this procedure neglects the decreasing velocities towards the wall in the boundary layer, one expects the integrated flow-rate to over-estimate the average diffuser channel flow rate $Q_o = Q/z_o$. Nevertheless, the integrated values are lower than the theoretical average flow rate through each diffuser channel by 3% for $\varphi = 0.034$ whereas they are by 1% higher for $\varphi = 0.031$. The obtained values are after all reasonably close to one, which confirms the quantitative error of measurements, phase averaging and integration procedure to be within ±5%.

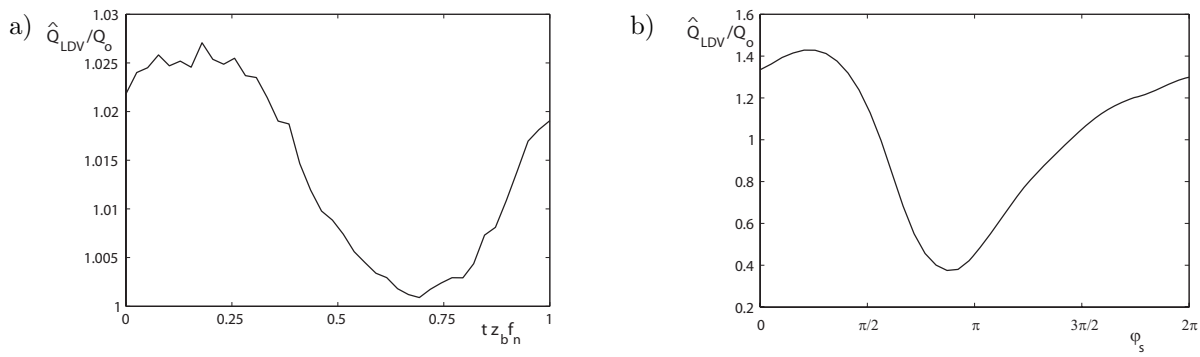

Figure 7.21: Integrated phase averaged channel flow rate with rotating stall $\varphi = 0.026$. a)Blade passage phase average, b)Stall phase average from sensor $S61$

The flow rate obtained from blade passage and stall phase averaged velocities for conditions with rotating stall at $\varphi = 0.026$ is represented in figure 7.21. As for the raw velocity, the influence of the blade passage phase becomes close to negligible in comparison with the impact of rotating stall, with over an order of magnitude of difference between both fluctuation amplitudes. Under these conditions the blade passage phase average has to be considered with care when compared to numerical simulations where the instantaneous flow rates are available without the doubts introduced by the reconstruction from single point measurements. The stall phase averaged integrated flow rate shows a rapid decrease of flow rate starting at $\pi/2$. Recalling the shape of the analytic phase as a function of time, figure 4.5, and the pressure signal, 7.13, the decrease of flow rate is even more abrupt in time than the averaging over the analytic phase suggests.

Guide Vane Wall Tangential Velocity

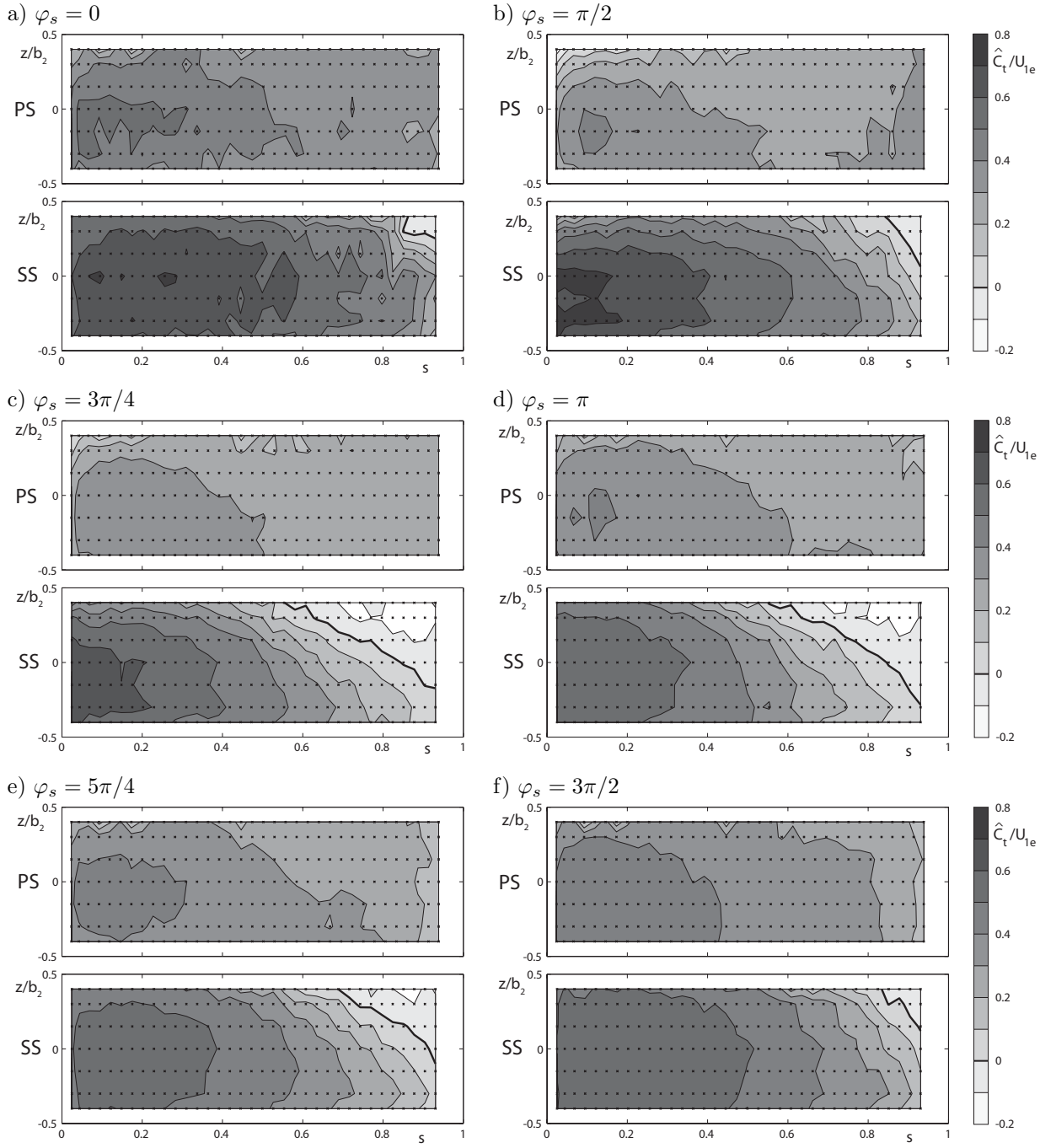

Figure 7.22: Stall phase averaged tangential velocity at $0.5mm$ normal distance from guide vane 4, measured by LDV at $\varphi = 0.026$

According to the stall phase averaged normal velocity in the guide vane throat section, a zone of reverse flow extends on the guide vane surface during the passage of a stall cell. A small zone of reverse flow always remains attached close to the trailing edge on the suction side. Attributable to the reversible operation of the machine, the guide vane

edge that is trailing edge in pump mode is particularly thick when compared to typical hydrofoil or pump diffuser blade trailing edges, sustaining the extended flow separation zone at trailing edge. The extent of the zone of reverse flow does only cover the last third of the chord and at a maximum the upper half of the channel. This supports the hypothesis that the root cause of flow separation is not the incidence error but rather the excessive diffusion towards the throat section and further downstream. The consequence of bad incidence would show at the leading edge of the guide vane profile.

Impeller Outlet Velocity Profiles

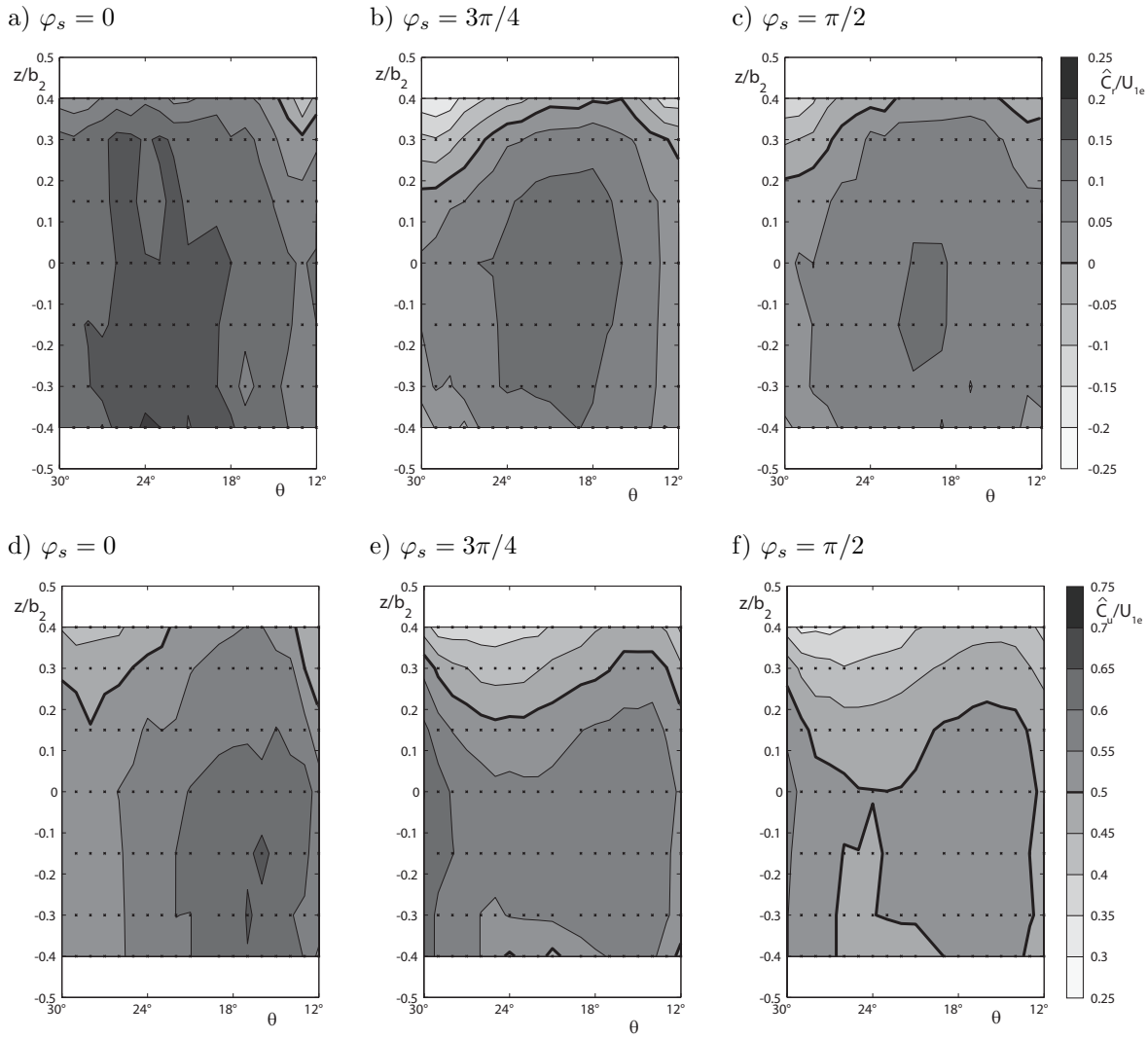

Figure 7.23: Stall phase averaged velocity on cylindrical section at impeller outlet at $\varphi = 0.026$. Top: a, b, c) Radial velocity, Bottom: d, e, f) Circumferential velocity

The velocity profiles at impeller outlet, represented in figure 7.23 are a key parameter for design of centrifugal pumps and for the validation of numerical simulations. Via Euler's turbomachinery equation they are directly related to the amount of energy transferred

from the impeller to the working fluid. On the other hand, the velocity profiles upstream of the diffuser have a major influence on flow separation in the diffuser. Several experimental studies and numerical-experimental comparisons done in the past essentially focus on this area [53] when dealing with local flow features.

The measurement grid is placed as close as possible to the impeller, but the influence of the guide vanes through there upstream pressure potential is clearly visible. Under conditions with rotating stall, the negative radial velocities at the internal diffuser side wall extend back very close to the impeller outlet. Since we found that the presence of stall concerns only one diffuser channel at a time, this can be qualified as a local flow deflection upstream of the separation zone in the guide vane throat. The circumferential component decreases in that zone too but does not reverse sign as does the normal velocity component in the guide vane throat section.

Flow Rate and Angular Momentum at Impeller Outlet

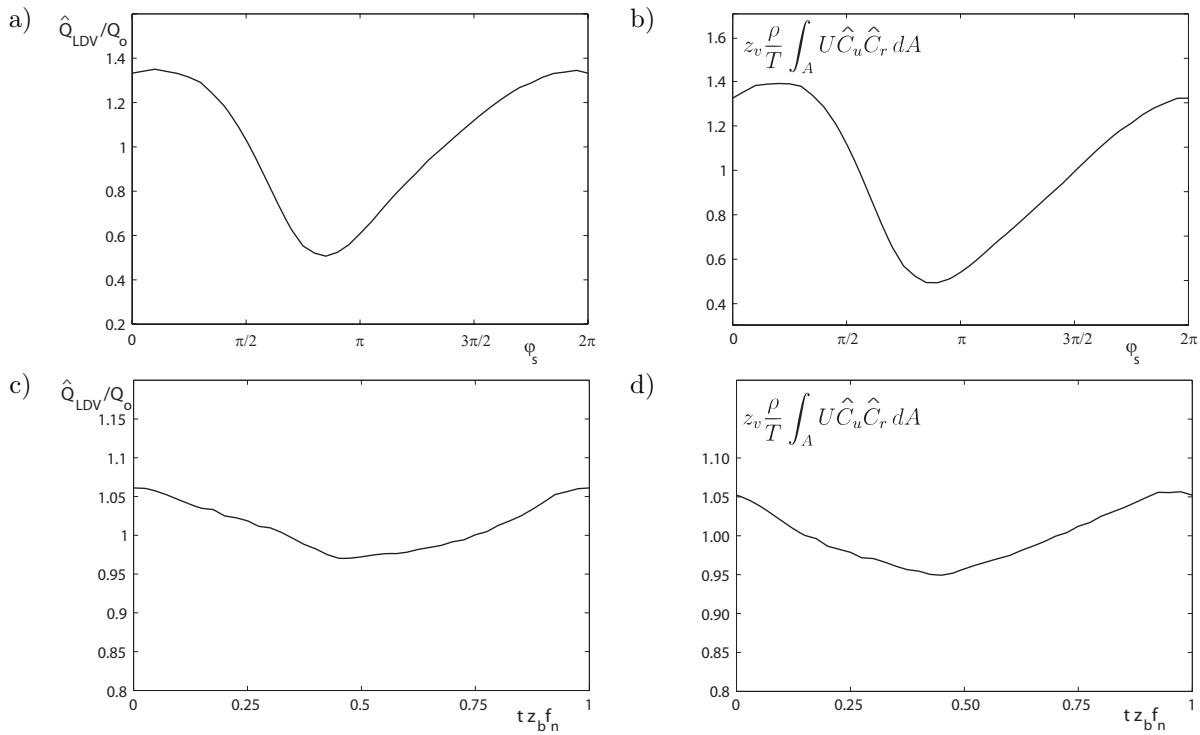

Figure 7.24: Flow rate and angular momentum flux integrated over the impeller outlet section, $\varphi = 0.026$. Top: Stall phase average, a) Flow rate, b) Angular momentum flux, Bottom: Blade passage phase average, c) Flow Rate, d) Angular momentum flux

The integration of flow rate and phase averaged flux of angular momentum through the cylindrical section represented in figure 7.24 show that they are in phase, close to perfectly scalable. The influence of the impeller blade passage on section flow rate fluctuations is more pronounced than at the guide vane throat section, but small compared to the fluctuations induced by the rotating stall.

7.4 Flow Pattern Summary

The thin zones of flow reversal appearing and disappearing on the guide vane suction side and on the interior diffuser side wall agree well with thin flow reversal zones identified by Lee and Gerontakos [83] during onset of stall on oscillating airfoil represented in figure 7.25.

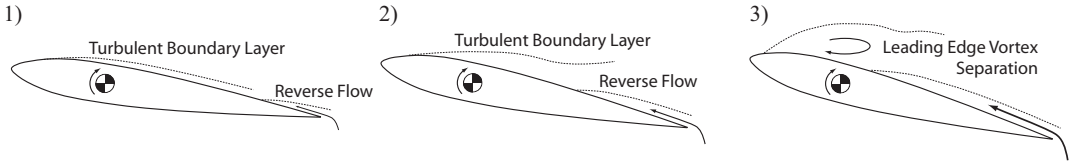

Figure 7.25: Reverse flow patterns on an oscillating airfoil [83]

Their analysis based on smoke pattern visualizations and hot film sensor arrays show these flow reversal zones expanding from the trailing edge towards the leading edge just before complete stall characterized by separation of the leading edge vortex. In the case of the guide vanes, the backward progression of the reverse flow is not initiated by a pitching movement, but the time-dependent pressure conditions around the guide vane are quite similar to the pitching airfoil conditions. When the neighboring channel (between GV 3 and 4) is stalled, the pressure in that channel rises close to the level of the spiral casing, while the flow on the suction side of the guide vane is accelerated, leading to decreasing pressure. This creates a suction effect, similar to a nozzle pump, driving fluid from the pressure to the suction side of the guide vane, across the gap between guide vanes and stay vanes. This situation is similar to the conditions when a pitching airfoil approaches its maximum incidence angle, the pressure difference between pressure side and suction side rises until it reaches a point where the flow reverts.

In the investigation of periodic phenomena occurring with forced oscillation of air- or hydrofoils, the reduced frequency κ is an essential nondimensional parameter expressing the ratio of the convective timescale to the period of oscillation:

$$\kappa = \frac{\pi f l_c}{C_\infty} \tag{7.3}$$

The sequence of flow patterns of stall onset represented in Figure 7.25 were observed at relatively low reduced frequency of $\kappa = 0.1$. The authors have evaluated the influence of reduced frequency and concluded that the phenomenon of reverse flow persists at constant critical pitch angle for $\kappa < 0.2$. At higher reduced frequencies, the influence of inertia of flow increases: The separation of the leading edge vortex is delayed to higher pitch angles. Evaluating the reduced frequency of a single guide vane based on the stall frequency at $\varphi = 0.026$, a throat bulk velocity of $0.4u_{1e}$ and a chord length of $l_o = 0.0955m$ yields a value of $\kappa_s = 0.005$, 20 times lower than the airfoil experiment. So, a single air- or hydrofoil oscillating at relatively low reduced frequencies and reaching stall periodically is a suitable study case to assess the accuracy of numerical simulation relevant to the stall phenomenon in turbomachines. The studies of Bourdet [18; 19] show large differences of different RANS-turbulence models in such study cases. Nevertheless, the progression of a stall cell from one channel to the next, represented in figure 7.26 shows other plausible

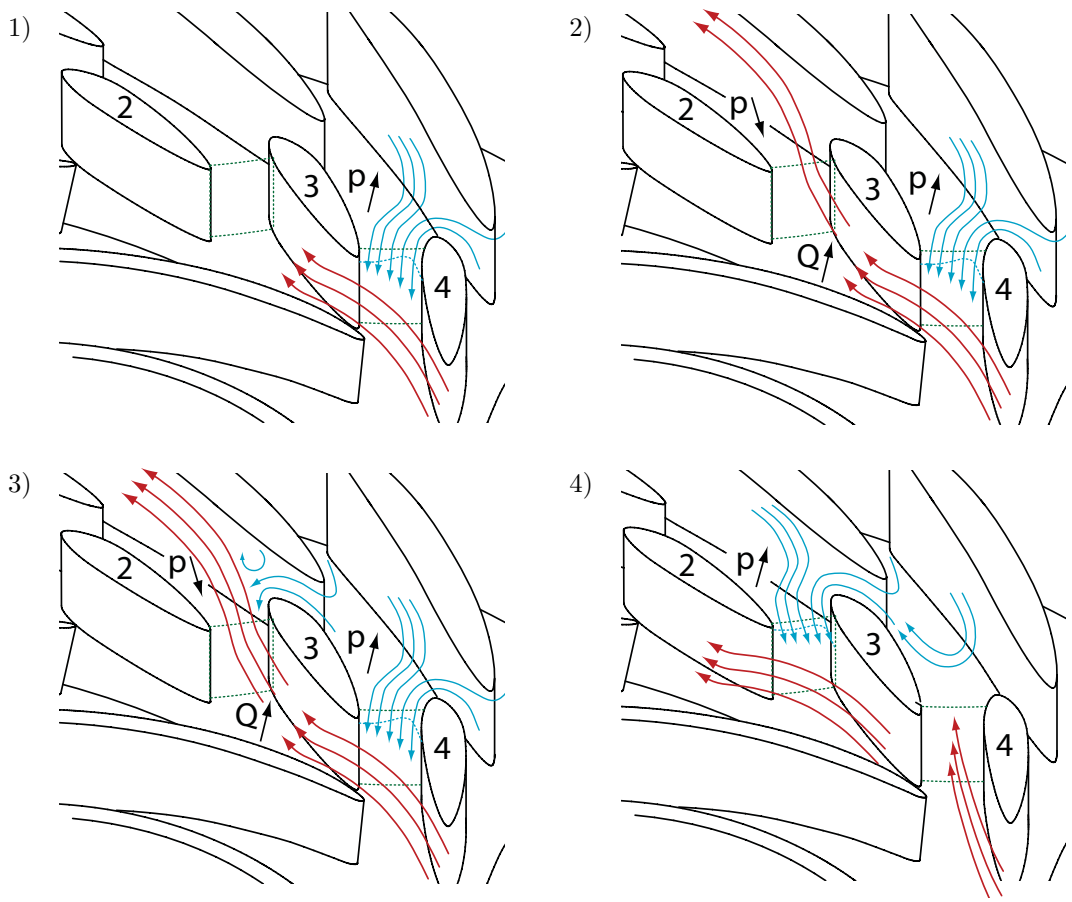

Figure 7.26: Schematic evolution of flow patterns

mecanisms determining the time constants that determine the stall angular precession rate. Phase (1) shows separated flow in the channel between GV 3 and GV4, which induces stagnating flow in the according stay vane channels. As a consequence, the pressure in the area between GV 3 and 4 and the corresponding stay vanes rises, phase (2) to finally reach the spiral casing pressure. At the same time, the flow from the impeller circumvents the stalled GV channel, leading to higher flow velocities, and thus lower pressure in the neighboring GV channel. This pressure rise leads to a secondary flow from this area to the neighboring channel, showing low pressure due to the high flow velocity induced by the increased relative GV channel flow rates. At phase (3) This flow around the trailing edge of the GV triggers flow separation on GV 3, finalising the progression of the stall cell to this GV channel, phase (4).

The temporal evolution of the flow deceleration in the stay vane channels and the resulting pressure rise is not only due to the dynamics of flow separation as encountered with the single stalling hydrofoil, but also influenced by inertia effects, the length of the channels being the main parameter influencing the time constants that finally determine the rotation rate of the stall cells. Together with the smaller radial gaps in the RSI region, this differentiates the studied pump turbine scale model from industrial centrifugal pumps, showing smaller radial gaps and a single bladed diffuser component instead of the combination of stay vanes and guide vanes.

Visual observations together with audible noise confirm the onset of cavitation vortex cores shed periodically in the guide vane channels as depicted in figure 7.27. It appears that the pressure in the vortex core reaches the vaporization pressure, despite the fact that it is located at the high pressure side of the impeller. Similar cavitating vortex cores have been reported from flow visualization in industrial centrifugal pumps, where they were observed to extent back into the impeller. This supports the hypothesis that the flow separation might have its origin in a disequibrium of the impeller flow, leading to the flow separation on the impeller hub (i) with cavitating vortex cores attached to the impeller blades.

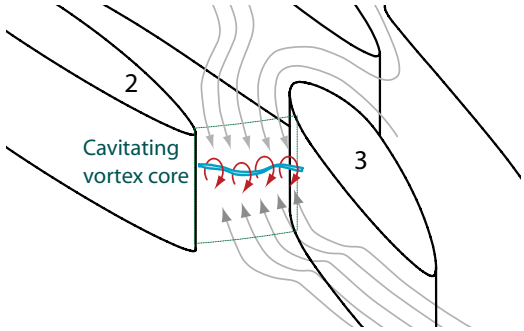

Figure 7.27: Cavitating vortex core in the shear layer between reverse flow and sound throughflow

Chapter 8

Rotating Stall Time Dependent Simulations

8.1 Numerical Setup

8.1.1 Computing Domain and Space Discretization

The simulation domain for the time-dependent numerical simulations of the part-load flow of the considered pump-turbine includes the straight conical inlet section, the impeller with its 9 blade passages, the diffuser made of 20 guide vane and stay vane passages and the spiral casing. Given the rotating stall phenomenon observed experimentally, steady approaches or the restriction of the model to an angular segment using periodicity were not considered. The model includes the main flow passages and wetted surfaces, the labyrinths, side room and according leakage flows are not taken into account. With the conclusions drawn from the steady numerical simulations and the requirement of simulating a large number of impeller revolutions to detect phenomena such as rotating and alternate stall, the use of a mesh satisfying strict criteria of mesh independence of the solution is not feasible, as a large number of operating conditions are to be evaluated with the available computational resources. Table 8.1 summarizes the number of nodes along the main dimensions: Interior to exterior section (i-e), blade to blade (b-b) and streamwise along the blade (stream). The resulting mesh sizes and y^+ value ranges on the wall boundaries determined by the first element size normal to the boundary are listed. The element size expansion ratio that controls the growth of the node spacing from the solid surfaces is set to 1.3. Figure 8.1 represents an overview of the mesh that is block structured and almost hexahedral (more than 98% of the elements), making use of some prismatic elements in so-called swept blocks, used where a more regular discretization can be achieved using such elements.

The particular features of the time-dependent flow in part load, governed by the onset of flow separation in the diffuser, either as a regular stationary or rotating pattern, makes mesh convergence studies based on global performance numbers at a given flow rate condition meaningless for another flow rate since the flow patterns are subject to drastic changes. From the experimental investigations, reverse flow zones in the diffuser are expected, leading to high velocity gradients in the center of the channels, far from the wall boundaries. Cavitating vortex cores have been observed in the shear layer between reverse flow and sound through flow, despite the generally high surrounding pressure level.

	n_{i-e}	n_{b-b}	n_{stream}	Nodes per Channel	Nodes Total	y^+
Cone				14′000	126’000	120-180
Impeller	28	36	110	184′000	1’656’000	30-90
Guide, Stay Vane	25	35	35, 60	110′000	2’200’000	60-100
Spiral Casing				–	490’000	150-200
Total				–	4’472’000	-

Table 8.1: Main mesh dimensions, node numbers and achieved boundary layer resolution

A further concentration of nodes towards the blade and side wall boundaries to improve the prediction of boundary layer flow would necessarily impair the ability of the numerical model to represent such strong gradients in the remainder of the domain.

8.1.2 Time Discretization and Convergence

Treutz has investigated the influence of the simulation time step width for time-dependent simulation of the flow in a volute pump [144] using a numerical method similar to the one used in this study. He concludes that a time step corresponding to 120 timesteps per revolution is sufficient to obtain a satisfactory prediction of fluctuating global integrated quantities. Zobeiri investigated pressure fluctuations due to rotor-stator-interactions in Francis turbines [163] using 720 time steps per impeller revolution. In more detailed comparisons [162], the difference versus simulations using 360 time steps per revolution is shown to be negligible. For the simulation of part-load flow in pumping mode the choice of the time step is a matter of compromise: On one hand, an accurate time discretization is desirable, on the other hand, the time intervals that need to be simulated are of the order of 10 impeller revolutions and more. Clark [28] has established a methodology to qualify convergence of time-periodic simulations, separating the deterministic time periodic components from higher frequency phenomena (vortex shedding) superposed onto this periodic solution. He proposes to compare discrete Fourier transform components and to evaluate cross-correlation measures of successive periods. In case of massive flow separation in diffuser channels, the flow is heavily affected by low frequency phenomena that are not periodic with respect to the impeller revolution. Statistical analysis can momentarily not be applied to the simulation results in this frequency range since the available simulation time interval’s length is insufficient.

For the assessment of the time step size, a numerical simulation at low flow rate ($\varphi = 0.028$), where massive flow separation in the diffuser occurs, is conducted from the same initial state (after 21 impeller revolutions) for 3 more revolutions using 360, 720 and 1440 time steps per revolution. The evolution of pressure at sensor $S61$ and normalized channel flow rate of guide vane channel 3 are compared in figure 8.2.

It is seen in these time domain plots that the different simulations evolve similarly during the first revolution. Noticeable differences start to develop during the second revolution. From the third revolution on, the instantaneous channel flow rate distributions obtained with different time step sizes differ clearly. Time- and space integrated error estimators as proposed by [120] would obviously take very large values in such cases. Comparing the evolution of quantities of interest in figure 8.2, no fundamental difference

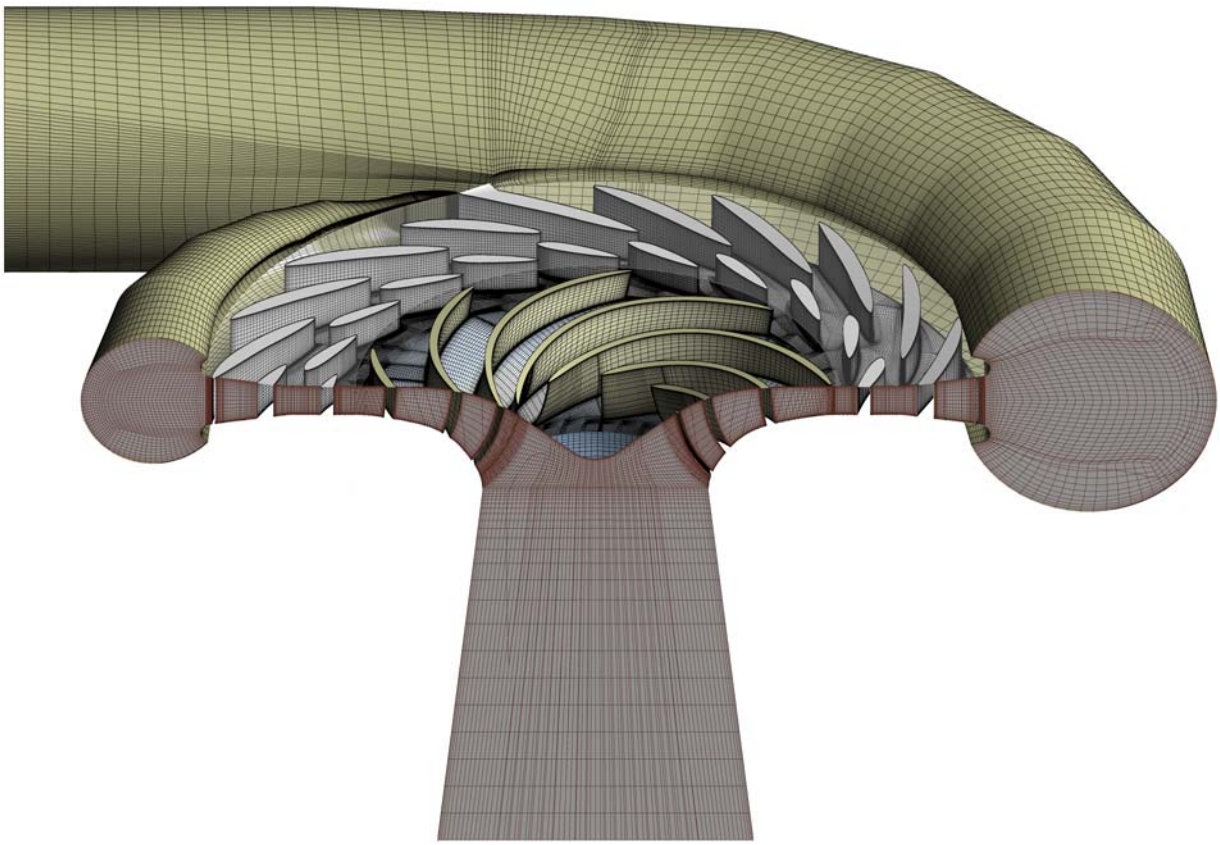

Figure 8.1: Meshes for the time-dependent simulations.

in the randomly varying pressure and guide vane channel flow rates can be observed.

Spectral power estimates of the pressure at $S61$ are evaluated from the same three simulations using Welchs periodogram technique and represented in figure 8.3. Overlapping hamming windows of a length of 1.5 impeller revolutions are applied. The influence of spectral leakage is restricted to low frequencies by the use of the hamming windows,[58], the energy at BPF and higher can reasonably be compared. This part of the power spectra

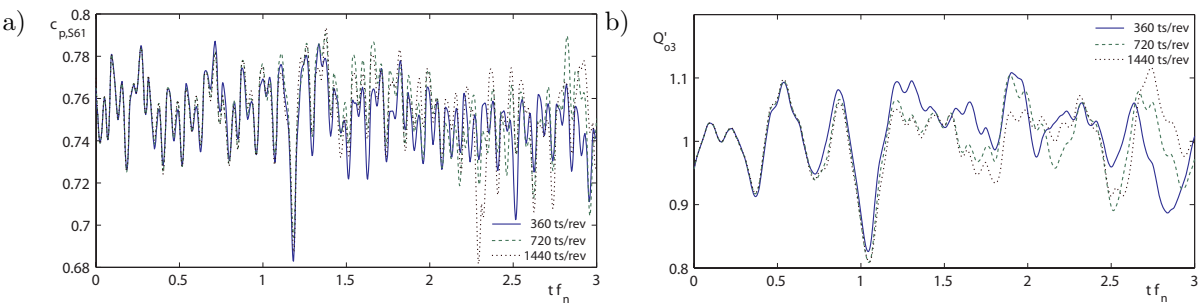

Figure 8.2: Evaluation of time discretization by monitoring of quantities of interest over 3 impeller revolutions. a) Pressure coefficient at sensor $S61$, b) Relative diffuser channel flow rate (diffuser channel 3)

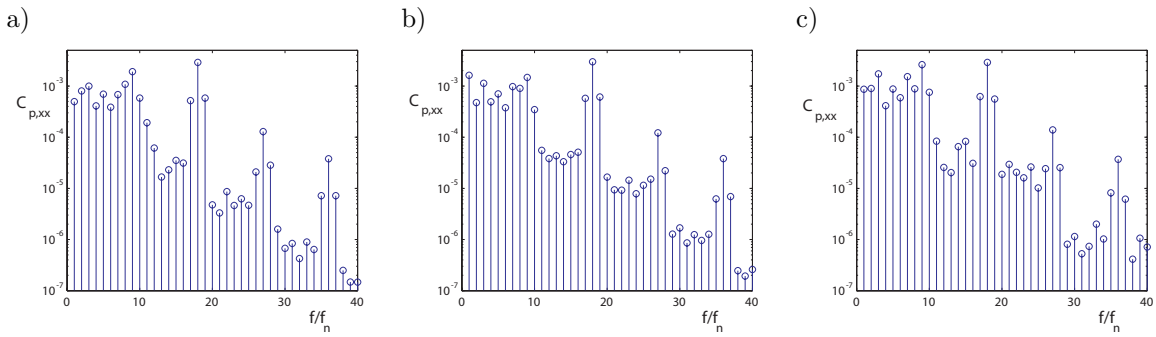

Figure 8.3: Time discretization dependency of pressure power spectra estimate. a) 360 time steps per rev., b) 720 time steps per rev., c) 1440 time steps per rev.

representing the deterministic fluctuations due to blade passage compares well between the three simulations.

The presented method is used for all investigated operating points: A time discretization of 360 time steps per revolution is used for 20 impeller revolutions. This simulation is continued for 3 further revolutions while a second validation simulation using half the time step size is conducted for the same time interval to verify that there is no fundamental change in circumferential flow rate and pressure repartition. A certain difference in the randomly fluctuating distribution is accepted.

8.2 Validation of Time Dependent Simulation Results

8.2.1 Global Performance and Rotating Stall Patterns

The time-dependent simulations predict rotating stall patterns similar to the ones that were determined experimentally. But they are in quantitative disagreement with experiments, since they are predicted for flow rates that are sensibly different from the corresponding experimental conditions. Three different global flow patterns are identified in the numerical simulation results and represented together with the energy coefficient, in figure 8.4. The energy coefficient in numerical simulations is evaluated by energy balances over the CFD domain inlet and outlet sections $\bar{3}$ and 5, that do not differ significantly from the reference sections where pressure measurements are taken in experiments. The flow regimes identified in the numerical simulation results compare to experimental results as follows:

- At $\varphi > 0.037$ and higher, the flow simulation results in a uniform circumferential flow repartition that corresponds most closely to the results obtained from experiment at $\varphi > 0.030$, while a numerical simulation at $\varphi = 0.034$ develops an irregular circumferential nonuniformity pattern.

- At $\varphi = 0.032$, the flow simulation results in a regular circumferential nonuniformity showing 4 cells of higher pressure and lower diffuser channel flow rates. The pat-

tern rotates slowly in the same sense of rotation than the impeller. This pattern corresponds to what was found experimentally at $\varphi = 0.026$.

- At $\varphi = 0.028$, $\varphi = 0.026$ and $\varphi = 0.024$ the simulation results show a high circumferential nonuniformity that does not exhibit any regularity. Zones of low diffuser channel flow rate and high pressure appear and disappear at different locations on the circumference in a stochastic manner. This behavior has no experimental counterpart and the difference in global behavior makes a detailed comparison futile.

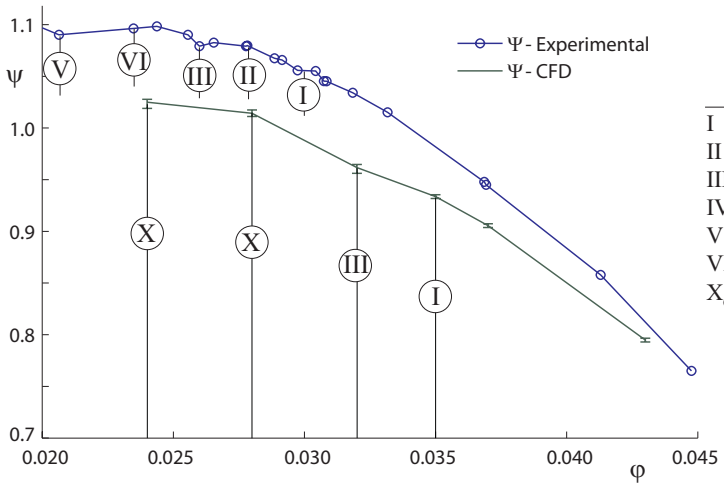

	φ_{EXP}	φ_{CFD}	$k_{s\text{-}EXP}$	$\omega_{s\text{-}EXP}$	$\omega_{s\text{-}CFD}$
I	0.030	0.034	incipient stall		
II	0.028	-	3	0.016 ω	–
III	0.026	0.032	4	0.021 ω	0.029 ω
IV	0.024	-	5	0.024 ω	–
V	0.021	-	5	0.014 ω	–
VI	0.015	-	4	0.028 ω	–
X_{CFD}	-	<0.030	Evenly distributed stall		

Figure 8.4: Comparison of experimental and numerical results, energy coefficient and stall modes

The offset of flow rate where onset of rotating stall is predicted by numerical simulation is of about 20% and the underprediction of energy coefficient of about 5%, nearly over the whole characteristic curve. In the given configuration, finding possible reasons for the shift and compensating the simulated characteristic may improve the prediction of flow rate while aggravating the error in energy coefficient. Thus, a correction of the unknown leakage flow rate in simulations by including additional in-and outflow boundaries would lead to a higher flow rate in the simulated impeller, leading to lower transferred energy. By this effect, it lowers the absolute frame flow angle α_2 and with it the misaligned incidence and the necessary deceleration. So an accurate modelling of leakage flow would tend to shift the incidence of stall on the guide vanes to lower flow rates. On the other hand, the prediction of the energy coefficient prediction would be impaired by this modeling improvement. In any case, the shift of flow rates by such a correction is typically about an order of magnitude smaller than the 20% offset in prediction of critical flow rate.

There is nevertheless a strong interest to analyze to what extent the flow fields obtained by simulation at different flow rates show time-dependent features corresponding to the experimental results. Similarity of global flow patterns shows that time-dependent numerical simulation can reproduce phenomena such as rotating stall and that the results of these simulation can help to validate the mechanism of propagation and to understand what parameters can influence the onset, intensity and revolution rate of the rotating stall.

8.2.2 Comparison of Results with similar Stall Patterns

Simulations show a regular rotating stall pattern at $\varphi = 0.032$. The propagation of zones of high and low pressure at the rotor-stator face and their impact on the pressure distribution on the impeller blades near trailing edge is shown in figure 8.5.

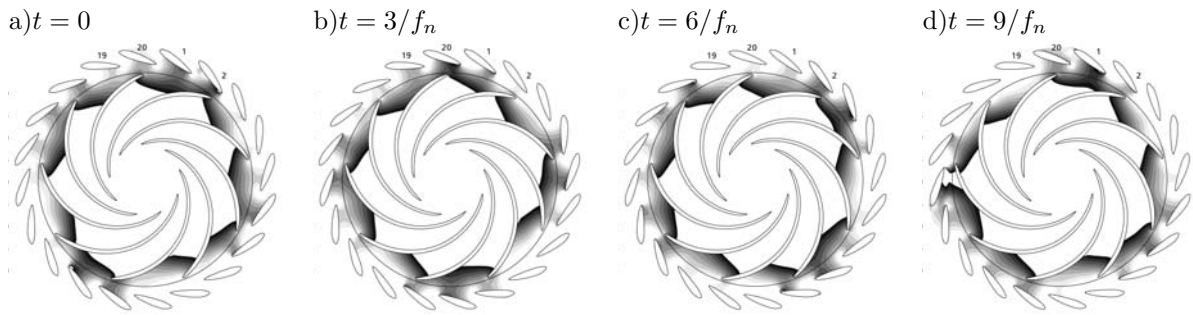

Figure 8.5: Circumferential pressure distribution from simulation at $\varphi = 0.032$

The filled contours represent a relatively small band of pressure values that visualizes the circumferential extension of the zone of high pressure that corresponds to low diffuser channel flow rates. As can be seen especially in 8.5d the progression of the high pressure zone in numerical simulation is not always regular. The distinct high pressure zones present around GV 20 and 15 at $t = 3/f_n$ (b) come closer to each other at $t = 6/f_n$ (c). Both finally merge into one large high pressure zone at $t = 9/f_n$ (d). A tendency to deviations from the regular rotating wave pattern in the first quarter of the volute, around guide vane channels $17 - 18$ was also observed in the experimental investigations, see figures 7.8 and 7.9. The high pressure zone found at $GV\,12$ at $t = 0$ propagates regularly and is found at $GV\,8$ after 9 impeller revolutions.

Pressure Fluctuation at the Rotor-Stator Interface

The pressure fluctuations close to the rotor-stator interface are the most obvious indicators of rotating stall. Their waveform and amplitude govern the mechanical stresses the impeller blades and shrouds are exposed to as well as the time-dependent torque exerced from the fluid on the guide vanes. A comparison of a time interval of 10 revolutions of the pressure signals identifying rotating stall experimentally in the stationary system (recall figure 7.9) represented in figure 8.6 shows a good agreement of the amplitude, local repartition and progression of the high and low pressure zones, as far as this can be judged from such a short period available from numerical simulation.

In more detail, the raw pressure fluctuations under rotating stall conditions from time dependent numerical simulation ($\varphi = 0.032$) and from experiment ($\varphi = 0.026$) are compared in figure 8.7.

The basic low frequency pattern connected to rotating stall is in satisfactory agreement.

The blade passing influence is clearly visible in the time plots. The energy at frequencies above the BPF is determined using Welchs spectral power estimate method [151] using a (Hamming) window width of 3 impeller revolutions to yield frequency estimate

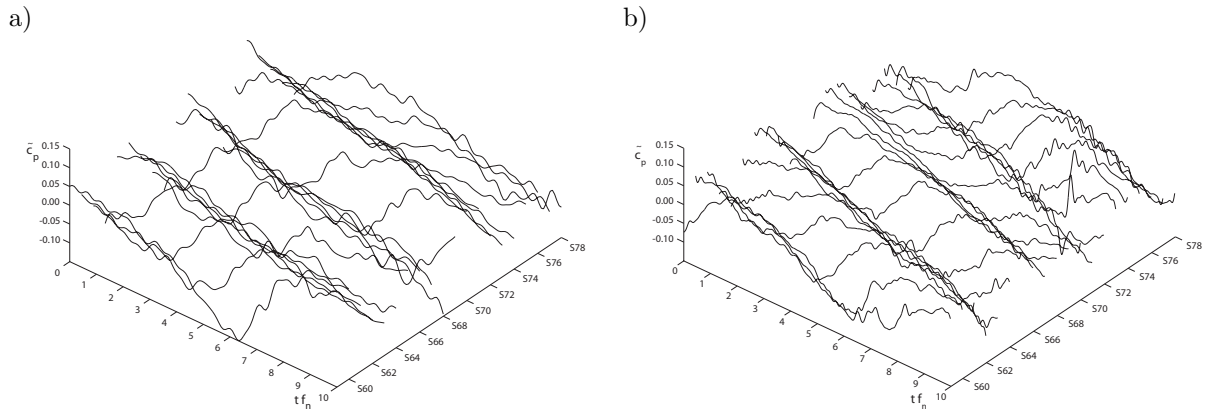

Figure 8.6: Comparison of circumferential stall progression based on low pass filtered pressure fluctuations at 20 sensors S59-S78. a)Experimental at $\varphi = 0.026$, b)Simulation at $\varphi = 0.032$

bins that are commensurable with the impeller rotation rate multiples. The values of the blade passing frequency $9f_n$ and its first two harmonics agree well between simulation and experimental investigation. The experimental pressure data exhibit broad band pressure fluctuations containing about 10 times the power found at the same frequencies in the simulations, especially in the band between the blade passing frequency and its second harmonic $27f_n$.

As for the processing of the LDV data under rotating stall conditions, the stall phase is derived from the analytic phase of the pressure signal at the sensor closest to the rotor stator interface and located in the investigated guide vane passage, following equations (4.25) to (4.26). Figure 8.8 shows the evolution of the analytic phase over time for experimental and simulation results. In agreement with the time plot, figure 8.7 the phase from experimental results shows a steeper slope corresponding to the shorter increasing period of the saw-tooth like pattern while the phase derived from the simulation results leads to a nearly constant slope. The difference in period determining the revolution rate of the stall pattern is obvious in this example.

Pressure Fluctuations along a Guide Vane Channel

The pressure evolution along the neighboring guide vane channels 3 and 4 corresponds well to the experimental data represented in figure 8.9 in two main aspects.

- The phase of increasing pressure at sensors $S61$ and $S62$ is accompanied by large fluctuations of the pressure at the guide vane throat section, $S55$ and $S56$, that can at times reach the pressure level of the spiral casing.

- In the development of the typical sawtooth shape, the neighboring channels show an inversely synchronized behavior. When the pressure in channel 4 increases quickly, indicating its stall, channel 3 is fed with additional flow, momentarily leading to a higher pressure recovery: The pressure at $S61$ decreases. When the pressure increase in channel 3 reaches its maximum level, channel 4 begins to stall.

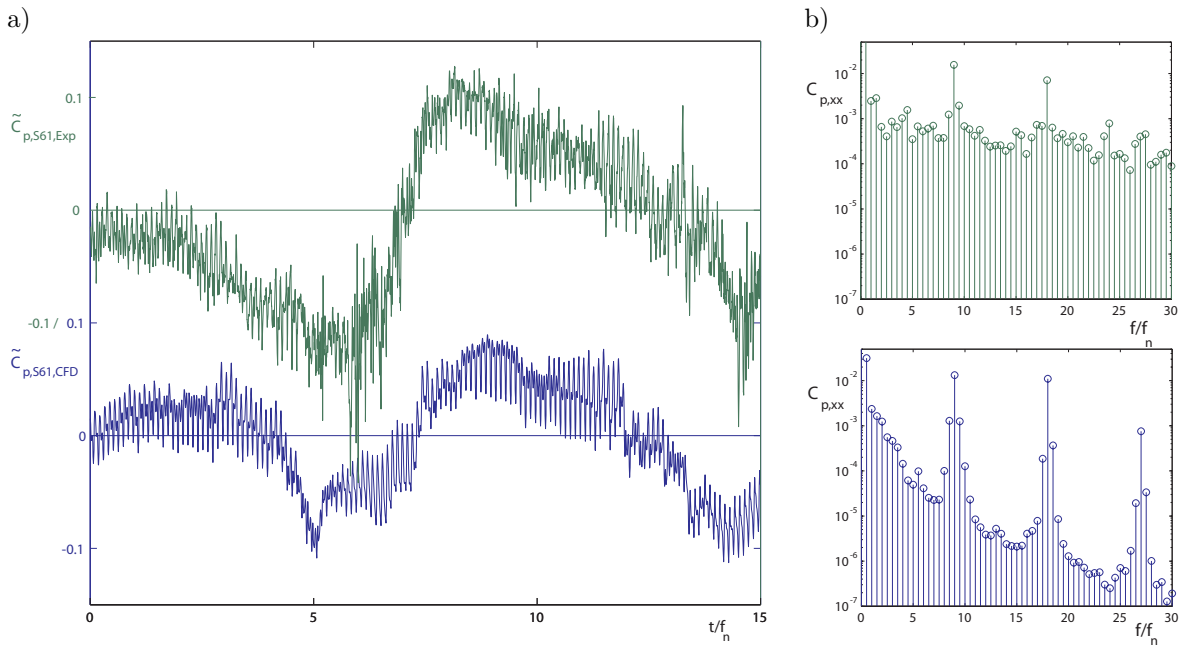

Figure 8.7: Comparison of pressure fluctuations at reference sensor $S61$ for GV-channel 4, Top: Experimental, $\varphi = 0.026$, Bottom: Simulation,$\varphi = 0.032$. a) Evolution over 15 impeller revolutions b) Power spectra

One main difference between the experimental and the numerical results is in almost constant pressure at section $v4$ at the stay vane inlet shown in the numerical results, while the measurements clearly show fluctuations that are synchronous with those measured closer to the rotor-sator interface.

Diffuser Channel Flow Rate Fluctuation and Repartition

The non-uniform circumferential pressure field is related to a non-uniform repartition of the total volume flow rate Q into diffuser channel flow rates $Q_{o,k}$ for $k = 1$ to z_o. The dimensionless relative flow rate coefficient is defined as the ratio of instantaneous channel

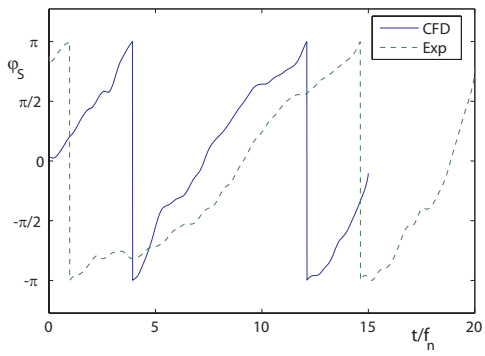

Figure 8.8: Comparison of stall phase: Experimental vs. CFD.

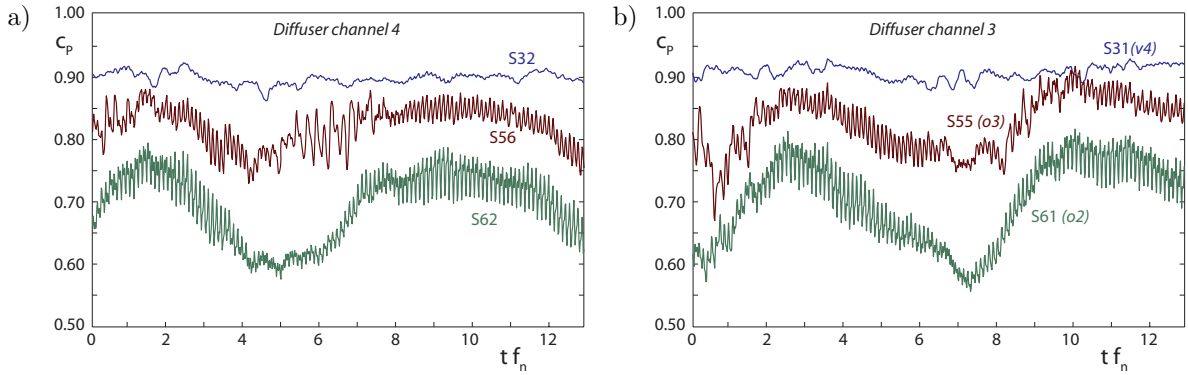

Figure 8.9: Pressure evolution in guide and stay vane channels from numerical simulation. a) Channel 4 ($S61$, $S55$, $S31$), b) Channel 3 ($S62$, $S56$, $S32$); (compare to figure 7.13)

flow rate over mean channel flow rate: $Q'_{o,k} = z_o Q_{o,k}/Q$. Figure 8.10 represents the evolution of flow rate repartition of all 20 diffuser channels over 10 impeller revolutions .

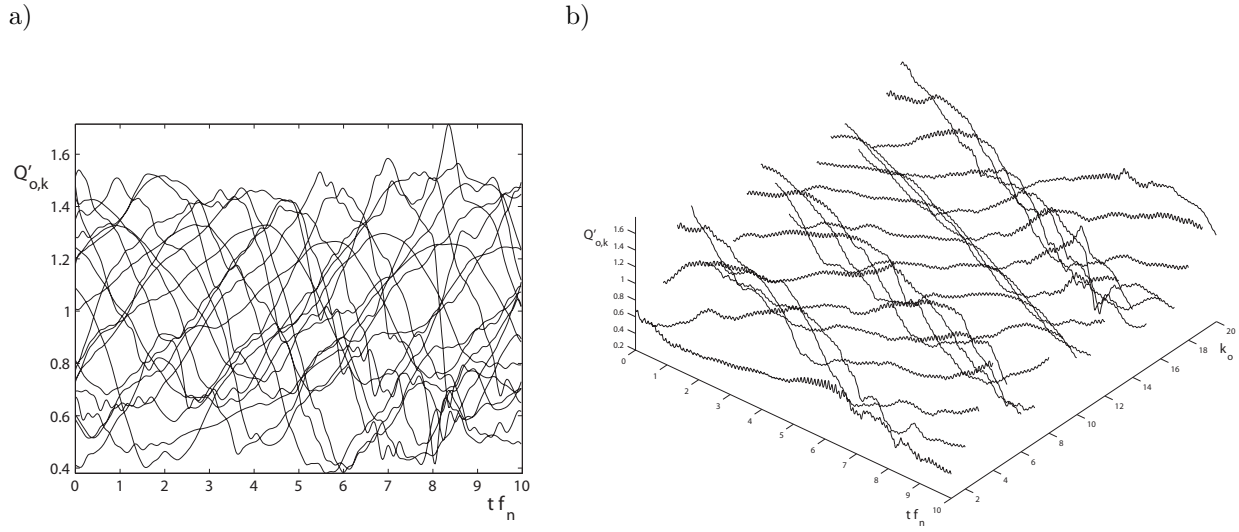

Figure 8.10: Diffuser channel flow rates. a) All channels over time, b) 3D-representation visualizing circumferential progression of stall cells

The integrating character of channel flow rates when compared to pressure leads to time evolutions that are less disturbed by peaks of blade passages or local events such as passage of vortex cores over a given location. Furthermore, the fluctuation range of instantaneous channel flow rates gives a clear indication of the importance of the circumferential imbalance, when faced to fluctuation ranges as observed here, there is obviously some important flow nonumiformity involved. This makes the diffuser channel flow rates a suitable indicator for stall monitoring in simulation. The plot lines represent unfiltered values from numerical simulation time steps. For the short available time interval, 2D DFT is not suitable to determine the rotation rate of the stall cells, since it suffers from spectral leakage. An estimate of the unnormalized autocovariance function is computed for each of the flow rate time series containing N samples:

$$\langle R_{Q',o,kk}[m]\rangle = \sum_{n=0}^{N-m-1} \left(Q'_{o,k}[n+m] - \overline{Q'_{o,k}}\right)\left(Q'_{o,k}[n] - \overline{Q'_{o,k}}\right) \tag{8.1}$$

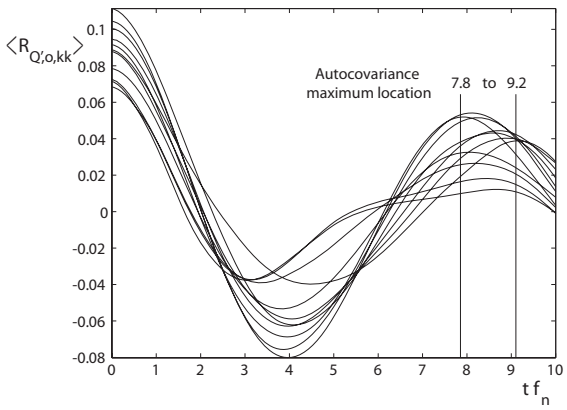

Figure 8.11: Identification of stall rotation rate by autocovariance function

The signal period is identified by the function's first maximum reasonably far from origin. These maximum correlation time lag values are located between $7.8/f_n$ and $9.2/f_n$, see figure 8.11, leading to a revolution rate of 0.027ω to 0.032ω, which is noticeably higher than the value of 0.021ω found experimentally for the 4 cell stall mode at $\varphi = 0.026$ and all other stall mode propagation velocities.

The high frequency fluctuations due to blade passage are clearly visible, but small compared to the fluctuations due to the rotating stall phenomenon. The simulated flow rates range from 0.4 and 1.6 times the mean channel flow rate. This is the order of magnitude found for flow rate fluctuation determined from the integration of the stall phase averaged LDV measurements, ranging from 0.4 to 1.4, see figure 7.21.

The stall phase averaging processing used for the experimental LDV point data is applied to the instantaneous flow rates integrated from the simulation fluxes at every timestep, using the data from diffuser channels 3 to 12 to get a statistically relevant number of samples for every phase. The result is represented in figure 8.12a.

As a result of the averaging, the peak-to-peak amplitude of phase averaged fluctuations is smaller than the range of peak values of the individual channel's flow rates. The qualitative shape of the flow rate and maximum channel flow rate coefficient of 1.40 corresponds well to the experimental findings, while the minimum peak value is higher than the one determined experimentally, but in the right order of magnitude (0.55 from CFD versus 0.4 from LDV measurements).

Figure 8.12b shows the diffuser channel flow rate phase average with respect to the impeller blade passing, it agrees well with the experimental finding that in the case of stall, the deterministic velocity and flow rate fluctuations are an order of magnitude smaller than the fluctuations due to the stall.

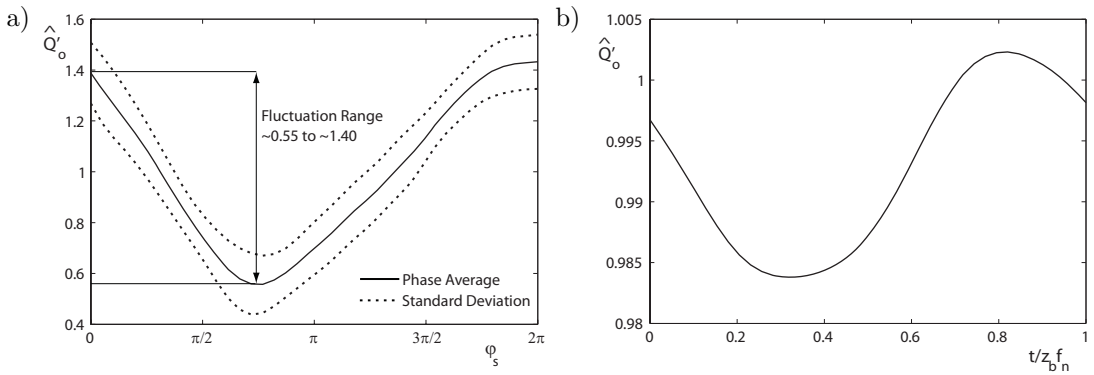

Figure 8.12: Diffuser channel flow rates from simulation. a) Stall phase average, b) Blade passage phase average;(compare to figure 7.21)

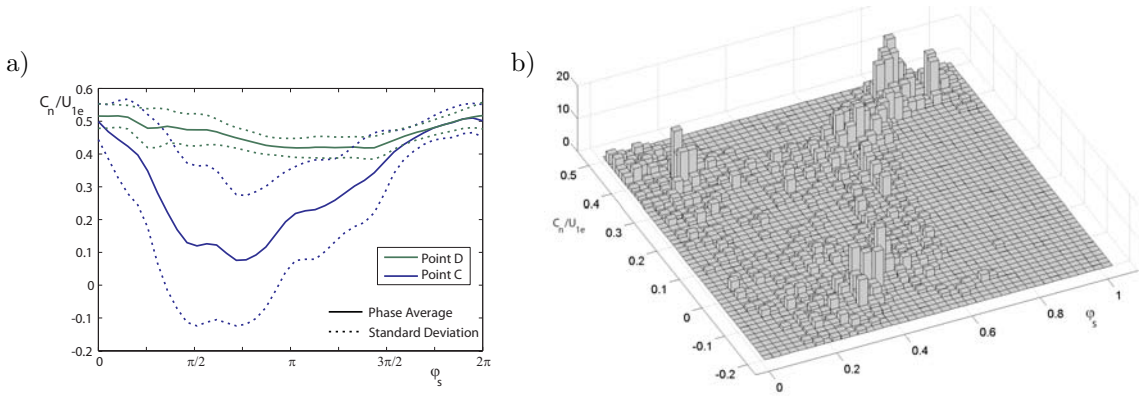

Figure 8.13: Example velocity stall phase averages. a) Phase average and standard deviation, point C and D (points defined on figure 7.15, compare to figure 7.17b), b) Bin count histogram, point C

Guide Vane Throat Velocity Field

The velocity fields in the guide vane throat are extracted from a set of 180 stored timesteps over 10 impeller revolutions and the same stall phase averaging processing as for the LDV values is performed. In order to get a statistically relevant number of samples for each stall phase bin, profiles from guide vane channel 3 to 12 are used since they are considered having a sufficiently similar behavior. The channels in the narrow part of the spiral casing and the two nearest channels to the spiral casing tongue are discarded, since the pressure and flow rate evolution in the time plots figure 8.6 and 8.10 indicate a difference in behavior due to the presence of the tongue of the spiral casing.

The individual velocity values in points C and D and their standard deviations are represented in figure 8.13a. Figure 8.13b depicts as height of the columns the number of velocity samples acquired falling into the represented intervals of phase and velocity (so called bin counts). The standard deviation is high and it appears that the normal velocity at point C does not undergo the same passage close to zero or negative at each of the stall passages.

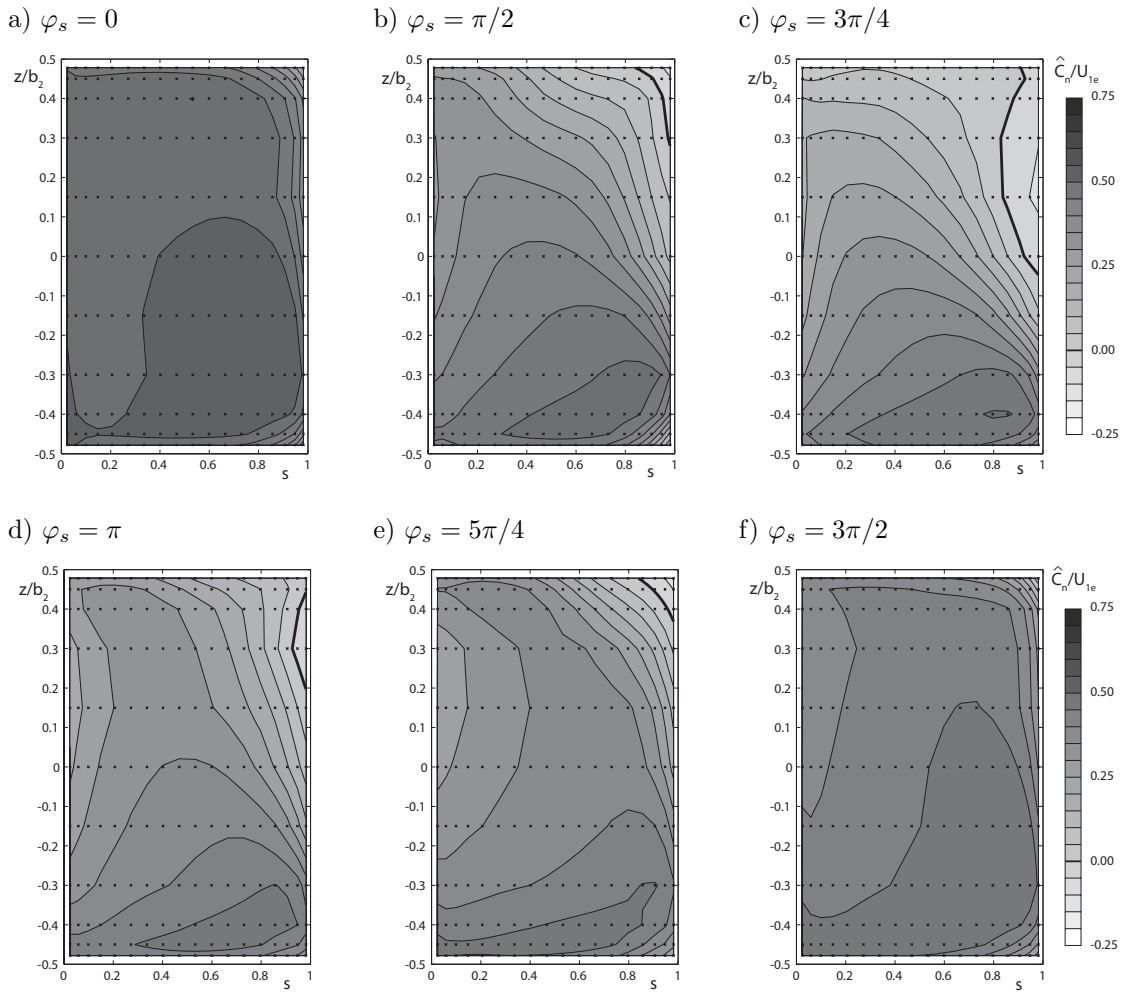

Figure 8.14: Normal velocity in the guide vane throat section from numerical simulation, stall phase averaged at $\varphi = 0.032$. a-f) Phase angles from 0 to $3\pi/2$; (compare to figure 7.19)

The onset of reverse flow predicted by numerical simulation in the throat section is less abrupt than found in experiment. This shows in a slower increase of pressure and decrease of flow rates and velocities. The averaged flow field exhibits only a small zone of reverse flow which extends more along the guide vane compared to experiment, where the reverse flow is more intense and extends along the diffuser side wall. This assumption of a lower intensity of the reverse flow zone can be discussed in two aspects:

- The averaging includes periods where stall was found to be less intense than in others, as seen in the histogram plots of flow rate or local velocity. Instantaneous plots with largest recirculation zones are identified by searching for minimal instantaneous flow rates amongst all timestep data and represented in figure 8.15.
- The simulation results considered have been obtained at a higher flow rate than the experimental ones. The fact that the propagation of stall zones compares well does not imply that the local flow patterns are similar in all aspects.

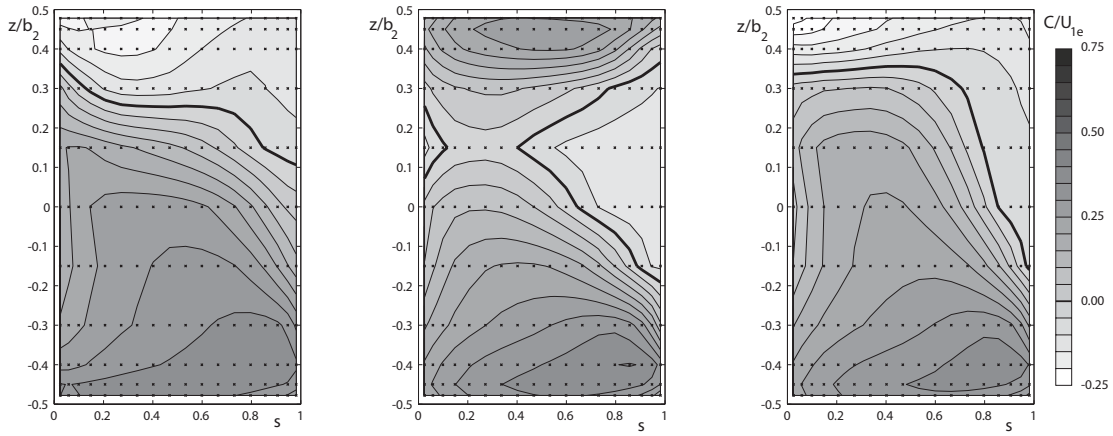

Figure 8.15: Instantaneous normal velocity in the guide vane throat section from numerical simulation, arbitrary instants with low channel flow rate; (compare to stall phase averaged experimental results in figure 7.19)

It can be concluded that the modelling approach and the numerical method do not totally inhibit the appearance of reverse flow zones as extended as found from experiment. The conditions necessary for this are not met in most of the channels, while the extreme values can reach states of high reverse flow with different local velocity distributions. The low pressure conditions susceptible to lead to the cavitating vortex cores observed in the experimental investigations, see figure 7.27 have by far not been reproduced by the numerical simulations, even not at the moments of most intense reverse flow.

Guide Vane Tangential Velocity

As represented in figure 8.16 in comparison to figure 7.22, the extension of the reverse flow zone through the stall phase, delimited by the line of zero tangential velocity, is in good agreement with the experimental results.

Impeller Outlet Velocity

The stall phase averaged flow fields at the impeller outlet sections represented in figure 8.17 show a qualitative disagreement when compared to the experimental figure 7.23. The reverse radial flow component close to the interior diffuser side wall does not show up. Radial and circumferential velocity however are higher than average in zones close to both side walls. None of the 1640 instantaneous flow field samples show a negative radial velocity zone as found in the experimental investigations. This leads to the conclusion that the difference in flow rate conditions, the physical modeling and the numerical method do not represent the backward propagation of the reverse flow jet present at the guide vane throat up to the considered cylindrical section.

Figure 8.18 shows the stall phase averaged flow rate through the cylinder sections corresponding to the LDV measurement section. As the normal velocity profiles suggest, the fluctuation of flow rate is less pronounced than in experiment.

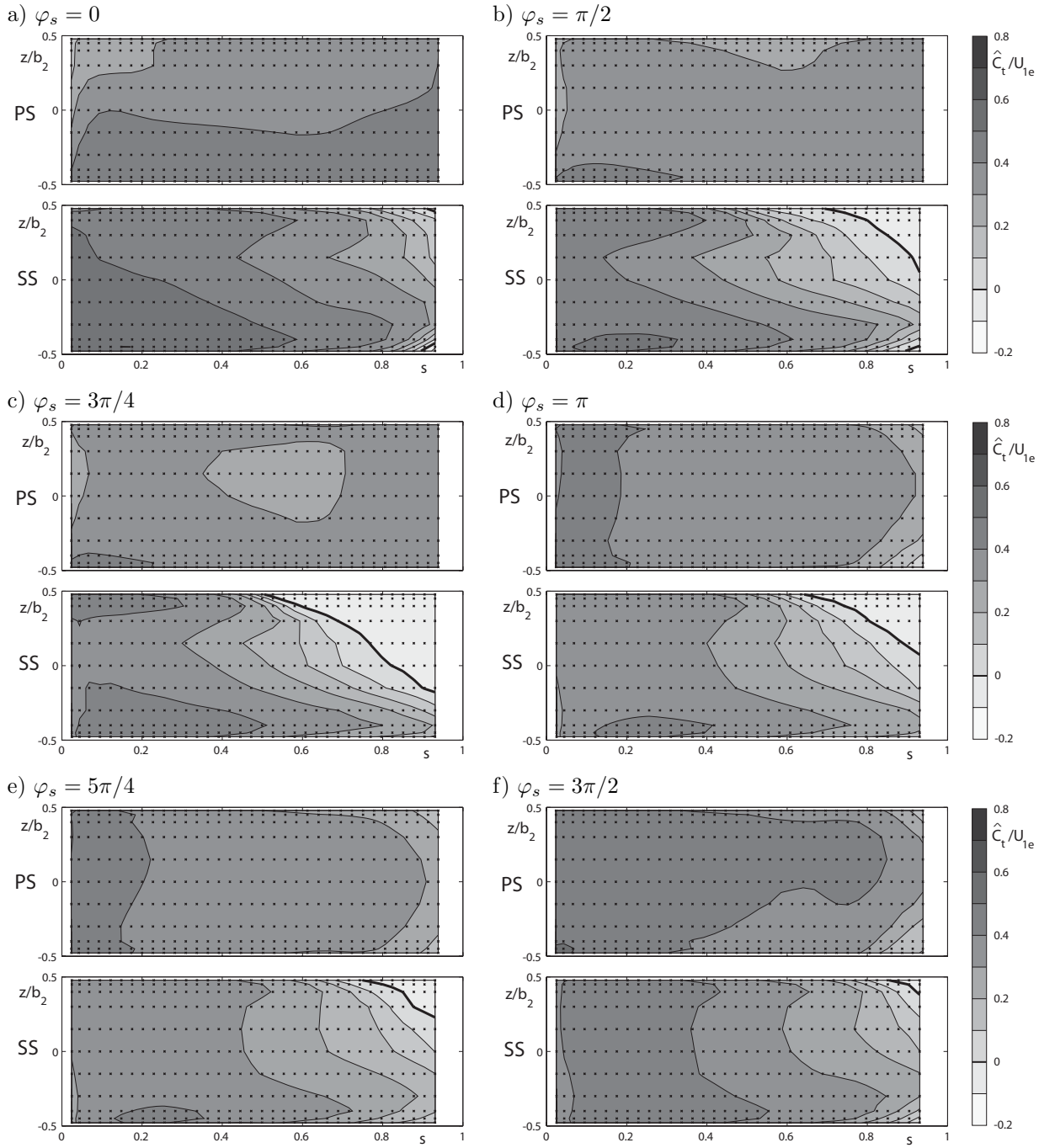

Figure 8.16: Stall phase averaged tangential velocity close to guide vane 4 from simulation, $\varphi = 0.032$; (compare to figure 7.22)

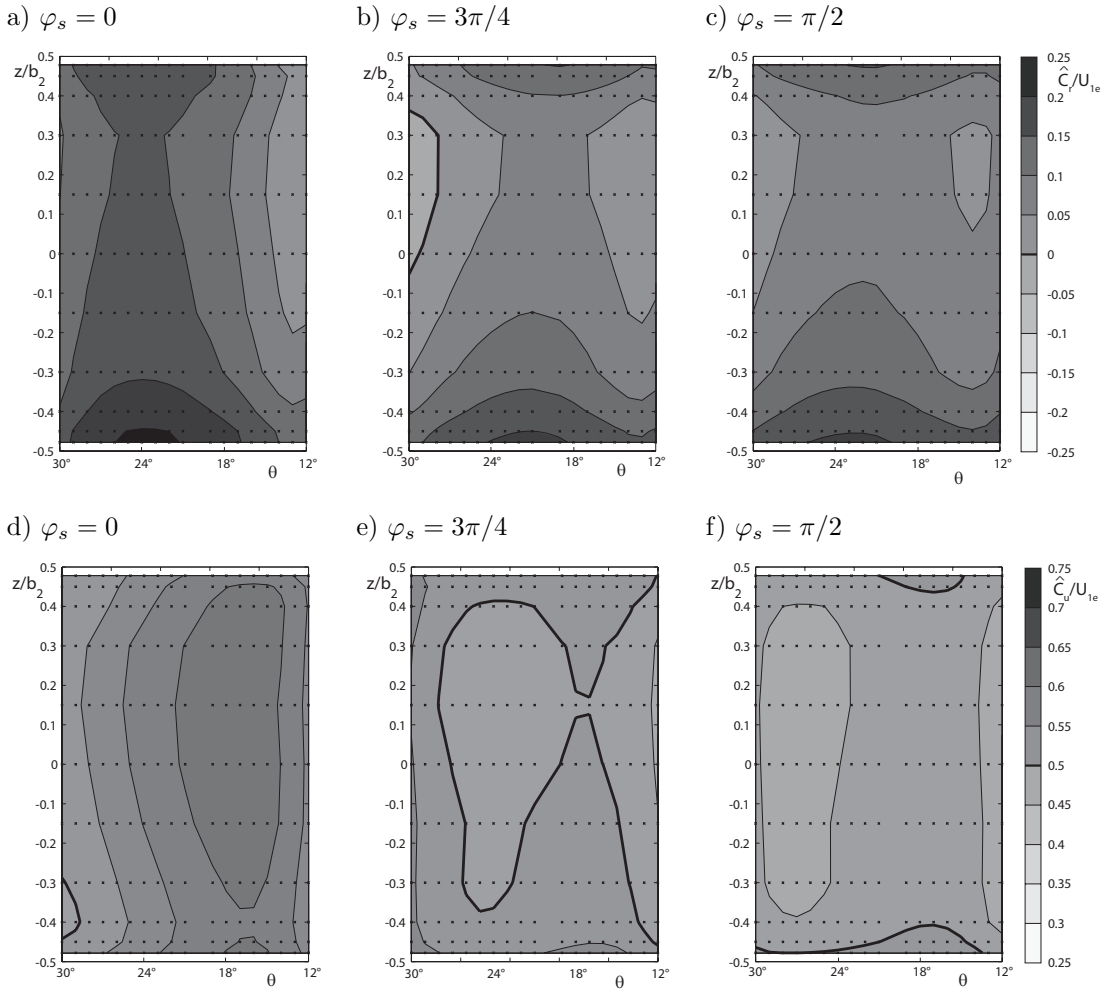

Figure 8.17: Stall phase averaged velocity at cylindrical section at impeller outlet from numerical simulation at $\varphi = 0.032$. Top: a,b,c) Radial velocity, Bottom: d,e,f) Circumferential velocity; (compare to figure 7.23)

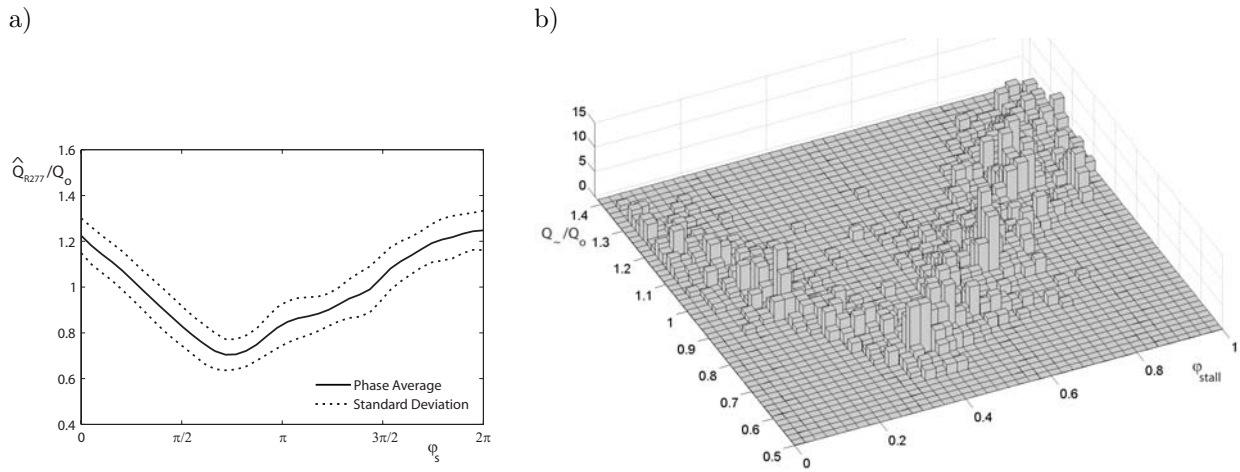

Figure 8.18: Stall phase averaged local flow rate at the impeller outlet section from numerical simulation at $\varphi = 0.032$. a) Phase average with standard deviation (compare to figure 7.24a), b) Bin count histogram

Part IV

Multi-Scale Numerical Modelling

Chapter 9

Mass Flow Weighted Periodic Inlet Condition

Despite the ongoing performance increase of computers and more efficient implementations of parallel computing algorithms, simulations of entire turbomachines using the transient-rotor-stator approach remains a challenging and time-costly operation. Such simulations using meshes satisfying strict criteria of mesh independence as established by [79] can practically not be achieved. The results obtained with the study cases of chapters 8 and 6 show important quantitative disagreement when compared to experimental investigation results. Even though the stationary approach numerical simulations in chapter 5 have not shown a strong sensibility of the predicted energy-discharge characteristic on the mesh refinement, the accuracy of time-dependent numerical simulations is expected to benefit from mesh refinement, enabling the use of advanced turbulence modelling approaches such as Large Eddy Simulation (LES) and hybrid RANS-LES approaches such as Detached Eddy Simulation.

In the context of LES and DNS simulations, a common technique to specify inlet boundary conditions is to use profiles that are extracted from the same flow simulation further downstream in the domain [118]. As this procedure termed "streamwise periodic boundary condition" converges, the inlet boundary conditions provide a good representation of fully developed turbulent flow conditions (e.g. in a channel), without further modeling assumptions needed to artificially generate the resolved turbulent structures, as presented by [88]. A similar technique consists in running a second simulation containing the upstream domain concurrently or beforehand and to use time-dependent profiles from such a simulation as inlet boundary conditions [87; 31].

The work of O'Kubo et al. [109] has established one-dimensional laws for the instantaneous flow rate of an impeller channel, based on its inertial length, showing that this essential parameter of an impeller channel's time-dependent behavior is independent of flow rate. Sano et al. [126; 125] have shown that features of rotating stall in a vaned diffuser can be reproduced to some extent using an actuator disk model for the impeller. In simulations of hydro-acoustic phenomena in Francis turbines, one-dimensional modeling of diffuser channels and discretization of spiral casings by pipe segments have proven to reproduce the acoustic phenomena in the spiral casing that are excited by rotor-stator interaction [106; 121].

While some cases of flow instabilities in centrifugal pump impellers were reported [47; 115; 114], the case studies investigated in this work, dealing with negative slope of

the characteristic close to BEP, confirm the hypothesis of sound impeller through flow as long as the impeller flow is guided by the impeller blades. The complex rotor-stator interaction takes place in the triangular zone that is open towards the rotor-interface while the influence back into the impeller channel is confined to a one-dimensional pressure-potential influence that determines the instantaneous operating point of the impeller channel.

The mass flow weighted periodic inflow boundary condition approach consists in discretizing only one reference impeller channel with a three-dimensional mesh resolving the Navier-Stokes equation. The time-dependent flow rate repartition among the impeller channels is determined by a 1-dimensional approach based on linearized partial differential equations based on the specific relative energy level at section 1^*. The velocity profile extracted from the fully resolved channel is used as a shape function for the velocity components applied on the remaining channel inflow boundary conditions implemented at section 1^*.

9.1 1D-Impeller Channel Model

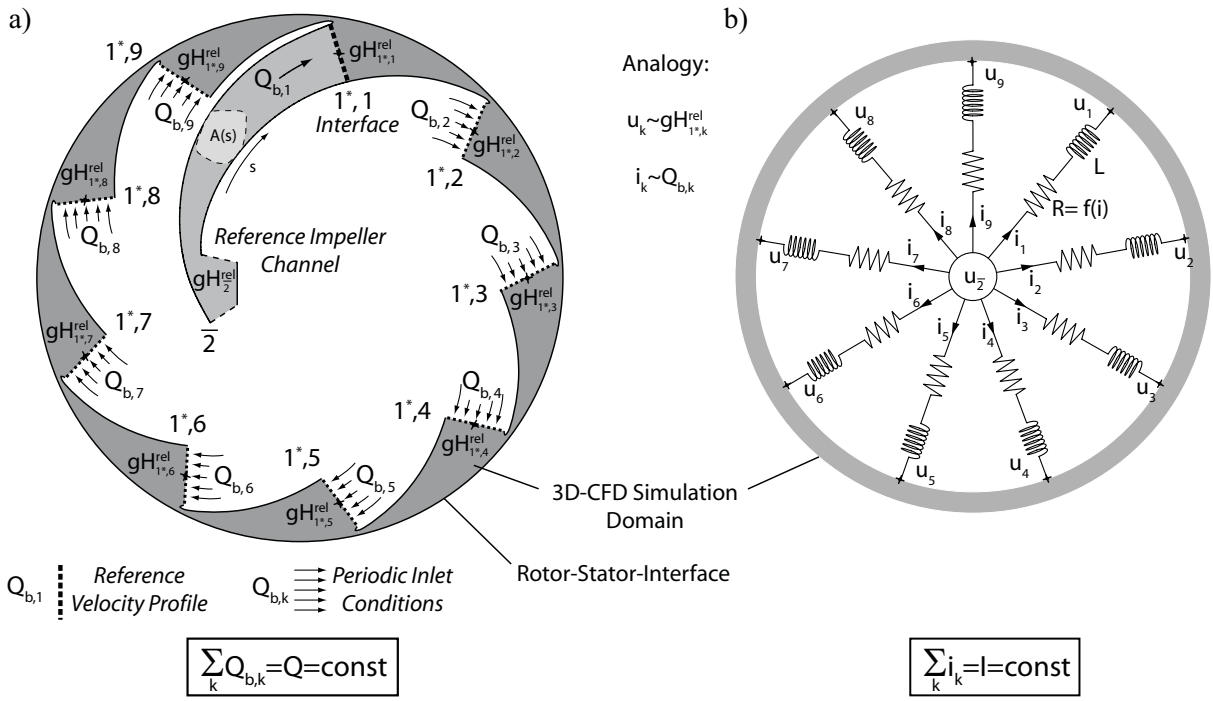

Figure 9.1: One-dimensional impeller channel model. a)Flow modelling diagram, b)Equivalent electrical scheme

The time-dependent behavior of any one of the impeller channels (index $k = 1 \rightarrow z_b$) of a centrifugal pump, see fig. 9.1, is governed by the specific relative hydraulic energy balance on a streamline from section $\bar{2}$ to $1^*, k$ in the rotating impeller inertial frame,

assuming no hydro-acoustic effects.

$$\int_{\bar{2}}^{1^*,k} \frac{\partial W}{\partial t} ds + gH_{1^*,k}^{rel} - gH_{\bar{2}}^{rel} + gH_{r\bar{2}\div 1^*,k} = 0 \tag{9.1}$$

The viscous losses are modeled to be a quadratic function of the flow rate with a positive impeller channel flow rate:

$$gH_{r\bar{2}\div 1^*,k} = R_b Q_b |Q_b| = R_b Q_{b,k}^2 \tag{9.2}$$

Assuming at all times, $W(s) = Q_b/A(s)$ and defining the impeller channel hydraulic impedance L_b:

$$L_b = \int_{\bar{2}}^{1^*} \frac{1}{A(s)} ds \tag{9.3}$$

Equation (9.1) writes

$$L_b \frac{dQ_{b,k}}{dt} + gH_{1^*,k}^{rel} - gH_{\bar{2}}^{rel} + R_b {Q_{b,k}}^2 = 0 \tag{9.4}$$

The loss term can be further linearized considering only small fluctuations of impeller channel flow rates around their time average value given by the total pump flow rate Q/z_b, the latter expression being at the same time the arithmetic, spatial, average of the channel flow rates $Q_{b,k}$:

$$gH_{r\bar{2}\div 1^*,k} = R_b \left(\frac{Q}{z_b}\right)^2 + 2R_b \frac{Q}{z_b}\left(Q_{b,k} - \frac{Q}{z_b}\right) = 2R_b \frac{Q}{z_b} Q_{b,k} - R_b \left(\frac{Q}{z_b}\right)^2 \tag{9.5}$$

Equation (9.4) is of the same type than those governing voltage and current in an electrical scheme made of an inductance and a variable resistance depending linearly on the current. The impeller is represented by the equivalent electrical diagram represented in figure 9.1b. A comprehensive presentation of the use of such analogy for modelling of hydroelectric systems is given by [105]. Specific relative hydraulic energy $gH_{1*,k}^{rel}$ is equivalent to voltage u_k, flow rate $Q_{b,k}$ is equivalent to current i_k:

$$L\frac{di_k}{dt} + u_k - u_{\bar{2}} + R_k i_k = 0 \qquad \text{with} \quad R_k = k_R i_k \tag{9.6}$$

It is assumed that the relative specific energy $gH_{\bar{2}}^{rel}$ upstream of the impeller is identical for all channels, which is justified by the configuration of an inlet eye common to all impeller channels of the centrifugal pump. This translates into the common voltage level $u_{\bar{2}}$ in the equivalent electrical diagram. According to equation (9.5), small fluctuations of branch current i_k around I/z_b are considered and the dependency of the resistance on the current is resolved by linearization:

$$L\frac{di_k}{dt} + u_k - u_{\bar{2}} + k_R \left(\frac{I}{z_b}\right)^2 + 2k_R \frac{I}{z_b}\left(i_k - \frac{I}{z_b}\right) = 0 \tag{9.7}$$

Summing up all equations for $j \epsilon [1\, z_b]$ yields:

$$L \underbrace{\sum_{j=1}^{z_b} \frac{di_j}{dt}}_{=0} + \sum_{j=1}^{z_b} u_j - z_b u_{\bar{2}} + z_b k_R \left(\frac{I}{z_b}\right)^2 + 2k_R \frac{I}{z_b} \underbrace{\sum_{j=1}^{z_b}\left(i_j - \frac{I}{z_b}\right)}_{=0} = 0 \tag{9.8}$$

Inserting the resulting relation

$$\frac{1}{z_b}\sum_{j=1}^{z_b} u_j = u_{\bar{2}} - k_R\left(\frac{I}{z_b}\right)^2 \tag{9.9}$$

into equation (9.7) allows to eliminate the unknown voltage $u_{\bar{2}}$:

$$L\frac{di_k}{dt} + u_k - \frac{1}{z_b}\sum_{j=1}^{z_b} u_j + 2k_R\frac{I}{z_b}i_k - 2k_R\left(\frac{I}{z_b}\right)^2 = 0 \tag{9.10}$$

Passing back to the hydraulic variables describing the impeller channel behavior yields:

$$\frac{dQ_{b,k}}{dt} = \frac{1}{L_b}\left(gH^{rel}_{1^*,k} - \frac{1}{z_b}\sum_{j=1}^{z_b} gH^{rel}_{1^*,j}\right) + \frac{2R_bQ}{z_bL_b}\left(Q_{b,k} - \frac{Q}{z_b}\right) \tag{9.11}$$

Declaring the notation $\mathbf{Q}_b$ and $\mathbf{gH}^{rel}_{1*}$ for the z_b-component vectors of channel flow rates and relative specific hydraulic energy the equations governing the evolution of impeller flow are expressed in matrix notation:

$$\frac{d}{dt}\mathbf{Q}_b = \beta_L\,\mathbb{K}\,\mathbf{gH}^{rel}_{1^*} + \beta_r\,\mathbb{K}\,\mathbf{Q}_b \tag{9.12}$$

With the parameters

$$\beta_L = \frac{1}{L_b} \qquad \text{and} \qquad \beta_r = \frac{2R_bQ}{L_bz_b} \tag{9.13}$$

$\mathbb{K} = \mathbb{I} - \frac{1}{z_b}\mathbb{J}$, given the identity matrix $\mathbb{I}$, $I_{ij} = \delta_{ij}$, and the unit matrix $\mathbb{J}$, $J_{ij} = 1$. Multiplication with $\mathbb{K}$ can be interpreted as an operator centering the z_b component's values of a vector around their arithmetic average.

Implementation based on pressure and relative flow rate

The first implementation of the model and the corresponding parameter identification based on the study case of part III is based on numerical simulation pressure values $p^*_{1^*,k}$ and relative channel flow rate $Q'_{b,k} = Q_{b,k}/(Q/z_b)$. Expanding the specific relative hydraulic energy gH^{rel}_{1*} in equation (9.4) yields

$$L_b\frac{dQ_b}{dt} + \left(\frac{W^2-U^2}{2} + \frac{p}{\rho} + gz\right)_{1^*} - gH^{rel}_{\bar{2}} + K_bQ_b^2 = 0 \tag{9.14}$$

Assuming that relative velocity scales with flow rate at section 1^*, $W_{1^*} = Q_b/A_{1^*}$:

$$L_b\frac{dQ_b}{dt} + \left(\frac{-U^2}{2} + \frac{p}{\rho} + gz\right)_{1^*} - gH^{rel}_{\bar{2}} + \left(K_b + \frac{1}{2A^2_{1*}}\right)Q_b^2 = 0 \tag{9.15}$$

Following the formalism of equations (9.4) to (9.11) with $u_k = \left(\frac{-U^2}{2} + \frac{p}{\rho} + gz\right)_{1^*,k}$, the resolution of the equivalent electrical scheme yields:

$$\begin{aligned}\frac{dQ_{b,k}}{dt} = \frac{1}{L_b}&\left(\left(\frac{-U^2}{2} + \frac{p}{\rho} + gz\right)_{1^*,k} - \frac{1}{z_b}\sum_{j=1}^{z_b}\left(\frac{-U^2}{2} + \frac{p}{\rho} + gz\right)_{1^*,j}\right)\\ &+ \frac{Q}{z_bL_b}\left(2K_b + \frac{1}{A^2_{1*}}\right)\left(Q_{b,k} - \frac{Q}{z_b}\right)\end{aligned} \tag{9.16}$$

U depends only on geometry, $U_{1*,k}^2 = 1/z_b \sum_{j=1}^{z_b} U_{1*,j}^2$ for any channel k. With the definition of the numerical simulation pressure coefficient $c_p^* = (p + \rho g z - p_{ref})/(0.5\rho U_{1e}^2)$ and the dimensionless relative flow rate $Q'_{b,k}$, we obtain for every channel:

$$\frac{dQ'_{b,k}}{dt} = \frac{z_b U_{1e}^2}{2QL_b}\left(c_{p1^*,k}^* - \frac{1}{z_b}\sum_{j=1}^{z_b} c_{p1^*,j}^*\right) + \frac{Q}{z_b L_b}\left(2K_b + \frac{1}{A_{1*}^2}\right)\left(Q'_{b,k} - 1\right) \tag{9.17}$$

and the corresponding matrix form:

$$\frac{d}{dt}\mathbf{Q}'_b = \beta_p^* \,\mathbb{K}\, \mathbf{c}_{p1^*}^* + \beta_q^* \,\mathbb{K}\, \mathbf{Q}'_b \tag{9.18}$$

With the parameters

$$\beta_p^* = \frac{z_b U_{1e}^2}{2QL_b} \qquad \text{and} \qquad \beta_q^* = \frac{Q}{z_b L_b}\left(2R_b + \frac{1}{A_{1*}^2}\right) \tag{9.19}$$

9.2 Numerical Implementation

The prototype implementation of the periodic inlet condition into the CFX-5 Solver is realized by solving equations (9.12) and (9.18) explicitly at the beginning of every time step using the current values of the last time step for the equation right side terms. Technically, it is implemented by combining available export functionality and User-Fortran subroutines to specify the boundary condition profiles. Defining the guided part of the reference impeller channel upstream of 1^* and the part for the rotor-stator interface region as separate mesh regions, the flow solution on the interface between the meshes is stored in cgns-format [2] at the end of every time step. The parallel computing environment of the CFX-5 solver is based on the master-slave concept with the master node solely dedicated to do file I-O operations while the compute nodes receive all information via interprocess communication (MPI or PVM). This results in the following implementation steps for the custom boundary condition:

- At the beginning of the run: Read the cgns mesh file on the master node and distributing it to all compute nodes
- At each start of time step: Read the variables from the last stored cgns variable data file on the master node and distribute it to all compute nodes
- First time boundary data are needed on a certain location for equation assembly: Compute a local index and coefficient map using a profile preserving interpolation technique - keep these local maps in memory for a given boundary patch, they are reused through the entire simulation
- At start of time step: Determine the flow rate repartition for the coming integration time step by an explicit Euler method, distribute the flow rate repartition to all compute nodes
- Every time boundary data are needed for equation assembly: Compute profile data by multiplying the data from the cgns files at indices indicated in the index map, multiplying by coefficients from the coefficient map. Each boundary integration point is obtained by linear combination of up to 4 stored values.

Time Integration

The terms on the right hand side of equation (9.12) or (9.18) are evaluated at the start of each time step integration. As a pressure value in the first implementation, a single pressure probe point at one location at the center of section 1^* is used; the mass flow weighted average of specific hydraulic energy is used for the improved implementation of the double suction pump study case. The values of the channel flow rates for the actual time step are determined explicitly by a first order Euler time integration. To avoid oscillations of flow rate and pressure values, occurring especially at the beginning of a simulation with unphysical initial values, the pressure value is staggered by half a time step, using the average of the last two time step levels 0 and 00. This adds a delay of $\Delta t/2$ to the behavior of the channel flow rate, which is acceptable for the small time steps required for a sufficient rotor stator interface time discretization. Together with a limiter on the actual flow rate variation per time step, active only on the first few time steps of a simulation, this allowed to stabilize the numerical procedure:

$$\mathbf{Q}' = \mathbf{Q}'^0 + \Delta t \left(\frac{1}{2}\beta_p^* \mathbb{K} \left(\mathbf{c}_p^0 + \mathbf{c}_p^{00} \right) + \beta_q^* \mathbb{K} \mathbf{Q}'^0 \right) \tag{9.20}$$

To account for accumulated velocity field interpolation errors that prove reproducible from time step to time step, the actual flow rate error is computed at the end of each time step to determine a common correction factor to all channel flow rates. This could easily be avoided with access to the boundary condition assemble, but is viable for the prototype implementation. The procedure converges to correction factors close to one and proves to keep the sum of relative flow rates stable within

$$\left| \sum_{k=1}^{z_b} Q'^{n+1}_k - z_b \right| < 2.10^{-4} \tag{9.21}$$

2D-Interpolation of the Boundary Values

For the interpolation of the boundary values, the procedure presented by Zhao [161] is adapted from two-dimensional planar grids to two-dimensional grids arbitrarily positioned in space. The solution of exact polynomial equations which is straightforward for planar elements is replaced by an iterative point projection on surface elements.

The algorithm treats the mesh nodes P_t of the target mesh sequentially as shown in figure 9.2. For each point P_t the elements of the source mesh that P_t can potentially be projected on are identified by a simple distance check. With an additional tolerance ϵ_R to allow extrapolation at the outer limits of the surface element patch the condition for eliminating elements is:

$$|\mathbf{X}_c - \mathbf{X}_t|^2 > \left((1+\epsilon_R)R_e\right)^2, \qquad R_e = \max\left\{ |\mathbf{X}_C - \mathbf{X}_i| \;\middle|\; i \in \{1,2,3,4\} \right\} \tag{9.22}$$

For the identified elements that are close to the point P_t it is then checked if:

$$((\mathbf{X}_j - \mathbf{X}_i) \times (\mathbf{X}_t - \mathbf{X}_i)) \cdot \mathbf{n} > 0 \tag{9.23}$$

for $i = [1,2,3,4]$ and $j = [2,3,4,1]$, until a corresponding element is found. When no such element is found, extrapolation is required since the target node is slightly outside

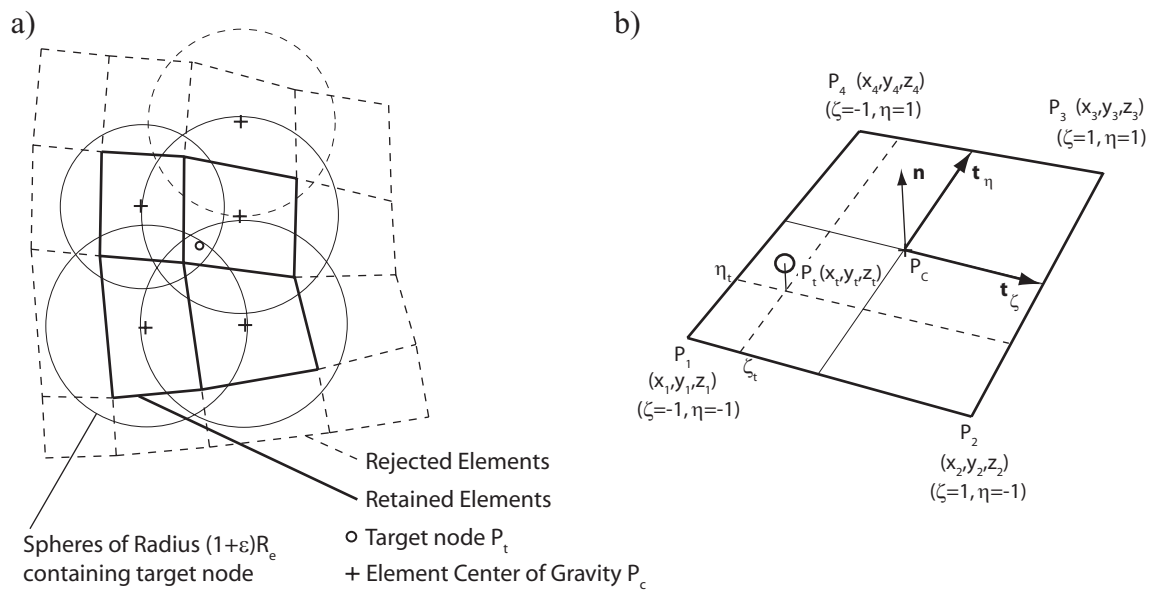

Figure 9.2: 2D-interpolation scheme. a) Fast element rejection criterium, b) Surface element parametrization

the source surface elements. The elements with the lowest ratio $(|P_tP_i| + |P_tP_j|)/(|P_iP_j|)$ is used to extrapolate. Once the element is chosen, dimensionless local coordinates η_t and ζ_z are computed by solving the following equation system:

$$\eta_t \mathbf{t}_\eta + \zeta_t \mathbf{t}_\zeta + \xi_t \mathbf{n} = \mathbf{X}_t - \mathbf{X}_C \tag{9.24}$$

The procedure is iteratively repeated with new basis vectors computed from iso-parameter lines inside the element, until a convergence criterium of 10^{-3} variation of η_t and ζ_t is met, which is after 2-4 iteration cycles depending on the orthogonality of the element. The interpolation rule for any scalar value ϕ from the 4 nodal values of the source element is:

$$\phi_t = \sum_{i=1}^{4} \sigma_i \phi_i \qquad \begin{aligned} \sigma_1 &= 0.25(1-\zeta)(1-\eta) \\ \sigma_2 &= 0.25(1+\zeta)(1-\eta) \\ \sigma_3 &= 0.25(1+\zeta)(1+\eta) \\ \sigma_4 &= 0.25(1-\zeta)(1+\eta) \end{aligned} \tag{9.25}$$

Faster schemes for nearest neighbor search (e.g. octree algorithms) and interpolation are known, but the computational cost of the current implementation has proved to be negligible compared to the resolution of the Navier-Stokes equations.

9.3 Validation: Rotating Stall in a Pump-Turbine

The mass flow weighted periodic inlet condition approach based on local pressure values at section 1* is validated on the case study of a Francis pump-turbine scale model showing rotating stall in the numerical simulation including all impeller channels at $\varphi = 0.032$, see chapter 8

9.3.1 Parameter Identification

From the simulation including all impeller channels conducted beforehand, all the terms of equation (9.18) containing the impeller channel parameters β_p^* and β_q^* are available for a relevant number of simulation time steps. Actually the implementation of the mass flow weighted periodic inlet condition was undertaken after validation of its applicability by the following parameter identification.

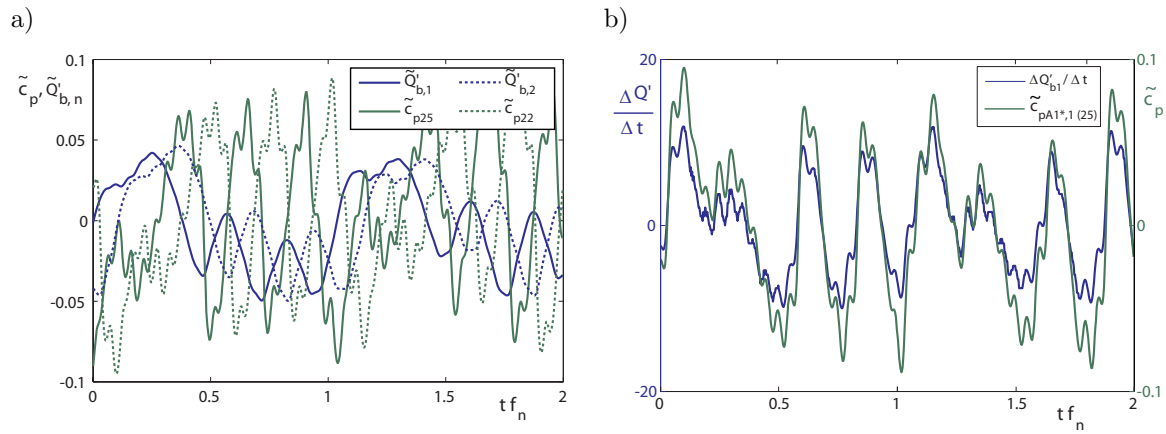

Figure 9.3: Correlation of pressure at impeller outlet and channel flow rate. a) Pressure and flow rate fluctuations for two consecutive impeller channels, b) Pressure fluctuation and channel flow rate variation per time step for impeller channel 1.

Time plots of pressure fluctuation and instantaneous impeller channel flow rate fluctuations, figure 9.3a, show that pressure and flow rate evolve in the same way for two consecutive impeller channels. The impeller channel flow rate is delayed in phase by $\pi/2$ with respect to the pressure. Tracing the relative impeller channel flow rate time derivative $\Delta Q'_{b,1}/\Delta t$ versus the pressure fluctuation values $\tilde{c}_{p,1*1}$ (at pressure sensor $P25$) reveals that the full domain simulation corresponds well to the monodimensional impeller model expressed in equation (9.4), with the pressure term being obviously the dominating over the resistance term.

A standard linear regression fit method on time domain data is chosen to identify numerical values of parameters for impeller channel modelling β_p^* and β_q^* of equation (9.18) from the full domain simulations. The method consists in a least-squares minimization of the vector $\boldsymbol{\epsilon}$ in:

$$\mathbf{Y} = \mathbf{X}\beta + \boldsymbol{\epsilon} \tag{9.26}$$

The vector of $z_b \cdot n_{ts}$ observations or response variable $\mathbf{Y}$, the matrix $\mathbf{X}$ of $(z_b \cdot n_{ts}) \times 2$ regressors and the parameter vector β are defined as follows with $i \in \{1, ..., n_{ts}\}$, $k \in \{1, ..., z_b\}$ and $l = (k-1) * n_{ts} + i$:

$$Y_l = \frac{\Delta Q'^{i}_{b,k}}{\Delta t} = \frac{Q'^{i}_{b,k} - Q'^{i-1}_{b,k}}{\Delta t} \tag{9.27}$$

$$X_{l,1} = c^{i}_{p,1*k} - \frac{1}{z_b}\sum_{j=1}^{z_b} c^{i}_{p,1*j} \qquad X_{l,2} = (Q'^{i}_{b,k} - 1)$$

$$\beta = \begin{pmatrix} \beta^*_p \\ \beta^*_q \end{pmatrix}$$

The following values are obtained for the parameters:

$$\beta^*_p = -167.5s^{-1} \qquad \beta^*_q = -29.30s^{-1}$$

A rough approximation to the equations (9.19) obtained with an approximate hydraulic inductance $L_b = l_{eq}/A_{eq}$ with the following length and cross section and neglecting the resistance yields:

$$A_{eq} = A_{1*} = 0.036m \times 0.060m \qquad l_{eq} = 0.300m$$
$$\beta^*_p = -151.7s^{-1} \qquad \beta^*_q = -30.86s^{-1}$$

This confirms a satisfactory agreement of the parameters identified from a 3-dimensional simulation with the simplified underlying assumptions on the flow in the impeller channels.

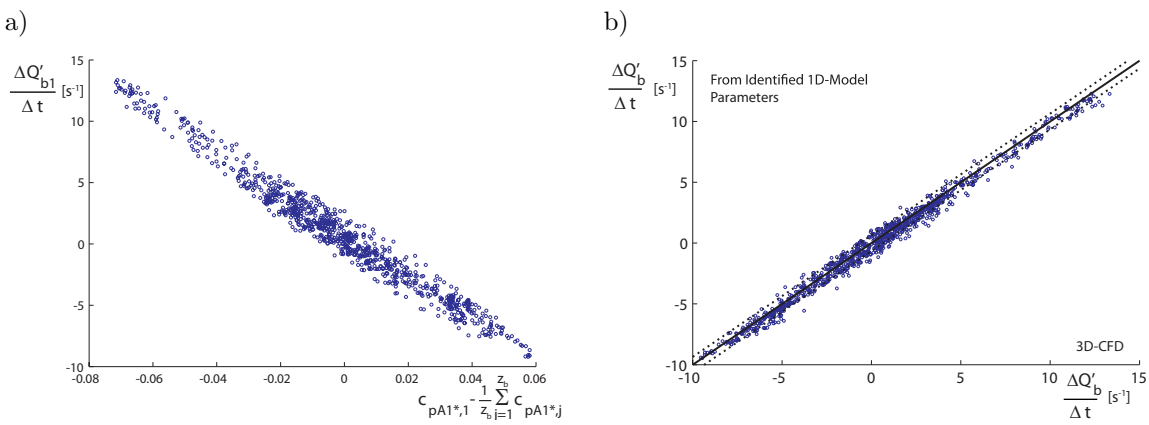

Figure 9.4: Identification of parameters for monodimensional impeller model a) Correlation of pressure at impeller channel outlet and flow rate variation per time step, b) Flow rate variation per time step obtained from identified parameters vs. full domain simulation flow rate variation, 95% confidence interval as dotted line

Figure 9.4a represents the correlation between the pressure values $c^{i}_{p,1*k}$ and the relative channel flow rate derivatives $\Delta Q'^{i}_{b,k}/\Delta t$, confirming that the pressure difference is the dominant influence governing the impeller channel flow rate evolution. Nevertheless, figure 9.4b, representing the flow rate derivative obtained by the two-regressor model with its fitted parameters β^*_p and β^*_q versus the original observations retrieved from the simulation shows that including the flow rate as a parameter improves the correlation.

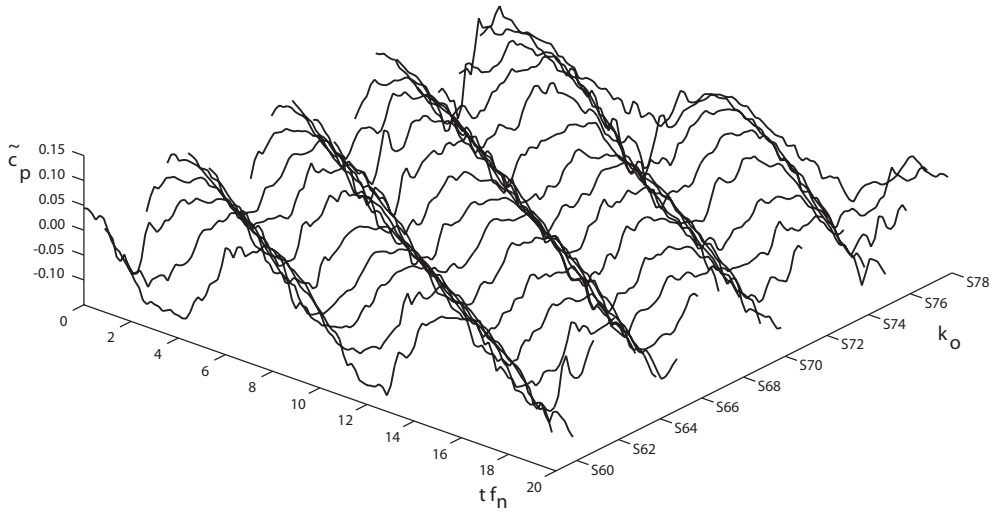

Figure 9.5: Pressure on sensors $S59$ to $S78$ at section $o2$; mass flow weighted periodic inlet conditions; (compare to figure 8.6)

9.3.2 Comparison to Full Domain Simulation

The simulation is performed at the same constant global flow rate and using the same mesh and numerical settings as the full domain simulation. As an initial solution, the variable fields from the full domain simulation are interpolated on the reduced domain grid.

Validation of Flow Distribution in the Diffusor

Due to the decreased problem size and possibly to a more regular repartition of the rotor-stator interface amongst the partitions, the numerical simulations using the periodic inlet boundary condition are computationally more efficient. A simulation of 40 impeller revolutions was conducted in 30 days using 8 processor cores divided over 2 compute nodes equipped with 6GB of memory each.

The global flow distribution and the pressure fluctuation level at the sensors close to the rotor-stator interface is well reproduced when compared to the full domain simulation, figures 8.6 and 8.10a. Figure 9.5 shows the pressure fluctuations on sensor locations $S59$ to $S78$. The rotating stall mode with $k_s = 4$ shows up in a more repeatable manner than in the shorter duration full simulation. Figure 9.6 represents the evolution of the diffuser channel flow rates over 30 revolutions. The flow rates of groups of 4 channels, located at 90° from each other, are nearly in phase. The range of diffuser channel flow rate fluctuations agrees reasonably with the one observed in the full domain simulations. Together with the increased regularity, the peak-to-peak range of those fluctuations is about 10% higher than in the full simulation.

The autocovariance functions of all pressure sensor signals is nearly identical, indicating a time lag of 8.6 to 8.8 impeller revolutions corresponding to 1/4 revolution of the stall wave, leading to a revolution rate of $\omega_S = 0.028\omega$. The pressure evolution along a diffuser channel and the pressure power spectra are given in figure 9.7 and compare well

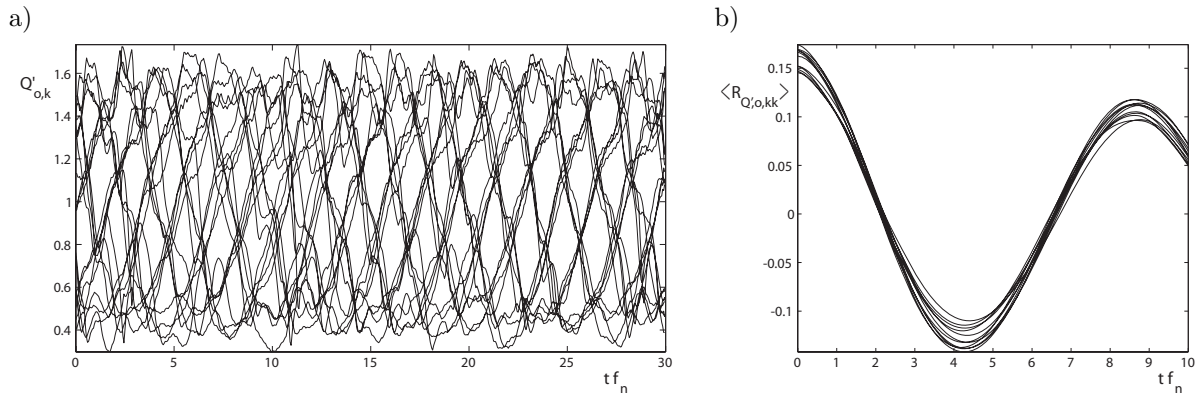

Figure 9.6: Diffuser channel flow rate distribution, mass flow weighted periodic inlet conditions. a) Diffuser channel flow rates, b) Autocovariance for rotation rate estimation (compare with figures 8.10 and 8.11)

with the results of the full simulation.

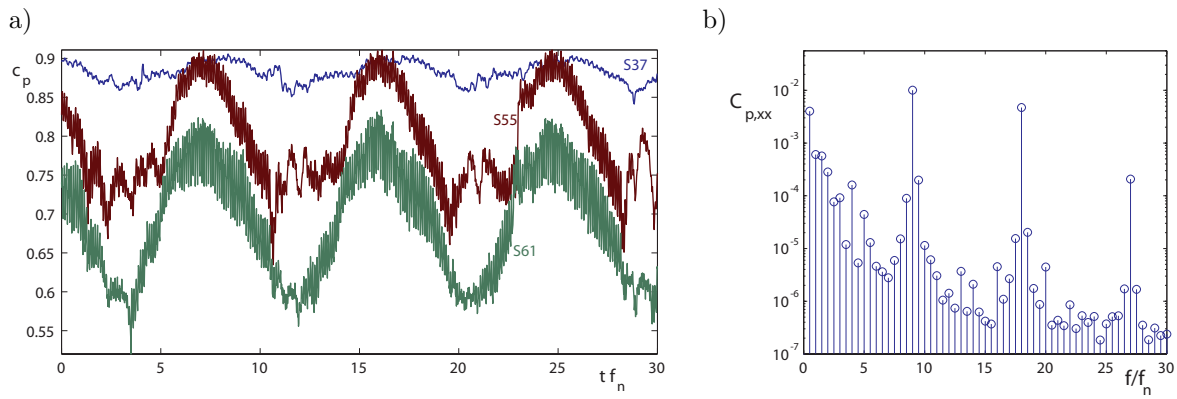

Figure 9.7: Pressure evolution in diffuser channel 3 and power spectra estimate at sensor S61, (compare with figures 7.13 and 8.7).

Impeller Flow Rate Fluctuations

The impeller channel parameters have been identified in order to best match the fluctuations of impeller channel flow rate. This is verified by the comparison of evolution of the impeller channel flow rate represented in figure 9.8. The peak-to-peak range of the fluctuations compares well. The fact that the established stall pattern is more regular and that the pressure fluctuation range is slightly higher is consistent with the slightly higher peak-to-peak amplitudes of the impeller channel flow rate fluctuations obtained when using the periodic inlet boundary conditions.

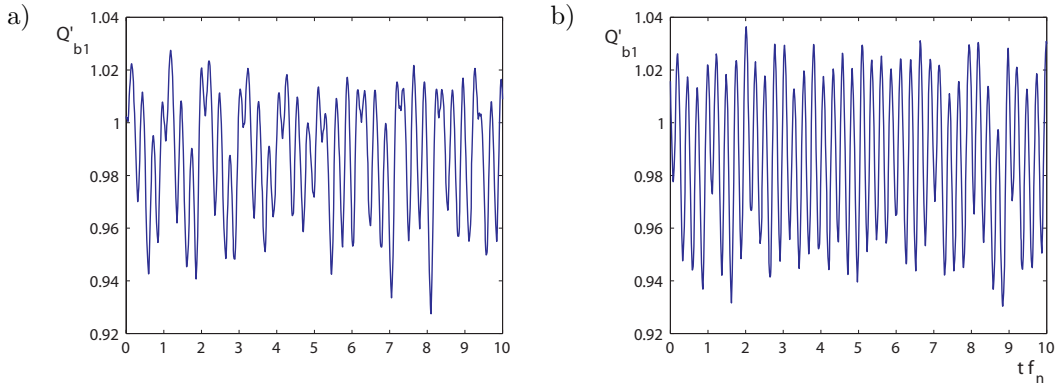

Figure 9.8: Impeller flow rate evolution over 10 impeller revolutions. a) Complete CFD simulations, b) CFD simulation using mass flow weighted periodic inlet conditions.

9.3.3 Validation of the Velocity Profile Scaling Procedure

A second important validation step is to justify the choice of scaling the velocity profiles linearly from the profile presently obtained from the reference channel. To this effect, velocity profiles at section 1* are extracted from the full domain simulation at stall conditions, where channel flow rate fluctuations are the highest. The impeller channel flow rates are fluctuating between 94% and 104% of its mean values. The same approach as the one used by the periodic inlet boundary condition is applied at every simulation time step with the results of the full simulation. Velocity profiles for channels $k = 2..z_b$ are interpolated from the reference channel $k = 1$ by scaling with the flow rate ratio $Q_{b,k}/Q_{b,1}$. Figure 9.9 compares the profiles of normal velocity on section 1* obtained from full domain simulations at the maximum value of channel flow rate and the corresponding minimum.

In this worst case situation for the linear scaling approach, minimum channel flow rate being considered as the reference, the figure shows that the overall velocity distributions correspond well. A closer analysis of the local scaling factor $W_{n,k}/W_{n,1}$, 9.9c shows that the velocity profiles do in fact not scale linearly with the instantaneous flow rate. The error between the profiles extracted at high flow rate from the full domain simulation and the one scaled from a minimum flow rate profile is of the order of the flow rate difference itself. Compared to the peak normal velocity in the section, the velocity error in the profile is up to 4%, but in zones of low normal velocity, the local relative error is higher. The reason for the relatively large difference of the fluctuations predicted by linear scaling and the one extracted from the full domain simulation lies in the highly nonuniform velocity field at section 1*. Possible improvements of the determination of the velocity profiles applied to the inlet conditions are discussed in chapter 9.5.

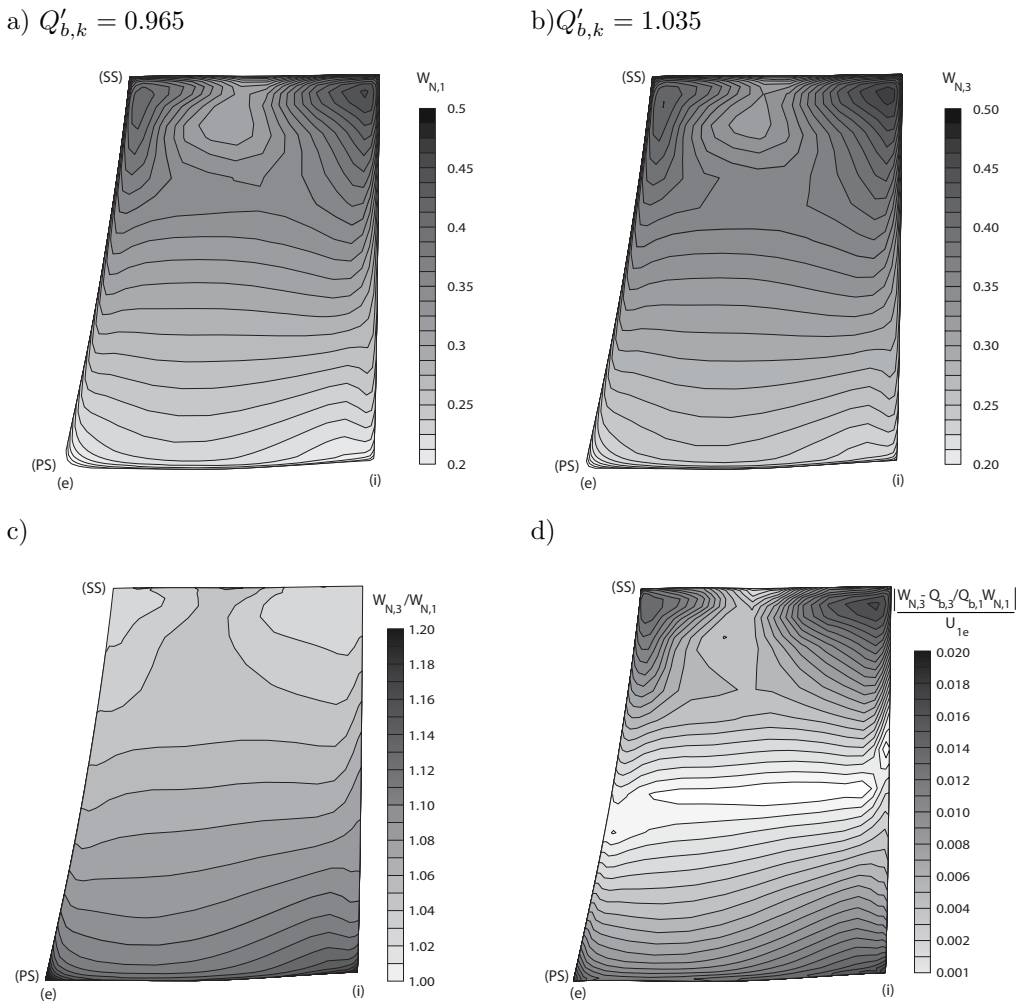

Figure 9.9: Validation of normal velocity scaling procedure: Example of direct scaling. a) Normal relative velocity at reference section $1*, 1$, b) Normal relative velocity at section $1*, 3$, c) Local velocity ratio, d) Error with flow rate ratio scaling.

9.4 Validation: Flow Rate Imbalance in a Double Suction Pump

In a double suction pump, the use of the mass flow weighted periodic inlet condition seems particularly beneficial as the number of impeller channels is twice as high than in a normal pump with the same hydraulic impeller design. Furthermore, the flow patterns obtained in part load for the full simulation revealed to be a particularly challenging study case for this approach.

Validation of Velocity Profiles at Section 1^* from Full Simulation

The asymmetrical velocity profiles at the rotor-stator interface suggest that the full simulation results must be evaluated to determine the degree to which this asymmetry affects the velocity profile at the section 1^*.

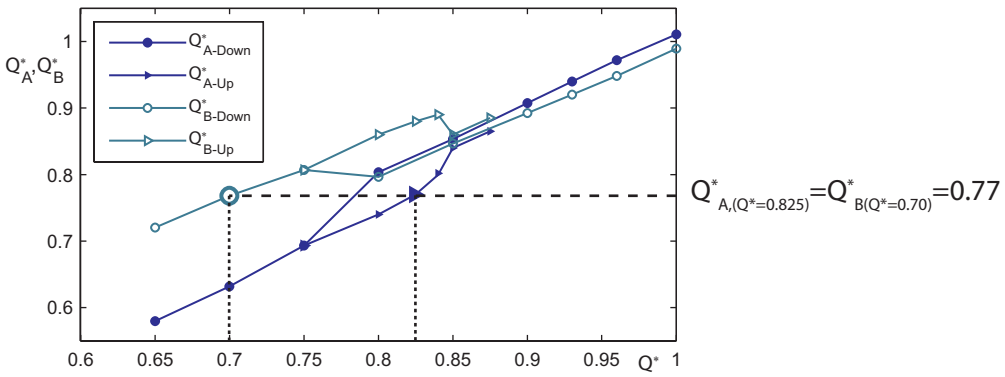

Figure 9.10: Asymmetrical flow configurations characterized by equal relative impeller side flow rates

Time-averaged profiles on the reference plane section 1^* and four further downstream are extracted from two different simulations showing asymmetrical flow, characterized by the same time averaged impeller side flow rate, as shown in figure 9.10. As qualitatively shown in the radial velocity profile graph on figure 9.11 and discussed for the conditions U and S, the averaged profiles on the rotor stator interface are far from being symmetric under these conditions. The evolution of the radial velocity component along the five planes shows that the difference can mainly be attributed to the flow on the last two planes while the flow on the first plane, corresponding to section 1^* is sufficiently close to symmetrical. The formation of the secondary flow vortices sketched in figure 9.11 is coherent with the asymmetric pressure field in the diffuser that comes along with the flow separation. The fact that the differences in the radial component in section 1^* are negligible compared to the changes that the flow undergoes in the triangular zone after the trailing edge supports the use of the periodic inlet conditions even for this case of highly asymmetrical flow in the rotor-stator interface region.

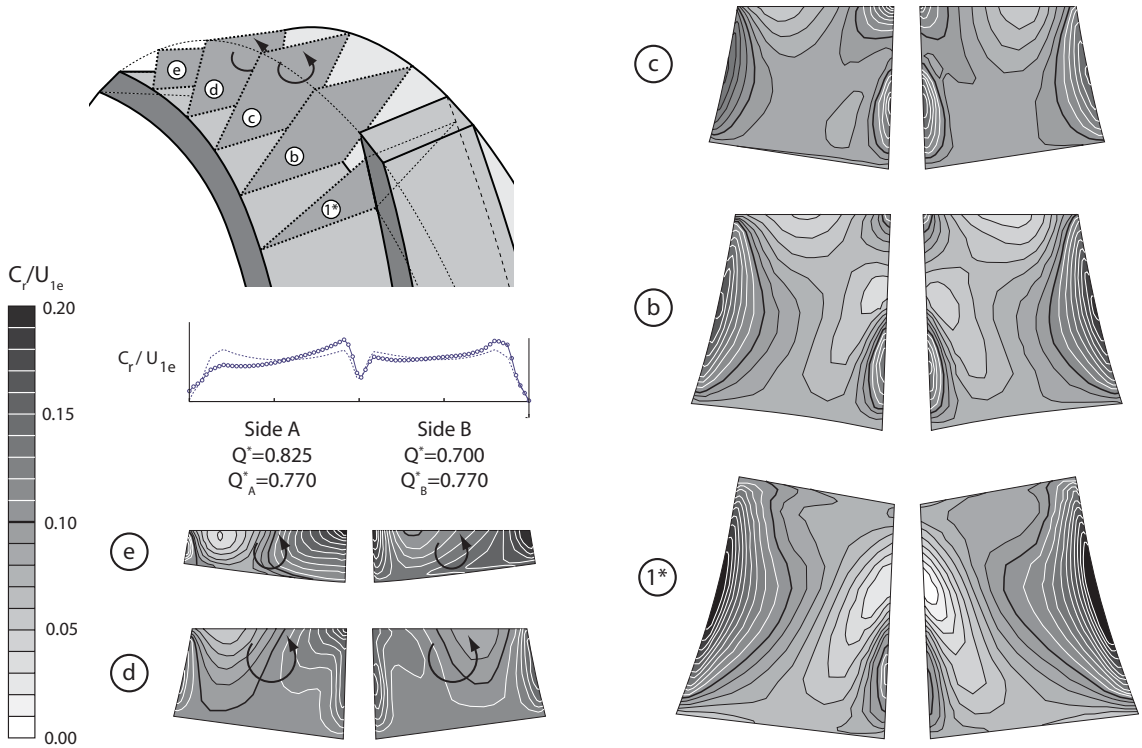

Figure 9.11: Radial velocity contours along 5 planes in proximity of the rotor-stator interface

Model Implementation and Parameter Identification

The periodic inlet conditions are applied using the same meshes that were used for the entire simulation. The size of the meshes in the rotating domain is reduced from 790′000 nodes to 308′000 nodes. The direct scaling of velocity profile from the reference channel by flow rate ratio is implemented. This is particularly critical since the time-average of the profiles on both impeller sides is expected to be different when the flow rate disequilibrium is established.

Numerical stability of the explicit scheme used to determine the flow rate repartition at the beginning of every time step is more difficult to obtain than in the pump-turbine study case, due to the smaller radial gap in the rotor-stator interface region. This constrains the simulation time steps to small values for the first blade passage simulated after interpolation of initial values, it is divided by 8 compared to the full simulation. For the remainder of the simulation a time step corresponding to 1/840 impeller revolution is used, which is half as large as the one used in the full model simulation. This time step limitation can certainly be overcome by an improved implementation using an implicit coupling or correction of the energy-flow rate relation along the internal coefficient loops within a time step.

For the identification of the parameter values, it is shown with this validation that no simulation of the full domain is necessary beforehand to identify the parameter values. Approximative values for the one-dimensional model's parameters are determined using geometrical properties of an average streamline according to equations (9.13): The ap-

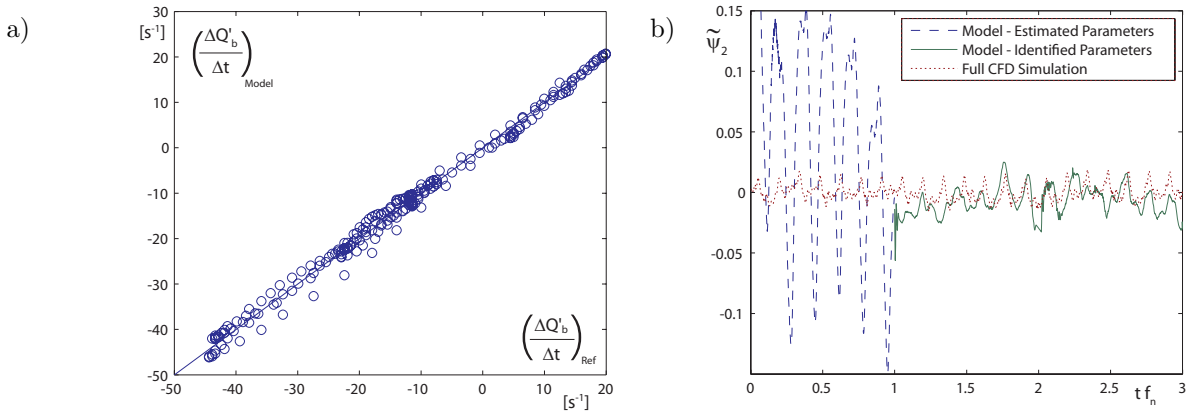

Figure 9.12: Parameter identification from preliminary simulation using estimated parameter values. a) Flow rate variation per time unit: 1D-model vs. CFD Simulation of reference channel, b)Fluctuations of relative hydraulic energy at $\bar{2}$ with estimated ($tf_n < 1.0$) and identified parameters ($tf_n > 1.0$) compared to full simulation.

proximative values are used to start the simulations with. Data on the sections of the reference channel $k = 1$ and the reference channel upstream energy $gH_{\bar{2}}^{rel}$ are retrieved and used to determine more accurate parameter values from this simulation with equation (9.4) reformulated to contain β_L and β_r.

$$\frac{dQ_{b,k}}{dt} = \beta_L \left(gH_{\bar{2}}^{rel} - gH_{1^*,k}^{rel}\right) + \beta_r \left(\frac{z_b}{2Q} {Q_{b,k}}^2\right) \tag{9.28}$$

The parameter identification procedure by linear regression fit is left aside the solver according to the current practice of executing time-dependent turbomachinery simulations by time intervals of limited length, typically one impeller revolution per run.

The result of the linear regression procedure is assessed by comparing the flow rate variation per time unit predicted by the model versus the one used in the CFD simulation with the preliminary parameters, see figure 9.12a. This comparison, as well as equation (9.28) involves the values of section $\bar{2}$. When using the model, equation (9.11) is used, that relies exclusively on values from the sections 1_k^*. Though the estimated parameters are considered insufficiently precise to serve for the definitive simulation setup, they lead to flow rate fluctuations of the reference channel that are sufficiently representative of the behavior in the final simulation and since that are a relevant basis for the improved parameter identification. The increased accuracy of representation achieved with the identified parameters is confirmed by a comparison of the fluctuation of relative specific hydraulic energy at $\bar{2}$. The fluctuation amplitude predicted with the identified parameters is in reasonable agreement with the full model when using the identified parameters while too high fluctuation amplitude were predicted using the estimated parameters.

Comparison to Full Simulation Results

Figure 9.13 shows the evolution of flow rate repartition between the impeller sides for simulations using the mass flow weighted periodic inlet conditions. The bifurcation to the

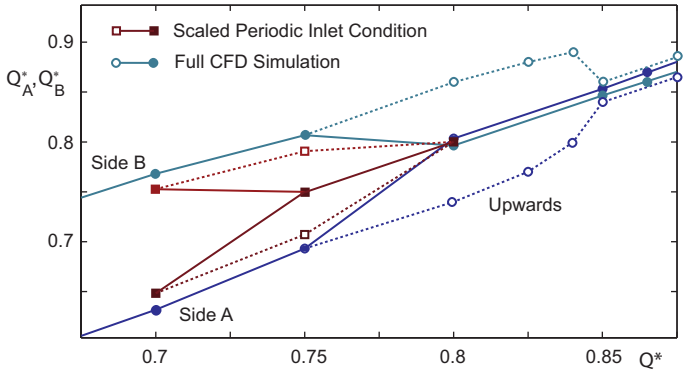

Figure 9.13: Evolution of the flow rates of both impeller sides: Comparison of periodic scaled inlet conditions vs. full simulation domain.

asymmetrical state occurs at lower flow rates and the hysteresis is less pronounced. At 80% BEP flow rate the full domain simulation exhibits two different, stable flow patterns depending on increase versus of flow rate. In contrast, the simulation using the scaled inlet conditions predicts a symmetric repartition of flow rates in any case. It is interesting to note that the reference channel chosen is located on impeller side B. By the scaling procedure based on the instantaneous reference channel profile a substantial error is made as the overall range of instantaneous channel flow rate differences sum up to 20% of the average flow rate, 10% due to the time-averaged difference of both impeller sides and ±5% of time-dependent fluctuations due to the variable energy level caused by alternate stall. Though the approach can reproduce the bifurcation to uneven flow rate repartition, there are serious quantitative errors caused by the velocity scaling procedure.

As for the full model, a stationary alternate pattern of stalled and unstalled diffuser channel is predicted from simulation at flow rates higher than 80% BEP, as represented in figure 9.4 as compared to figure 6.4. As for the pump-turbine study case presented in chapter 8, the circumferential distribution of diffuser channel flow rates pattern tends to be more pronounced and regular for the mass flow weighted periodic inlet conditions than with the full simulation domain.

The pressure fluctuations at the probe location on section 2, see figure 6.2, obtained using the mass flow weighted periodic inlet conditions are compared to those predicted by the full simulation in figure 9.15. As can be expected due to the more pronounced alternate stall of diffuser channels the dotted plot lines of the individual diffuser channels show a clearer distinction in groups of high and low diffuser channel flow rate with the mass flow weighted periodic inlet conditions than with the full simulation domain.

The overall pressure fluctuation range and waveform that reflects the staggered arrangement of the impeller blades are well reproduced, making the scaled inlet periodic condition approach a suitable tool to estimate pressure fluctuations in the complex situation of a double sided staggered impeller with staggered blades with a reduced computational effort. When using the approach of separate simulations for the reference impeller channel and the rotor-stator interface and diffuser domain (see chapter 9.5), modifications on the diffuser could be evaluated at lower cost based on the same impeller channel outflow characteristics.

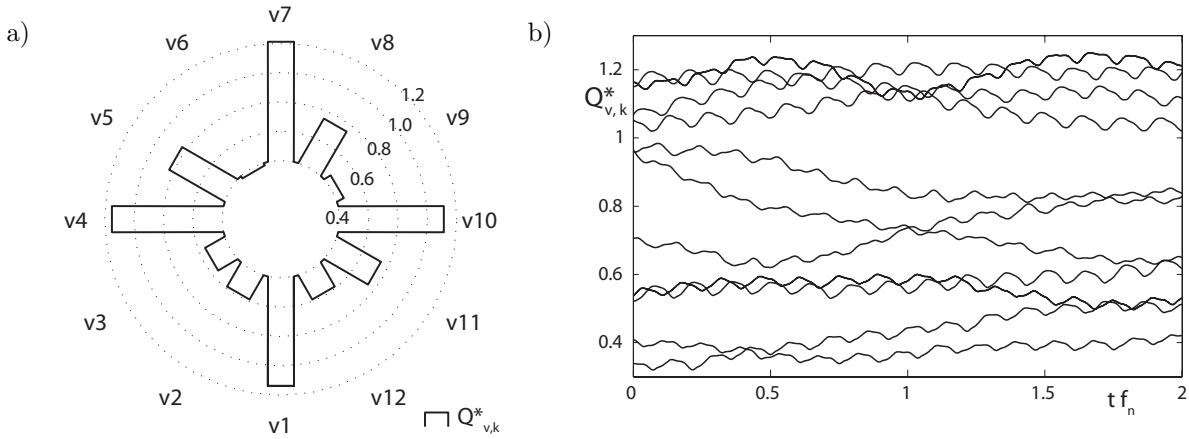

Figure 9.14: Circumferential distribution of diffuser channel flow rates at 80% BEP flow rate. a) Instantaneous circumferential distribution, b) Time evolution of all channels; (compare to figure 6.4)

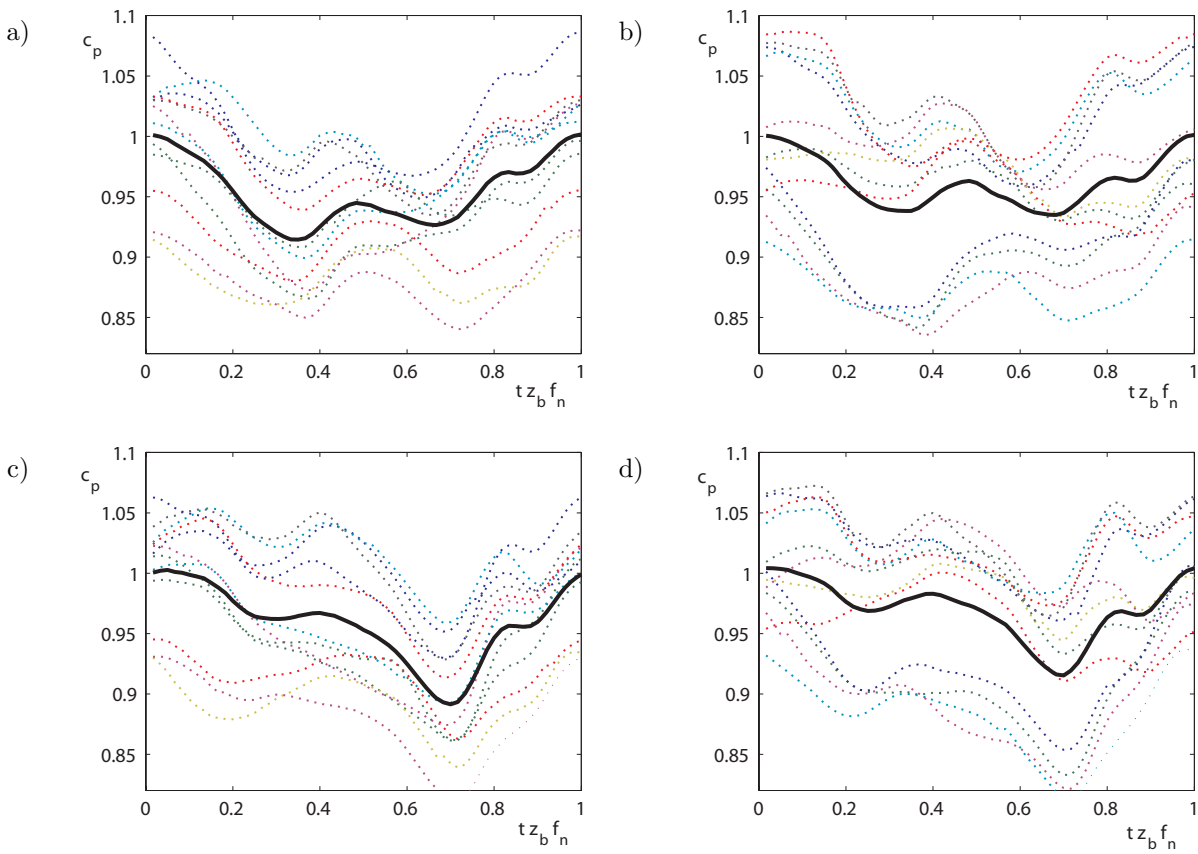

Figure 9.15: Blade-passage phase averaged pressure coefficient at points $p_{2\,v,k}$, $Q^* = 0.80$, symmetrical flow; individual values for each diffuser channel (dotted) and average of all channels (solid). a) Full CFD simulation, side A, b) Mass flow weighted periodic inlet conditions, side A, c) Full CFD simulation, side B, d) Mass flow weighted periodic inlet conditions, side A

9.5 Further Developments of the Periodic Inlet Condition Approach

9.5.1 Alternative Velocity Profile Scaling Procedures

Though the model implementation using the instantaneous profile from the reference section yields satisfactory results, several alternative procedures are briefly presented here, since for the case of the pump turbine with rotating stall the comparison of velocity profiles from the full simulation versus the ones obtained by simple scaling revealed significant differences.

The normal velocity component W_n as the one carrying the mass flow and most of the momentum through the section is considered. As an integral error indicator, the area weighted L^2-norm of the normal velocity differences between the model and the full CFD solution is used, based on a proposal of Roache [120] for solution differences over different control volume discretizations. With the control surface areas $a_{1*,i}$ of the section 1*:

$$\|\Delta W_n\|_{A_{1*},Model} = \left(\frac{\sum_i a_{1*,i}(W_{n,Model} - W_{n,CFD})_i^2}{U_{1e}^2 \sum_i a_{1*,i}} \right)^{1/2} \tag{9.29}$$

A simple alternative to the scaling from the instantaneous profile of the reference channel is to use a time-average profile $\overline{W_{n,b,1}(x,y,z)}$ obtained by averaging n_{ts} time steps of a given time period as a base profile for scaling.

$$\overline{W_{n,b,1}(x,y,z)} = \frac{1}{n_{ts}} \sum_{j=1}^{n_{ts}} \left(W_{n,CFD,b,1}(x,y,z)\right)_j \tag{9.30}$$

$$W_{n,ScaleMean,b,k}(x,y,z,t) = \frac{Q_{b,k}(t)}{Q/z_b} \overline{W_{n,b,1}(x,y,z)} \tag{9.31}$$

The relative errors are reduced in amplitude by a factor 0.5, while the qualitative repartition of errors remains the same as for the instantaneous approach. Both versions of velocity scaling, from instantaneous or from time average values, result in velocity fluctuations that are opposite to a simple consideration based on the time-dependent Bernoulli equation applied to different streamlines. A better though still simple approach is to add a constant normal velocity all over the surface in order to obtain the desired instantaneous flow rate:

$$W_{n,AddConst,b,k}(x,y,z,t) = \overline{W_{n,b,0}(x,y,z)} + \frac{Q_{b,k}(t) - Q/z_b}{A_{1*}} \tag{9.32}$$

This procedure decreases the error to about 30% of the original instantaneous scaling, which is an improvement, though not convincing.

The next step in complexity is to assume a locally variable flow rate scaling factor that is multiplied by the global flow rate ratio. This is equivalent to having a different local

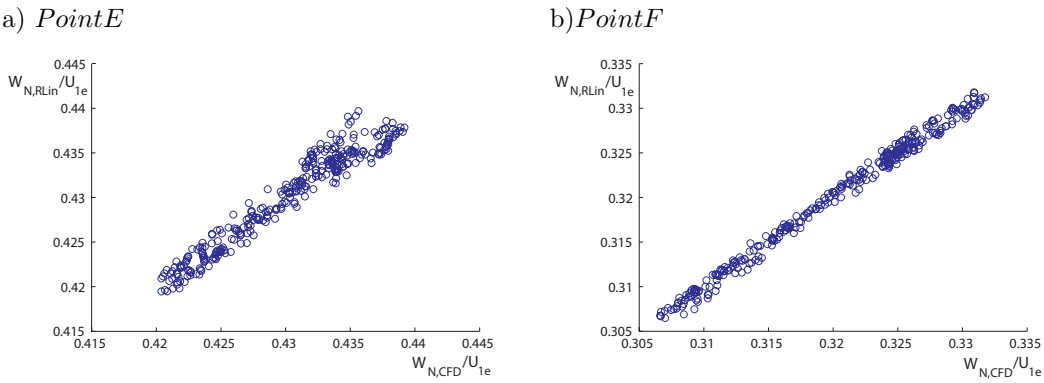

Figure 9.16: Normal velocity profile linear regression fit: Model versus data from complete simulation at selected points. a) Point E, b) Point F

impedance factor for every boundary control surface element. The normal velocity profiles at section 1* of all impeller channels of the entire machine simulation are considered. For every nodal value on the surface, a local velocity scaling factor is determined using a linear regression fit for the normal velocity with the instantaneous channel flow rate fluctuation and its derivative as independent variables:

$$W_{n,RLin,b,k}(x,y,z,t) = \overline{W_{n,b,0}(x,y,z)} + \gamma_Q(x,y,z)\frac{Q_{b,k} - Q/z_b}{A_{1*}} + \gamma_{dQ}(x,y,z)\frac{dQ_{b,k}}{dt} \quad (9.33)$$

Examples of the best and worst local regression fits of the normal velocity modeled, $W_{n,RLin}$ with reference to the velocity extracted from the full domain simulation $W_{n,CFD}$ is shown in figure 9.16 for the Points E and F, which present the highest resp. lowest standard deviation of the modeled versus full simulation values.

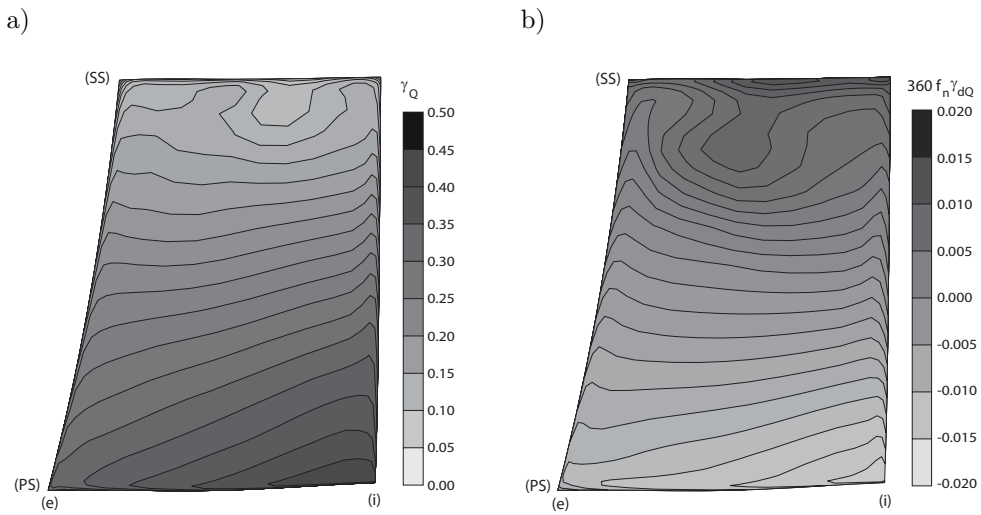

Figure 9.17: Local parameters for normal velocity profile model obtained by linear regression fit

The local model parameters γ_Q and γ_{dQ} are depicted in figure 9.17. The dominating independent variable is the channel flow rate, while the correction added by the derivative improves the prediction to a minor degree. The profile of the flow rate parameter γ_Q can be qualified as being inversely proportional to the mean velocity distribution, which corroborates the point that the straightforward choice of scaling velocity profiles is not the best.

a)$Q'_{b,k} = 0.998$ b)$Q'_{b,k} = 0.976$

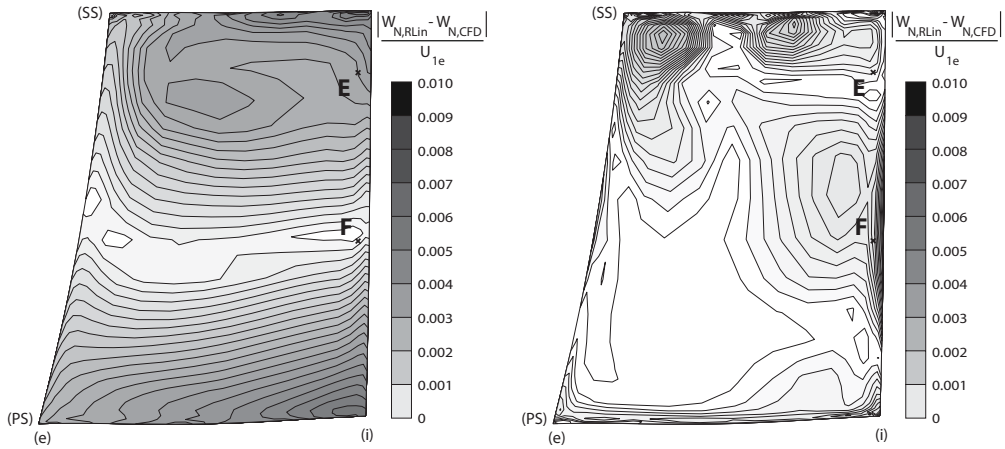

Figure 9.18: Local repartition of normal velocity differences. a) Maximum L^2-Norm, b) Improved L^2-Norm

The application of this local model thus reduces the error on large parts of the surface when compared with the simpler approaches. Figure 9.18 shows the error repartition for the time step and passage where the highest and lowest standard deviation of normal velocity values are assessed. In the case with the highest deviation, the model behaves only slightly better than the simpler approaches. But for the majority of time steps and passages, the qualitative behavior is like the one depicted in figure 9.18 b, with a small region of higher deviation in the high normal velocity "jet" zone close to the blade suction side. The transition from the two high velocity spots near hub and shroud to the low velocity central channel part does not correspond well to the model assumptions. For the rest of the section surface, the use of this model reduces the error substantially.

Figure 9.19 shows histograms of the area weighted standard deviation for normal velocity values (corresponding to the L^2-norm of the volume flux for this particular variable) evaluated for all channels and every 10th of 360 time steps of a revolution. The statistical distribution of this error is compared for the simple scaling model, 9.19a, the addition of a constant normal velocity to the mean value, 9.19b, and for the linear regression fit approach, 9.19c. The proposed procedure introducing two additional, locally variable parameters can significantly improve the modelling of the upstream channels. It can simply be built on top of the original modelling of the channel by a streamline equation. More sophisticated models, using more elaborate parameter identification techniques can be considered to improve the procedure. They can principally act and be based on integral

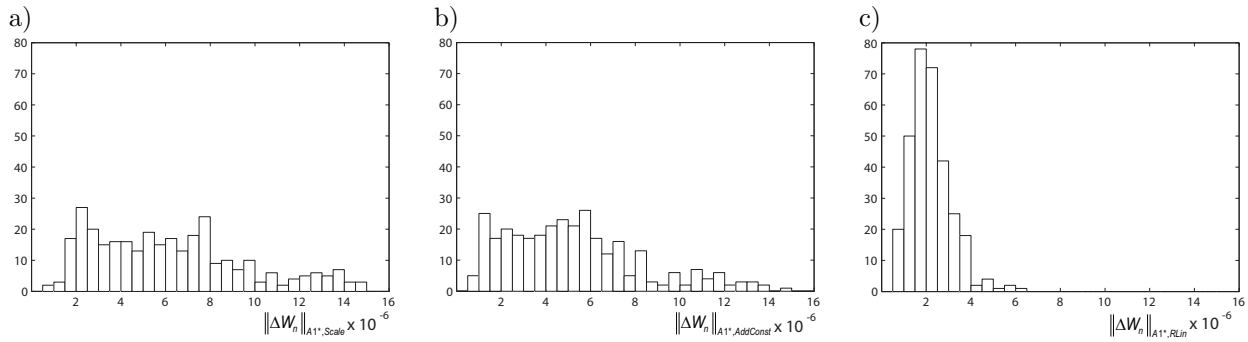

Figure 9.19: Histograms of L^2-norm error estimator of different modeling approaches for normal velocity. a) Scaling from instantaneous profile b) Adding a constant value from mean profile c) Model with locally variable coefficients fitted to full simulation data

and local values. Besides instantaneous values they could take into account time history or derived quantities such as an analytic phase.

9.5.2 Assessment of a Simplified Model

In cases such as the pump-turbine presented in chapter 7 with a large radial gap between impeller blade trailing edges and diffuser blade leading edges, one may ask if the fluctuation of impeller channel flow rates of about $\pm 4\%$ has a relevant influence on the presence and the circumferential propagation mechanism of the stall cells and on the pressure fluctuation amplitudes in the rotor-stator interaction zone. The large radial gap region allows a mixing of the flow exiting the different impeller channels before entering into the guide vanes. The ability of the implemented model to let the impeller channel flow rates evolve as a function of the upstream pressure level is suppressed by multiplying the channel parameters β_p^* by 10^{-2} and β_q^* by 10^2 for a short transition phase. Finally the relative channel flow rates are fixed to 1. Finally, in the simplified model the flow profile from the reference channel is simply copied to the remaining 8 inlet locations.

This fixed relative flow rate simulation on 6 revolutions is compared to the ongoing simulation using the variable flow rate model. The pressure evolution along one channel, see figure 9.20 remains similar, though not identical. The peak-to-peak amplitude at blade passing frequency on pressure sensor location $S61$ becomes slightly higher in the decreasing pressure phase. The fluctuations in the guide vane throat, sensor $S55$, around the pressure minimum are less pronounced with the simplified fixed flow rate model. The overall progression of the stall pattern persists, as seen in the continuous diffuser channel flow rate evolution represented in figure 9.21.

Given the considerable overall quantitative disagreement of the numerical model with the experiment, the influence of the variable flow rate in the impeller channels is of secondary importance for this study case.

A comparison of pressure at section $\bar{2}$ obtained for the double suction pump study case, compare figure 9.15, using the variable flow rate model versus fixed flow rates is represented in figure 9.22. Even in this case of small radial gap between the impeller channels and the diffuser blade leading edge the variable flow impeller channel flow rates

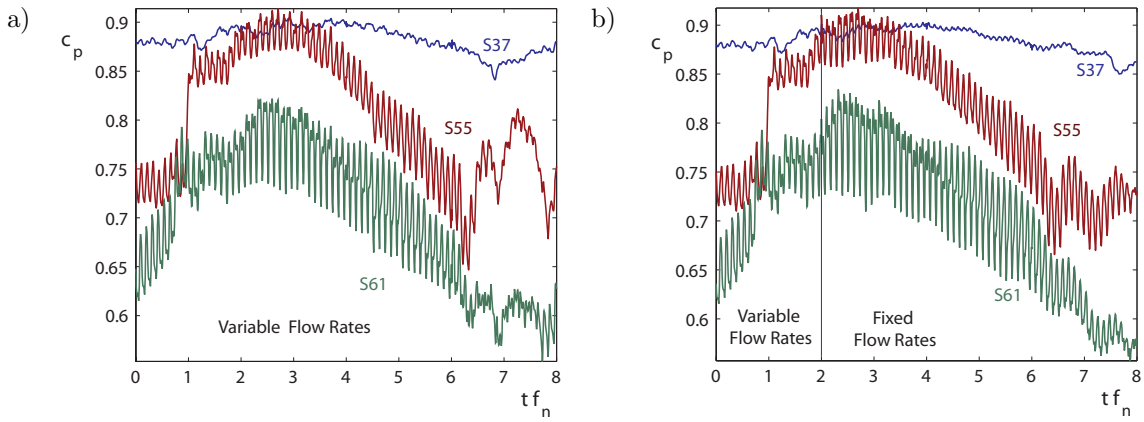

Figure 9.20: Pressure evolution. a) Mass flow weighted periodic inlet condition using variable flow rates, b) Periodic inlet condition switching to fixed flow rates

have only a slight influence. The impeller channel flow rate fluctuation of the order of magnitude of ±4% does not impact much on the pressure evolution at the diffuser channel inlet. Recalling the electrical analogy presented in figure 9.1 one can conclude that the impeller channels are characterized by a high impedance compared to the behavior of the alternate stall cells governing the upstream pressure level. In the local frame, the attenuation of pressure fluctuations due to the finite impedance of the impeller channel flow is barely detectable on the average of all pressure probes. From the phase average of individual probes it can be seen that the maxima caused by the individual blade passages are more pronounced for the simulation using the fixed flow rates. Still, it is confirmed that the simplified approach using fixed flow rates yields valuable results for the blade passage phase averaged pressure fluctuations. But the simplified approach cannot reproduce the uneven repartition of flow rate between impeller sides.

9.5.3 External Implementation of Impeller Channel Modelling

Satisfying results are obtained using the mass flow weighted periodic inlet conditions implemented in the flow solver, regrouping the reference impeller channel resolved by the Navier-Stokes equation in the same simulation than rotor-stator interface region and diffuser domain. An approach separating the determination of the impeller channel exit profiles is appealing due to the following advantages:

- Further size reduction of the main simulation (rotor-stator interface and diffuser) domain and possible improvements of parallel scalability. Partitioning approaches driven by an equilibrated repartition of the rotor-stator-interface control volumes are easier to handle without the reference impeller channel.

- Fully deterministic rules for the impeller channel behavior seem to converge faster towards pronounced patterns of alternate and rotating stall. This is a limitation of the model in one sense, but is also a way to focus the analysis on the influence of diffuser design suppressing some of the additional degrees of freedom introduced by the full impeller model. Modifications of impeller side stagger or even on design

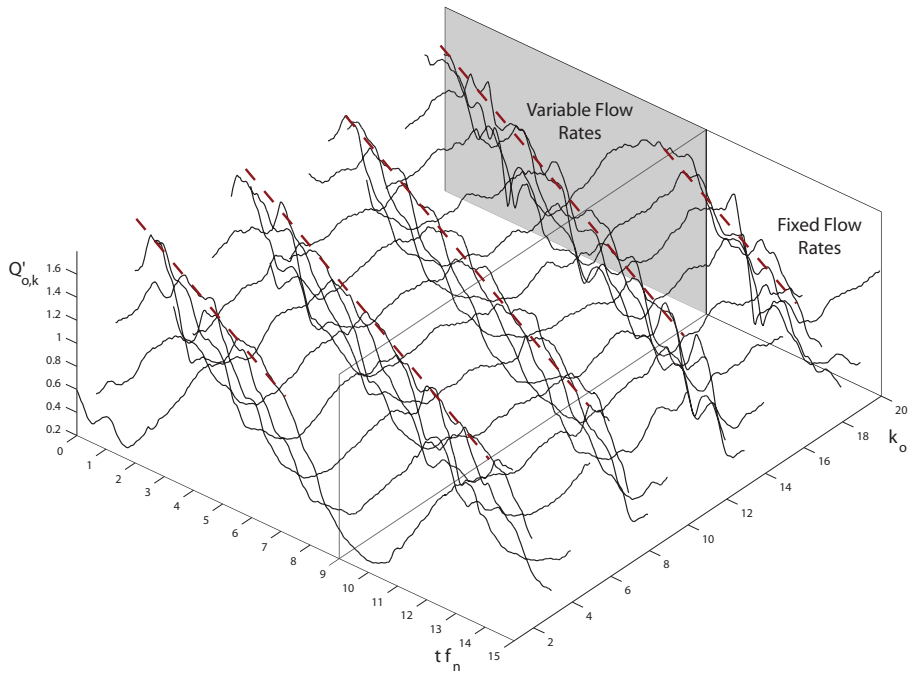

Figure 9.21: Evolution of the flow distribution in the diffuser when switching from variable to fixed impeller channel flow rates

details at the impeller outlet can be covered by this approach if the section 1* is chosen at a reasonable distance upstream of the impeller blade trailing edge.

- When relevant differences in instantaneous impeller channel flow rate occur, the instantaneous reference impeller channel flow rate is not of much value to determine the flow profiles for the remaining inlet conditions, as seen in the double suction pump case study. An improved procedure to generate profiles to determine the inlet condition profiles as proposed in 9.5.1 is easier to implement separately from the core CFD solver as the parameter identification can take advantage of large databases acquired from several independent simulations.

Figure 9.23b schematically represents such an approach compared to the implemented prototype 9.23a. A main issue emerges from the formulation of a suitable, numerically stable outlet condition that would ideally not require an expensive rotor-stator interface technique while providing a sufficiently accurate model to generate the pressure potential influence acting upstream of the diffuser blades.

A second question arises from the inlet flow rate boundary which must be imposed to allow identification of the relevant parameters determining the velocity profiles at 1*. An approach using the combined simulation domain to provide the external profile database and parameter identification tool with "learning" datasets seems an appropriate solution to these problems. The procedure applied during this "learning" phase of the modeling tool is represented in figure 9.23c. Compared to the implemented procedure, figure 9.23a, this could benefit from a highly refined mesh in the impeller channel and the relevant downstream rotating domain part together with a coarser mesh in the diffuser. Once the model for the velocity profiles is built, the reduced domain of figure 9.23b with

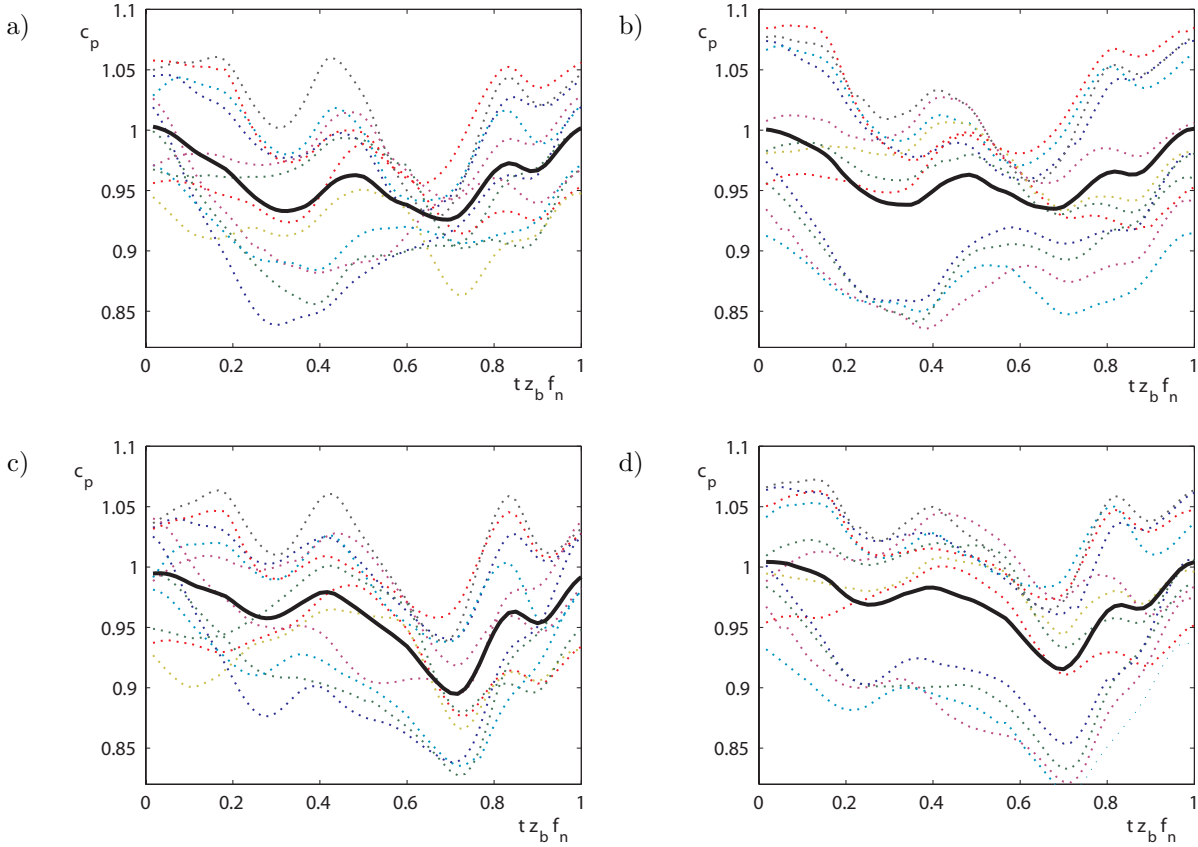

Figure 9.22: Blade-passage phase averaged pressure coefficient at points p_{2vi}, $Q^* = 0.80$, symmetrical flow; individual values for each diffuser channel (dotted) and average of all channels (solid). a) Model with fixed channel flow rates, side A, b) Model with variable flow rate, side A, c) Model with fixed flow rates, side B, d) Model with variable flow rate, side B

a fine mesh can be used. The external tool providing boundary conditions could be coupled to the CFD solver by interprocess communication via TCP-IP as is successfully done for monodimensional simulation tools providing boundary conditions for 3D-CFD simulations. This method can be compared to the current practice to split simulation domains and transfer velocity profiles used in steady simulation approaches, transferring however a more sophisticated parametric model instead of a simple profile.

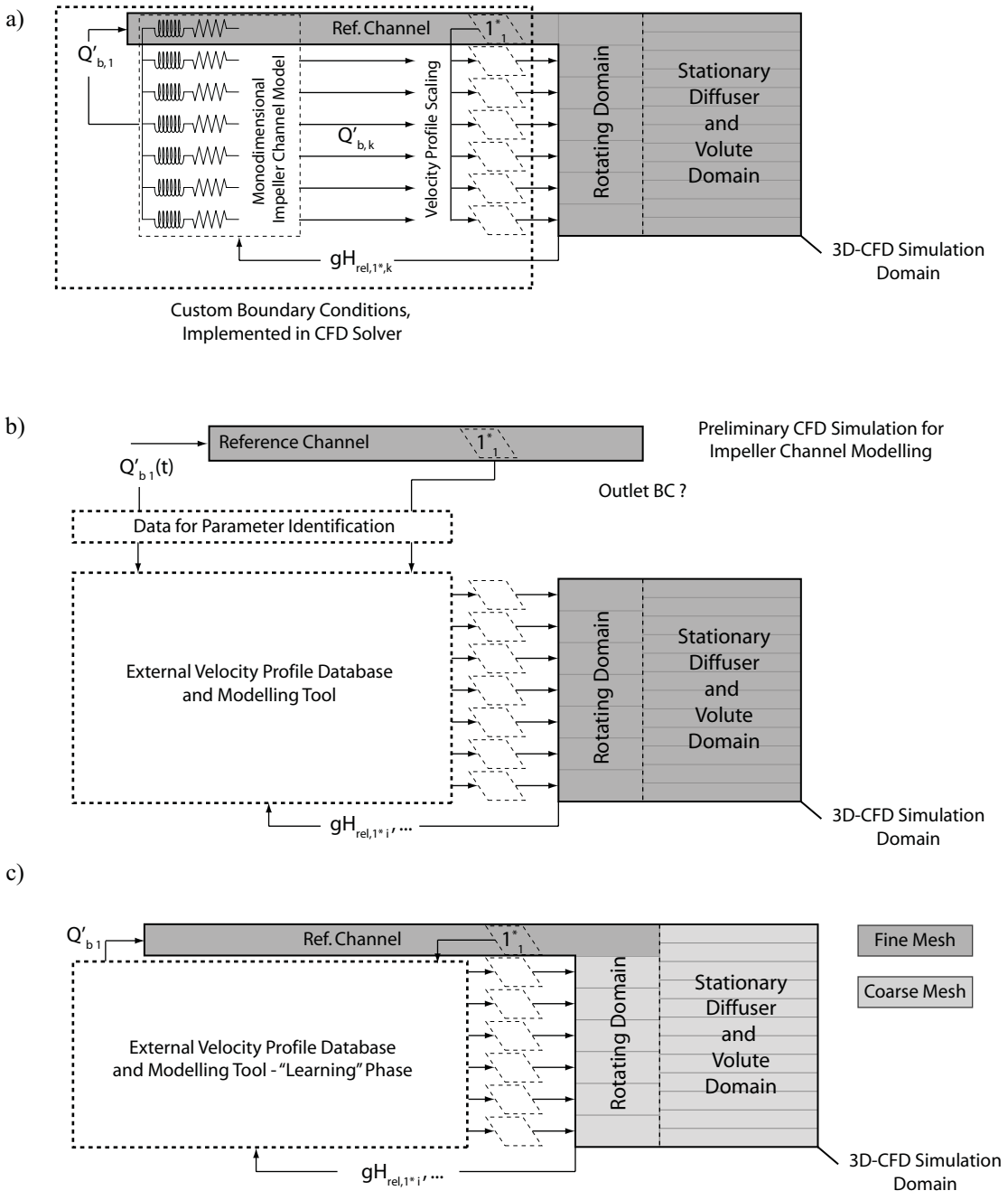

Figure 9.23: Different approaches and software architectures for impeller channel modelling. a) Custom boundary condition in CFD solver as implemented, b) External profile database and modelling tool, c) Learning phase with complete diffuser domain coarsely meshed

Conclusions & Perspectives

Conclusions & Perspectives

Conclusions

The present work is a contribution to the physical analysis and numerical simulation methodology of part load flow in radial centrifugal pumps. Three different case studies are analyzed and show different flow phenomena occurring in radial centrifugal pumps and pump-turbines with positive slope on the energy-discharge characteristic.

Steady state simulations assuming periodicity of the different blade channels show how a sudden change of flow topology in the diffuser at decreasing flow rates induces increased viscous losses, impinging severely on the energy coefficient of the pump-turbine.

A numerical study on a double suction pump shows flow separation in separate diffuser channels in form of stationary or rotating stall. Furthermore, an imbalance of flow rates between both impeller sides is found for discharge conditions below 80% of BEP flow rate. This is caused by a symmetry-breaking flow separation on one of the diffuser side walls that is manifest through an asymmetric pressure distribution leading to different pressure levels upstream of both impeller sides. A hysteresis between the onset of the imbalance at decreasing flow rates and the return to balanced flow rates at increasing flow rates is found. The sparse available experimental data do not allow to confirm this interesting hypothesis found from the numerical simulation, but the decrease of the energy coefficient related to the occurrence of the flow imbalance corresponds well to a segment of positive slope in the measured energy-discharge characteristic. As for the pump-turbine study case, the critical flow rate where the positive slope in the characteristic curve is predicted does not correspond well to the one found by measurement.

Since no sufficiently detailed experimental flow surveys are available to validate the complex three-dimensional flow found with the two first study case numerical simulations, complementary numerical and experimental investigations on the part-load flow in a Francis pump-turbine scale model are carried out. Experimental flow surveys obtained from simultaneous transient pressure measurements with non-intrusive optical velocity measurements (laser-Doppler-velocimetry, LDV) are compared to the results obtained from time-dependent numerical simulation based on unsteady RANS turbulence modelling.

The experimental study shows the occurrence of rotating stall over a large range of part load operating conditions from 40% to 85% of BEP flow rate. The dependency of the number of stall cells and of its rotation velocity of the flow rate is evidenced by 2D DFT analysis of transient pressure measurements. The simultaneous LDV and transient pressure measurements are implemented for operating conditions where rotating stall with 4 stall cells rotating at 0.021ω occurs. A stall phase based on pressure measurements is

defined and velocity fields on two-dimensional sections of interest are reconstructed from the point-wise LDV measurements by phase averaging with respect to this stall phase. The results of this analysis show the evolution of flow separation in a diffuser channel along the passage of the stall cell. It was found that the flow separation zone originating from the guide vane trailing edge grows until reverse flow extends over the upper third of the guide vane throat section. By integration of the normal velocity field over the guide vane throat the instantaneous diffuser channel flow rate is found to fluctuate in a range from 40% to 140% of the average channel flow rate Q/z_v.

Qualitatively similar flow with an occurrence of stall with 4 stall cells, including the evolution of flow separation during a stall cell passage, is found with time-dependent numerical simulation using RANS turbulence modelling, but at a sensibly higher flow rate than in experiment. The computational cost of the time-dependent simulation is considerable due to the sizes of the simulation meshes ($4.5 \cdot 10^6$ nodes) and to the long simulation times needed to capture low frequency phenomena such as rotating stall: More than 20 impeller revolutions were simulated for each considered operating point.

In consideration of this fact, comprehensive studies on the influence of additional parameters, such as a comparison of different varieties of RANS turbulence models, turn out to be impractical with the current simulation approaches. The relevant refinement of the simulation meshes that is necessary to take advantage of advanced numerical modelling such as LES or DES remains a major challenge to the implementation of efficient numerical tools.

The lack of quantitative accuracy of such time dependent simulations can be attributed to the high numerical diffusion, as evidenced by the preliminary numerical case studies, and to the inability of common RANS turbulence models to predict the time-evolution of flow separation correctly. Given the complex interaction of the occurrence of flow separation with the time constants impressed by the inertia of the flow in the diffuser channels, the accurate prediction of the time-dependent separated flow in such a diffuser remains a major challenge for numerical simulation methods.

In consideration of the encouraging qualitative results of the numerical simulation together with the quantitative discrepancies, a novel modelling approach is developed. It is based on the assumption of sound flow in the impeller channels, replacing the major part of the impeller channel computing domain by a one-dimensional modelling approach. So, the computational cost for a given simulation can be significantly reduced, or a better spatial resolution of the relevant rotor-stator interface and diffuser regions can be achieved under given computational cost constraints.

The prototype implementation of the approach into a commercial finite volume solver consists in a custom inlet boundary condition, best described as a mass flow weighted periodic inlet condition. It is validated for the challenging cases of a pump turbine with rotating stall and a double suction pump with an imbalance of impeller side flow rates. For the rotating stall case, an excellent agreement with the results of the full simulation is found. For the double suction pump case, the hysteresis of flow rate imbalance can not be exactly reproduced, but possible improvements of the models are proposed to better take into account the difference of average impeller channel flow rates between one impeller side and the other.

Perspectives

The time-dependent numerical simulation method based on a finite-volume discretization of the RANS-equations has proven its ability to predict complex flow phenomena in centrifugal pumps and pump-turbines. Diffuser flow separation, the resulting rotating stall and a plausible impeller side flow rate imbalance in a double suction configuration are predicted qualitatively. In consideration of the quantitative disagreement with experiments, improvements in accuracy of the numerical methods are required to qualify numerical simulation as a reliable tool to predict part-load behavior of centrifugal pumps for design purposes:

Enhanced Turbulence Modelling: The Reynolds-averaged approach determining the Reynolds stresses with a two-equation turbulence model is the best feasible simulation approach within the limit of today's computational resources. With further advances in high performance computing together with algorithmic improvements leveraging the potential of massively parallel computing environments, advanced numerical methods requiring higher spatial and temporal resolution will come within reach in the next decade. Large Eddy Simulation (LES) and hybrid approaches such as Detached Eddy Simulation (DES) are likely to enhance the accuracy of numerical simulation for turbomachinery applications when compared to time-dependent RANS approaches. However, a thorough validation of such models on simpler, but relevant study cases is mandatory before application to entire turbomachine configurations. Relevant study cases are oscillating hydrofoils or branched diffusers, where time dependent inlet conditions or time-varying geometry triggers flow separation. Study cases where flow separation triggered by a simple blade-wake interaction come even closer to the real flow situation in turbomachines. The capability of accurate prediction of the onset of flow separation and of the subsequent evolution of the flow field in such study cases qualifies a modelling approach for the prediction of part-load flow in centrifugal pumps.

Numerical Procedure: Numerical simulation with the usual upwind-based discretization schemes for finite volumes in complex geometry suffers from numerical diffusion, manifest in an imbalance of the modeled viscous dissipation versus energy fluxes through the control volume boundaries. While in steady state or time-dependent RANS-based computations, these errors tend to cancel out with the diffusion introduced by the turbulence model, the conservation of kinetic energy is essential in methods resolving the large turbulent scales. Alternative numerical methods and discretization schemes conserving kinetic energy better, such as centered schemes in finite volume methods, are more demanding in terms of the quality of the volume mesh and limit the time discretization step size due to their reduced numerical stability. These additional constraints constitute a challenge for the application of advanced numerical methods with high Reynolds number flows in complex geometries such as turbomachines. Improvements in numerical methods alleviating some of the constraints are highly desirable.

Toward Multi-Scale Modelling

The mass flow weighted periodic inlet condition developed and validated in this work allows discarding a relevant part of the 3-dimensional simulation domain of the impeller. This considerable economy of computing resources permits the use of relevantly refined meshes. Especially, the increase in computational cost when refining the reference impeller channel mesh is not multiplied by the number of impeller channels. This brings the use of turbulence models resolving the large turbulent scales in time-dependent simulation into reach. However, some improvements and extensions to the current implementation are desirable to further increase its benefits.

An implementation of the boundary condition as an external tool with a well defined interface makes it possible: (i) to use this tool with different flow solvers, (ii) to build a complex tool keeping track of flow profiles obtained from the ensemble of realized numerical simulations and use this as a basis for an improved modelling, (iii) to include other existing tools implementing additional physical modelling such as variable rotational velocity and fluctuating net mass flow due to hydro-acoustic effects. A successful coupling implementation of a commercial flow solver with a 1-dimensional hydro-acoustic simulation software by interprocess communication as well as the approaches currently used for fluid-structure-interaction can serve as an implementation model for a tool that generates space- and time-dependent boundary conditions.

The use of this approach with methods resolving the large turbulent scales adds a level of complexity to the generation of inlet boundary conditions depending on space and time, since the relevant turbulent structures have to be imposed in a physically coherent manner by the inlet boundary condition. The most appealing implementation is a tool regrouping the functionality of post-processing and analysis of former simulations with the capability to generate physically realistic inlet conditions as a function of quantities extracted from the concurrent numerical simulation.

The principle of the implemented boundary condition can directly be applied to the related approach of decomposition of the simulation domains of complex application in two totally separate flow simulations. The formulation of a surrogate model for the time-dependent inlet condition of the second domain leverages a procedure commonly used in simulation of stationary flows to its application with time-dependent flow problems. Instead of transferring a static velocity profile from the upstream to the downstream domain flow simulation, a model is formulated and its parameters are identified from the upstream domain simulation and serve to generate boundary condition values depending on time and downstream flow variables.

The same principle as shown in this work for the identification of the parameters governing the impeller channel flow rates can readily be applied when 3-dimensional numerical flow simulations are consulted to identify parameters such as hydraulic inductance (inertial length), hydraulic resistance of isolated components of complex systems. 3-dimensional simulations including the effects of fluid compressibility, phase changes and fluid-structure interaction can provide the hydraulic capacitance values, essential to the modelling of hydro-acoustic phenomena. By this way, 3-dimensional numerical flow simulation can contribute to the successful 1-dimensional modelling of systems that are too complex to be treated by a 3-dimensional approach. It is an attractive alternative where analytical or experimental methods are not practical.

Bibliography

References

[1] IEC 60193 International Standard - Hydraulic turbines, storage pumps and pump turbines - Model acceptance tests. International Electrotechnical Commission, 1999.

[2] CGNS, the CFD general notation system-standard interface data structures. The CGNS Steering Sub-committee of the AIAA CFD Committee on Standards, 2002.

[3] CFX-11: ANSYS-CFX solver theory guide. ANSYS Canada Ltd., 2006.

[4] *ERCOFTAC SIG SPHERIC IIIrd International Workshop Proceedings* (Lausanne, Switzerland, 2008).

[5] Abramian, M., and Howard, J. Rotating laser-Doppler anemometry system for unsteady relative flow measurements in model centrifugal impellers. *Journal of Turbomachinery 116*, 2 (1994), 260–268.

[6] Adrian, R., and Yao, C. Power spectra of fluid velocities measured by laser doppler velocimetry. *EXP. FLUIDS 5*, 1 (1987), 17–28.

[7] Albrecht, H.-E., Borys, M., Damaschke, N., and Tropea, C. *Laser Doppler and Phase Doppler Measurement Techniques*. Springer Verlag, Berlin, 2003.

[8] Ali, I., Escobar, M., Kaltenbacher, M., and Becker, S. Time domain computation of flow induced sound. *Computers and Fluids 37*, 4 (2008), 349–359.

[9] Apsley, D., and Leschziner, M. Advanced turbulence modelling of separated flow in a diffuser. *Flow, Turbulence and Combustion 63*, 1 (2000), 81–112.

[10] Arndt, N., Acosta, A., Brennen, C., and Caughey, T. Rotor-stator interaction in a diffuser pump. *Journal of Turbomachinery 111*, 3 (1989), 213–221.

[11] Ausoni, P., Farhat, M., Escaler, X., Egusquiza, E., and Avellan, F. Cavitation influence on von Kármán vortex shedding and induced hydrofoil vibrations. *Journal of Fluids Engineering, Transactions of the ASME 129*, 8 (2007), 966–973.

[12] Bendat, J. S., and Piersol, A. G. *Random Data : Analysis and Measurement Procedures*. John Wiley and Sons, 2000.

[13] Benedict, L., Nobach, H., and Tropea, C. Estimation of turbulent velocity spectra from laser doppler data. *Measurement Science and Technology 11*, 8 (2000), 1089–1104.

[14] Berger, E., and Wille, R. Periodic flow phenomena. *Annual Review of Fluid Mechanics 4*, 1 (Jan. 1972), 313–340.

[15] Berger, S., Talbot, L., and Yao, L. Flow in curved pipes. *Annual Review of Fluid Mechanics 15* (1983), 461–512.

[16] Bolleter, U. Blade passage tones of centrifugal pump. *Vibrations 4* (1988), 8–13.

[17] Bosch, G., and Rodi, W. Simulation of vortex shedding past a square cylinder with different turbulence models. *International Journal for Numerical Methods in Fluids 28*, 4 (1998), 601–606.

[18] Bourdet, S. *Analyse physique d' écoulements compressibles instationnaires autour de structures portantes dans le contexte d'interaction fluide-structure.* PhD thesis, Institut National Polytechnique de Toulouse, 2005.

[19] Bourdet, S., Braza, M., Hoarau, Y., El Akoury, R., and Ashraf, A. Prediction and physical analysis of unsteady flows around a pitching airfoil with the dynamic mesh approach. *Revue européenne de mécanique numérique - Fluid Structure Interaction 16* (2007), 451–476.

[20] Bourgoyne, D., Hamel, J., Ceccio, S., and Dowling, D. Time-average flow over a hydrofoil at high Reynolds number. *Journal of Fluid Mechanics 496*, 496 (2003), 365–404.

[21] Bradshaw, P. Turbulent secondary flows. *Annual Review of Fluid Mechanics 19* (1987), 53–74.

[22] Braun, S. Extraction of periodic waveforms by time domain averaging. *Acustica 32*, 2 (1975), 69–77.

[23] Brennen, C. *Hydrodynamics of Pumps.* Oxford University Press and Concepts ETI Inc., 1994.

[24] Breuer, M., Jovičić, N., and Mazaev, K. Comparison of DES, RANS and LES for the separated flow around a flat plate at high incidence. *International Journal for Numerical Methods in Fluids 41*, 4 (2003), 357–388.

[25] Broersen, P. Time series models for spectral analysis of irregular data far beyond the mean data rate. *Measurement Science and Technology 19*, 1 (2008).

[26] Catalano, P., and Amato, M. An evaluation of RANS turbulence modelling for aerodynamic applications. *Aerospace Science and Technology 7*, 7 (2003), 493–509.

[27] Chieng, C., and Launder, B. On the calculation of turbulent heat transport downstream from an abrupt pipe expansion. *American Society of Mechanical Engineers, Heat Transfer Division, HTD 13 3*, 2 , Apr.-Jun. 1980 (1980), 189–207.

[28] Clark, J., and Grover, E. Assessing convergence in predictions of periodic-unsteady flowfields. *Journal of Turbomachinery 129*, 4 (2007), 740–749.

[29] Clarke, D. Designing phase-locked loops for instrumentation applications. *Measurement: Journal of the International Measurement Confederation 32*, 3 (2002), 205–227.

[30] Davidson, L., and Dahlstrom, S. Hybrid LES-RANS: An approach to make les applicable at high reynolds number. *International Journal of Computational Fluid Dynamics 19*, 6 (2005), 415–427.

[31] de Villiers, E. *The Potential of Large Eddy Simulation for the Modeling of Wall Bounded Flows.* PhD thesis, Imperial College of Science, Technology and Medecine, 2006.

[32] Dengel, P., and Fernholz, H. Experimental investigation of an incompressible turbulent boundary layer in the vicinity of separation. *Journal of Fluid Mechanics 212* (1990), 615–636.

[33] Drazin, P., and Reid, W. *Hydrodynamic stability.* Cambridge University Press, 1981.

[34] Dupont, P. *Etude de la dynamique d'une poche de cavitation partielle en vue de la prédiction de l'érosion dans les turbomachines hydrauliques.* PhD thesis, EPFL, LMH, 1991.

[35] Durst, F., A., M., and J.H., W. *Principles and practice of laser-Doppler anemometry.* Academic Press, London, 1981.

[36] Eckhardt, B., Schneider, T., Hof, B., and Westerweel, J. Turbulence transition in pipe flow. *Annual Review of Fluid Mechanics 39* (2007), 447–468.

[37] Ehrich, F.-F. Aerodynamic stability of branched diffusers. *J Eng Power Trans ASME 92 Ser A*, 3 (1970), 330–334.

[38] Eisele, K., Zhang, Z., Casey, M., Gülich, J., and Schachenmann, A. Flow analysis in a pump diffuser - part 1: LDA and PTV measurements of the unsteady flow. *Journal of Fluids Engineering, Transactions of the ASME 119*, 4 (1997), 968–977.

[39] Eng, F., and Gustafsson, F. Downsampling non-uniformly sampled data. *Eurasip Journal on Advances in Signal Processing 2008* (2008).

[40] Faler, J., and Leibovich, S. Disrupted states of vortex flow and vortex breakdown. *Physics of Fluids 20*, 9 (1977), 1385–1400.

[41] Farhat, M., Natal, S., Avellan, F., Paquet, F., and Couston, M. On-board measurements of pressure and strain fluctuations in a model of a low head francis turbine, part 1: Instrumentation. In *Proceedings of the XXIst IAHR Symposium on Hydraulic Machinery and Systems, Lausanne, Switzerland,* (2002).

[42] Felten, F., and Lund, T. Kinetic energy conservation issues associated with the collocated mesh scheme for incompressible flow. *Journal of Computational Physics 215*, 2 (2006), 465–484.

[43] Ferziger, J. H., and Peric, M. *Computational methods for fluid dynamics.* Springer-Verlag, Berlin, 1999.

[44] Frank, S., Heilmann, C., and Siekmann, H. Point-velocity methods for flow-rate measurements in asymmetric pipe flow. *Flow Measurement and Instrumentation 7*, 3-4 (1996), 201–209.

[45] Gallaire, F., Ruith, M., Meiburg, E., Chomaz, J.-M., and Huerre, P. Spiral vortex breakdown as a global mode. *Journal of Fluid Mechanics 549* (2006), 71–80.

[46] Giezendanner, R., Keck, O., Weigand, P., Meier, W., Meier, U., Stricker, W., and Aigner, M. Periodic combustion instabilities in a swirl burner studied by phase-locked planar laser-induced fluorescence. *Combustion Science and Technology 175*, 4 (2003), 721–741.

[47] Ginter, F., and Staubli, T. Numerical analysis of flow instability and hysteresis in a shrouded centrifugal pump impeller. In *American Society of Mechanical Engineers, Fluids Engineering Division* (1998).

[48] Gourdain, N., Burguburu, S., Leboeuf, F., and Miton, H. Numerical simulation of rotating stall in a subsonic compressor. *Aerospace Science and Technology 10*, 1 (2006), 9–18.

[49] Greitzer, E. Stability of pumping systems - the 1980 freeman scholar lecture. *Journal of Fluids Engineering, Transactions 103*, 2 (June 1981), 193–242.

[50] Grossmann, S. The onset of shear flow turbulence. *Reviews of Modern Physics 72*, 2 (2000), 603–618.

[51] Grotjans, H. *Turbulenzmodelle Höherer Ordnung für komplexe Anwendungen.* PhD thesis, TU München, 1999.

[52] Guedes, A., Kueny, J.-L., Dan Ciocan, G., and Avellan, F. Unsteady rotor analysis of a hydraulic pump-turbine - CFD and experimental approach. In *Proceedings of the XXIst IAHR Symposium on Hydraulic Machinery and Systems. Lausanne, September 9.-12.* (2002).

[53] Gugau, M. *Ein Beitrag zur Validierung der numerischen Berechnung von Kreiselpumpen.* PhD thesis, TU Darmstadt, 2004.

[54] Gülich, J.-F. *Centrifugal Pumps.* Springer-Verlag, Berlin, 2008.

[55] Gülich, J. F., and Egger, R. Part-load flow and hydraulic stability of centrifugal pumps, tr-100219. Tech. rep., EPRI, 1992.

[56] Haller, G. Exact theory of unsteady separation for two-dimensional flows. *Journal of Fluid Mechanics 512* (2004), 257–311.

[57] Hamkins, C., and Flack, R. Laser velocimeter measurements in shrouded and unshrouded radial flow pump impellers. *Journal of Turbomachinery 109*, 1 (1987), 70–76.

[58] Harris, F. On the use of windows for harmonic analysis with the discrete fourier transform. *Proceedings of the IEEE 66*, 1 (1978), 51–83.

[59] Henry, P. *Turbomachines hydrauliques - Choix illustré de réalisations marquantes.* Presses polytechniques et universitaires romandes, Lausanne, 1992.

[60] Herbst, A., and Henningson, D. The influence of periodic excitation on a turbulent separation bubble. *Flow, Turbulence and Combustion 76*, 1 (2006), 1–21.

[61] Hergt, P., and Brenner, R. Visuelle Untersuchung der Strömung im Leitrad einer Kreiselpumpe. *Schweizerische Bauzeitung 86*, 40 (1968), 716–720.

[62] Herley, C., and Wong, P. W. *Efficient Minimum Rate Sampling of Signals with Frequncy Support over Non-Commensurable Sets.* Birkhaeuser, 2001, ch. 13, pp. 271–291.

[63] Hodder, A. *Double-fed asynchronous motor-generator equipped with a 3-level VSi cascade.* PhD thesis, Ecole polytechnique fédérale de Lausanne, 2004.

[64] Hodkiewicz, M. R. *The effect of partial-flow operation on the axial vibration of double-suction centrifugal pumps.* PhD thesis, University of Western Australia, 2005.

[65] Horlock, J. H., and Lakshminarayana, B. Secondary flows - theory, experiment and application in turbomachinery aerodynamics. *Annual Review Of Fluid Mechanics 5* (1973), 247–280.

[66] Höss, B., Leinhos, D., and Fottner, L. Stall inception in the compressor system of a turbofan engine. *Journal of Turbomachinery 122*, 1 (2000), 32–44.

[67] Hüttl, T. J., and Friedrich, R. Direct numerical simulation of turbulent flows in curved and helically coiled pipes. *Computers & Fluids 30*, 5 (June 2001), 591–605.

[68] Inoue, M., Kuroumaru, M., Yoshida, S., and Furukawa, M. Short and long length-scale disturbances leading to rotating stall in an axial compressor stage with different stator/rotor gaps. *Journal of Turbomachinery 124*, 3 (2002), 376–384.

[69] Jaberg, H., and Hergt, P. Head curve stability in radial pumps. In *Proceedings of the 1997 2nd European Conference on Turbomachinery - Fluid Dynamics and Thermodynamics, Antwerpen, Belgium, 5-7 March* (University of Technology, Graz, Austria, 1997), pp. 365–372.

[70] Johnson, D. A., Pedersen, N., and Jacobsen, C. Measurements of rotating stall inside a centrifugal pump impeller. In *Proceedings of FEDSM2005 2005 ASME Fluids Engineering Division Summer Meeting and Exhibition* (June 19-23 2005).

[71] Jones, W., and Launder, B. The prediction of laminarization with a two-equation model of turbulence. *International Journal of Heat and Mass Transfer 15*, 2 (1972), 301–314.

[72] Joubarne, E., Guibault, F., Braun, O., and Avellan, F. Vorticity-based mesh adaptation for vortex capture. In *10th ISGG Conference on Numerical Grid Generation, Crete, Greece* (2007).

[73] Kaltenbach, H.-J., Fatica, M., Mittal, R., Lund, T., and Moin, P. Study of flow in a planar asymmetric diffuser using large-eddy simulation. *Journal of Fluid Mechanics 390* (1999), 151–185.

[74] Kaupert, K., Holbein, P., and Staubli, T. A first analysis of flow field hysteresis in a pump impeller. *Journal of Fluids Engineering, Transactions of the ASME 118*, 4 (1996), 685–691.

[75] Kergourlay, G., Younsi, M., Bakir, F., and Rey, R. Influence of splitter blades on the flow field of a centrifugal pump: Test-analysis comparison. *International Journal of Rotating Machinery 2007* (2007), –.

[76] Kiya, M., Shimizu, M., and Mochizuki, O. Sinusoidal forcing of a turbulent separation bubble. *Journal of Fluid Mechanics 342* (1997), 119–139.

[77] Krause, N., Zähringer, K., and Pap, E. Time-resolved particle imaging velocimetry for the investigation of rotating stall in a radial pump. *Experiments in Fluids 39*, 2 (2005), 192–201.

[78] Lakshminarayana, B. *Fluid Dynamics and Heat Transfer of Turbomachinery.* John Wiley and Sons, New York, 1996.

[79] Lardeau, S., and Leschziner, M. A. Unsteady RANS modelling of wake-blade interaction: computational requirements and limitations. *Computers & Fluids 34*, 1 (2005), 3–21.

[80] Launder, B. Second-moment closure and its use in modelling turbulent industrial flows. *International Journal for Numerical Methods in Fluids 9*, 8 (1989), 963–985.

[81] Launder, B. Current capabilities for modelling turbulence in industrial flows. *Applied Scientific Research 48*, 3-4 (1991), 247–269.

[82] Launder, B., and Spalding, D. The numerical computation of turbulent flows. *Computer Methods in Applied Mechanics and Engineering 3*, 2 (1974), 269–289.

[83] Lee, T., and Gerontakos, P. Investigation of flow over an oscillating airfoil. *Journal of Fluid Mechanics 512* (2004), 313–341.

[84] Lesieur, M., and Métais, O. New trends in large-eddy simulations of turbulence. *Annual Review of Fluid Mechanics 28* (1996), 45–82.

[85] Liu, X., and Rodi, W. Experiments on transitional boundary layers with wake-induced unsteadiness. *Journal of Fluid Mechanics 231* (1991), 229–256.

[86] Ljevar, S., de Lange, H., and van Steenhoven, A. Two-dimensional rotating stall analysis in a wide vaneless diffuser. *International Journal of Rotating Machinery 2006* (2006), –.

[87] Lund, T., Wu, X., and Squires, K. Generation of turbulent inflow data for spatially-developing boundary layer simulations. *Journal of Computational Physics 140*, 2 (1998), 233–258.

[88] Mahesh, K., Constantinescu, G., and Moin, P. A numerical method for large-eddy simulation in complex geometries. *Journal of Computational Physics 197*, 1 (2004), 215–240.

[89] Mauri, S. *Numerical Simulation and Flow Analysis of An Elbow Diffuser*. PhD thesis, EPFL, LMH, 2002.

[90] Mauri, S., Kueny, J., and Avellan, F. Werlé-legendre separation in a hydraulic machine draft tube. *Journal of Fluids Engineering, Transactions of the ASME 126*, 6 (2004), 976–980.

[91] McDougall, N. M. A comparison between the design point and near-stall performance of an axial compressor. *Journal Of Turbomachinery-Transactions Of The Asme 112*, 1 (Jan. 1990), 109–115.

[92] McDougall, N. M., Cumpsty, N. A., and Hynes, T. P. Stall inception in axial compressors. *Journal Of Turbomachinery-Transactions Of The Asme 112*, 1 (Jan. 1990), 116–125.

[93] Meilen, C., Fröhlich, J., and Rodi, W. Lessons from LESFOIL project on large-eddy simulation of flow around an airfoil. *AIAA Journal 41*, 4 (2003), 573–581.

[94] Menter, F. Two-equation eddy-viscosity turbulence models for engineering applications. *AIAA journal 32*, 8 (1994), 1598–1605.

[95] Menter, F. A comparison of some recent eddy-viscosity turbulence models. *Journal of Fluids Engineering, Transactions of the ASME 118*, 3 (1996), 514–519.

[96] Menter, F. Eddy viscosity transport equations and their relation to the k-ε model. *Journal of Fluids Engineering, Transactions of the ASME 119*, 4 (1997), 876–884.

[97] Miner, S., Beaudoin, R., and Flack, R. Laser velocimeter measurements in a centrifugal flow pump. *Journal of Turbomachinery 111*, 3 (1989), 205–212.

[98] Miskovish, R., and Brennen, C. Some unsteady fluid forces on pump impellers. *Journal of Fluids Engineering, Transactions of the ASME 114*, 4 (1992), 632–637.

[99] Miyabe, M., Maeda, H., Umeki, I., and Jittani, Y. Unstable head-flow characteristic generation mechanism of a low specific speed mixed flow pump. *Journal of Thermal Science 15*, 2 (2006), –.

[100] Monin, A. *Statistical Fluid Mechanics, Vol.1, Mechanics of Turbulence*. MIT Press, Cambridge, 1971.

[101] Muggli, F., Eisele, K., Casey, M., Gülich, J., and Schachenmann, A. Flow analysis in a pump diffuser - part 2: Validation and limitations of CFD for diffuser flows. *Journal of Fluids Engineering, Transactions of the ASME 119*, 4 (1997), 978–984.

[102] Münch, C., and Métais, O. Large eddy simulations in curved square ducts: Variation of the curvature radius. *Journal of Turbulence 8* (2007), 1–18.

[103] Nagahara, T., Inoue, Y., Sato, T., Sakata, S., Nishimura, K., and Kato, C. Investigation of the flow field in a multistage pump by using LES. In *Proceedings of the American Society of Mechanical Engineers Fluids Engineering Division Summer Conference* (2005), vol. 1 PART B, pp. 1321–1329.

[104] Nallasamy, M. Turbulence models and their applications to the prediction on internal flows: a review. *Computers and Fluids 15*, 2 (1987), 151–194.

[105] Nicolet, C. *Hydroacoustic Modelling and Numerical Simulation of Unsteady Operation of Hydroelectric Systems.* PhD thesis, École polytechnique fédérale de Lausanne, 2007.

[106] Nicolet, C., Ruchonnet, N., and Avellan, F. One-dimensional modeling of rotor stator interaction in francis pump-turbine. In *Proceedings of ISROMAC-11, ASME: International Symposium on Transport Phenomena and Dynamics of Rotating Machinery , Honolulu, Hawaii, USA,* (February 26-March 2 2006).

[107] Nikitin, N., Nicoud, F., Wasistho, B., Squires, K., and Spalart, P. An approach to wall modeling in large-eddy simulations. *Physics of Fluids 12*, 7 (2000), 1629–1632.

[108] Nobach, H., Müller, E., and Tropea, C. Efficient estimation of power spectral density from laser doppler anemometer data. *Experiments in Fluids 24*, 5-6 (1998), 499–509.

[109] O'Kubo, E., Hakamata, Y., Tsujimoto, Y., Uemura, T., and Tsurusaki, H. Study on the inertial effective length of two-dimensional centrifugal impeller flow channel. *Nippon Kikai Gakkai Ronbunshu, B Hen/Transactions of the Japan Society of Mechanical Engineers, Part B 57*, 533 (1991), 121–128.

[110] Pannatier, Y., Nicolet, C., Kawkabani, B., Deniau, J., Schwery, A., Avellan, F., and Simond, J.-J. Transient behaviour of variable speed pump turbine units. In *24th Symposium on Hydraulic Machinery and Systems, Foz do Iguassu, Brazil, October27-31* (2008).

[111] Parrondo-Gayo, J., González-Pérez, J., and Fernández-Francos, J. The effect of the operating point on the pressure fluctuations at the blade passage frequency in the volute of a centrifugal pump. *Journal of Fluids Engineering, Transactions of the ASME 124*, 3 (2002), 784–790.

[112] Patankar, S., Pratap, V., and Spalding, D. Prediction of turbulent flow in curved pipes. *Journal of Fluid Mechanics 67*, pt 3 (1975), 583–595.

[113] Pavesi, G., Ardizzon, G., and Cavazzini, G. Unsteady flow field and noise generation in a centrifugal pump impeller with a vaneless diffuser. In *Proceedings of the American Society of Mechanical Engineers Fluids Engineering Division Summer Conference* (2005), vol. 1 PART B, pp. 1331–1338.

[114] Pedersen, N., Byskow, R.-K., and Jacobsen, C.-B. Flow in a centrifugal pump impeller at design and off-design conditions - part ii: Large eddy simulations. *Journal of Fluids Engineeering 125* (January 2003), 73–83. noch lesen.

[115] Pedersen, N., Larsen, P.-S., and Jacobsen, C.-B. Flow in a centrifugal pump impeller at design and off-design conditions - part i: Particle image velocimetry (PIV) and laser doppler velocimetry (LDV) measurements. *Journal of Fluids Engineeering 125* (January 2003), 61–72.

[116] Perrig, A. *Hydrodynamics of the free surface flow in Pelton turbine buckets.* PhD thesis, Ecole polytechnique fédérale de Lausanne, 2007.

[117] Piomelli, U. Recent development in large-eddy simulations. In *Proceedings of the 1999 3rd ASME/JSME Joint Fluids Engineering Conference, FEDSM'99, San Francisco, California, USA, 18-23 July* (1999), pp. 1–.

[118] Poinsot, T. Boundary conditions for direct simulations of compressible viscous flows. *Journal of Computational Physics 101*, 1 (1992), 104–129.

[119] Rabiner, L., and Crochiere, R. *Multirate digital signal processing.* Prentice Hall, Englewood Cliffs, 1983.

[120] Roache, P.-J. *Verification and validation in computational science and engineering / by Patrick J. Roache.* Hermosa, Albuquerque, NM, 1998.

[121] Ruchonnet, N. Modélisation mono dimensionnelle des interactions rotor stator dans les pompes turbines francis. Master's thesis, EPFL, 2005.

[122] Ruelle, D., and Takens, F. On the nature of turbulence. *Communications in Mathematical Physics 20*, 3 (1971), 167–192.

[123] Ruith, M., Chen, P., Meiburg, E., and Maxworthy, T. Three-dimensional vortex breakdown in swirling jets and wakes: Direct numerical simulation. *Journal of Fluid Mechanics 486*, 486 (2003), 331–378.

[124] Rütten, F., Schröder, W., and Meinke, M. Large-eddy simulation of low frequency oscillations of the dean vortices in turbulent pipe bend flows. *Physics of Fluids 17*, 3 (2005), –.

[125] Sano, T., Nakamura, Y., Yoshida, Y., and Tsujimoto, Y. Alternate blade stall and rotating stall in a vaned diffuser. *JSME International Journal, Series B: Fluids and Thermal Engineering 45*, 4 (2002), 810–819.

[126] Sano, T., Yoshida, Y., Tsujimoto, Y., Nakamura, Y., and Matsushima, T. Numerical study of rotating stall in a pump vaned diffuser. *Journal of Fluids Engineering, Transactions of the ASME 124*, 2 (2002), 363–370.

[127] Schönemann, F. *Vom Schöpfrad zur Kreiselpumpe.* VDI Verlag, Duesseldorf, 1987.

[128] Schwery, A., Fass, E., Henry, M., Bach, W., and Mirzaian, A. Pump storage power plants - ALSTOM's long experience and technological innovations. In *Hydro 2005 - Villach Austria, 17.-20. October* (2005).

[129] Shan, H., Jiang, L., and Liu, C. Direct numerical simulation of flow separation around a NACA 0012 airfoil. *Computers and Fluids 34*, 9 (2005), 1096–1114.

[130] Shi, F., and Tsukamoto, H. Numerical study of pressure fluctuations caused by impeller-diffuser interaction in a diffuser pump stage. *Journal of Fluids Engineering, Transactions of the ASME 123*, 3 (2001), 466–474.

[131] Siekmann, H. E. *Strömungslehre - Grundlagen.* Springer, Berlin, 2000.

[132] Simpson, R. L. Turbulent boundary-layer separation. *Annual Review of Fluid Mechanics 21*, 1 (1989), 205–232.

[133] Sinha, M., Pinarbasi, A., and Katz, J. The flow structure during onset and developed states of rotating stall within a vaned diffuser of a centrifugal pump. *Journal of Fluids Engineering, Transactions of the ASME 123*, 3 (2001), 490–499.

[134] Soranna, F., Chow, Y.-C., Uzol, O., and Katz, J. The effect of inlet guide vanes wake impingement on the flow structure and turbulence around a rotor blade. *Journal of Turbomachinery 128*, 1 (2006), 82–95.

[135] Spalart, P. Strategies for turbulence modelling and simulations. *International Journal of Heat and Fluid Flow 21*, 3 (2000), 252–263.

[136] Spalart, P., and Allmaras, S. One-equation turbulence model for aerodynamic flows. *Recherche aerospatiale 1*, 1 (1994), 5–21.

[137] Spalart, P., Deck, S., Shur, M., Squires, K., Strelets, M., and Travin, A. A new version of detached-eddy simulation, resistant to ambiguous grid densities. *Theoretical and Computational Fluid Dynamics 20*, 3 (2006), 181–195.

[138] Spence, R., and Amaral-Teixeira, J. Investigation into pressure pulsations in a centrifugal pump using numerical methods supported by industrial tests. *Computers and Fluids 37*, 6 (2008), 690–704.

[139] Stricker, H. *Strömungstechnische Untersuchungen axialer Laufräder von Rührwerken der kommunalen Abwasserbehandlung.* PhD thesis, TU Berlin, 1996.

[140] Tamm, A. *Beitrag zur Bestimmung der Wirkungsgrade einer Kreiselpumpe durch theoretische, numerische und experimentelle Untersuchungen.* PhD thesis, TU Darmstadt, Fachbereich Maschinenbau, 2002.

[141] Temmerman, L., Leschziner, M., Mellen, C., and Fröhlich, J. Investigation of wall-function approximations and subgrid-scale models in large eddy simulation of separated flow in a channel with streamwise periodic constrictions. *International Journal of Heat and Fluid Flow 24*, 2 (2003), 157–180.

[142] Tennekes, H., and Lumley, J. *A first course in turbulence.* MIT Press, 1976.

[143] Tobak, M., and Peake, D. J. Topology of three-dimensional separated flows. *Annual Review of Fluid Mechanics 14* (1982).

[144] Treutz, G. *Numerische Simulation der instationären Strömung in einer Kreiselpumpe.* PhD thesis, TU Darmstadt, Fachbereich Maschinenbau, 2002.

[145] Tunstall, M., and Qarvey, J. On effect of sharp bend in fully developed turbulent pipe flow. *Journal of Fluid Mechanics 34*, pt 3 (1968), 595–608.

[146] Ubaldi, M., and Zunino, P. An experimental study of the unsteady characteristics of the turbulent near wake of a turbine blade. *Experimental Thermal and Fluid Science 23*, 1-2 (2000), 23–33.

[147] Wang, H., and Tsukamoto, H. Fundamental analysis on rotor-stator interaction in a diffuser pump by vortex method. *Journal of Fluids Engineering, Transactions of the ASME 123*, 4 (2001), 737–747.

[148] Wang, H., and Tsukamoto, H. Experimental and numerical study of unsteady flow in a diffuser pump at off-design conditions. *Journal of Fluids Engineering, Transactions of the ASME 125*, 5 (2003), 767–778.

[149] Wang, P., Bai, X., Wessman, M., and Klingmann, J. Large eddy simulation and experimental studies of a confined turbulent swirling flow. *Physics of Fluids 16*, 9 (2004), 3306–3324.

[150] Watanabe, H., and Tsukamoto, H. Numerical study of unsteady flow in inducer mounted diffuser pumps at design and off-design conditions. In *24th Symposium on Hydraulic Machinery and Systems, Foz do Iguassu, Brazil, October27-31* (2008).

[151] Welch, P. The use of fast fourier transform for the estimation of power spectra: A method based on time averaging over short, modified periodograms. *IEEE transactions on audio and electroacoustics 15*, 2 (1967).

[152] Wen, C.-Y., and Lin, C. Two-dimensional vortex shedding of a circular cylinder. *Physics of Fluids 13*, 3 (2001), 557–558.

[153] Wernert, P., and Favier, D. Considerations about the phase averaging method with application to ELDV and PIV measurements over pitching airfoils. *Experiments in Fluids 27*, 6 (1999), 473–483.

[154] Wilcox, D. C. *Turbulence Modeling for CFD.* DCW Industries, 1998.

[155] Wilcox, D. C. *Basic Fluid Mechanics.* DCW Industries, 2000.

[156] Williamson, C. Vortex dynamics in the cylinder wake. *Annual Review of Fluid Mechanics 28* (1996), 477–539.

[157] Wissink, J., and Rodi, W. Direct numerical simulation of flow and heat transfer in a turbine cascade with incoming wakes. *Journal of Fluid Mechanics 569* (2006), 209–247.

[158] Wissink, J., and Rodi, W. Direct numerical simulations of transitional flow in turbomachinery. *Journal of Turbomachinery 128*, 4 (2006), 668–678.

[159] Yamanishi, N., Fukao, S., Qiao, X., Kato, C., and Tsujimoto, Y. LES simulation of backflow vortex structure at the inlet of an inducer. *Journal of Fluids Engineering, Transactions of the ASME 129*, 5 (2007), 587–594.

[160] Zhang, M., and Tsukamoto, H. Unsteady hydrodynamic forces due to rotor-stator interaction on a diffuser pump with identical number of vanes on the impeller and diffuser. *Journal of Fluids Engineering, Transactions of the ASME 127*, 4 (2005), 743–751.

[161] Zhao, C., Hobbs, B., Mühlhaus, H., and Ord, A. A consistent point-searching algorithm for solution interpolation in unstructured meshes consisting of 4-node bilinear quadrilateral elements. *International Journal for Numerical Methods in Engineering 45*, 10 (1999), 1509–1526.

[162] Zobeiri, A. *Time dependent phenomena in Francis Turbines.* PhD thesis, École polytechnique fédérale de Lausanne, 2009.

[163] Zobeiri, A., Kueny, J.-L., Farhat, M., and Avellan, F. Pump-turbine rotor-stator interactions in generating mode: Pressure fluctuation in distributor channel. In *23rd IAHR Symposium - Yokohama* (2006).

Olivier BRAUN

LIN - EPFL
Station 9
CH-1015 Lausanne (VD)

Tél. prof.:	+41 21 693 5906	
Portable:	+41 79 712 6376	Né le 24 août 1973
E-mail prof.:	olivier.braun@epfl.ch	Nationalité allemande
E-mail privé:	olivier.braun@web.de	Célibataire

FORMATION

2004-2009:	**Doctorat ès sciences techniques** École polytechnique fédérale de Lausanne (EPFL), Suisse
1991-2001:	**Dipl.-Ing. Maschinenbau** Technische Universität Berlin, Allemagne
1983-1991:	**Lycée Francais de Berlin, Allemagne** Baccalauréat C Abitur - cours approfondis Mathématiques, Physique

EXPÉRIENCES

2004-2009:	**École polytechnique fédérale de Lausanne (EPFL), Suisse.**
2004-2008:	**Laboratoire de Machines Hydrauliques (LMH).** Thèse de Doctorat: Part Load Flow in Centrifugal Pumps
Projets:	CTI-6806.1 Partload Stability en collaboration avec Sulzer Ltd, Winterthur Hydrodyna II Eureka 4150 en collaboration avec Andritz Hydro, Voith-Siemens Hydro, Alstom Power Hydro
2008-2009:	**Laboratoire d'Ingénierie Numérique (LIN).**
Projet:	Hydroptère - Optimisation par algorithme évolutionnaires et LES appliquées aux éléments porteurs d'un voilier sur hydrofoils
2001-2003:	**ANSYS Germany GmbH, Otterfing, Allemagne** Ingénieur support clientèle en CFD Support a l'utilisation, formation, développement d'outils spécialisés
1996-2001:	**Développeur de logiciel freelance** Implémentation d'un logiciel de calcul de parcours d'outils et optimisation de stratégies d'usinage pour aubes de compresseur de turbine à gaz clients: Siemens AG, Berlin, Allemagne; Erökar, Budapest, Hongrie
1993-1996:	**Siemens AG, KWU, Gasturbinenwerk Huttenstrasse** Divers stages d'usinage, de montage et d'ingénierie

COMPÉTENCES INFORMATIQUES

Systèmes:	Windows, Linux, AIX.
Program.:	C, C++, Fortran, Perl, MATLAB, Visual Basic
CFD:	CFX, Fluent, ICEM, OpenFoam, Paraview.
Bureautique:	MS-Office, LaTeX.
Multimédia:	Adobe Illustrator, Adobe Premiere

LANGUES

Allemand	Langue maternelle.
Français	Parlé, lu et écrit: couramment.
Anglais	Parlé, lu et écrit: bien.